UNIVERSITY OF LIVERPOOL

CHALLENGES IN THE SIMULATION OF LARGE SCALE, MEDIUM EXPOSED, INORGANIC NANOTUBES

Thesis submitted in accordance with the requirements of the University of Liverpool for the degree of Doctor in Philosophy

by

Emiliano Poli

Department of Chemistry

30/09/2015

Declaration

This dissertation describes work carried out between October 2011 and October 2015 in the Theory of Condensed Matter group at the Stephenson Institute for Renewable Energy, Liverpool, under the supervision of Dr. Gilberto Teobaldi.

I hereby declare that except where specific reference is made to the work of others, the contents of this dissertation are original and have not been submitted in whole or in part for consideration for any other degree or qualification in this, or any other university. This dissertation is my own work and contains nothing which is the outcome of work done in collaboration with others, except as specified in the text and Acknowledgements.

This dissertation contains fewer than 72,400 words including appendices, bibliography, footnotes, tables and equations.

Acknowledgments

The research presented in this thesis was made possible by support from EPSRC-UK (EP/I004483/1), which is gratefully acknowledged. This work made use of the University of Liverpool's, the N8 (EPSRC EP/K000225/1), ARCHER (via the UKCP Consortium, EP/K013610/1), and the STFC Hartree Centre (Daresbury Laboratory, UK) High Performance Computing facilities. The STFC Hartree Centre is a research collaboratory in association with IBM providing High Performance Computing platforms funded by the UK's investment in e-Infrastructure.

A special thank goes to "the General" Carlotta that supported me in all my decisions for four years. Without her I would not even started a Ph.D. All this work was possible thanks to her support and love.

I would also like to thank Dr. Gilberto Teobaldi, Dr. Ivan Scivetti and (future Dr.) Joshua Elliott that made this research possible. Without their friendship, advices, help and support I would have never be able to finish my Ph.D.

I am also grateful to the "Italians" that have been my companions through these years: Tommaso, Enzo, Luigi, Sergio and everyone that made my life in Liverpool a fantastic experience and not just a difficult, day to day, grind to finish the Ph.D.

To end I want to thank my family that has been supporting me for twenty nine years and counting. They are the best.

Dissemination List

The work presented in this thesis has been completely or partially disseminated via the following peer-reviewed journal articles:

- **E. Poli**, J.D. Elliott and G. Teobaldi. *Materials Research Innovations* 19, S272 (2015). *Large scale Density Functional Theory simulation of inorganic nanotubes: a case study on Imogolite nanotubes.*
- **E. Poli**, J. D. Elliott, L. E. Ratcliff, L. Andrinopoulos, J. Dziedzic, N. D. M. Hine, A. A. Mostofi, C. K. Skylaris, P. D. Haynes and G. Teobaldi, *J. Phys.: Condens. Matter*, in press. *The potential of Imogolite nanotubes as (co-)photocatalyst: a linear-scaling Density Functional Theory study*. This paper has been selected by the Editors for *J. Phys.: Condens. Matter LabTalk* research highlights: "Enhanced photocatalysis with inorganic open-ended nanotubes?"
- **E. Poli** and G. Teobaldi. *Cation-vacancy defects in aluminosilicate NTs: a linear-scaling DFT study*. To be submitted.
- **E. Poli**, J. D. Elliott and G. Teobaldi. *Termination effects and longitudinal band-bending in Imogolite nanotubes*. To be submitted.
- M. S. Amara, S. Rouzière, E. Paineau, **E. Poli,** J. D. Elliott, G. Teobaldi and P. Launois. *Quantitative X-ray and linear-scaling DFT resolution of the atomic structure of metal oxide nanotubes: the Imogolite case*. To be submitted.
- **E. Poli** and G. Teobaldi. *Hole-trapping at defective Imogolite Nanotubes: a constrained linear-scaling DFT study*. To be submitted.
- **E. Poli**, J. D. Elliott and G. Teobaldi. *Electron affinity sign inversion for molecular adsorbates at polarising inorganic nanotubes: impossible reduction made possible?* In preparation.

and **orally** presented, as contributed talk, at two internationally meetings:

- **E. Poli**, Cation-vacancy and electron-hole relaxation in single-walled aluminosilicate nanotubes: a linear-scaling Density Functional Theory study. Q14.00009 contribution to the American Physical Society March Meeting 2015. San Antonio, Texas, USA, March 2-6 2015.
- **E. Poli**, Cation-vacancy and electron-hole relaxation in single-walled aluminosilicate nanotubes: A linear-scaling density functional theory study. INOR-941 contribution to the American Chemical Society March Meeting 2015. Denver, Colorado, USA, March 22-26 2015.

Poster presentation at National and International meetings (6 events) are not reported for sake of brevity.

Contents

Emiliano Poli

Challenges in the simulation of large-scale, medium exposed, inorganic nanotubes

Prompted by growing environmental and energy concerns, increasing research is dedicated to the development of technologies capable of sustainably converting sunlight into commercially viable forms of energy such as chemical fuels. Crucial to this energy conversion is the availability of materials, photo-catalysts (PCs), capable of promoting redox chemistry following absorption of light. Since the macroscopic efficiency of PCs is governed by the atomistic details of the PCs interfaces with media and reactants, increasingly large efforts have been dedicated to the characterization and understanding of these interfaces, also by mean of first principle simulations.

In this context, we present a theoretical investigation of a rapidly growing class of one-dimensional nanomaterial, Imogolite nanotubes (Imo NTs), whose potential for photo-catalysis has so far been overlooked.

The first Chapter of the Thesis provides an overview of the current state of the art for research in PCs, and the theoretical framework needed for atomic-scale understanding and informed development of PCs. The computational underpinning of the research carried out for this Thesis, namely Density Functional Theory (DFT) and its linear-scaling (LS) implementation in the ONETEP program is presented and discussed in Chapter 2.

Ahead of presentation of the results of my original research, a small literature review on Imo NTs is provided in Chapter 3. Chapter 4 illustrates the applicability of LS-DFT to Imo NTs and, by mean of detailed benchmarking, sets best practice for simulations of these systems.

The potential of Imo NTs as (co-)PCs is explored in Chapter 5, where an extensive study of the structure, wall-polarization, absolute band-alignment, band-separation, and optical properties of several Imo NTs is presented and discussed. The simulations suggest possible profitable use of Imo NTs for both photo-reduction and hole-scavenging purposes. The occurrence of (near-)UV charge-transfer excitations is also observed, which may be effective for electron-hole separation and enhanced photo-catalytic performances. Finally, the effects

of the NTs' wall-polarization on the absolute alignment of electron and hole acceptor states of interacting water (H_2O) molecules are quantified and discussed.

Chapter 6 reports an extensive study of defects in Imo NTs. Electronic and optical characterization of the defective Imo NTs suggests energetically favourable separation of photo-generated electrons and holes via relaxation to different defect-sites, with the ensuing possibility of defect-centred photo-redox activity in defective Imo NTs.

The Thesis ends with the investigation of termination effects in Imo NTs. Chapter 7 presents results on the structural, electronic and optical characterization of representative finite Imo NTs models capable of simultaneous description of the NT-ends and bulk-like NT-core. The simulations reveal the presence of longitudinal band-bending and of NT core-end bands-separations, which in turn suggests advantageous relaxation mechanisms for photo-generated e*-h pairs along the NT axis, to the potential benefit of Imo NTs photo-catalytic reactivity.

CHALLENGES IN THE SIMULATION OF LARGE SCALE, MEDIUM EXPOSED, INORGANIC NANOTUBES

Chapter 1

Semiconductors for photo-catalysis: state of the art and underpinning theory

Abstract

This Chapter presents an overview of current research in photo-catalysis and the underpinning physical concepts. After an initial review of the state of the art experimental techniques to synthesise and engineer photo-catalysts (PCs), the theoretical concepts needed for the modelling of heterogeneous photo-catalytic processes are outlined. Particular attention is paid to the charge carrier generation-recombination in pristine and defective semiconductors and to the theoretical framework to describe charge transfer processes at the atomic scale. These concepts are needed to appreciate the link between macroscopic functioning of PCs and their atomic-structure and electronic properties, which is the research subject of this Thesis.

1.1 Background

A recently released United Nations (UN) report on the World Population Situation [1] provides compelling evidence on the ever increasing number of the global population. The report projects the world population to reach around 8.1 billion in 2025 and 9.6 billion in 2050. The UN report highlights a well-defined trend towards urbanization and ensuing growth of cities. Such trend is stronger in emerging countries that are undergoing a heavy process of industrialisation. These factors are the main players determining the exponential increase in energy request, consumption [2] and global pollution [3].

Many official reports [4, 5] stress the necessity of a change in the paradigms that define the current energy production, consumption and human environmental impact. It is clear that the fossil fuels consumption has to be gradually decreased to make space to alternative clean and renewable energy resources. The development and employment of these clean and renewable energy sources would be highly beneficial to diminish the environmental impact of humankind.

The World Health Organization's data on pollution of air [6], water [7] soil [8] and the International Energy Agency report on energy demand/consumption [9] altogether draw a grim picture of the state of the global environment resources. In this context, development of new sustainable technologies for energy production and/or waste disposal has become a central point of the international political agenda [10, 11, 12].

On these grounds, research on new functional materials to develop novel chemical technologies has been attracting constantly increasing interest. The Material Genome Initiative recently sponsored by the USA government is just one of the most prominent examples [13]. Photoactive materials, capable of absorbing and transforming (solar) light energy into chemical fuels or other industrially form such as current density, have been unquestionably instrumental in giving rise to new applications for alternative energy and environmental technologies.

Since the seminal discover of H_2O photolysis on TiO_2 electrode by Fuijshima and Honda in 1972 [14], the photo-response and chemical reactivity of semiconducting materials has been subject of extensive research. The interest in this class of compounds is rooted in their capability of converting the photon energy to initiate or influence a chemical reaction by energy or charge transfer. Such process is referred to as heterogeneous photo-catalysis (HPC). HPC has been accepted as potentially viable alternative to the traditional physicochemical process employed in the removal of pollutants from the environment and as a method for water photolysis and solar fuels generation. Such recognition is due to the impressive environmental advantages that HPC can offer: non-toxicity, total removal of pollutants and their by-products and high cost-effectiveness [15, 16, 17, 18, 19]. The rise in importance and impact of this field can be easily visualised by a simple research on the number of related publications and citations (see Fig. 1.1).

Persistent efforts over the last 40 years have led to significant progress in the field of HPC. Various are the examples of already commercialised technologies such as air purifier or self-cleaning windows [21]. In spite of these promising results, the development of HPC processes for the most important applications such as: molecular hydrogen production [22], organic fuels generation and the removal of CO_2 [23], pesticides [24], dyes [25], alophenoles [26] and other relevant pollutant from atmosphere and water are still not sufficiently developed to be used in commercial or industrial applications.

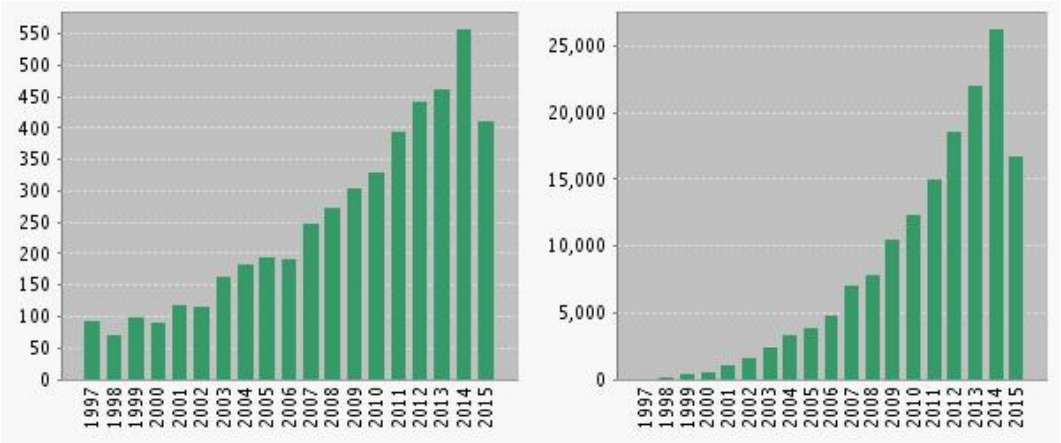

Figure 1.1. Number of publications per year (left panel) and citations per year (right panel) since 1997 obtained from a literature research using the string "heterogeneous photocatalysis*" [20]

The major challenge that the scientific community is currently facing is to find/develop semiconducting materials, the natural candidates for a heterogeneous photo-catalytic process, with the following properties: able to absorb in the visible/UV range, high charge carriers mobility, low defect presence to prevent charge recombination (vide infra), chemically and biologically inert and photo-stable, inexpensive, non-toxic and made of abundant elements.

Many of the inorganic semiconducting photo-catalysts (PCs) that have been extensively studied until now present some of these characteristic but all of them also suffer from heavy intrinsic limitations. Few notable examples are: ZnO photo-corrodes [27], CdS and CdTe are toxic [28, 29], $AgNbO_3$ is extremely expensive [30], WO_3 and SnO_2 are highly unstable in aqueous media [31, 32], and α-Fe_2O_3 and $SrTiO_3$ present a charge carrier recombination rate that is too high, leading, to date, to unviably low photo-catalytic efficiencies [33, 34]. A separate consideration needs to be done for TiO_2; the outstanding properties of this material have made it the focus of intense research and development of various commercial products based on it [35]. In spite of the remarkable results obtained, TiO_2 does present heavy limitations most notably the fact that, given its large band gap, TiO_2 can only absorb and utilise 5% of the total solar energy reaching the earth surface (daily average ~ 6 KWh/m^2 hence ~ 0.3 KWh/m^2).

The current limitations of the materials involved in HPC processes become self-evident considering that, in the last 40 years, more than 130 different inorganic semiconducting materials have been discovered and tested as photo-catalysts against the water splitting process. However, the highest efficiency obtained under visible light still remains under 3% [36].

In order to move past these limitations development and testing of innovative HPCs has been receiving growing interests from both the academic and industrial communities. This chapter provides an overlook on the practical and theoretical concepts and phenomena that needs to be harnessed and simultaneously fulfilled for the development of new photo-catalytic semiconductors.

1.2. The Physics of semiconducting photo-catalysts

1.2.1 Energy Band engineering.

The band structure, alignment and the band gap (BG) energy of a semiconductor are crucial for its functioning as PC. They govern the migration of carriers and the redox drive of excited electron and holes. The BG energy governs the energy of the photons which can absorbed by the material and the maximum energy of the photo-excited electron-hole (e*-h) pairs. Consequently, ongoing research efforts in photo-catalysis are targeted to the definition of systems with a BG allowing visible light absorption and suitable bands alignment with respect to selected reactants and pollutants.

The ideal BG to exploit the solar spectrum is between 1.6 and 3.1 eV, ideally matching the sun radiance peak at 1.6-2.1 eV [37]. Although absorbance of visible light is certainly desirable, the BG value just by itself has little use. In order to be effective in charge transfer (CT) processes the bands of the PC need to be suitably aligned with respect to the highest occupied molecular orbital (HOMO) for photo-oxidation, and the lowest unoccupied molecular orbital (LUMO) of the reactant considered for photo-reduction [37, 38]. Pending electron transfer kinetics considerations (vide infra), such an alignment will in principle permit the transfer of the photo-generated charge carriers (electrons and holes) from the PC to the reactant of interest.

To achieve a good compromise between the BG value and bands alignments is a formidable challenge, which can only be met by extensive understanding and careful engineering of materials (and their interfaces with the medium, vide infra). Precise modulation of the PC properties can be obtained in many different ways. The most common routes involve doping the semiconductor with different elements or solid-solution strategies. Other schemes to control the materials properties have been emerging in the last few years such as the synthesis of hierarchical composite structures and the functionalization of the photo-catalyst with visible light-sensitizer [38].

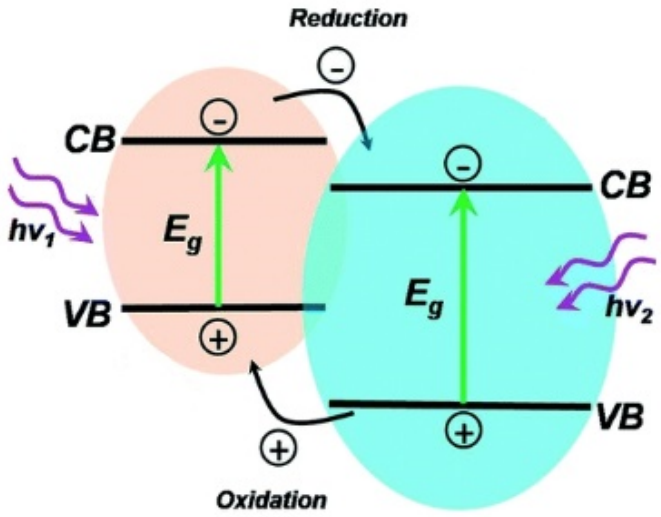

Figure 1.2. Illustration of the photo-oxidation and photo-reduction processes between two systems with different band-gap energies (E_g).

The band structure modification process normally follows three different approaches: (i) engineering of the Valence Band (VB) position with respect to the vacuum level, (ii) modification of the Conduction Band (CB), and (ii) continuous tuning of the VB and/or CB. These approaches are reviewed in the following Sections, and the corresponding state of the art presented.

1.2.1.1. VB modification

VB modification of semiconductors is generally obtained in two ways: doping with 3d-transition elements cations in d^{10} or $d^{10}s^2$ configuration or doping with non-metal elements anions.

Over the years, cation doping with 3d-transition elements has been one of the most commonly used strategies to narrow a semiconductor BG. The doping process relies on electron hybridisation of the *3d* levels of the dopant with the VB in order to shift the top edge of the VB higher in energy. The *3d* energy level position can be tuned by varying the concentration of the dopant. Various examples of this approach can be found in literature. Some of the most notable are: Cr, V, Mn, Fe, Nb, Mo, W, Nd, Ge, Sn and Pb doping of TiO_2 [39, 40, 41, 42] or Ni doping of $InTaO_4$ [43].

This BG modulation technique presents some crucial disadvantages. Introducing impurity ions in the lattice of the photo-catalyst creates a huge amount of defects in the structure and states in the BG that can act as electron and hole traps and recombination centres, quenching any further photochemical reactivity. The presence of localised d-states is also known to suppress the mobility of charge carriers in semiconductors [44, 45].

Non-metal anion doping is based on electron hybridisation of the dopant *2p* or *3p* states (from N, O, P, S, etc) with the top of the semiconductor VB of the semiconductor. These dopant states usually sit just above the VB edge. Debate is still ongoing in the scientific community on whether these states are really due to the dopant or to the impurity induced defects [46]. Although the physics behind them is still unclear, it is empirically established that the doping process leads to narrowing of the BG, which can be accordingly reduced to match the visible spectrum as required for visible-light PCs.

Anion doping presents considerable intrinsic limitations too. At low doping levels, the effects obtained are limited and the narrowing of the BG does not usually exceed 0.3 eV [47]. For higher levels of doping a larger narrowing of the BG can be obtained. However, the insertion of such a high concentration of anions can create severe instabilities in the PC. These instabilities usually lead to the decomposition of the photo-catalytic material with the formation of oxysulfides or oxynitrides [48, 49].

1.2.1.2. CB modification

Tuning of the CB of photo-catalytic materials has long attracted an incredible amount of interest since it is extremely difficult to find materials with the CB at a suitable level to reduce species of interest like H^+ to produce H_2, CO_2 to produce HCOOH or O_2 to produce $\bullet O_2^-$. The tuning of the CB has been proved substantially more challenging than VB-engineering. Narrowing of the BG to promote absorption of visible light is usually counter-productive when it comes to properly align the CB to the right potential to reduce species of interest. Depending on the type of material used as PC, the approach to the modulation of the CB can change. CB-engineering via doping is generally phenomenological and it is very difficult to find a general trend, contrary to doping-based approaches for VB modification.

Sato et al. have worked extensively on indates and antimonates such as $XInO_2$ (X=Li, Na), $YInO_4$ (Y=Ca, Sr), $Z_2Sb_2O_7$ (Z=Ca,Sr) and $CaSb_2O_6$. The substitution of alkali metal and alkaline-earth metal with elements lower in the periodic table proved useful in lowering CB edges (up to ~1.6 eV) [50].

The CB of semiconductor containing IIIa-group elements such as Bi_2XNbO_7 (X=Al, Ga, In) can be modulated if combined with narrow BG oxides such as Ag_2O_3, Fe_2O_3 and Cu_2O. In these cases, the narrow BG material in the solid-solutions helps to introduce visible light absorbance in the PC. The *s* and *sp* states of the IIIa-group elements in Bi_2XnbO_7 compounds are too high in energy and usually give rise to absorption in the UV region of the spectra. The mixing with the CB of the narrow BG material usually shifts these states down in energy.

Similar results have been reported following extensive work by Ouyang and co-workers [51]. They fabricated different samples of $AgXO_2$ (X=Al, Ga, In) and theoretically analysed the band structures of these materials. They found that the CB was mainly due to the *5s5p* states of Ag and the sp states from the X element of choice. Choosing X down in the periodic table resulted in a larger narrowing of the BG. However, in those cases where the BG decreased too much, the reduction potential for species of interest was reduced excessively, which further stress the contrasting requirements for the design of a visible-light reduction PC.

Another approach to manipulate the CB is based on the incorporation of d-block cations that have d^0 electronic configuration in the lattice of semiconducting PCs. Example of this approach have been reported for material such as $InXO_4$ (X= V, Nb, Ta) or BYO_4 (Y= Nb, Ta) [52, 53]. The elements of the V-group lower the CB edge and this effect gets smaller as the atomic number decreases. Similar effects have been observed also in system where Cr and Mo where incorporated in the structure [54].

1.2.1.3. Continuous tuning of the VB and/or CB

The type of band manipulations analysed in the previous section show promising results but, as said, present an unsolvable conundrum between visible-light absorbance and the presence of a high-energy, highly reductive, CB-edge. Engineering a material towards the visible light spectra usually leads to suppression of the redox drive for the PC considered. Also VB and CB modulation by doping or element substitution does not allow accurate control of the modifications induced on the material. It is hence more difficult to control the balance between the desired BG and the band alignments wanted. To reach a better control of BG tuning, the production of solid solution (i.e. a solid mixture where the crystal structure of the solvent remains unchanged after addition of a solid solute) PCs with continuously adjustable BG has been extensively explored. In these solid-solutions, the VB and the CB can be tuned separately or simultaneously.

Maeda et al., produced an oxynitride solid-solution $(ZnO)_x(GaN)_{1-x}$ [55] where the O/N and Zn/Ga ratios can be controlled by changing the nitriding process. Since the VB is comprised of N *2p* states and Zn *3d* states, increasing (decreasing) the O/N and Zn/Ga ratios increases (decreases) the repulsion between the p-d states with the net effect of raising the VB top edge and narrowing the BG.

An example of continuously tuneable CB in a PC is given by the series of β-$AgAl_{1-x}Ga_xO_2$ solid-solutions synthesised by Ouyang et al. [56]. The variable Al/Ga ratio allows modulation of the CB-edge composition so that continuous tuning of the BG between 2.19 and 2.83 eV can be obtained.

Continuous control of both CB and VB has been observed by Yao et al. [57] in the solid-solution $Ca_{1-x}Bi_xV_xMo_{1-x}O4$. $Ca_{1-x}Bi_xV_xMo_{1-x}O_4$ by altering the amount of Mo, V and B. In this case, the VB top edge is defined by Bi *6s* states while the bottom CB-edge comprises V *3d* states and Mo *4d* states. Consequently, different BG narrowing can be obtained by controlling the ratio of these elements.

1.2.1.4. Alternative approaches: hierarchical composites and organic dye sensitization

The growing interest in HPC has expanded the type of approaches used to engineer the BG of PCs. Study and synthesis of hierarchical composite structures and chemically functionalised material is nowadays common practice [58]. The idea behind hierarchical composites is to integrate and optimise the characteristic of different semiconductors in a single photo-catalytic system. Many examples, focused on different properties, have appeared in the specialised literature: from visible light sensitization [59], to improved transfer of photo-excited hot electrons to large BG semiconductors [60], to improved charge separation in PCs [61].

In recent years, semiconductor-semiconductor hierarchical structures have been investigated to improve visible light absorption in photo-catalytic systems. A narrow BG semiconductor such as CdS, WO_3 or PbS serves as light sensitizer to create photo-excited electron-hole pairs, which are then partially transferred to a wide band gap material such as ZnO or TiO_2 [62, 63].

This approach has been successful in few cases. However, many issues are still to be solved. The interface between the two semiconductors can lead to an increased presence of defects and enhance charge trapping and recombination. The occurrence of unfavourable band bending effects or local changes in the phases of the two semiconductors near the interface, with consequent undesirable changes in their properties, is another common problem. These, to date unsolved, shortcomings limit the efficiency of PCs obtained using this method, and the overall effectiveness of the approach.

Chemical functionalization towards visible-light sensitization of semiconducting substrates has also been extensively investigated, following the success of the strategy in dye-sensitized solar cells [64]. Sensitization to visible light is usually introduced via organic dyes that, following (visible) light absorption, inject excited charge carriers (electrons) in the semiconductor. While this process has been fruitful in many cases, it needs a high density of dye molecules on the surface of the semiconductor to suitably work, which makes nanostructuring of the system necessary [65]. The largest drawback for sensitized PCs is the stability of these composites, especially of the dye (sensitizer). Most dyes decompose during operation, leading to malfunctioning in the overall device. Another common issue is represented by the choice of the dye. While theoretically it is easy to find a molecule or composite that presents the right alignment of its HOMO and LUMO levels with the bands of

the PCs, in practice many candidates present low coupling with the system leading to unpractically slow kinetics [66] (more on this aspect will follow in Section 1.3.2).

Several other factors need to be taken into account for practical BG engineering. The BG value is dependent also on the temperature and pressure of the system. An increment in temperature usually leads to BG narrowing. This is due to a temperature-driven increase in the oscillations of the atoms of the PC, which in turn leads to sampling of larger atomic distances and hence a smaller BG [67]. For opposite reasons a high external pressure usually leads to an increment of the BG [68].

Another external factor to consider is the solvent/medium where the PC is supposed to operate. Adsorption of molecules of solvent or pollutant at the surface at the semiconductor can produce unwanted charge transfer, band bending effects or passivation of the PC surface changing its chemical, physical at the interface.

1.2.1.5. Limits of the energy band engineering approach

Obtaining the right band structure and bands alignment is of paramount importance in HPC. Hence, bands and BG engineering emerges as the natural choice to design an ideal photo-catalytic behaviour for a given semiconductor.

The importance of this approach is undeniable but too many are the aspects that the screening of material band gaps overlook. The approach to heterogeneous PCs band tuning is almost always phenomenological. The materials screened are usually already known semiconductors that have shown shortcomings as PCs (for example, N-doped rutile or CdS/ZnO co-catalysts) [69, 70]. When new materials are considered, often they are not the product of material engineering, and the exploration of their potential as PCs is just a consequence of their semiconducting and light absorbance properties [71, 72].

The experimental evidences collected by trial and error approaches cannot provide, in most cases, atom- and time-resolved information, which is needed to understand the correlation between the material atomic structure and the photo-catalytic properties (as an example, in many cases the dopant quantity cannot be measured accurately)[69, 73]. It is thus necessary to gain better and deeper insight into the relationships between the material structure and their properties in order to develop novel efficient, functional PCs.

In this aspect the bulk of the current PCs screening process seems to overlook important effects that can play a major role in defining the properties of a PC such as: polarisation effects [74], or the magnetic [75] and mechanochemical [76] properties of the candidate semiconductor. There is a growing literature showing how spontaneous polarization, internal electric fields, the presence of magnetic moment, and changes in the local coordination or

material preparation can drastically change the properties of a semiconductor. Comprehensive studies of these aspects [77, 78, 79] has started to shed light on how important is to consider the heterogeneous photo-catalytic process in all its complexity (not just band-alignments and BGs) to be able to effectively engineer efficient and commercially viable PCs.

1.2.2. Charge carrier formation/mobility/recombination in semiconductors

An efficient heterogeneous photo-catalytic process requires the semiconductor to be capable, upon photo-excitation, of generating a large number of separated charge carriers and efficiently transferring them first at the interface with the medium, and then to the reactants of interest.

A variety of structural parameters, external and internal conditions affects the efficiency of charge carriers generation and transfer through a semiconductor. The aim of this Section is to give a brief outline of the most important factors playing a role in this process.

1.2.2.1. Charge carrier generation

The first fundamental step in a HPC process is light adsorption by the semiconductor and the subsequent separation of charge carriers from the photo-generated electron-hole pairs. This process is inherently complex and can be affected by an incredible vast amount of variables such as the semiconductor particles shape, the light source, the temperature, the medium between semiconductor and light source, the presence of defects in the semiconductor, the presence of external magnetic or electric fields, etc [45]). The following theoretical model of the charge carrier generation is an approximation that considers the semiconductor as a single body with a flat surface receiving light photons, the medium is not considered, no external input of energy is present and the material does not present absorption due to defect centres (this aspect will be treated in Section 1.2.3).

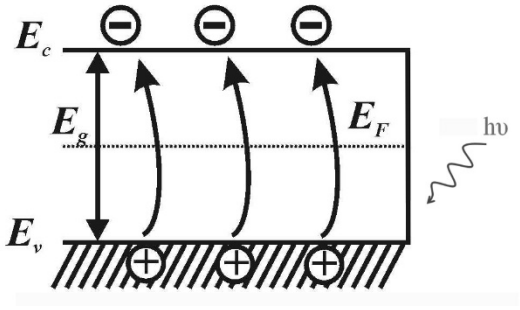

Figure 1.3. A simple model of charge carrier generation via photo-excitation in semiconductors. The semiconductor picture is highly idealised: a single body with a flat face receiving light photons, the medium is not considered, no external input of energy is present and the material does not present absorption due to defect centres.

For photo-excitation to occur, the face of the semiconductor needs to be irradiated by a beam of incident light. I_0 is the light beam intensity. For light-absorbing substances, one can write:

$$I_0 = I_R + I_T + I_A \tag{1.1}$$

where I_R is the reflected beam intensity, I_T is the transmitted beam intensity, and I_A is the absorbed beam intensity.

For moderate values of I_0, the different components can be expressed as:

$$I_R = RI_0 \tag{1.2a}$$

$$I_T = TI_0 \tag{1.2b}$$

$$I_A = AI_0 \tag{1.2c}$$

where R, T and A are the reflectance, transmittance, and absorbance dimensionless coefficients, respectively. Since the light energy needs to be conserved, their sum satisfies the equation:

$$R + T + A = 1 \tag{1.3}$$

The only part of the light beam involved in the generation of charge carrier is the absorbed one that, from Eq. 1.2c, can be expressed as:

$$A = (1 - R)[I - e^{-\alpha d}] \tag{1.4}$$

α is the linear absorption coefficient expressed in cm^{-1} and d is the thickness (in cm) of the plate irradiated.

The linear absorption coefficient α, dependent on the frequency ω, is defined as:

$$\alpha_{abs}(\omega) = \frac{(\hbar\omega) * number_{of_{transitions}} / (\frac{unit_{volume}}{unit_{time}})}{incident\_electromagneti\_flux} \tag{1.5}$$

Its magnitude varies greatly as a function of the semiconducting material and depends primarily on the electronic structure and symmetry of the semiconductor. Two are the cases to be considered: direct BG semiconductors (the minimum in the CB-energy and the maximum in the VB-energy occur for the same value of crystal momentum or, equivalently, at the same **k**-point of the irreducible Brillouin zone of the material), and indirect BG semiconductors (the minimum in the CB-energy and the maximum in the VB-energy occur at different values of crystal momentum).

In the case of direct BG semiconductors, the linear absorption coefficient depends on the frequency of the incoming photon and on the BG value of the material irradiated:

$$\alpha_{abs} \propto \frac{1}{\omega}\sqrt{\hbar\omega - E_g} \tag{1.6}$$

where ω is the frequency of the incoming photon absorbed and $E_g$is the band gap of the semiconductor.

In the case of indirect BG semiconductors phonons absorption and emission are involved in the excitation process in order to respect the energy momentum conservation rule. These processes produce a more complex picture where:

$$\alpha_{abs} \propto C_a \frac{\left(\hbar\omega - E_g - \hbar\omega_q\right)^2}{\exp\left(\frac{\hbar\omega_q}{k_B T}\right) - 1} + C_e \frac{\left(\hbar\omega - E_g - \hbar\omega_q\right)^2}{1 - \exp\left(\frac{-\hbar\omega_q}{k_B T}\right)} \tag{1.7}$$

with $C_a(C_e)$ being the probability of a photon absorption (emission). ω_q is the frequency of the photon involved in the absorption emission process.

Based on Eqs. 1.5, 1.6 and 1.7, Eq. 1.4 can be rewritten for more general cases as:

$$I_{(x)} = (1 - R) I_0 e^{-\alpha x} \tag{1.8}$$

with $I_{(x)}$ being the intensity of the light beam at distance x from the surface of the irradiated material. Equation 1.8 can easily be obtained from Eq. 1.9 that expresses the independence of the absorption coefficient α from the light intensity:

$$dI = -\alpha I_{(x)} dx \tag{1.9}$$

where dI is the fraction of light beam intensity absorbed at distance x.

Substituting Eq 1.8 into 1.9 one obtains an expression for the rate per unit area (dI/dx) at which the light beam intensity is absorbed by the semiconductor:

$$\frac{dI}{dx} = -\alpha I_0 e^{-\alpha x} \tag{1.10}$$

Absorption of the light energy generates charge carriers (photo-excited e* and holes) in the semiconductor. The charge carrier generation density can be expressed as:

$$g(x) = \chi\alpha I_0 e^{-\alpha x} \tag{1.11}$$

where χ is the quantum yield of internal photo-effects. This quantity describes the probability of a charge carrier to be formed, given the absorption of a photon.

The seminal work of Tauc, Koc and Antoncik [80, 81, 82] demonstrated that χ depends on the energy of the photon absorbed. In an intrinsic semiconductor with a very low density of defects, and depending on the energy of the photon (E_p), χ falls in one of three possible regimes. Ignoring processes other than band-to-band transitions, for $E_p < E_g$, χ is equal to 0

hence the photon absorbed has energy too low to promote an electron excitation. For $E_g < E_p < 2E_g$, χ is approximately constant and equal to 1 so that each photon absorbed promotes one electron excitation to the CB. For $E_p > 2E_g$, χ is larger than 1. This behaviour is due to free carrier multiplication processes such as Auger type recombination that permits the creation of more than one e*-h pair for each photon absorbed.

The limit $E_p > 2E_g$ is not strictly defined and varies from semiconductor to semiconductor. Tauc observed that for material where the effective mass of the excited electron is small compared to the effective mass of the correspondent hole χ is larger than 1 for energies lower than $2E_g$. Tauc also reported [80] that beyond the $E_p > 2E_g$ limit, χ shows a linear dependences with respect to E_p.

1.2.2.2. Charge carrier concentration/mobility in semiconductors

This Section provides a brief overview of the theoretical framework to describe charge carrier concentration and mobility in semiconductors. The interested reader is refereed to [83, 84] for a more extended discussion.

Following photo-generation of the electron-hole pair, the next fundamental step in a photo-catalytic reaction is the migration of one or both of the charged particles to the interfaces of the semiconductor. The efficiency of this process depends on the presence of polarizations and ensuing electrostatic fields in the semiconductor, the temperature at which the system operates, thence the thermal disorder, and the density of the charge carriers present. Migration of charge carriers can be hindered by many phenomena grouped under the name of recombination processes.

There are two main physical processes defining the mobility of electron and holes in a semiconductor: the carriers drift and their diffusion. In the absence of an electrostatic field, thermodynamics teaches us that electrons in a non-degenerate and non-relativistic electron gas (very crude approximation for CB electrons in semiconductor) move rapidly in all direction with thermal energy:

$$\frac{1}{2}m_n v_{th} = \frac{3}{2}k_B T \tag{1.12}$$

where m_n is the effective mass of the conduction electron and v_{th} the average thermal velocity.

In absence of an external bias, the random motion of the electrons lead to a net zero displacement. The motion of the electrons is a sequence of random scattering processes with lattice atoms or other scattering centres (such as impurities in the semiconductor). If a field E is present in the semiconductor, the electron will experience a force equal to $-eE$ and a

consequent acceleration between scattering events. The additional velocity gained in presence of the field E is called drift velocity, v_n and is expressed as:

$$v_n = -\left(\frac{e\tau_c}{m_n}\right)E \tag{1.13}$$

where e is the charge of the electron and τ_c is the mean free time between scattering events.

Eq. 1.13 can be rewritten as:

$$v_n = -\mu_n E \tag{1.14}$$

with:

$$\mu_n = \frac{e\tau_c}{m_n} \tag{1.15}$$

μ_n is the electron mobility and can be factorised in two components:

$$\frac{1}{\mu_n} = \frac{1}{\mu_l} + \frac{1}{\mu_i} \tag{1.16}$$

μ_l is the mobility due to scattering with lattice atoms and is inversely proportional to $T^{-1.5}$. μ_i is the scattering due to impurity and is proportional to $T^{-3/2}/N_T$, N_T being the total impurity concentration.

The carriers diffusion process and the charge-drift can be classically modelled using Fick's diffusion law. This law describes the flow from a region of higher density (of charge carriers) to one of lower density:

$$J_n = eD_n\frac{dn}{dx} \tag{1.17}$$

D_n is the diffusion coefficient and dn/dx is the gradient in the electron density.

The Einstein relation:

$$D_n = \left(\frac{k_B T}{q}\right)\mu_n \tag{1.18}$$

correlates D_n to μ_n. The considerations made up to now for electrons are valid (with the appropriate change of sign in the equations) for the holes in the VB too.

By combining Eq. 1.14, 1.15 and 1.17, the total current density can be written as:

$$J_n = e\mu_n nE + eD_n\frac{dn}{dx} + e\mu_p pE + eD_p\frac{dp}{dx} \tag{1.19}$$

where n is the density of conduction electrons and p is the hole density. These carrier concentrations are calculated in intrinsic semiconductors starting from their Fermi distribution at the equilibrium:

$$n_i = N_c \exp\left[\frac{-(E_c - E_F)}{k_B T}\right] \quad (1.20)$$

where n_i is the charge carrier density at the equilibrium in the PC, E_F is the Fermi energy, E_c is the conduction band minimum energy, and N_c is equal to:

$$N_c = 2\left(\frac{2\pi m_n k_B T}{h^2}\right) \quad (1.21)$$

An analogous expression can be written for the hole concentration:

$$p_i = n_i = N_v \exp\left[\frac{-(E_F - E_v)}{k_B T}\right] \quad (1.22)$$

Following the photo-excitation of e*-h^+ pairs, the concentration of charges changes from its equilibrium value. The concentration of the charges out of equilibrium is expressed as:

$$p_{ne} = n_{ne} = p_i + \tau_p G_L \quad (1.23)$$

where p_{ne} and n_{ne} are the non-equilibrium concentrations of hole and electrons, respectively. Where $p_{ne} = n_{ne}$ for an electro-neutral system. τ_p is the average lifetime of the charge carrier considered, and G_L is the rate of generation of charge carriers under constant irradiation. If the source of light is not constant in time, Eq. 1.23 becomes:

$$p_n(t) = p_i + \tau_p G_L \exp(-t/\tau_p) \quad (1.24)$$

With t measuring the time passed from when the light is switched off. These equations are valid in what is called low injection regime (i.e. n_{ne}=p_{ne} $\ll n_i = p_i$) that is the ideal regime at which a PC should work to limit recombination processes. It is worth noting that all the factors on the right side of Eq 1.24 depend on the atomic and electronic structure of the semiconductor of interest. This makes acquisition of atomistic scale understanding of a PC and its interfaces crucial for rational developments of PCs capable of sustaining high charge concentrations and offering high electron mobility.

1.2.2.3. Recombination processes in semiconductors.

The diffusion/drift of charge carries in PCs is hindered by e*-h pair recombination processes. In the intrinsic semiconductor limit, there are two possible recombination processes: direct band-to-band (BB) recombination and the Auger recombination.

The direct BB recombination is defined by annihilation of an electron-hole pair. This event can lead to the emission of a photon or the energy released is dissipated non-radiatively through coupling with lattice vibrations. The rate of the BB recombination process can be expressed as [83]:

$$R = \beta n_{ne} p_{ne} \tag{1.25}$$

where β is a proportionality constant describing the quantum efficiency of the PC, and n_{ne} and p_{ne} are the charge carriers concentrations right after the photo-excitation (i.e. at non-equilibrium value). If one considers the formation of charge carriers a steady state kinetic process (i.e.$\frac{dp_{ne}}{dt} = 0$, which is reasonable given the low concentration of charge carriers with respect to the total number of atoms), the net rate of charge-recombination can be expressed as:

$$U = \frac{p_{ne} - p_i}{\tau_p} \tag{1.26}$$

where τ_p is the average lifetime of the hole (same expression can be used for the electrons) and is given by:

$$\tau_p = \frac{1}{\beta p_0} \tag{1.27}$$

Eq. 1.26 shows that the increment of U (the recombination rate) depends directly on the non-equilibrium concentration of charge carriers, and inversely on the lifetime (τ_p) of such carriers. Consequently, to inhibit recombination processes and potentially boost the reactivity of a PC, it is important to operate at low injection limit (i.e. small concentration of non-equilibrium carriers) and within a high mobility regime (see Eq. 1.15)

The Auger recombination has usually a less relevant role in the definition of the overall efficiency of a PC. It is a process that involves the transfer of energy and momentum released by an electron-hole pair recombination to another electron or hole. These newly excited carriers then lose their excess energy via coupling to lattice vibrations. The three-body nature of this process makes it more unlikely to happen with respect to the BB recombination [85]. However, at high temperatures or high injection limit Auger recombination can play a non-negligible role in affecting the semiconductor behaviour.

The Auger recombination rate can be expressed as [86]:

$$R = \beta n_e^2 p_e \quad \text{or} \quad R = \beta n_e p_e^2 \tag{1.28}$$

depending on whether the energy and momentum are transferred to a hole or an electron. Since this process is a three body process, the corresponding kinetics is not as straightforward to describe as in the BB case [83]. Given the scope of this Thesis and its focus on single-electron excitation processes, the reader is referred to Ref. [83, 86] for a more extensive discussion of the Auger recombination process.

1.2.2.4. Excitons in semiconductors

In real PCs, photo-excitation does not always produce free charge carriers. The excitation process may give rise also to bound excited states, called excitons. These excited states consist of a CB electron and a VB hole bound to each other via Coulomb interactions. The ensuing quasiparticle is overall neutral and allows transport of energy in the material without a correspondent transport of net charge. Excitons are promoted by the stabilizing energy (E_{st}) due to Coulomb interaction between the electron-hole pair that reads:

$$E_{st} = \frac{-e^2}{\varepsilon r} \tag{1.29}$$

where r is the distance between the CB electron and the VB hole. ε is the semiconductor dielectric constant. ε governs the material capability of screening the potential of the charged pair. It plays an important role in defining the properties of the exciton (vide infra). Using ε as screening constant is an approximation that works for systems where r is larger than the lattice spacing of the material considered. Conversely, when r is smaller than the lattice spacing, a smaller value for ε should be used since the potential interaction between the electron and the hole is less screened by the overall crystal structure [87].

Excitons are mainly divided in two categories: Frenkel and Mott-Wannier excitons. Frenkel excitons have a relatively small radius r (comparable to or smaller than the lattice spacing) and high binding energies between 0.1-1.0 eV [87, 88]. Mott-Wannier excitons are characterised by large values of r, that can extend over tens sometimes hundreds of atoms. They usually occur in solids with large ε (such as ionic metal-oxide semiconductors); their binding energy is much lower than Frenkel excitons and it is usually around 0.01 eV [89, 90].

Excitons can be described by hydrogenic wave-functions. However, their binding energy are much smaller and their (quasiparticle) size much larger than the hydrogen atom. This is due to the screened Coulomb force between the electron hole pair and their small effective masses. They usually have short lifetime that can be extended in the order of the ns if a consistent overlap between the electron-hole wave functions is present leading to resonance stabilisation [87].

When an exciton is created through photo-excitation, there are three possible decay channels: 1) the exciton energy is dissipated through collision with the lattice sites; 2) the exciton is ionised releasing free charge carriers; or 3) it collapses to the ground state through radiative decay. Considering the small binding energy of excitons in semiconductor (hence in semiconducting PCs) they are relatively short lived and tend to ionise, releasing free charge

carriers [88]. The details through which excitons ionisation can be affected by permanent polarization in the PCs is a subject of growing interest, especially for his potential significance for enhanced HPC [89].

1.2.3. Defects in semiconductors and related properties

The intrinsic semiconductor model considered up to now is extremely useful to understand the basic physics behind photo-catalytic processes. However, being highly idealized, this model has little to none pertinence to real PCs.

In reality, semiconductors properties and performances are strongly affected by the presence of defects in the crystalline structure [90]. Defects are regions where the microscopic arrangement of ions differs drastically from the perfect crystalline repetitive structure. Defects in semiconductor can be categorised in three main classes: point defects, line defects or surface defects. All these defects have dramatic effects on the properties of semiconductors. Line and surface defects can be seen as metastable configurations of the crystal structure that can be brought back to equilibrium through annealing treatment [92]. The concentration of point defects is non-vanishing even at thermal equilibrium and they are at the base of fundamental processes to modulate materials properties. Given the natural presence of point defects and their fundamental contribution in determining the properties and reactivity of semiconducting PCs, this Section will concentrate exclusively on this typology of defect.

1.2.3.1. Thermodynamic features of point defects

Point defects are present in a semiconductor at thermal equilibrium and their occurrence is an intrinsic thermodynamic feature of every solid. If a perfect crystal with N atom is considered as starting material, the presence of n_v impurities (vacancies included) will be very small with respect to N: $n_v/N \ll 1$.

Given the scarcity of vacancies, the interaction between them can be ignored, to a first approximation, so that the change in the overall Gibbs energy can be expressed in terms of the enthalpy of formation for each vacancy and the entropy associated with the formation of the defect. The entropy contribution can be divided in two main factors: vibrational entropy and configurational entropy. Vibrational entropy and enthalpy of formation are proportional to the number of vacancies created (n_v). The configurational entropy is a more complex function. The global change in Gibbs energy can be expressed as:

$$\Delta G = n_v(\Delta H - T\Delta S_{vib}) - T\Delta S_{config} \tag{1.30}$$

The configurational entropy can be written as:

$$\Delta S_{config} = k\ln W \tag{1.31}$$

with W being the probability distribution of a certain defect configuration in the material lattice. Given the huge amount of atoms (and defects) present in a solid, Stirling's approximation can be used so that:

$$\Delta G = n_v(\Delta H - T\Delta S_{vib}) - Tk(N\ln\frac{N+n_v}{N} + n_v\ln\frac{N+n_v}{n_v}) \tag{1.32}$$

At equilibrium, the change in Gibbs energy will be at a minimum with respect to n_v, hence $\delta\Delta G/\delta n_v = 0$. From equation 1.32 $\delta\Delta G/\delta n_v$ reads:

$$\frac{\delta\Delta G}{\delta n_v} = \Delta H - T\Delta S_{vib} + kT\ln\frac{n_v}{N+n_v} \tag{1.33}$$

Eq. 1.33 can be rearranged into:

$$\frac{n_v}{N+n_v} = \exp\left(\frac{\Delta S_{vib}}{k}\right)\exp\left(-\frac{\Delta H}{kT}\right) \tag{1.34}$$

where $\frac{n_v}{N+n_v}$=[v] is the concentration of defects. From Eq. 1.34 it can be seen that at any temperature T>0 a solid contains point defects. It is hence evident the intrinsic presence of defects in semiconductors.

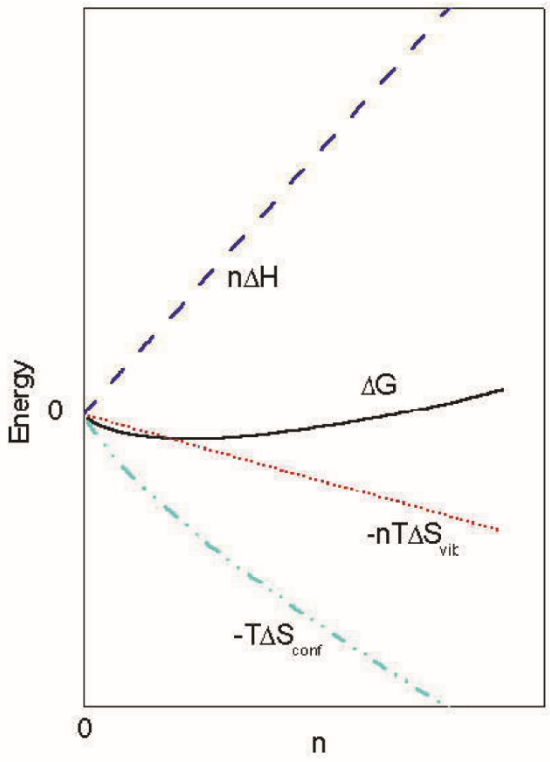

Figure 1.4. Example of the variation in enthalpy (ΔH), vibrational (ΔS_{vib}) and configurational (ΔS_{conf}) entropy, and Gibbs free energy (ΔG) with the concentration of vacancies (n) in an elemental solid. The ΔG minimum for n≠0 makes it evident that defect-free semiconductors do not exist in reality.

1.2.3.2. Point defect classification

Charge, type of impurity, and site topology are just some of the possible criteria to distinguish between the different cases.

The most basic distinction for point defects is that they can be either intrinsic or extrinsic. Intrinsic defects maintain the overall composition of the material hence no hetero-atoms are involved. On the contrary, extrinsic defects involve the presence of hetero-atoms (impurities).

Point defects can be further classified using the following approach.

- Vacancies: they are defects created by a missing atom in the lattice.
- Substitutional defect: an atom of type A is replaced by an atom of type B in its lattice position.
- Interstitial defect : an atom of type A occupies an interstitial site in the lattice.

- Antisite defect: these are particular type of substitutional defects. In a lattice formed by the elements A and B, the A and B atoms swap positions i.e. an atom A occupies a B- site and/or vice-versa.
- Schottky defect: these are a double vacancy where both a cation(s) and the correspondent anion(s) are missing from the material lattice. These vacancies form so that the material stoichiometry and the charge neutrality are conserved.
- Frenkel defect: the displacement of a cation or anion from its lattice position promotes the correspondent creation of an interstitial impurity and a vacation site. As for Schottky defects, the stoichiometry and charge neutrality of the lattice is conserved when a Frenkel defect is formed.

Many of the defects listed above contribute to the populations of charge carriers in semiconductor. Defects that can contribute free electrons to the host crystal are called donors, while the ones which can contribute holes (i.e. remove free electron) are named acceptors. Few are the cases where impurities in the material can contribute more than one electron or hole per atom. These defects are referred to as double acceptor or double donors. When the impurities in the lattice have the same valence electrons as the host they substitute; these defects are called iso-valent or iso-electronic.

While a great variety of defects is present in each and every semiconducting PC, usually the properties of the most stable and abundant defect dominates. A larger thermodynamic stability for a given defect, result in a higher concentration in the semiconductor (at equilibrium). As a result, the properties of defective materials are generally strongly modulated by the properties of the most abundant defects. This makes evaluation of defect formation energies, and their electronic characterization, of utmost importance for atomic-scale understanding of semiconductors and semiconducting PCs.

1.2.3.3. Defects influence on semiconductor electronic and chemical structure

The presence of defects in semiconductors leads to drastic changes in the band structure of the host itself. A defect can introduce new energy levels in the BG the perfect crystal or in the bands of the crystal itself, consequently changing the electronic properties of the PC.

Defect states are usually categorised as shallow or deep. Generally, shallow defect states are localised in the band gap within 25 meV within the VB or CB edges or in the bands themselves always within that limit. All the other defect states localised in the BG or in the band of the semiconductor are considered deep defect states.

Different physical schemes can be used to model the two different types of behaviour. Defects that give rise to shallow states are usually modelled through the so called “effective

mass approximation" (i. e. EMA). More advanced methods (such as Green's function, perturbative methods, DFT methods, ecc...) can be used. However, their results are qualitatively comparable to EMA ones, and their application computationally more demanding, which makes use of the EMA very reasonable.

To understand why the EMA is applicable to the shallow defect states case, let us consider a substitutional P atom (donor) in a Si lattice. The P nucleus has a proton (hence a positive charge) more than the Si ones. The same goes for the number of electrons. The Si environment screens the interaction between the extra valence electron and the positive extra charge so that the impurity can be approximated as a hydrogen atom embedded in a Si lattice. This approximation takes in account the fact that the mass of the nucleus of the impurity is substantially larger than the one of a hydrogen atom, and that the interaction between the nuclei and the electrons is heavily screened by the material environment, which makes the extra valence electron is usually easy to remove. The same type of approach can be applied for an acceptor comparing it to a positron bound to a negatively charged muon.

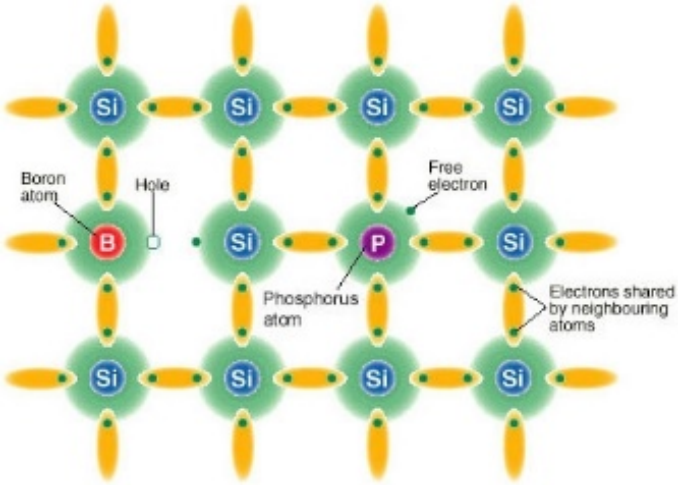

Figure 1.5. Graphical representation of shallow defects (B in red and P in purple) due to substitution in silica lattice.

In order to quantify the screening of the defect charge by the semiconductor lattice, the simplest approach is to assume that the charge is screened by the dielectric constant of the host material. The Coulomb potential of the donor/acceptor ion can then be written as:

$$V_s = \pm \frac{e^2}{4\pi\varepsilon_R r} \tag{1.35}$$

where ε_R is the static (relative) dielectric constant of the perfect crystal. Since the motion of the defective charge carriers is affected by both the crystal potential and the impurity potential, the Schrödinger equation for the defect will read:

$$(H_0 + U)\Psi = E\Psi(r) \tag{1.36}$$

where H_0 is the one-electron Hamiltonian of the perfect crystal, and U is the potential energy of the defective charge in the screened Coulomb potential V_s:

$$U = -|e|V_s \tag{1.37}$$

In the EMA, U represents a slow varying perturbation. Since a comprehensive discussion on the EMA and its implication is beyond the scope of this section, only the basic concepts will be treated. For a comprehensive presentation the reader is referred to references [90] and [84].

In the simplest version (i.e. non-degenerate, parabolic conduction band minima) of the EMA, the energy eigenvalues E of the donor-defect form a Rydberg series. For this reason they are called “Hydrogenic levels”. Their analytical form is:

$$E_N = E_\infty - \frac{R^*}{N^2} \tag{1.38}$$

where E_∞ is the conduction band energy of the pure semiconductor, N is the principal quantum number and R^* is called effective Rydberg constant and reads:

$$R^* = \frac{m^*}{m} * \left(\frac{1}{\varepsilon_0}\right)\left(\frac{e^4 m_0}{2\hbar^2}\right)\left(\frac{1}{(4\pi\varepsilon_0)^2}\right) \tag{1.39}$$

where m* is the effective mass of the electron/hole due to the defect.

The extent in real space of these defects hydrogen states is measured in term of Bohr acceptor (donor) radius a*:

$$a^* = \left(\frac{\varepsilon_0 m_0}{m^*}\right)\left(\frac{\hbar^2}{m_0 e^2}\right)(4\pi\varepsilon_0) \tag{1.40}$$

The solutions for the energy levels of the EMA (Eq. 1.40) are schematically depicted in Fig. 1.6:

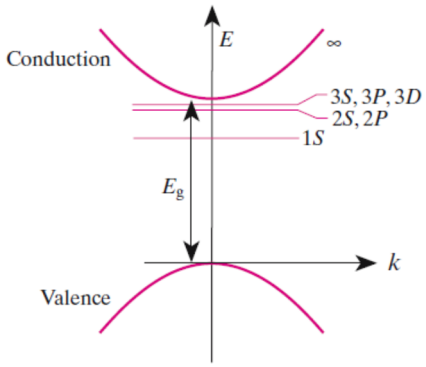

Figure 1.6. Schematic diagram of the n=1, 2 and 3 bound states of a shallow donor near a non-degenerate, parabolic conduction band low-energy edge.

The envelope functions ($\mathrm{C(R)}$) that characterises these defect-state are the eigenvectors of the equation:

$$\left[-\left(\frac{\hbar}{2\mathrm{m}^*}\right)\frac{\partial}{\partial \mathrm{R}^2}+\mathrm{U(R)}\right]\mathrm{C(R)} \approx \mathrm{E_N C(R)} \tag{1.41}$$

Once $\mathrm{C(R)}$ is obtained, it has to be multiplied by a Wannier (or Block) function(s) to obtain the wave function of the hydrogenic defect state that reads:

$$\Psi(\mathbf{r}) = \sum_{\mathrm{i}} \mathrm{C}(\mathbf{R}_{\mathrm{i}}) N^{-\frac{1}{2}} \sum_{\mathbf{k}} \exp[-\mathrm{i}\mathbf{k}\cdot(\mathbf{R}_{\mathrm{i}}-\mathbf{r})] u_{\mathbf{k}}(\mathbf{r}) \tag{1.42}$$

These solutions are applicable only to the case of parabolic, non-degenerate CB minima. However, the other possible cases usually differ only in the need of using an effective mass tensor wave equation to calculate envelope functions [90]. These complex wave-functions take in account the anisotropy present in the CB structure and the different mobility of the defective charge carriers in different dimensions.

The EMA method generally offers an optimal accuracy-viability trade-off since it provides qualitatively right answers for shallow defect states. Nonetheless, as shown by Eq. 1.42, it accounts only for local modification of the crystal potential. It has been demonstrated how the electrostatic interactions decay length is very relevant for understanding the effects of defects on a material [91]. In Chapter 6, the issue of the decay length of defect-perturbation will be explicitly considered for defects in one-dimensional tubular insulators (Chapter 6).

From a structural point of view, defects that give rise to shallow states do not usually modify drastically the lattice atomic structure and potential of the semiconductor. Although some atomic displacement has to be expected, the main effect that this type of impurity has on the

overall behaviour of a semiconductor is that they release free charge carriers. This effect is central in doping of semiconductors.

Conversely, defects that generate deep states tend to introduce heavier changes in the electronic atomic structure and potential of the semiconductor. These changes are so profound that cannot be accurately described by perturbative approaches. A huge effort has been devoted through the years by the scientific community to found a proper scheme to model these type of defects. However, a conclusive solution is yet to be reached. Many approximations are used to calculate the electronic structures and potentials of defective semiconductor with deep states. Extensive reviews on this subject can be found in Refs. [91] and [92].

A vast choice of methods can be used to model deep state defects. The electronic structures in these cases can be modelled by tight binding approaches [93], Density Functional Theory [94], Green Function methods [95], and extended Huckel [96] methods. Depending on the specific case, a method can perform better that the others. Hence, the type of model to adopt has to be chosen carefully to maximise accuracy-viability trade-offs for the simulation of defects.

Deep defective sates are usually associated with sizable lattice relaxations. They are usually induced by the presence of vacancies, double vacancies, highly charged defect sites or extended defects centres. Usually, anion and cation vacancies present strong optical activity. These are known as F centres and V centres (or in some cases coloured centres) [97, 98]. The substantial modifications that the presence of deep defect states induces in the material structure tend to lead to trapping of charge carrier at these defect sites. This issue is of paramount importance for HPC since the trapping of charge carrier and their ensuing recombination prevents possible transfer to reactants quenching the efficiency of PCs.

1.2.3.4. Optical activity of defects

The presence of defects usually leads to drastic changes in the spectroscopic behaviour of PCs. As every other aspect regarding the Physics of defects, a multitude of different cases can be present. This variety makes it complex to provide a comprehensive discussion. Accordingly, in this Section only the most relevant cases will be considered.

One of the most relevant examples of optical activity by defects is the absorption due to surface states. Since 1975 Zecchina and co-workers have been analysing the behaviour of these states in alkaline-earth metal oxides (i.e. MgO, CaO, SrO, and BaO) [99]. These compounds invariably showed absorption peaks at energy substantially lower than the material BG. The unexpected absorption peaks were correlated to the presence of surface states associated to under-coordinated oxygen atoms present at the surface. A lower coordination number

seemingly corresponded to absorption of lower energy light. Deeper investigation of MgO and CaO has shown that the photo-excitation of the surfaces of these materials leads to a charge separation process and trapping of electrons and holes on different surface sites.

Another class of defects with a fairly understood spectroscopic behaviour are the cation and anion vacancies in metal oxides. As explained in the previous Section, these types of vacancies introduce deep defect states in the BG and are usually labelled as F (oxygen vacancies) and V (metal cation vacancies) centres.

Oxygen vacancies in metal-oxide lattices can originate three different types of centres: 1) doubly charged and optically inactive F^{2+} centres, 2) optically active F^{+} centres trapping one electron, and 3) neutral; F centres trapping two electrons. The latter two types of defects are fundamental in understanding the formation of free electron in a photo-catalyst and its spectroscopic absorption. These types of vacancies are present in almost all metal oxides relevant for HPC such as: ZnO, MnO, Al_2O_3 and TiO_2 [100, 101, 102, 103]. In all the different materials studied, F centres (F^{2+} excluded) tend to present similar behaviour although the respective absorption spectra and defective energy level changes.

F^{+} centres introduce defect-states localized deep in the BG, generally few eV above the VB edge. The first excited state of these centres usually is found just below or at the edge of the CB. Similar considerations are valid for F centres, the only differences being that the defective states are even deeper in the BG with respect the F^{+} ones, and that their excitation almost always leads to population of the semiconductor CB. The presence of these defective centres heavily influence the absorption properties of the PC, typically red-shifting the absorption. While the red-shifting opens up the possibility of achieving visible light absorption, the presence of deep centres, and their e*-h trapping and recombination properties, makes their presence detrimental to efficient photo-catalysis.

F^{+} centres are the cause of another process that influences the photo-catalytic properties of a semiconductor: under optical excitation these centres can transform in F centres by trapping a second electron and creating a hole in the VB. This behaviour has been observed in different materials such as MgO, Al_2O_3 and TiO_2 [100, 101, 103].

Cation vacancies centres are generally responsible for trapping of one or two holes leading to substantial lattice distortions and formation of V^{-} (one trapped hole trapped) and V (two trapped holes) centres. Hole localisation leads to a red-shift in the absorption of the material where the vacancies are present. However, the excitations involved with these optical transitions are usually between sites around the defect and do not produce free carrier in the PC. Numerous are the semiconductors where this hole localisation has been observed, the most studied cases are the one of SrO, MgO and SiO2 [104, 105, 16].

1.2.3.5. Charge carrier concentration and recombination processes in defective semiconductor

In a semiconducting material the presence of defects affects majorly the formation, mobility and depletion of charge carriers. When a defect-state is introduced in the BG, the photo-generated charge carrier can occupy these states. Especially deep states can limit the mobility of the charge carriers and induce faster e*-h recombination.

The presence of defect changes the carriers' concentration in the semiconductor. The defect induced changes in the electronic structure make it easier to introduce an electron (in the case of a donor) in the CB or a hole (in case of an acceptor) in the VB. Defect states also changes the Fermi energy level in the semiconductor.

When the equilibrium is broken by photo-excitation, the definition of Fermi energy (which assumes equilibrium) breaks down. The system needs to reach a new equilibrium. The ensuing process can be divided in two parts characterized by different kinetics and time scales. In the first step, local equilibrium in each of the bands at the same **k**-point is reached. This process is called thermalisation and it usually occurs in picoseconds. It is the time needed for multiple scattering events to absorb some of the excitation energy. Once local equilibrium is reached, the local concentration of charge carriers in each band can be given in terms of the Fermi distribution formula:

$$n_e = N_c * \exp\left(-\frac{E_c - E_F^e}{kT}\right) \tag{1.43}$$

$$n_h = N_v * \exp\left(-\frac{E_F^h - E_v}{kT}\right) \tag{1.44}$$

where N_c and N_v are given by Eq 1.21, E_c is the conduction band minimum, E_v is the valence band maximum. Eqs. 1.43 and 1.44 show that, in a non-equilibrated semiconductor after thermalisation, two different Fermi energies for electrons and holes can be determined. E_F^h and E_F^e are hence called Quasi-Fermi energies.

The product of the carrier densities can now be expressed as:

$$n_e * n_h = n_i^2 \exp\left(\frac{E_F^e - E_F^h}{kT}\right) \tag{1.45}$$

If the equilibrium expressions for the carrier densities are considered (Eq 1.20, 1.22), and their product substituted to n_i^2, then the quasi Fermi energies can be calculated as:

$$E_F^e = E_C - kT\ln\left(\frac{N_c}{n^e}\right) \tag{1.46}$$

$$E_F^h = E_v + kT\ln\left(\frac{N_v}{n^e}\right) \tag{1.47}$$

in a timescale between nanoseconds and milliseconds the equilibrium between the two bands will be restored through decay of the hot electron (hole) or recombination processes.

Deep defect states play a central role in this part of the equilibration process. Many different model and schemes have been developed through the years to describe defect assisted recombination of charge carriers. Out of these, the Shockeley Read Hall (SRH) model [106] is undoubtedly the most widely accepted and used. Figure 1.7 shows the rates, events, and energy levels that are central to the SRH model. Processes of interest are: the electron capture by a deep defect state with rate R_d^e, the electron excitation by a deep defect states with rate R_u^e, the hole capture by (or electron decay from) a deep defect state with rate R_u^h and the hole decay to (or electron excitation by) the VB from a deep defect state with rate R_d^h.

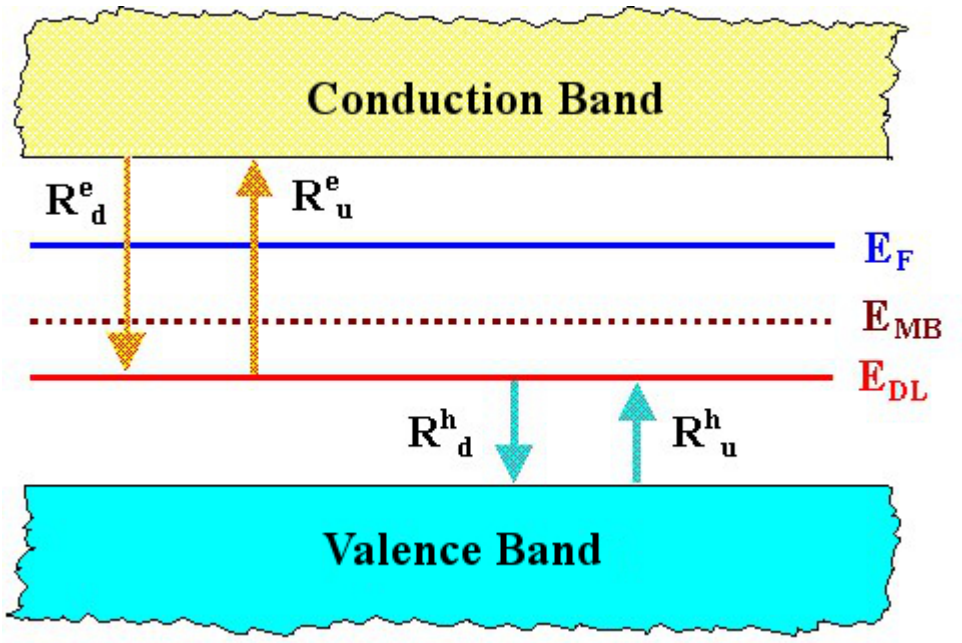

Figure 1.7. Schematic diagram of the processes and energies used in the SRH model. E_F is the Fermi energy, E_{DL} is the energy of the deep defective state of interest and E_{MB} is the mid gap level in the semiconductor. The process depicted are electron capture by a deep defect state (R_d^e), electron excitation by a deep defect states (R_u^e), hole capture by a deep defect state (R_u^h) and hole decay to the VB from a deep defect state (R_d^h).

In this situation the concentration of electrons/holes on the deep levels can still be given by the Fermi distribution equations:

$$n_{DL}^{-} = N_{DL} f(E_{DL}, T) \approx N_{DL} \exp\left(-\frac{E_{DL}-E_F}{kT}\right) \tag{1.48}$$

$$n_{DL}^{0} = N_{DL}[1 - f(E_{DL}, T)] \approx N_{DL}\exp\left(-\frac{E_F - E_{DL}}{kT}\right) \quad (1.49)$$

where E_{DL} is the energy of the deep level state, N_{DL} is the density of the impurity states in the semiconductor, n_{DL}^{-} is the concentration of impurity states with an electron trapped, and n_{DL}^{0} is the concentration of impurity states with a hole trapped. The different rates of the processes in the SRH scheme can be expressed as:

$$R_d^e = v\sigma^e n^e n_{DL}^0 \quad (1.50)$$

where v is the average velocity of the electrons and σ^e is the scattering cross section; and:

$$R_u^e = r'(N_c - n^e)n_{DL}^- \approx r'N_c n_{DL}^- \quad (1.51)$$

with r' being a proportionality constant that depends on the localisation of the electron around the trap. N_c is a variable accounting for the mobility of the charge carrier and can be obtained from Eq. 1.21. In Eq. 1.51, the product $r'N_c$ is defined as the emission probability for electrons in the deep level (e^e). Assuming local equilibrium between the defect states and the CB bands, $R_u^e = R_d^e$, which in turns leads to:

$$e^e = \frac{v\sigma^e n^e N_{DL}\exp\left(-\frac{E_{DL} - E_F}{kT}\right)}{N_{DL}\exp\left(-\frac{E_F - E_{DL}}{kT}\right)} \quad (1.52)$$

this equation can be rewritten as:

$$e^e = v\sigma^e n_i \exp\left(\frac{E_{DL} - E_{MB}}{kT}\right) \quad (1.53)$$

where $E_{MB} = E_C - E_V/2$ and $n_i = N_c\exp(-E_C - E_{MB}/kT)$. The emission probability for holes in deep level e^h can thence be expressed as:

$$e^h = v\sigma^h n_i \exp\left(\frac{E_{MB} - E_{DL}}{kT}\right) \quad (1.54)$$

Considering the kinetic of the Generation recombination processes we can write the rate of change for the two charge carrier as:

$$\frac{dn_e}{dt} = G_{perfect} + G_{ne} - R_{perfect} + R_u^e - R_d^e = G_{ne} - (R_d^e - R_u^e) \quad (1.55)$$

and:

$$\frac{dn_h}{dt} = G_{perfect} + G_{ne} - R_{perfect} + R_d^h - R_u^h = G_{ne} - \left(R_u^h - R_d^h\right) \quad (1.56)$$

with $G_{perfect}$ being the generation rate for charge carriers in the perfect semiconductor, G_{NE} being the generation rate in defective semiconductor and $R_{perfect}$ being the recombination rate

in the perfect semiconductor. When the. VB and CB are in local equilibrium with the defect states $R_d^e - R_u^e = R_u^h - R_d^h$. The term $R_d^e - R_u^e$ can also be expressed as:

$$R_d^e - R_u^e = R_{ne} - R_{perfect} = R_{ne} - G_{perfect} = U_{DL} \tag{1.57}$$

where U_{DL} is the difference between the recombination to the deep level and the emission from it; U_{DL} can be calculated as:

$$U_{DL} = \frac{v\sigma^e N_{DL}(n^e n^h - n_i^2)}{n^e + n^h + 2n_i \cosh\left(\frac{E_{DL} - E_{MB}}{kT}\right)} \tag{1.58}$$

If one rewrites $n^{e,h} = n^{e,h}(equ) + \Delta n$:

$$U_{DL} = v\sigma^e N_{DL} \frac{[n^e(equ) + \Delta n][n^h(equ) + \Delta n] - n_i}{n^e(equ) + n^h(equ) + 2\Delta n + 2n_i \cosh\left(\frac{E_{DL} - E_{MB}}{kT}\right)} \tag{1.59}$$

Considering the hole as minor charge carrier in the semiconductor (i.e. their concentration is lower than for the electrons):

$$U_{DL} = \frac{dn_e}{dt} = \frac{v\sigma^h N_{DL} n^h(equ)}{n^h(equ) + 2n_i \cosh\left(\frac{E_{DL} - E_{MB}}{kT}\right)} \tag{1.60}$$

this differential equation has solution:

$$\Delta n_e(t) = \Delta n_e(t = 0) \exp\left(\frac{t}{\tau}\right) \tag{1.61}$$

where τ is the minority carrier lifetime that read as:

$$\tau = \frac{1}{v\sigma^h N_{DL}} \tag{1.62}$$

Eqs. 1.61 and 1.62 highlight how the lifetime of the charge carrier (τ) in a defective semiconductor is inversely proportional to the density of the deep defect-states (N_{DL}) i.e. to the concentration of the impurities, n_{DL}^-, n_{DL}^0 originating such defect-states. Furthermore, and following Eq. 1.60, the closer the defect-states to the mid-band energy level (E_{MB}), the faster the recombination rate. This result reiterates the significance of computational studies aimed at evaluating defect-states alignment and defect-concentration in semiconductors with potential for HPC.

1.2.4. Surface activity and selectivity

In several cases, the potential of a semiconductor as PC is usually analysed on the basis of its bulk properties. However, the reactions of interest take place at the surface of the material [107]. The surface-medium interface is also of extreme importance since it determines the potential or concentration gradient that promotes the migration of the charge carries to the surface itself, making the heterogeneous PC efficient. It is thence of extreme relevance to consider PC surface properties in the assessment of a heterogeneous PC.

Surface properties are extremely sensitive the pH, ionic strength and chemical nature of the medium they are exposed to. As a result, several studied have focused on the possibility of harnessing the surface-dependent photo-catalytic properties of semiconductors [107, 108, 109]. Two are the main methods adopted so far: i) the synthesis of particles with controlled shape/morphology to maximise the surface/volume ratio and the exposure of reactive sites, and ii) surface engineering via control of the pH of the medium to surface is exposed to.

1.2.4.1. Morphology dependent surface properties

The synthesis of single crystal with highly reactive exposed facets or particles with controlled morphology has attracted growing interest in the HPC community. The main issue in the controlled synthesis of PC-nanoparticles is the stability of reactive surfaces. High-energy surfaces tend to quickly disappear during the growth of the system. Inorganic ions and organic polymers have been used as capping agents to control the growth of nanoparticles and isolate selected facets. The synthesis of 1D, 2D and 3D materials has also opened completely new perspective in HPC.

The most employed semiconductor in this type of studies is obviously TiO_2 given its relevance to HPC. Yang and co. [108] used HF under hydrothermal condition to obtain anatase crystals with a high percentage (i.e. ~50%) of reactive {001} facets. A similar approach was adopted to synthesise single crystals with an even a higher percentage of exposed {001} surface [110]. In this case, a mixture of HF and 2-propanol was used as capping agent. Other studies [111] reported the synthesis of hollow TiO_2-anatase spherical nanoparticles with ~20% of the surface composed of {001} highly reactive facets. In this particular experiment it was shown that the photo-catalytic behaviour of the system could be tuned varying the percentage of the {001} surface present. This result highlights the correlation between surface morphology and PC reactivity. Following the same line of action, TiO_2 mesoporous microspheres covered by {001} surface were also obtained using highly concentrated H_2SO_4 solutions [112].

Although the largest efforts by the scientific community have been to date devoted to TiO_2, similar strategies and techniques have been explored to produce other PCs. The synthesis of BiVO4 nanoplates with exposed {001} facets was observed to yield elevate photo-catalytic activity for the degradation of RhB [113]. Single crystals of Ag_3PO_4 were produced with two different shapes to study morphology effects on the degradation of the methyl orange [113]. Ag_3PO_4 crystal were synthesised as rhombic dodecahedron with exposed {110} surface and as cubes with {001} facets. The {110} dodecahedron resulted to be photo-catalytically more active. This result is consistent with the fact that the {110} surface has higher energy that the {001} one. Another interesting case of improved reactivity due to the material morphology is the production of nanoparticles with high two dimensional anisotropy. Such morphology heavily increases the presence of active sites on the surface and exhibits unique charge properties. These nanoparticles, known as nanosheets [114], can be synthesised for a variety of new photo-catalysts such as $KCa_2Nb_3O_{10}$, $Ba_5Ta_4O_{15}$ $HCa_2Nb_3O_{10}$ and $TiNbO_5^-$.

Although the understanding of the possible relationships between the reactivity and the morphology of a material is far from complete, these examples show the major effects that shape control can have on the performances of PCs.

1.2.4.2. pH dependent surface properties

The surfaces of a semiconductor are an extremely dynamic environment. The presence of different conditions at the interface with the external environment/medium can very well activate or inhibit catalytic processes. External conditions assume an even more relevant role when it comes to the PCs stability. Numerous are the cases of promising materials that are not stable enough in performing conditions to be used in real world applications [27, 115].

The charge properties and the surface absorption (i.e. chemisorption and physisorption) mechanisms are heavily influenced by the acidity of aqueous media. When a PC is contacted to a water solution, it exists a pH at which the net charge of PC-surface is zero (point of zero charge, pzc). Once this point is known for a determined type of surface it is possible to properly analyse the effects that a change in pH has on the interface reactivity. Different studies [109, 116] show that, around the pzc, semiconductor oxides appear to be hydroxilated (M^+OH^-) and that, as long as the pH does not change excessively, a significant production of hydroxyl radical can be observed under illumination.

When the solution pH is excessively acid, the surface of the semiconductor will be protonated (MOH_2^+) and positively charged. Conversely, following increase of the pH towards basic conditions, the semiconductor surface will become negatively charged ($MO^- + H_2O$). These charged states hinder the absorption of reactants of interest on the semiconductor surface. If the reactant is also in a charged state, which may be induced by the pH of the solution, the

photo-catalyst will repel it. Studies of photo-degradation of phenol and cresol in presence of Mn-doped ZnO [109, 110] show that, if the pH is acid enough so that both the species are positively charged, the photo-activity of the catalyst is greatly reduced. The same concept is applicable to solution with pH basic enough to lead to the surface and the reactants being both negatively charged.

The pH of the medium has an important influence also on the stability of the PC itself. Under photo-catalytic condition, the presence of charges at the surfaces of the semiconductor can lead to unwanted reactions capable of corroding the PC. The most notorious example of this type of degradation process is ZnO. Exposed to constant irradiation ZnO corrodes in both alkaline and acid solutions, releasing different species in the environment: Zn^{2+} in acid solution, $Zn[(OH_4)]^{2-}$ in alkaline solution [117]. Photo-corrosion problems are well known also for CdS [28]. In this respect, it is safe to state that TiO_2 owes a lot of its notoriety also to its remarkable stability in aqueous solutions, which facilitate experimental investigations.

The findings exposed in this Section demonstrate the pivotal role that the dynamics at medium-exposed interfaces have in defining the PCs real reactivity. The fluctuations in the surface-medium arrangement in fact determine the local charge redistribution and polarisation at the interfaces. Understanding of the atomic structure and electronic properties of the PC-medium interfaces is thence of paramount importance for future development of efficient PCs

1.2.5. Theoretical insight into charge-transfer and photo-catalytic performances

As explained in the previous Sections, the basic requirements for a PC of strong visible light-absorbance, efficient e*-h separation and transfer to reactants are well established. Simultaneous fulfilment of these conditions is a formidable challenge and requires materials with an extremely diversified set of suitable properties. These properties inherently depend on the atomic composition, structure, and dynamics of the PC/medium/reactants interface. To date, the main hurdle to the development of industrially viable PCs resides in the lack of understanding of the correlation between the desired properties and the atomistic requirements needed to induce them. This motivates the growing efforts in atomic-scale characterization and understanding of PCs and their medium/reactant-exposed interfaces.

First principle simulations can access, to a certain degree of accuracy, the atomic and electronic factors that determine the PCs properties and functioning. This information can be used to understand and inform development of novel PCs and photo-catalytic strategies. Given their relatively (with respect to experimental work) inexpensive cost, computational approaches to screen photo-catalytic materials have become integral part of research in HPCs.

Central to any HPC process is the charge transfer (CT) process between the PC and the reactants.

Once the semiconductor is excited, and the electron-hole pair dissociated, the reactivity of the system is governed by the capability of efficiently transfer the charge carriers to the reactant at the interface. Non-adiabatic CT processes between weakly coupled donor and acceptors pairs in condensed phases are most effectively described using Fermi Golden rule. This formula, obtainable from application of time dependent perturbation theory, states that the transition rate ($k_{I\to F}$) between initial ($|I\rangle$) and final ($|F\rangle$) states of energy E_I and E_F reads:

$$k_{I\to F} = \frac{2\pi}{\hbar}|\langle F|H'|I\rangle|^2 \delta(E_F - E_I) \tag{1.63}$$

where H' is the time-dependent perturbation that arises from the interaction with electro-magnetic fields or nuclear vibrations. If the ET is faster than nuclear motion, $|I\rangle$ and $|F\rangle$ can be considered purely electronic states (i.e. $|f\rangle$ and $|i\rangle$). Conversely, if the ET process is slower or comparable to the time scale of nuclear motions, then the vibronic wave-function needs to be considered so that $|I\rangle=\prod_k|f_i\rangle|\chi_{i,k}\rangle$, with $|\chi_{i,k}\rangle$ being the vibrational wave-function.

Since CT photo-catalytic processes at the interface of a semiconductor usually involve manifolds of states and not a single electronic state, Eq. 1.63 can be expanded as:

$$k_{I\to F} = \frac{2\pi}{\hbar}\sum_{n_i} p(E_{i,n_i}) \sum_{n_f}|\langle f,\chi_f|H'|i,\chi_i\rangle|^2 \delta(E_{i,n_i} - E_{f,n_f}) \tag{1.64}$$

where $p(E_{i,n_i}) = e^{-E_{i,n_i}/k_BT}/\sum_{n_i} - E_{i,n_i}/k_BT$ is the probability of finding the system in an initial state $|i,\chi_i\rangle$; and $\langle f,\chi_f|H'|i,\chi_i\rangle = \langle f|H'|i\rangle\langle\chi_f|\chi_i\rangle$, with $\langle\chi_f|\chi_i\rangle$ being the overlap between vibrational wave-function (Franck-Condon factor). The third term in Eq. 1.64, $\delta(E_{i,n_i} - E_{f,n_f})$, is the Dirac Delta function of the energy difference between the two electronic states involved in the CT. Accordingly, Eq. 1.64 can be further rearranged as :

$$k_{I\to F} = \frac{2\pi}{\hbar}\sum_f \langle f|H'|i\rangle^2 \sum_{n_i,n_f} p(E_{i,n_i})\langle\chi_f|\chi_i\rangle \delta(E_{i,n_i} - E_{f,n_f}) \tag{1.65}$$

Eq. 1.65 indicates that the rate of the ET process in condensed phase is mainly determined by three factors: the difference in energy between the two states involved in the ET, the Franck-Condon factor, and the electronic coupling between the two states. Understanding what atomic composition and arrangement is most effective in optimising these factors is the holy grail of theoretical research in HPCs. The next Sections will describe common computational approaches to the approximated evaluation of these terms.

1.2.5.1. Bands alignment

The difference in energy of the two states involved in the CT process in Eq. 1.65 is related to the band alignment between the reactant and the PC at the PC/reactant (medium) interface. In a photo-reductive CT event, an electron needs to be transferred from the bottom of the PC CB to the LUMO of the reactant. Conversely, in a photo-oxidative CT, a hole needs to be transferred from the top of the PC VB to the HOMO of the reactant.

The position of the PC VB and CB edges with respect to the reactant e-acceptor (LUMO) and h-acceptor (HOMO) states is an important parameter for the efficiency of a PC towards a given reactants [64]. To maximise the PC efficiency, the best possible band alignment is obtained when the PC VB-edge is (just, mind the Dirac Delta Function in Eq. 1.65) below the HOMO of the reactant, or the PC CB-edge is (just) above the LUMO of the reactant.

Modelling of band alignment for different semiconductors is nowadays common practice to initially screen their potential as PC or photo-electrodes [118]. This process involves the calculation of the band structure of the semiconductor at the desired (or better practical) level of accuracy, and the ensuing alignment of the band edges with respect to the vacuum level used as common reference.

The simulation results, however, need to be taken carefully, depending on the approximations of the simulation method used. First of all, depending on the method used, different alignments can be obtained. While very sophisticated (and computationally expensive) methods can give very accurate results (i.e. application of GW to post-process hybrid DFT [119] results), the computational cost of these methods limits their use to small systems that are usually unrealistic approximations of real PC/reactant interfaces. Good practice is to verify the accuracy vs affordability compromise of a given simulation method for the class of systems in consideration, then to calculate the band edges alignments with the method offering the best compromises [120].

To date, most calculations of bands alignment consider highly idealised systems in vacuum and neglect PC-media interfaces, which can be profoundly different from the vacuum-exposed ones. Albeit computationally convenient, this approximation may be severely inaccurate so that efforts have starred to be devoted to more realistic simulation of PC-medium interfaces [121]

The use of idealised system structure fails also when the reactivity of the PC is governed by the presence of defects. Determining accurate band edges for defective material is an even more difficult problem than for pristine material. Simulation of overestimated defect concentrations can greatly bias the results and computed band alignment. Solution to this

problem is the object of intense research in the field and in Chapter (6) some progress, based on the use of linear-scaling DFT will be presented.

However, and in spite of the many approximations and accuracy compromises involved, calculated band alignment for HPC-materials has proved to be extremely useful and convenient for initial screening of new material for photo-catalysis [118, 119, 120], and in the elucidation of media-PC interfaces [121].

1.2.5.2. Electronic coupling

The $\langle f|H'|i\rangle$ term in Eq. 1.65 is called electronic coupling and it is a measure of how much the electronic states involved in the CT interact with (are coupled to) each other. The rate of a CT process is strongly affected by the electronic coupling since it depends on the square of $\langle f|H'|i\rangle$. Eq. 1.65 is valid in the weak-coupling limit, which is relevant to HPC CT processes where the reactant is usually not covalently bond to the PC, thence physically separated by a few Angstroms from the PC surface. In this limit there are a number of different ways to calculate the electronic coupling.

Calculation of the electronic coupling rests on suitably definition of the states involved in the CT process. Use of the Born-Oppenheimer (BO) approximation to construct electronic Hamiltonians leads to the formulation of adiabatic electronic states (i.e. states onto whose basis the BO Hamiltonian is diagonal). Adiabatic states change as the nuclei move since the (electronic BO) Hamiltonian changes owing to the different electron-nuclear and inter-nuclear interactions. However, conceptually, Eq. 1.65 requires a measure of the electronic coupling from wave-functions (states) independent of the nuclear motion along the CT reaction coordinate. The donor (or the acceptor) must maintain the extra charge regardless of the nuclear positions. This, in turn requires, the definition of (diabatic) states whose character (electron on the donor or electron on the acceptor) does not (strongly) change along the CT reaction coordinate. Although for any system with more than two atoms strictly diabatic-states cannot be built on the basis of (readily available in the BO approximation) adiabatic-states, several methods to minimise the dependence of the approximated diabatic representation on the nuclear coordinates have been developed.

Three are the most common used approaches: the direct coupling calculation, the generalised Mulliken-Hush scheme, and the fragment charge difference method (that is a derivation of the Mulliken-Hush scheme).

To calculate the electronic coupling between the states involved in the CT a two-state model is generally used. In this model the Hamiltonian can be expressed in two different representations:

$$\begin{pmatrix} E_i & H_{if} \\ H_{if} & E_f \end{pmatrix} \leftrightarrow \begin{pmatrix} E_1 & 0 \\ 0 & E_2 \end{pmatrix} \tag{1.67}$$

where the left matrix represent the two diabatic states at the beginning (E_i) and end (E_f) of the CT process. The right matrix instead represents the adiabatic eigenstates involved in the CT process. These eigenstates are expressed as:

$$E_{1,2} = \frac{E_i + E_f}{2} \pm \sqrt{\left(\frac{E_i - E_f}{2}\right)^2 + H_{if}^2} \tag{1.68}$$

The coupling (H_{if}) can then be calculated using one of the different methods discussed in the following.

The most widely used, and easiest to apply, method is the direct calculation (DC) [143] of the electronic coupling. This method starts with two charge-localised excited-states of the system that are supposed to mimic of the initial and final state of the CT $|i\rangle$ and $|f\rangle$. DC assumes that the CT-eigenstates are symmetric and antisymmetric linear combinations of these two excitation localized states, $(|\Psi_i\rangle + |\Psi_f\rangle)/\sqrt{2 \pm 2S_{if}}$ where:

$$S_{if} = \langle i|f\rangle \tag{1.69}$$

is the overlap integral between the two states.

The coupling is then calculated as half of the energy difference of these two eigenstates:

$$V_{if} = \frac{H_{if} - S_{if}(H_{ii} + H_{ff})/2}{1 - {S_{if}}^2} \tag{1.70}$$

where

$$H_{if} = \langle i|H|f\rangle \tag{1.71}$$

is the matrix element of the Hamiltonian.

The biggest assumptions in the DC calculations is that the two reference states chosen $|i\rangle$ and $|f\rangle$ represent strictly-diabatic states and that the states involved in the CT are the linear combinations of these two charged separated configuration. As a result, the accuracy of the results depends on how accurately diabatised $|i\rangle$ and $|f\rangle$ are.

The Generalised Mulliken-Hush (GMH) [122] is a more formal approach where an additional operator is applied to define charge-localised states, which are then used to calculate the electronic coupling. The additional operator is the dipole moment operator. This choice find justification in the realisation that, being the charged localised on either the donor or acceptor, there should be zero dipole moment (charge sharing) between the donor and acceptor

state. The electronic coupling expression is then reformulated with the use of the dipole moment operator, and calculated in the space of the eigenstates directly involved in the CT:

$$V_{if} = \frac{\mu_{12}\Delta E_{12}}{\sqrt{(\mu_1-\mu_2)^2+4{\mu_{12}}^2}} \tag{1.72}$$

where μ_{12} is the transition dipole moment and ΔE_{12} is the energy difference between the two "diabatic" states. μ_1 and μ_2 are the permanent dipoles of the two states considered.

The fragment charge difference (FCD) [122] method follows exactly the same principle of the GMH approach, but it uses a charge difference operator. The system is divided in two fragments: donor and acceptor. The charge difference matrix read as:

$$\Delta q = \begin{pmatrix} \Delta q_1 & \Delta q_{12} \\ \Delta q_{12} & \Delta q_2 \end{pmatrix} \tag{1.73}$$

with:

$$\Delta q_{mn} = \int \rho_{mn}(r)dr_{\epsilon\,\mathrm{Donor}} - \int \rho_{mn}(r)dr_{\epsilon\,\mathrm{Acceptor}} \tag{1.74}$$

where diagonal elements (i.e. Δq_{mm}) are taken by the one particle density matrix and the off-diagonal elements (i.e. Δq_{mn}) are evaluated using the transition densities expressed as:

$$\rho_{mn}(r) = N\int \dots \int dr_2 \dots dr_N \Psi_m(r, r_2 \dots r_N)\Psi_n(r, r_2 \dots r_N) \tag{1.75}$$

In this particular space-representation, the two charge-localised states are those that either diagonalise Δq or maximise the charge separation. In this approximation, the electronic coupling can be expressed as:

$$V_{if} = \frac{\Delta E_{12}|\Delta q_{12}|}{\sqrt{(\Delta q_1-\Delta q_2)^2+4{\Delta q_{12}}^2}} \tag{1.76}$$

1.2.5.3. Franck-Condon factor

The Franck-Condon factor (FCF) is the square overlap integral between the nuclear wave-functions associated with different electronic potential surfaces. The FCFs stems from the expression of the intensity of an electric dipole transition $I_{\mu\kappa}$ between two vibronic states. $I_{\mu\kappa}$ is proportional to the square of the electric transition dipole moment $M_{\mu\kappa}$ that in the adiabatic approximation reads as:

$$M_{\mu\kappa} \approx \langle \chi_{k,\kappa}(Q) | \langle \psi_\kappa(q,Q) | M(q,Q) | \psi_m(q,Q) \rangle | \chi_{m,\mu}(Q) \rangle =$$

$$\langle \chi_{k,\kappa}(Q) | M_{k,m}(q,Q) | \chi_{m,\mu}(Q) \rangle \tag{1.77}$$

Where $\psi_\kappa(q,Q)$ or $\psi_m(q,Q)$ and $\chi_{k,\kappa}(Q)$ or $\chi_{m,\mu}(Q)$ are the final (k,κ) or initial (m,μ) electronic and vibrational states of the system, respectively. $M_{k,m}(q,Q)$ is the electronic transition dipole moment, and q and Q are the electronic and nuclear degrees of freedom. If the BO approximation is used, there is no analytical expression for $M_{k,m}(Q)$. In practice an approximated solution to $M_{k,m}(Q)$ can be found using its Taylor expansion around the equilibrium position Q_0 . If the first term approximation of the Taylor expansion is used, the Franck-Condon approximation is obtained. Such approximation neglects the Q dependence of the electronic dipole transition moment. This approximation reduces the evaluation of the vibronic transition intensities to the computation of the overlap integral between the vibrational wave-functions of the electronic transition of interest.

The FCF can be calculated under various different assumptions [123, 124]. The the most common approximations are the single mode approximation and the multidimensional FCF calculation.

In the FCF single mode approximation, all the vibronic manifolds of the states involved in the CT process are treated as a single effective quantum mode with average energy $\hbar\nu$ approximated to be the same in the start and end state of the CT process. This assumption restricts the donor-acceptor system (i.e. PC-reactant) to a single degree of freedom of the initially multidimensional potential surface. In this framework, the (approximately quadratic) adiabatic potentials for the reactant (D*A) reads:

$$U_r(Q) = \frac{\hbar\nu}{2}Q^2 \tag{1.78}$$

while the one for the products (D^+A^-) is:

$$U_p(Q) = \frac{\hbar\nu}{2}(Q-\Delta)^2 + \Delta G \tag{1.79}$$

where $\Delta G = U_p(\Delta) - U_r(0)$ is the free energy of the CT process, and Δ is the distance along the nuclear reaction coordinate Q between reactants and products. The reorganization energy (λ) can be defined as the change in free energy necessary to move the reactant atoms to the product configuration and to move the solvent (medium) atoms as if they were solvating the product but without the CT happening. A picture to better understand the meaning of λ can be seen in Fig.1.8.

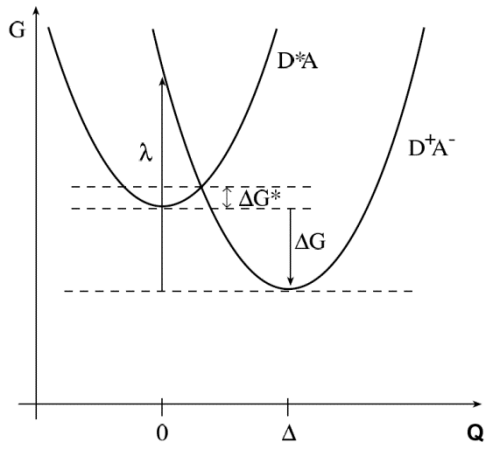

Figure 1.8. One dimensional (diabatic) potential energy surfaces for reactants (D*A) and products (D^+A^-) state as a function of the (nuclear) reaction coordinate Q.

λ can be expressed as:

$$\lambda = \frac{\hbar\omega}{2}\Delta^2 \tag{1.80}$$

According to the Franck-Condon approximation, the jump between the potential energy surfaces occurs at fixed nuclear coordinates (i.e. it is a vertical transition) and if the transition is radiation-less the energy remains conserved (i.e. it is a horizontal transition). Both these conditions are met at the point of intersection of the parabolas so that an expression for the activation energy can be deduced:

$$E_{A=}\frac{(\Delta G+\lambda)^2}{4\lambda} \tag{1.81}$$

In the single mode approximation, the FCF can be expressed as:

$$FCF = \frac{1}{\sqrt{4\pi\lambda k_B T}}\sum_\nu e^{-S}\frac{S^\nu}{\nu!}\exp\left[-\frac{(E+\Delta G+\lambda+\nu h\omega)}{4\lambda k_B T}\right] \tag{1.82}$$

where S is a dimensionless constant equal to:

$$S = \frac{\Delta^2}{2} = \frac{\lambda}{\hbar\omega} \tag{1.83}$$

S is called the Huang-Rhys factor that gives a measure of the electron-phonon coupling in the system. ν is a temperature dependent Bose factor $\nu = (e^{\hbar\omega/k_B T} - 1)^{-1}$.

When the single mode approximation does not hold (as for example in solvent controlled dynamics [123]) the multidimensional FCFs need to be calculated. This type of calculations are computationally very expensive and can be carried out only for very small atomistic

models [124]. The contribution of each vibrational mode to the relaxation energies (where the relaxation energy is the sum of the energies of the vibronic states involved in the CT reaction) can be obtained by expanding the potential energies of the neutral and charge separated states in a power series of their normal coordinates (they will be called Q_1 and Q_2).

$$\lambda_i = \sum \lambda_j = \sum \hbar\omega_j S_j \tag{1.86}$$

where:

$$\lambda_j = \frac{k_j}{2} \Delta Q_j{}^2 \tag{1.87}$$

with ΔQ_j being the displacement along normal modes (NM) and:

$$S_j = \lambda_j / \hbar\omega_j \tag{1.88}$$

where S_j is the Huang-Rhys factor for each FCF calculated for on each vibrational mode of the system of interest in the neutral and charge separated states.

The standard rectilinear NM are obtained as linear combination of Cartesian displacements:

$$Q_j = \sum_k L_{j(k)} \left[q_j{}^0 - q_j \right] \tag{1.89}$$

where L is the matrix that connects the 3N-6 normal coordinates with the set of 3N mass-weighted Cartesian coordinates q_j. The NM Q_1 and Q_2 of the neutral and charge separated states obtained by Eq. 1.89 are related by a transformation consisting of a multidimensional rotation and a translation:

$$Q_1 = JQ_2 + \Delta Q \tag{1.90}$$

where J is the Duschinsky [125] matrix describing the mixing of the normal coordinates of the two states.

Once the NM of the two states are known, Eq. 1.77 can be rewritten as:

$$\left\langle \chi_{k,\kappa}(Q) \middle| M_{k,m}(q,Q) \middle| \chi_{m,\mu}(Q) \right\rangle \approx M_{k,m}(q,Q) \left\langle \prod_{j=1}^{3N-6} \varphi(Q_1) \middle| \prod_{j=1}^{3N-6} \varphi(Q_2) \right\rangle \tag{1.91}$$

where the right side of the equation represent the expression of the multidimensional FCF in the NM Q_1 and Q_2. The Franck-Condon integrals for the 3N-6 normal coordinates are then evaluated by recurrence relation as shown in the work of Doktorov [126].

Whereas (differently approximated) calculation of the electronic coupling for PCs and dye-sensitised solar cells is becoming relatively common [127, 128], direct computation of the FCF for realistic systems (PC-medium-reactant interfaces) is still beyond the reach of DFT-based approaches. Improvement in this respect would lead to a better understanding of the FCF

variations with respect to the atomic composition of the system. Since the FCF depends on the vibrational quantization of the CT-states, the possibility of designing it on the base of the system configurations would be extremely desirable for rational development of novel and better PCs.

1.3. (Differently informed) Nano-structuring the photo-catalysts

1.3.1. Advantages of nanomaterials for HPC applications

From the previous Section it is clear that the efficiency of a PCs as determined by electronic lines-ups, electronic couplings and FCF stems from the atomic structure of the overall PC-reactant-medium interface. Prompted by encouraging experimental observations, nanostructuring of the PC is currently believed to hold great promise for the development of innovative and more efficient PCs.

Since the discovery of carbon nanotubes the last two decades have seen an explosion of interest in nanostructured materials. Such interest has been fuelled by the fascinating physico-chemical properties that these materials present and their potential for technological applications, HPC included.

The advantages in using nanomaterials (nanoporous systems, nanorods, nanotubes) for HPCs applications are multiple: the large surface-to-volume ratio and the volume confinement effects [129] may lead to peculiar chemical reactivity different from bulk materials. In addition, the reduced dimensions and increased surface area of nanomaterials tend to favour fast migration of the photo-generated carriers to the surface enhancing the possibility of CT processes. Another advantage of nanomaterials is the possibility of generating associative properties such as: “electron coupling assembly” where two nano-particles in close contact create a new shared electronic state [130]; “plasmon-exciton coupling assembly” in which two or more particles under illumination show plasmon-exciton interaction, originating appealing optical properties [131], or “optical coupling assembly”, where regular matrices of nanomaterials present collective absorption states, favouring the creation of an excited state [132]. In addition to all these emerging properties, previous substantial experimental efforts have made it possible to achieve a good synthetic control of the morphology of various nanoparticles, opening up for the design and synthesis of heterogeneous and hierarchical super-structures [133].

In spite of these documented or potential advantages of nanomaterials for HPC, there is also an important potential drawback to consider. The quantum confinement due to the reduced dimension of the materials can limit photo-catalytic efficiencies because of the ensuing

increase in the recombination probabilities for charge carriers. It is thence fundamental for nano-PCs to present a gradient in potential or charge carriers' concentration from the core to the periphery to favour fast carriers migration, lowering the e*-h recombination probability. Such gradient necessary for the migration can also be provided through the electronic excitation.

A multitude of nanomaterials have been synthesised for applications in HPC. The easiest way to classify them is by dimensionality. Zero-dimensional (0D) spherical materials (quantum dots) have been suggested as innovative PCs due especially to their large surface area. However, this type of particles presents strong quantum confinement effects due to their small dimensions. To ameliorate this problem, it is common practice to synthesise hetero-structured core-shell nanoparticles to facilitate the migration of the charge carriers. Highly effective PCs are obtained by this approach such as Ag/AgCl nano-sphere [134] or Cds/Au/TiO_2 nanoparticles that are capable of mimicking natural photosynthetic systems [135].

One-dimensional (1D) nanostructures have started to receive growing attention. Given their relevance to the study presented, they are considered in detail in the next section.

Very recently, two-dimensional (2D) platelets have emerged as interesting nano-structures for HPCs. Their highly anisotropic shape can originate peculiar chemical reactivity and intriguing charge-accumulation processes on the medium-exposed facets of these materials. It is still extremely difficult to synthesise this type of materials given their low stability and tendency to surface reconstruction. However, few examples based on TiO_2 [136] and WO_3 [137] have already been synthesised and their HPC performances characterized.

Three-dimensional (3D) nano-porous materials and hetero-structures are widely used in HPC since they present a very large surface area, allowing in principle substantially increased diffusivity of reactant and products with respect to bulk materials. Usually, noble metal particles are grafted into these materials to improve their efficiency by reducing the recombination of the electron-hole pairs. Furthermore, 3D nano-materials show unique confinements effect that can enhance their selectivity and reactivity. Examples of 3D PCs are nano-porous zeolites [138], with Ag particles embedded in WO3 and $BiVO_4$ coated of silica.

1.3.2. 1D nanomaterials for HPC applications

The increased aspect ratio of 1D nanostructures has been recently shown to be linked to an increased photo-catalytic activity as a result of the highly anisotropic diffusion of separated e*-h. Another beneficial aspect of 1D nanostructures is the possibility of using them as building blocks for the synthesis of hierarchical heterogeneous composites, which opens up for design and development of innovative and versatile HPC systems [139]. Although a great amount of studies has been published in recent years on this topic, for sake of brevity, here we report only a few illustrative examples.

Fujishima and co-workers have succeeded in synthetizing synthesized highly ordered TiO_2 nanotubes array for nonselective degradation of pollutants [140]. It was shown that increasing the length of the nanotube over a certain range (from 0.2µm to 17 µm) improved the photo-catalytic activity of the system. These results support the theory that the length of the 1D structure favours the e*-h separation or at least the access to reactive sites.

Wu and co-workers have reported a study of novel TiO_2 nanobelts [141]. The experimental characterization, complemented by DFT simulations, shows enhanced reactivity of the nanobelt with respect to bulk TiO_2 and 0D nanoparticles. The enhancement in reactivity is attributed to a higher mobility of the charge carriers, probably due to the anisotropic growth of {101} facets in this 1D nanomaterial.

A very interesting example of the potential of 1D nanomaterials for HPC is given by the work of Zhu and co-workers. They reported the synthesis of C_3N_4 nanorods from nanoplates [142]. The high crystallinity of the nanorods was found to inhibit e*-h recombination, stressing the importance of 1D material morphology for HPC performances. This example is extremely appealing as based on cheap metal-free materials, which could be easily scaled up towards commercially viable production of environmental benign PCs.

The importance of careful engineering in 1D nanostructure for HPC is further stressed by the work of Yang's group [143]. TiO_2 thin-films were deposited on Si nanowires as photo-anode and electrically connected to a TiO_2 nanowire photo-cathode. This system was designed to explore the possibility of generating H_2 and O_2 from H_2O, under a photo-catalytic Z-scheme [144, 145]. Under solar illumination photo-generated e* went from the Si nanowires to the surface of the anode to reduce protons and generate H_2. In parallel, the photo-generated h in the TiO_2 nanowires oxidised water to produce O_2. The holes from Si and electrons from TiO_2 recombined in the electrical contact, completing the relay of the Z-scheme.

NiS-CdS nanorods are another example of how careful engineering of 1D PCs can lead to enhancement of their properties. The work of Yu et al. [146] demonstrates how the presence

of a field in the composite nanostructures due to the p-n junction between the two components led to a faster charge carriers mobility and better photo-catalytic activity.

Another case of the use of asymmetric functionalization of 1D nanostructured substrates for enhanced 1D PCs can be found in the work of Song et. al. [147]. CdSe nanorods were observed to show different reactivity depending on whether they were coated at one extremity or both with a Pt-tip. When the Pt tip was put only on one extremity the reactivity of the system was enhanced. Conversely, when both ends of the nanorod were coated with Pt, the reactivity of the PC decreased. This work unambiguously demonstrates how the occurrence of longitudinal polarizations along 1D nanostructure, effective in biasing e*-h and diffusions can majorly affect the system PC reactivity.

Prompted by these intriguing examples, the research in this thesis has been mostly focused in understanding, via computer simulations, how permanent polarizations in 1D nanomaterials can be most effectively used towards design of enhanced HPC strategies based on this class of materials. Give the simultaneous relevance of efficient e*-h separation and suitable alignment between PC and reactant electronic states, special attention has been paid also to the interplay between the occurrence of polarization (beneficial for e*-h separation) and the polarization-induced shifts in the electronic states of species interacting with the polarising PC.

References

[1] United Nation, Department of Economic and Social Affairs *Concise Report on the World Population Situation in 2014* 2014.

[2] World Energy Resources *Energy resource survey 2013* 2013.

[3] Venkatesan A. K., Halden R. U. *Scientific Reports* 2013 **4** 3731.

[4] World Health Organization *GLAAS 2014 Report* 2014.

[5] Cohen A., Diver W. R., Gapstur S. M., Turner M. C. *Environmental Health Perspectives* 2014 **122** (4) 397.

[6] Global Health *Observatory Burden of disease from Ambient Air Pollution for 2012* 2012.

[7] United Nation *The United Nations World Water Development Report 2015* 2015.

[8] United States Environmental Protection Agency *Final Report: Metals Soil Pollution and Vegetative Remediation* 2012.

[9] International Energy Agency *Key World Energy Statistics in 2011*, 2011.

[10] https://www.gov.uk/government/policies/low-carbon-technologies

[11] United States Environmental *Protection State Policies to Support Renewable Energy*

[12] https://ec.europa.eu/energy/en/topics/renewable-energy/national-action-plans

[13] https://www.mgi.gov/

[14] Fujishima A., Honda K. *Nature* 1972 **238** 37.

[15] Tai C., Jiang G. *Chemosphere* 2005 **59** 321.

[16] Doong R. A., Maithreepala R. A., Chang S .M. *Water Sci Technol* 2000 **42** (7) 253.

[17] Institut National de l'environnement industriel et de risqué (INERIS). http://www.ineris.fr/

[18] Muruganandham M., Sobana N., Swaminathan M. *J Hazard Mater B* 2006 **137** 1371.

[19] Saien J., Soleymani A. R. *J Hazard Mater* 2007 **144** 506.

[20] Thomson Reuters *Web of Knowledge. Thomson Reuters* 2013

[21] Paz Y., Luo Z., Rabenberg L., Heller A J. *Mater. Res.* 1995 **10** 2842.

[22] De Lasa H., Serrano B., Salaices M. *Photocatalytic Reaction Engineering*. Springer, 2005 NewYork

[23] Usubharatana P., McMartin D., Veawab A., Tontiwachwuthikul P. *Ind. Eng. Chem. Res*. 2006 **45** 2558.

[24] Chatterjee D., Mahata A. *Appl Catal B* 2001 **33** 119.

[25] Rajeshwar K., Osugi M. E., Chanmanee W. *J Photochem Photobiol C* 2008 **9** 171.

[26] Kabra K., Chaudhary R., Sawhney R.L. *Ind Eng Chem Res* 2004 **43** 7683.

[27] Kudo A., Miseki Y. *Chem. Soc. Rev*. 2009 **38** (1) 253.

[28] Shen S., Guo L. *Mater Res Bull* 2008 **43** 437.

[29] Hodes G., Manassen J., Cahen D. *J Electrochem Soc* 1981 **128** 2325.

[30] Jiao C., Yang Z. M., Wan Z., Pa A. *Journal of Nanomaterials* 2013 **2013** 1.

[31] Randin J. P. *Journal of Electronics Materials* 1978 **7** (1) 47

[32] Gupta S. M. *High Energy Chemistry* 2012 **46** (1) 1.

[33] Wei Q., Zhang Z., Li Z., Zhou Q., Zhu Y. *J. of Phys. D: Appl. Phys* 2008 **41** (20) 202002.

[34] Watanabe T., Hashimoto K. *Chem. Mater*.,2000 **12** (1) 3.

[35] von Goetz N., Fabricius L., Westerhoff P. *Environ Sci Technol*. 2012 **46** (4) 2242.

[36] Ning G., Ding D., Wang X. *Int. J. of Hydrogen Energy* 2015 **40** (5) 2107.

[37] Hagfeldt A and Gratzel M *Acc. Chem. Res.* 2000 **33** 269

[38] Dibbell R. S., Youker D. G., Watson D. F., *J. Phys. Chem. C* 2009 **113** 18643.

[39] Yamashita H., Ichihashi Y., Takeuchi M., Kishiguchi S., Anpo M. *J. Synchrotron Radiat.* 1999 **6** 451.

[40] Herrmann J. M., Disdier J., Pichat P. *Chem. Phys. Lett.* 1984 **108** 618.

[41] Borgarello E., Kiwi J., Gratzel M., Pelizzetti E., M. Visca, *J. Am Chem. Soc.* 1982 **104** 2996.

[42] Karakitsou K. E., Verykios X. E. *J. Phys. Chem.* 1993 **97** 1184

[43] Ye J. H., Zou Z. G. *J. Phys. Chem. Solids* 2005 **66** 266.

[44] Bisquert J *PCCP* 2008 **10** 3175

[45] Quaranta A. A., Ottaviani G., Canali C., Jacoboni C. *Solid State Electronics* 1977 **20** (2) 77

[46] Chen X. B., Burda C., *J. Am. Chem. Soc.* 2008 **130** 5018.

[47] Li X. K., Kikugawa N., Ye J. H. *Adv. Mater*. 2008 **20** 3816

[48] Ishikawa A., Takata T., Kondo J. N., Hara M., Kobayashi H., Domen K. *J. Am. Chem. Soc.* 2002 **124** 13547.

[49] Zhang X., Ai Z. H., Jia F. L., Zhang L. Z. *J. Phys. Chem. C* 2008 **112** 747.

[50] J. Sato, N. Saito, H. Nishiyama, Y. Inoue *J. Phys. Chem. B* 2001 **105** 6061.

[51] S. X. Ouyang, N. Kikugawa, D. Chen, Z. G. Zou, J. H. Ye, *J. Phys. Chem. C* 2009 **113** 1560.

[52] Z. G. Zou, J. H. Ye, H. Arakawa, *Chem. Phys. Lett.* 2000 ***332*** 271.

[53] Z. G. Zou, J. H. Ye, K. Sayama, H. Arakawa, *Chem. Phys. Lett.* 2001 **343** 303.

[54] S. X. Ouyang, Z. S. Li, Z. Ouyang, T. Yu, J. H. Ye, Z. G. Zou, *J. Phys. Chem. C* 2008 **112** 3134.

[55] K. Maeda, K. Teramura, D. L. Lu, T. Takata, N. Saito, Y. Inoue, K. Domen, *Nature* 2006 **440** 295.

[56] S. X. Ouyang, J. H. Ye, *J. Am. Chem. Soc.* 2011 **133** 7757.

[57] W. F. Yao, J. H. Ye, *J. Phys. Chem. B* 2006 **110** 11188

[58] Y. P. Bi, S. X. Ouyang, J. Y. Cao, J. H. Ye, *Phys. Chem. Chem. Phys.* 2011 **13** 10071.

[59] Officer D. L., Burrel A. K., Campbell W. M. Coord. Chem. Rev. 2004 **248** (13) 1363.

[60] X. Zong, H. J. Yan, G. P. Wu, G. J. Ma, F. Y. Wen, L. Wang, C. Li, *J. Am. Chem. Soc.* 2008 **130** 7176.

[61] Y. P. Bi, S. X. Ouyang, J. Y. Cao, J. H. Ye, *Phys. Chem. Chem. Phys.* 2011 **13** 10071

[62] G. M. Wang, X. Y. Yang, F. Qian, J. Z. Zhang, Y. Li, *Nano Lett.* 2010 **10** 1088

[63] J. Hensel, G. M. Wang, Y. Li, J. Z. Zhang, *Nano Lett.* **2010**, *10*, 478.

[64] B. O'Regan and M. Gratzel. Nature, 1991 **353** 740.

[65] Caruso R., Cheng Y. B., Huang F., Cheng D. *Adv.Mater*. 2009 **21** (21) 2206

[66] Gratzel M. *Inorg. Chem.* 2005 **44** (20) 6841.

[67] O'Donnell K. P., Chen X. Appl. Phys. Lett. 1991 **58** 2924.

[68] Wei S., Zunger A. *Phys. Rev. B*. 1999 **60** 5404.

[69] Chen S.C., Lin J. L. *Chem. Commun.*, 2012 **48** 2528.

[70] Han W., Ren L., Qi X., Liu Y., Wei X., Huang Z., Zhong J *Appl Surf Sci* 2014 **299** 12.

[71] Nakagawa S., Kato H. *J. Phys. Chem. B* 2000 **104** (3) 571.

[72] Efstathiou P., Irvine J. T. S., Xu. X. *Nature Materials* 2012 **11** 595.

[73] X. K. Li, N. Kikugawa, J. H. Ye, *Adv. Mater.* **2008**, *20*, 3816

[74] Rohrer G. S., Li L., Salavdor P.A. Nanoscale 2014 **6** 24

[75] H. Okumura, et al. *Catal. Today* 2015 To be published

[76] Saito F., Sato T., Zhang Q. *Journal of the American Ceramic Society* **87** (6) 1116.

[77] N. Umezawa, O. Y. Shuxin, J. H. Ye, *Phys. Rev. B* 2011 **83** 035202.

[78] V. I. Anisimov, F. Aryasetiawan, A. I. Lichtenstein *J. Phys.: Condens. Mat.* 1997 **9** 767

[79] Serpone N., Ryabchuk V. K., Emeline A. V. *J. Phys. Chem. B*, 1999 **103** (8) 1316.

[80] Tauc. J. *Czechosl. Journ. Phys* 1958 **9** 95

[81] Koc C. *Czechosl. Journ. Phys* 1957 **7** 91.

[82] Antoncik E., Gaur N. K. S. *J. Phys C* 1978 **11** 735.

[83] Sze S. M. *Semiconductor Devices Physics and Technology* 1978 Jhon Wiley and Sons Inc.

[84] Cardona C., Yu. Y. P. *Fundamentals of semiconductors* 2005 Springer Ed.

[85] Haug A. *J. Phys C: Solid State Phys* 1983 **16** 4159.

[86] Goetzberger, A. *Crystalline Silicon Solar Cells* 1998 John Wiley & Sons Ltd.

[87] Ueta M., Kanzaki H., Kobayashi K., Toyozawa Y., Hanamura E. *Excitonic Processes in Solids* 1986 **60** 1

[88] Rappe A., Grinberg I., West D. V., Stein D.M. *et. al Nature* 2013 **503** 509

[89] Wang Z. L., Liu H., Jiang H., Yang R., Huang X. *Nanoletters* 2014 **15** 2372

[90] Pantelides S. T. *Rev. Mod. Phys*. 1978 **50** 797

[91] Neugebauer J., Kresse G., Janotti A., Van de Walle C. G. *Rev. Mod. Phys* 2014 **86** 253.

[92] Lany S., Zunger A. *Phys. Rev B.* 2008 **78** 235104.

[93] O'Reilly O. P., Lindsay A. *Journal of Physics: Conference Series* 2012 **242** 012002.

[94] Limpijumnong S.,Van de Walle C. G. *Phys. Rev. B* 2004 **69**, 035207.

[95] Alkauskas A., Broqvist P., Pasquarello A. *Phys. Rev. Lett.* 2008 **101** 046405

[96] Larkins F. P. *J. Phys C.:Solid State Phys.* 1971 **4** (18) 3065

[97] Muto T. *Prog. Theor. Phys*. 1949 **4** (2) 181

[98] Dolgov S.A., Kärner T., Lushchik A., Maaroos A., Nakonechnyi S., Shablonin E. *Phys. Solid State* 2011 **53** 1244.

[99] Zecchina A., Lofthouse M.G., Stone F.S. *Phys. Chem. Condens. Phases* 1975 **71** 1476.

[100] Crawford H.J. *Semiconduct. Insulat*. 1982 **5** 599.

[101] Seebauer E.G., Kratzer M.C. *Mater. Sci. Eng. R* 2006 57.

[102] Kuznetsov V.N., Serpone N. *J. Phys. Chem. C* 2009 **113** 15110.

[103] Lisachenko A. *J. Photochem. Photobiol. A* 2008 **196** 127.

[104] Henderson B., Werts J.E. *Defects in the Alkaline Earth Oxides* 1977 Taylor & Francis Ltd, London.

[105]. Schirmer O.F *J. Phys. Condens. Matter* 2006 **18** R667.

[106] Shockley W., Read W. T. *Physical Review* 1952 **87**(5) 835.

[107] Li C., Li M., Zhang J. Angew. Chem. Int. Ed. 2008 47(9) 1766

[108] H. G. Yang, C. H. Sun, S. Z. Qiao, J. Zou, G. Liu, S. C. Smith, H. M. Cheng, G. Q. Lu, *Nature* 2008 **453** 638.

[109] Gaya U. I., Abdullah A. H., Zainal Z. *et al J Hazard Mater* 2009 **168** 57

[110] G. Liu, C. H. Sun, H. G. Yang, S. C. Smith, L. Z. Wang, G. Q. Lu, H. M. Cheng, *Chem. Commun*. 2010 **46** 755.

[111] S. W. Liu, J. G. Yu, M. Jaroniec *J. Am. Chem. Soc.* 2010 **132** 11914.

[112] Colon G., Fernandez-Garcia M. *Chem. Rev*. 2012 **112** 1555.

[113] G. C. Xi, J. H. Ye *Chem. Commun.* 2010 **46** 1893.

[114] Y. Ebina, T. Sasaki, M. Harada, M. Watanabe *Chem. Mater*. 2002 **14** 4390.

[115] Lathasree S., Rao A. N., SivaSankar B. *J Mol Catal* A Chem 2004 **223** 101.

[116] Degen A., Kosec M. *J Am Ceram Soc* 2003 **86** 2001

[117] Zhang L., Cheng H., Zong R. *et al. J Phys Chem C* 2009 **113** 2368

[118] Sokol A., Watson G. G., Sherwood P. *et al. Nature Materials* 2013 **12** 798.

[119] Hinuma Y., Grüneis A., Kresse G., Oba F. *Phys. Rev. B* **90** 155405.

[120] Klein A. *J. Phys.: Condens. Matter* 2015 **27** 134201.

[121] Opalka D. *et al. J Phys Chem B* 2015 **119** 9651.

[122] Hsu C. P. *Accounts of Chemical Reasearch* 2009 **42** (4) 509

[123] Nitzan A, *Chemical Dynamics in Condensed Phases: Relaxation, Transfer and Reactions in Condensed Molecular Systems*. 2006, Oxford University Press

[124] Guo J., Pugliesi I., Müller-Dethlefs K., Dessentb C. E. H. *J. Chem. Phys*. 2007 **127** 234308.

[125] Duschinsky F. *Acta Phisicochim URSS* 1937 **7**, 551.

[126] Doktorov E. V., Malkin I. A., Manko V. I. *J. Mol. Spectrosc*.1977 **64** 302

[127] Liu T and Troisi A. 2014 *Adv. Funct. Mater.* **24** 925

[128] Sleigh J P, McMahon D P, Troisi A 2009 *App. Phys. A* **95** 147

[129] Weng B., Liu S., Tang Z.R., Xu Y. J. *RSC Adv*., 2014 4 12685

[130] Crooker S. A., Hollingsworth J. A., Tretiak S., Klimov V. I. *Phys. Rev.Lett.* 2002 **89** 186802.

[131] Tian Y., Tatsuma T. *J. Am. Chem. Soc.* 2005 **127** 7632.

[132] Joannopoulos D., Villeneuve P. R., Fan S. H. *Nature* 1997 **386** 143

[133] Tao A., Sinsermsuksakul P., Yang P. *Nat. Nanotechnol.* 2007 **2** 435

[134] Choi M., Shin K. W., Jang J. *Journal of Colloid and Interface Science* 2012 **341** 83

[135] Yun H.J., Lee H., Kim N.D., Lee D.M., Yu S., Yi J. *ACS Nano* 2011 **5** 4084.

[136] Lee E., Jang J. *et al. Journal of Hazardous Materials* 2012 **219** 13

[137] Chen D., Sun J., Gao L. *et al*. *Nanoscale* 2012 **4** 5431

[138] Li G., Zhang D., Yu J.C., *Chemistry of Materials* 2008 **20** 3983

[139] Weng B., Liu S., Tang Z. R., Xu Y. J, *RSC Adv***.**, 2014 **4** 12685-12700

[140] Liu Z., Zhang X., Nishimoto S., Murakami T., Fujishima A., *Environ. Sci. Technol*. 2008 **42** 8547

[141] Wu N., Wang J., Tafen D. N., Wang H., Zheng J. G., Lewis J. P., Liu X., Leonard S. S., Manivannan A., *J. Am. Chem. Soc*., 2010 **132** 6679

[142] Bai X., Wang L., Zong R., Zhu Y., *J. Phys. Chem. C*, 2013 **117** 9952

[143] Liu C., Tang J., Chen H. M., Liu B., Yang P., *Nano Lett*., 2013 **13** 2989

[144] Nozik A. J., *Appl. Phys. Lett*., 1976 **29** 150

[145] Liu C., Hwang Y. J., Jeong H. E., Yang P., *Nano Lett*.,2011 **11** 3755

[146] Zhang J., Qiao S. Z., Qi L., Yu J., *Phys. Chem. Chem. Phys*.,2013 **15** 12088

[147] Bang J. U., Lee S. J., Jang J. S., Choi W., Song H., *J. Phys. Chem. Lett.*, 2012, 3, 3781.

Chapter 2

Linear-scaling Density Functional Theory in ONETEP

Abstract

In this Chapter an introduction to the theory of linear scaling Density Functional Theory (LS-DFT) and its implementation in the ONETEP program is presented. The Chapter begins with an introduction to the Born-Oppenheimer approximation and Density Functional Theory, with attention to the aspect underpinning the applicability of DFT, namely plane-wave basis set, periodic boundary conditions and the pseudopotential approximation. The LS-DFT approach is then described and the key aspects of its implementation in ONETEP analysed. Special attention is paid to the Density Matrix formulation of DFT, (psinc functions) basis-set, and Non-Orthogonal Wannier functions. The main algorithms used for the calculation of self-consistent DFT energies and forces in ONETEP are explained. The Chapter ends with an overview of several other computational techniques such as Coulomb cutoff, conduction-state optimisation, and absorption spectra simulation, which have been used for the research presented in this Thesis.

2.1. The Born-Oppenheimer approximation

The simplest approach to model a semiconductor is to consider a solid at 0 K. All the information on the system are contained in the vibronic wave-function $\Psi(\mathbf{R},\mathbf{r})$ that is the solution of the time-independent Schrödinger equation and depends on both the nuclear ($\mathbf{R}$) and electronic ($\mathbf{r}$) degrees of freedom:

$$\hat{\mathrm{H}}\Psi(\mathbf{R},\mathbf{r}) = \left(\hat{\mathrm{T}}_{\mathrm{n}}(\mathbf{R}) + \hat{\mathrm{T}}_{\mathrm{e}}(\mathbf{r}) + \mathrm{U}_{\mathrm{e}}(\mathbf{r}) + \mathrm{U}_{\mathrm{n}}(\mathbf{R}) + \mathrm{U}_{\mathrm{en}}(\mathbf{R},\mathrm{r})\right)\Psi(\mathbf{R},\mathbf{r}) = \mathrm{E}\Psi(\mathbf{R},\mathbf{r}) \quad (2.1)$$

where $\hat{\mathrm{T}}_{\mathrm{n}}(\mathbf{R})$ and $\hat{\mathrm{T}}_{\mathrm{e}}(\mathbf{r})$ are the kinetic energy operators for the nuclei and the electrons, respectively. $\mathrm{U}_{\mathrm{e}}(\mathbf{r})$, $\mathrm{U}_{\mathrm{n}}(\mathbf{R})$ and $\mathrm{U}_{\mathrm{en}}(\mathbf{R},\mathbf{r})$ are the potentials due to the Coulomb electrostatic interaction between electrons only, nuclei only (both repulsive), and between electrons and nuclei (attractive). The Hamiltonian for the system can be further expanded to read:

$$\hat{H} = -\frac{1}{2}\left[\sum_{i=1}^{N_{elec}} \nabla_{r_i}^2 + \sum_{I=1}^{N_{nuclei}} \frac{1}{M_I} \nabla_{R_I}^2\right] + \frac{1}{2}\sum_{i=1}^{N_{elec}} \sum_{j\neq 1}^{N_{elec}} \frac{1}{|r_i - r_j|} -$$

$$\sum_{I=1}^{N_{nuclei}} \sum_{i=1}^{N_{elec}} \frac{Z_I}{|R_I - r_i|} + \sum_{I=1}^{N_{nuclei}} \sum_{J\neq 1}^{N_{nuclei}} \frac{Z_I Z_J}{|R_I - R_J|} \quad (2.2)$$

From now on in this chapter Hartree and atomic units are used hence $\hbar = e = m_e = 4\pi\epsilon_0 = 1$.

The time-independent Schrödinger equation can be easily converted into the time dependent one. Since the Hamiltonian is time-independent its solutions can be extended in the time domain multiplying the purely spatial function $\Psi(\mathbf{R}, \mathbf{r})$ of Eq.2.1 by a time dependendent function. The wave-function in the time dependent case will then look like:

$$\Psi(\mathbf{R}, \mathbf{r}, t) = \Psi(\mathbf{R}, \mathbf{r})\Theta(t) \quad (2.3)$$

where we recall that $\Psi(\mathbf{R}, \mathbf{r})$ is the many body time-independent solution to the Schrödinger equation [1] and $\Theta(t)$ is the time dependent part. Given an initial phase (θ_0) for each eigenvalue of equation 2.1 the time evolution looks:

$$i\frac{\partial}{\partial t}\Theta(t) = \varepsilon\Theta(t) \rightarrow \Theta(t) = \exp(i\theta_0 - i\varepsilon t) \quad (2.4)$$

Consequently, the time dependent Schrödinger equation reads:

$$\hat{H}\Psi(\mathbf{R}, r, t) = i\hbar\frac{\partial}{\partial t}\Psi(\mathbf{R}, r, t) \quad (2.5)$$

The wave-function contains all the information about the physical properties of the combined ionic and electronic parts of the system. Such a huge amount of information needs somehow to be approximated [2]. The first approximation that is usually made is based on the different masses of the electrons and nuclei. Since the mass of a proton ($1.672621777(74)\times10^{-27}$ Kg) and of a neutron ($1.674927351(74)\times10^{-27}$ kg) is over three order of magnitude larger than the mass of the electron (9.10938215×10^{-31} Kg), nuclei are substantially more massive than electrons. As a result, for a steady solution to the Schrodinger equation, the velocity of the electrons is orders of magnitude larger than for the nuclei. Therefore, it is plausible to approximate the motion of the electrons as instantaneous with respect to that of the nuclei. Such difference in timescales implies that the electrons can relax to their lowest energy configuration extremely quickly (instantaneously) following changes in the nuclear configuration. This is the physical justification of the Born-Oppenheimer adiabatic approximation (BO) [3].This approximation allows to treat the electrons as they were moving in a static potential generated by the nuclei, which allows to treat the nuclear and electronic degrees of freedom separately. On this basis, the vibronic wave-function can be factorised on the basis of independent functions of the nuclear and electronic coordinates as:

$$\Phi(\mathbf{r}_i, \mathbf{R}_I) = \Psi(\mathbf{r}_i; \mathbf{R}_I)\eta(\mathbf{R}_I) \tag{2.6}$$

here the semicolon indicates that the electronic wave-function is parametrically and not directly dependent on the nuclear coordinates **R**. On the basis of the BO adiabatic approximation, an electronic time-independent Schrödinger equation can be defined for each nuclear configuration $\mathbf{R}_I$:

$$\sum_{i=1}^{N_{elec}} \left[-\frac{1}{2}\nabla_{\mathbf{r}_i}^2 + \frac{1}{2}\sum_{j\neq i}\frac{1}{|\mathbf{r}_i - \mathbf{r}_j|} - \sum_{I=1}\frac{Z_I}{|\mathbf{R}_I - \mathbf{r}_i|} \right] \Psi = E\Psi \tag{2.7}$$

the solution of this equation will be the central topic of this Chapter. The solution for the nuclear wave-function part of the system can be found using the full Hamiltonian in Eq. 2.1 on the separable wave-function expressed in Eq. 2.6. The resulting ionic Schrödinger equation is then:

$$\sum_{J=1}^{N_{nuclei}} \left[-\frac{1}{2M_J}\nabla_{\mathbf{R}_j}^2 + E(\{\mathbf{R}_I\}) + \frac{1}{2}\sum_{J,K\neq J}^{N_{nuclei}} \frac{Z_J Z_K}{|R_J - R_K|} \right] \eta = \varepsilon\eta \tag{2.8}$$

Due to the BO approximation, the nuclear dynamics can only be evaluated on the electronic potential energy surface (i.e. $E(\{\mathbf{R}_I\})$) obtained for the fixed nuclear positions (Eq. 2.7). In this approximation, the coupling of the electronic wave-functions with the nuclear one, which can be substantial, is neglected. In spite of this, a priori severe, approximation, the electronic ground state of many systems is well described using the BO approach. The approximation is however known to break down for some important cases such as high energy and excitation processes, crossing of ground and excited states, or strongly electron-phonon coupled processes as in charge-transfer (see Chapter 1) or emergence of superconductivity [4, 5, 6].

2.2. Density Functional Theory

Density Functional Theory (DFT) is a formally exact first principles theory used to describe a quantum mechanical many body system. This formalism is based on two outstanding intuitions, underpinned by mathematical proofs. First, although the wave function contains an excessive and intractably large amount of information, once the electron density, the density of states and the density pair correlation function are known almost all the observable of interest can be deduced [7]. Second, in order to reduce the amount of information involved in the many-body problem a paradigm shift is necessary: instead of using the electronic wave-function as descriptor of a system, the electronic charge density can be used as central quantity to solve the electronic time-independent Schrödinger equation. This paradigm shift permits to move from a physical quantity (the wave-function) that is a function of 3N coordinates (N is the number of atoms in the system) to another one (the electronic density) depending on only

3 coordinates. In practical calculations, where a discretised grid of M points is employed this change in the description of the system implies passing from a M^{3N} scaling to a M^3 one.

This paradigm change was first proposed by Thomas and Fermi in 1927 [8]. However limitations were present in the original model, such as the impossibility of describing the atomic shell structure and the poor representation of the electronic density near the nuclei and for valence electrons. These limitations prevented the Thomas-Fermi model from becoming commonly used [9]. Conversely, the seminal work of Hohenberg and Kohn [10] in 1964 unambiguously proved that a system ground state can be, in principle exactly, expressed as a functional of the electronic density. Kohn and Sham [11] in 1965 further developed this concept, laying the basis for the numerical development of DFT and its application to the study of real systems.

2.2.1. Hohenberg and Kohn theorems

Central to the following discussion is the electronic density, $n(\mathbf{r})$, that in a system characterised by a normalised *N*-electron wave-function (i.e. $\langle\Psi|\Psi\rangle = 1$) read as:

$$n(\mathbf{r}) = \langle\Psi|\hat{n}|\Psi\rangle = \int \prod_{i=2}^{N} d\mathbf{r}_i |\Psi(\mathbf{r},\mathbf{r}_2,\ldots,\mathbf{r}_N)|^2 \tag{2.9}$$

where:

$$\hat{n} = |\Psi\rangle\langle\Psi| \tag{2.10}$$

The electronic density at a given point gives the probability of an electron occupying an infinitesimal space centred at that point.

The first Hohenberg Kohn theorem states that:

For any system of interacting particles in an external potential $V_{ext}(\mathbf{r})$, the density is uniquely determined. In other words, the external potential is a unique functional of the density. This means there is a one-to-one mapping between the ground state electronic density of a system (n_0) and the external potential that act on it, except for an additive constant.

This theorem can be proven by contradiction. Let us assume the existence of two potentials, different from each other by more than just an additive constant, $V(\mathbf{r})$ and $V^1(\mathbf{r})$ and yielding to the same ground state electronic density $n(\mathbf{r})$. Different Hamiltonians are built from $V(\mathbf{r})$ and $V^1(\mathbf{r})$ and are named $\hat{H}$ and $\hat{H}^1$. These Hamiltonians are applied to different eigenfunctions $|\Psi_0\rangle$ and $|\Psi_0^1\rangle$, obtaining different energies E_0 and E_0^1. As starting hypothesis, it can be written:

$$E = \langle\Psi_0|\hat{H}|\Psi_0\rangle < \langle\Psi_0^1|\hat{H}|\Psi_0^1\rangle \tag{2.11}$$

Making use if the Variational principle, Eq. 2.11 can be rewritten as:

$$\langle\Psi_0^1|\hat{H}|\Psi_0^1\rangle = \langle\Psi_0^1|\hat{H}^1|\Psi_0^1\rangle + \langle\Psi_0^1|(\hat{H}-\hat{H}^1)|\Psi_0^1\rangle = E_0^1 + \int[\,V(\mathbf{r}) - V^1(\mathbf{r})]\,n(\mathbf{r})d\mathbf{r} \quad (2.12)$$

Substituting the right end side of Eq. 2.13 in Eq. 2.12, the following expression can be obtained:

$$E_0 < E_0^1 + \int[\,V(\mathbf{r}) - V^1(\mathbf{r})]\,n(\mathbf{r})d\mathbf{r} \quad (2.13)$$

The same result can be obtained for E_0^1 hypothesising $E_0^1 = \langle\Psi_0^1|\hat{H}|\Psi_0^1\rangle < \langle\Psi_0|\hat{H}|\Psi_0\rangle$:

$$E_0^1 < E_0 + \int[V^1(\mathbf{r}) - V(\mathbf{r})]\,n(\mathbf{r})d\mathbf{r} \quad (2.14)$$

Adding Eq. 2.13 and 2.14:

$$E_0 + E_0^1 < E_0^1 + E_0 \quad (2.15)$$

which is in itself a contradiction. Thus, two different potentials giving rise to the same ground state density cannot exist. From this theorem it can also be deduced that, since the Hamiltonian and total number of electrons are determined by $n(\mathbf{r})$, so it will be the many body wave-function and, consequently, all the other properties derivable from the Hamiltonian.

The second Hohenberg Kohn theorem states:

A universal functional for the energy $E[n(\mathbf{r})]$, yielding the energy of the system with charge density, $n(\mathbf{r})$, can be defined in terms of the density itself. The exact ground state for a given $V_{ext}(\mathbf{r})$ is the global minimum value of this functional.

The proof of this theorem is straightforward: it was previously shown that $n(\mathbf{r})$ determines $V_{ext}(\mathbf{r})$ and N. N and $V_{ext}(\mathbf{r})$ permit to define $\hat{H}$, therefore Ψ. It then follows that Ψ is a functional of $n(\mathbf{r})$. Thence it can be written:

$$E[n(\mathbf{r})] = \langle\Psi[n(\mathbf{r})]|\hat{H}|\Psi[n(\mathbf{r})]\rangle \quad (2.16)$$

where $E[n(\mathbf{r})]$ is called energy functional that can be expressed as:

$$E[n(\mathbf{r})] = F[n(\mathbf{r})] + \int d\mathbf{r}\; V_{ext}(\mathbf{r})n(\mathbf{r}) = \langle\Psi[n(\mathbf{r})]|\hat{F} + \hat{V}|\Psi[n(\mathbf{r})]\rangle =$$

$$\langle\Psi[n(\mathbf{r})]|\hat{H}|\Psi[n(\mathbf{r})]\rangle \quad (2.17)$$

in Eq. 2.17 the equality $\hat{H} = \hat{F} + \hat{V}$ has been used. The operator $\hat{F}$, called universal functional and valid for any number of electrons and any external potential, is defined as:

$$\hat{F} = \hat{T} + \hat{V}_{int} = \sum_{i=1}^{N} -\frac{1}{2}\nabla_{\mathbf{r}_i}^2 + \frac{1}{2}\sum_{j\neq i}^{N}\frac{1}{|\mathbf{r}_i-\mathbf{r}_j|} \quad (2.18)$$

where $\hat{\mathrm{T}}$ is the kinetic energy operator and $\hat{\mathrm{V}}_{\mathrm{int}}$ is the operator associated with total potential energy in the system.

The Variational principle asserts that:

$$\langle \Psi' | \hat{\mathrm{F}} | \Psi' \rangle + \langle \Psi' | \hat{\mathrm{V}}_{\mathrm{ext}} | \Psi' \rangle > \langle \Psi | \hat{\mathrm{F}} | \Psi \rangle + \langle \Psi | \hat{\mathrm{V}}_{\mathrm{ext}} | \Psi \rangle \tag{2.19}$$

where Ψ is the ground state function and Ψ' is another wave-function related to the electronic density $\mathrm{n}'(\mathbf{r})$.

Hence:

$$\mathrm{F}[\mathrm{n}'(\mathbf{r})] + \int \mathrm{d}\mathbf{r}\ \mathrm{V}_{\mathrm{ext}}(\mathbf{r})\mathrm{n}'(\mathbf{r}) > \mathrm{F}[\mathrm{n}(\mathbf{r})] + \int \mathrm{d}\mathbf{r}\ \mathrm{V}_{\mathrm{ext}}(\mathbf{r})\mathrm{n}(\mathbf{r}) \tag{2.20}$$

Since $\hat{\mathrm{V}}_{\mathrm{ext}}$ is the same for the two cases it can be concluded that:

$$\mathrm{E}[\mathrm{n}'(\mathbf{r})] > \mathrm{E}[\mathrm{n}(\mathbf{r})] \tag{2.21}$$

This theorem demonstrates that the process of calculating the ground state energy of an N-electron system correspond to the Variational minimisation of the energy functional $E[n(\mathbf{r})]$ with respect to the electronic density. This formulation was extended and generalised by Levy and Lieb [12, 13, 14, 15], who redefined the universal functional and extended the validity of these theorems to degenerate ground states. Another number of different formulations of DFT exist, like spin-DFT, ensemble DFT, current-DFT [15]. These are extensions of the theorems discussed previously (Eqs 2.11-2.21) and, for sake of compactness, they will not be reported here.

2.2.2. Kohn-Sham equations

The Hohenberg Kohn theorems allow, in principle, exact evaluation of the energy and ground state electronic density $[\mathrm{n}(\mathbf{r})]$ of any system. The choice of the electronic density distribution $\mathrm{n}(\mathbf{r})$ as basic physical quantity introduces however a serious drawback. To date, although its existence is mathematically proved, there is no known global functional $\hat{F}$ of $\mathrm{n}(\mathbf{r})$ to calculate the exact kinetic energy or electron-electron potential. Hence, exact solution of the DFT problem, although in principle possible, is effectively not viable. In 1965 Kohn and Sham [11] proposed a solution to this problem by suggesting the following expression for the total energy as functional of the electronic density $\mathrm{n}(\mathbf{r})$:

$$\mathrm{E}[\mathrm{n}(\mathbf{r})] = \int \mathrm{V}(\mathbf{r})\mathrm{n}(\mathbf{r})\,\mathrm{d}\mathbf{r} + \frac{\mathbf{1}}{\mathbf{2}} \int\int \frac{\mathrm{n}(\mathbf{r})\mathrm{n}(\mathbf{r}')}{|\mathbf{r}\text{-}\mathbf{r}'|}\,\mathrm{d}\mathbf{r}\,\mathrm{d}\mathbf{r}' + \mathrm{G}[\mathrm{n}(\mathbf{r})] \tag{2.22}$$

In this equation, the first term $\int \mathrm{V}(\mathbf{r})\mathrm{n}(\mathbf{r})\,\mathrm{d}\mathbf{r}$ represents the Coulomb interaction between electrons and nuclei, the second $\frac{\mathbf{1}}{\mathbf{2}} \int\int \frac{\mathrm{n}(\mathbf{r})\mathrm{n}(\mathbf{r}')}{|\mathbf{r}\text{-}\mathbf{r}'|}\,\mathrm{d}\mathbf{r}\,\mathrm{d}\mathbf{r}'$ term, also known as Hartree potential,

accounts for the repulsive interaction between the electrons, and the last term is a universal functional of the electron density $G[n(\mathbf{r})]$ (similar to $F[n(\mathbf{r})]$, whose definition is independent from $V(\mathbf{r})$. The problem inherent to Eq. 2.22 is to find an expression for $G[n(\mathbf{r})]$ that allows calculation of the ground state energy of the system. The innovative assumption of Kohn-Sham DFT lies in considering the electrons of the system as non-interacting particles. This approximation permits to calculate easily the kinetic energy ($T_s[n(\mathbf{r})]$) of the system without taking in account electron correlation. It also allows maintaining all the single electron wave-functions of the non-interacting electrons (i.e. the Kohn-Sham states) orthogonal. All the contributions left out by the non-interacting electron approximation (i.e. many body effects) are placed in the so-called exchange-correlation potential ($E_{xc}[n(\mathbf{r})]$) that is a functional of the density. The universal functional is then expressed as:

$$G[n(\mathbf{r})] = T_s[n(\mathbf{r})] + E_{xc}[n(\mathbf{r})] \tag{2.23}$$

The non-interacting system is set up to have the same density as the original system through the use of an effective potential V_{KS}. The use of the Variational principle to perform the energy functional minimisation it can be written:

$$\delta[\, E[n(\mathbf{r})] - \mu(\int d\mathbf{r}\, n(\mathbf{r}) - N)] = 0 \tag{2.24}$$

where a Lagrange multiplier μ has been introduced to maintain the total electron number N as required for a closed system. For the normal interacting many-body system, Eq. 2.24 gives the Euler-Lagrange formula in terms of the energy functional (as defined in Eq. 2.17), chemical potential (μ) and external potential V_{ext}:

$$\frac{\delta F[n(\mathbf{r})]}{\delta n(\mathbf{r})} + V_{ext}(\mathbf{r}) = \mu \tag{2.25}$$

As previously mentioned, the system of non-interacting electrons is required to have the same electronic density of the normal interacting system at its minimum. Thus, an expression equivalent to Eq. 2.25 for the Kohn-Sham case can be deducted:

$$\frac{\delta T[n(\mathbf{r})]}{\delta n(\mathbf{r})} + \int \frac{n(\mathbf{r}')}{|\mathbf{r}-\mathbf{r}'|} d\mathbf{r}' + V_{xc}[n(\mathbf{r})] + V_{ext}(\mathbf{r}) = \mu \tag{2.26}$$

Given the one-to-one mapping (first HK theorem) between density and potential, the effective Kohn-Sham potential for the system of non-interacting particles read as:

$$V_{KS}[n(\mathbf{r})] = \int \frac{n(\mathbf{r}')}{|\mathbf{r}-\mathbf{r}'|} d\mathbf{r}' + V_{xc}[n(\mathbf{r})] + V_{ext}(\mathbf{r}) \tag{2.27}$$

with $V_{xc}[n(\mathbf{r})]$ defined as:

$$V_{xc}[n(\mathbf{r})] = \frac{\delta E_{xc}[n(\mathbf{r})]}{\delta n(\mathbf{r})} \tag{2.28}$$

Substituting Eq. 2.28 in 2.27 one obtains:

$$\frac{\delta T[n(\mathbf{r})]}{\delta n(\mathbf{r})} + V_{KS}[n(\mathbf{r})] = \mu \tag{2.29}$$

Eq. 2.29 must in principle yield to the same ground state density of the original interacting system (Eq. 2.26), provided E_{xc} (then V_{xc}) is exactly known, which is never the case in real calculations (see above). The solution to Eq. 2.29 can be found using a set of *N* single particle Schrödinger equations:

$$\hat{H}_{KS}\Psi_i = \left[-\frac{1}{2}\nabla^2 + \hat{V}_{KS}(\mathbf{r})\right]\Psi_i = \epsilon_i\Psi_i \tag{2.30}$$

This set of equations is called the Kohn-Sham equations and their eigenfunctions are called Kohn-Sham orbitals (or states). Provided the exact E_{xc} is available, The Kohn-Sham orbitals reproduce the ground state electronic density of the real many body system through the equivalence:

$$n(\mathbf{r}) = \sum_{i=1}^{N} f_i|\Psi_i(\mathbf{r})|^2 \tag{2.31}$$

where f_i is the occupation number of each Kohn-Sham orbital. This formalism is in principle exact, provided the exact expression for E_{xc} is known (which to date is not the case).

The total energy of the system can be calculated through a self-consistent solution to the Kohn-Sham equations (Eq. 2.30). Once a guess density is given or approximately constructed as input. Eq. 2.30 is solved to obtain the single particle Kohn-Sham orbitals. These orbitals are then used to build a new electronic density using Eq. 2.31. The process is repeated until the input and output densities are the same, within some pre-established numerical threshold, allowing numerical self-consistency between potential and density.

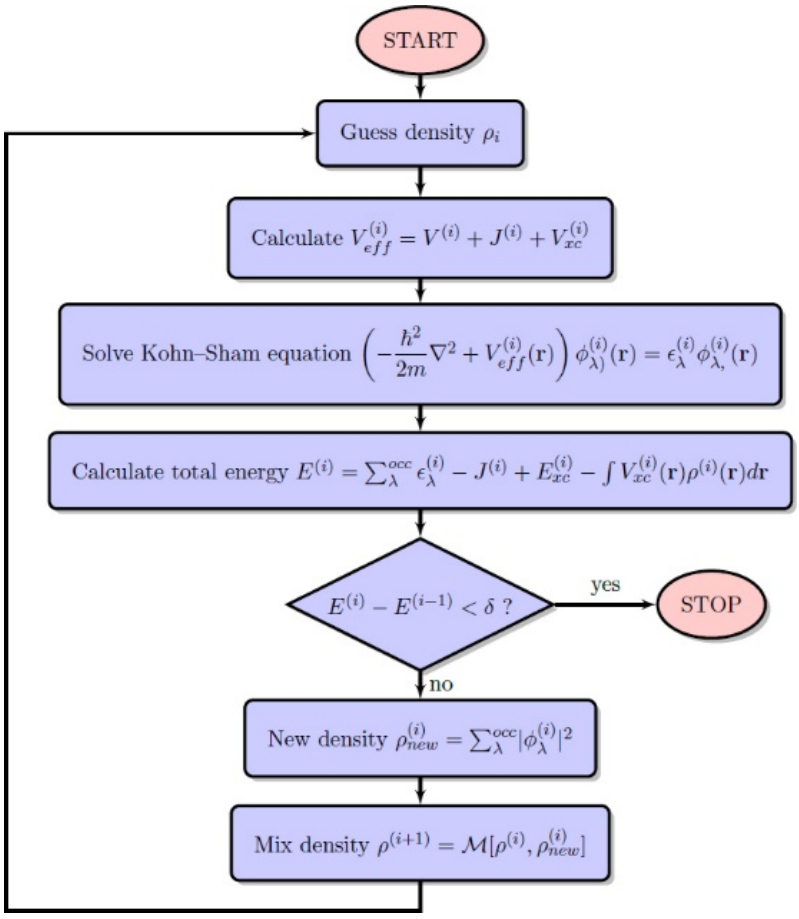

Figure 2.1. Flow chart summarising the iterative Self-Consistent Field (SCF) solution of the Kohn-Sham DFT problem (Eq. 2.30).

2.2.3. Exchange and Correlation

As previously mentioned, DFT is an exact theory provided $\mathrm{E_{xc}}[\mathrm{n}(\mathbf{r})]$ is known. In practice, however, since $\mathrm{E_{xc}}[\mathrm{n}(\mathbf{r})]$ is not known (apart from the homogenous electron gas), the explicit form of the exchange-correlation needs to be approximated.

The exchange correlation comprises of two factors: the difference in kinetic energies between the interacting and non-interacting systems, which is equal to:

$$\mathrm{T_c}[\mathrm{n}(\mathbf{r})] = \mathrm{T}[\mathrm{n}(\mathbf{r})] - \mathrm{T_s}[\mathrm{n}(\mathbf{r})] \tag{2.32}$$

and the difference between the Coulomb electrostatic interactions in the two system written as:

$$\mathrm{U_c}[\mathrm{n}(\mathbf{r})] = \mathrm{U}[\mathrm{n}(\mathbf{r})] - \mathrm{U_H}[\mathrm{n}(\mathbf{r})] \tag{2.33}$$

where $\mathrm{U_H}[\mathrm{n}(\mathbf{r})]$is the Hartree potential.

The exchange-correlation energy can also be expressed as the electrostatic interaction between the inhomogeneous electron density distribution $n(\mathbf{r})$ and a charge depletion hole density generated by exchange correlation effects produced by $n(\mathbf{r})$ itself. $E_{xc}[n(\mathbf{r})]$ then reads:

$$E_{xc}[n(\mathbf{r})] = \frac{1}{2}\int\int d\mathbf{r}\, d\mathbf{r}' \frac{n(\mathbf{r})n_{xc}(\mathbf{r},\mathbf{r}')}{|\mathbf{r}-\mathbf{r}'|} \tag{2.34}$$

$n_{xc}(\mathbf{r},\mathbf{r}')$ can be expressed as the density pair correlation function [17]. It has been shown [18] that $E_{xc}[n(\mathbf{r})]$ depends only on the spherical average of $n_{xc}(\mathbf{r},\mathbf{r}')$ and satisfies the sum rule:

$$\int d\mathbf{r}'\, n_{xc}(\mathbf{r},\mathbf{r}') = \int d\mathbf{r}'\, n_x(\mathbf{r},\mathbf{r}') = -1 \tag{2.35}$$

with $n_x(\mathbf{r},\mathbf{r}')$ being the charge depletion generated by exchange interaction only.

One of the earliest approximations used for the exchange-correlation energy is the local density approximation (LDA) [19]. This approximation is based on the assumption that the electronic density of the system varies slowly so that the system is locally homogeneous despite its overall behaviour (that can be inhomogeneous). These hypotheses are at the heart of the most popular LDA parameterisation of E_{xc}, obtained from fitting of Monte Carlo simulation results [18] on the basis of the analytical formula proposed by Mann and Brueckner for the high density limit [20]:

$$E_{xc}^{LDA}[n(\mathbf{r})] = \int \epsilon_{xc}^{LDA}\big(n(\mathbf{r})\big)n(\mathbf{r})\, d\mathbf{r} \implies V_{xc}^{LDA}(\mathbf{r}) = \frac{\delta E_{xc}^{LDA}[n(\mathbf{r})]}{\delta n(\mathbf{r})} =$$

$$\epsilon_{xc}^{LDA}\big(n(\mathbf{r})\big) + n(\mathbf{r})\frac{d\epsilon_{xc}^{LDA}(n)}{dn}\Big|_{n=n(\mathbf{r})} \tag{2.36}$$

In spite of its simplicity, the LDA approximation is found to reproduce well the physical properties of many systems, some with very inhomogeneous charge densities. However, it tends to over-bind the systems simulated, underestimate band gaps, and, given its strictly local construction, long-range dispersion terms. These deficiencies are due to spurious self-interaction errors [19] i.e. the conditions $E_c[n(\mathbf{r})] = 0$ and $E_x[n(\mathbf{r})] = U_H[n(\mathbf{r})]$ are not respected by the LDA parameterisation for one-electron systems. Conversely, the successes of this approximation are mainly due to the fact the LDA expression of the exchange-correlation obeys the sum rule for the exchange-correlation hole (Eq. 2.35).

The Generalised Gradient Approximation (GGA) [21] is another extremely popular choice as exchange-correlation approximation. Its popularity is due to the fact that is a semi-local extension of the LDA, which limits the associated computational overheads. In the GGA

approximation to E_{xc}, the gradient of the density at a given point in space is taken into account together with the density itself.

$$E_{xc}^{GGA}[n(\mathbf{r})] = \int d\mathbf{r}\ F_{xc}^{GGA}(n(\mathbf{r}), |\nabla n(\mathbf{r})|, \nabla^2 n(\mathbf{r}), \dots) \quad (2.37)$$

Depending on the form of the function F_{xc}^{GGA}, different approximations can be parameterized within the Generalised Gradient scheme. A very widely used GGA functional is the Perdew, Burke, and Ernzerhof (PBE) one [21], constructed using analytical conditions known for the exact functional. The GGA approximation can give better level of accuracy especially for molecular systems. However, many deficiencies are still present, especially in terms of underestimated band gaps and long range dispersion interactions [21].

Many other approximations to the exchange-correlation functional, of different complexity and computational cost, have been developed over the years. Some of the most popular choices are: hybrid functionals [22], which mix exactly calculated Hartree-Fock exchange with local and semi-local approximations to the system exchange; self-interaction corrected functionals [18], and subspace-corrected (+U) methods [23]. Since the functional mostly used in this thesis is the PBE, for the sake of brevity, the theoretical and computational details of these functionals will not be discussed here. The interested reader is referred to Refs. [24, 25] for a recent overview of the choice of functionals currently available.

2.2.4. Bloch's Theorem and Periodic Boundary Conditions

Currently, aperiodic DFT calculations on extremely large (>500 atoms) systems are prohibitive if not computationally impossible even when adopting computationally convenient approximations to the exchange-correlation functional. The application of periodic boundary conditions (PBC) permits to describe extended system on the premises that the atoms in the system are arranged in a periodic lattice. The benefits of the use of PBC are clear: extended systems can be reduced to much smaller ones composed by a cell containing only few atoms.

The mathematical justification to reduce the solution of an infinite problem into solving a finite number of Kohn Sham equations is Bloch's Theorem.

Let us consider a perfect crystal with an infinitely repeated periodic arrangement of the nuclei with Bravais lattice points:

$$\mathbf{R} = n_1\mathbf{a}_1 + n_2\mathbf{a}_2 + n_3\mathbf{a}_3 \quad (2.38)$$

where the position of each point of the Bravais lattice is defined by the vector $\mathbf{R}$, with $\{\mathbf{a}_i\}$ being the primitive lattice vectors. Being the system periodic, the potential at each point of the lattice can be expressed as:

$$V(\mathbf{r}+\mathbf{R}) = V(\mathbf{r}) \tag{2.39}$$

Accordingly, the Schrödinger equation for this system reads:

$$\hat{H}|\Psi\rangle = \left(-\frac{1}{2}\nabla^2 + V(\mathbf{r})\right)|\Psi\rangle = \varepsilon|\Psi\rangle \tag{2.40}$$

Given the periodicity of the system potential, the Hamiltonian will have the same periodicity. A translation operator, $\hat{T}_{\mathbf{R}}$, can then be defined as:

$$\hat{T}_{\mathbf{R}} f(\mathbf{r}) = f(\mathbf{r}+\mathbf{R}) \tag{2.41}$$

Such translation operator follows the relation:

$$\hat{T}_{\mathbf{R}}\,\hat{T}_{\mathbf{R'}} = \hat{T}_{\mathbf{R'}}\,\hat{T}_{\mathbf{R}} = \hat{T}_{\mathbf{R}+\mathbf{R'}} \tag{2.42}$$

since two successive translations can always be expressed as another translation, and the order of the translations does not matter. Because the $\hat{T}_{\mathbf{R}}$ and $\hat{H}$ operators have the same periodicity, they commute and share the same set of eigenfunctions:

$$\hat{H}|\Psi\rangle = \varepsilon|\Psi\rangle \tag{2.43}$$

and:

$$\hat{T}_{\mathbf{R}}|\Psi\rangle = c(\mathbf{R})|\Psi\rangle \tag{2.44}$$

From Eq. 2.42, it follows that the following relation for the translation eigenvalue holds:

$$c(\mathbf{R}+\mathbf{R}') = c(\mathbf{R})c(\mathbf{R}') \tag{2.45}$$

Let $\mathbf{a}_i$ be the three primitive vectors of the Bravais lattice; $c(\mathbf{a}_i)$ can always be written as

$$c(\mathbf{a}_i) = e^{2\pi i x_i} \tag{2.46}$$

where x_i is the direction of the translation. Considering the definition of the Bravais lattice vector in Eq. 2.38 then $c(\mathbf{R})$ can be expressed as:

$$c(\mathbf{R}) = c(\mathbf{a}_1)^{n_1} c(\mathbf{a}_2)^{n_2} c(\mathbf{a}_3)^{n_3} \tag{2.47}$$

Eq.2.47 is precisely equivalent to:

$$c(\mathbf{R}) = e^{i\mathbf{k}\mathbf{R}},\ \ \mathbf{k} = \sum_{j=1}^{3} x_j \mathbf{b}_j\,,\ \mathbf{a}_i\mathbf{b}_j = 2\pi\delta_{ij} \tag{2.48}$$

where x_i are usually complex multipliers for the reciprocal lattice vectors $\{\mathbf{b}_j\}$:

$$\mathbf{k} = x_1\mathbf{b}_1 + x_2\mathbf{b}_2 + x_3\mathbf{b}_3 \tag{2.49}$$

Considering the definition of the translation operator (Eq. 2.41), it can be written:

$$\hat{T}_{\mathbf{R}}\Psi(\mathbf{r}) = \Psi(\mathbf{r}+\mathbf{R}) = c(\mathbf{R})\Psi = e^{i\mathbf{kR}}\,\Psi(\mathbf{r}) \tag{2.50}$$

The wave-function can consequently be labelled by its wave-vector **k** and its band index n, which refer to each independent eigenstate that can occur for each value of the reciprocal vector:

$$\Psi_{n\mathbf{k}}(\mathbf{r}+\mathbf{R}) = e^{i\mathbf{kR}}\,\Psi_{n\mathbf{k}}(\mathbf{r}) \tag{2.51}$$

Eq. 2.51 is Bloch's theorem that can be equivalently expressed in term of a periodic function with the same periodicity of the lattice:

$$u_{n\mathbf{k}}(\mathbf{r}) = e^{-i\mathbf{kR}}\,\Psi_{n\mathbf{k}}(\mathbf{r}) \Longrightarrow \Psi_{n\mathbf{k}}(\mathbf{r}) = e^{i\mathbf{kR}}u_{n\mathbf{k}}(\mathbf{r}) \tag{2.52}$$

Bloch's theorem demonstrates that any wave-vectors in the system considered can be back-traced to a wave-vector inside the first Brillouin zone (the smallest possible primitive unit-cell in the reciprocal space defined by the closest points to the origin of the reciprocal lattice). Let define the wave-vector **k'**:

$$\mathbf{k'}=\mathbf{k}+\mathbf{G} \tag{2.53}$$

with **G** being any linear combination of the reciprocal vectors $\{\mathbf{b}_j\}$ and with **k** being any wave-vector lying in the first Brillouin zone. Substituting Eq. 2.53 into Eq. 2.52 one obtains:

$$\Psi_{n\mathbf{k'}}(\mathbf{r}) = e^{i\mathbf{k'r}}u_{n\mathbf{k'}}(\mathbf{r}) = e^{i\mathbf{kr}}\left[e^{i\mathbf{Gr}}\,u_{n\mathbf{k'}}(\mathbf{r})\right] = e^{i\mathbf{kr}}\,u_{n'\mathbf{k}}(\mathbf{r}) = \Psi_{n'\mathbf{k}}(\mathbf{r}) \tag{2.54}$$

Eq. 2.54 shows that the electronic wave-function of a periodic system is completely defined on the basis of the wave-functions at different **k**-points within the first Brillouin zone. The number of **k**-points in the Brillouin zone however diverges if the system is infinite (or the sampling of the unit cell is made with infinitesimal steps) so that once again continuous integration over the cell used as sample should be used. However, it is demonstrated that eigenvalues and wave-functions vary smoothly with respect to **k.** Hence, only a small number of well selected wave-vectors can be used to sample the Brillouin zone [26].

Bloch's theorem obviously does not apply if the translational symmetry breaks down (See Fig. 2.2) such as for molecules, defective crystal or mixed hetero-structures. This problem is usually circumvented by using a supercell approach where a system representative of the one of interest is placed at the centre of the simulation unit cell and the rest of it is padded with enough vacuum, or defect-free regions, so that the repetitive images are isolated. In practice the size of the supercell is increased (computational resources permitting) until the total energy of the system is converged with respect to the system dimensions.

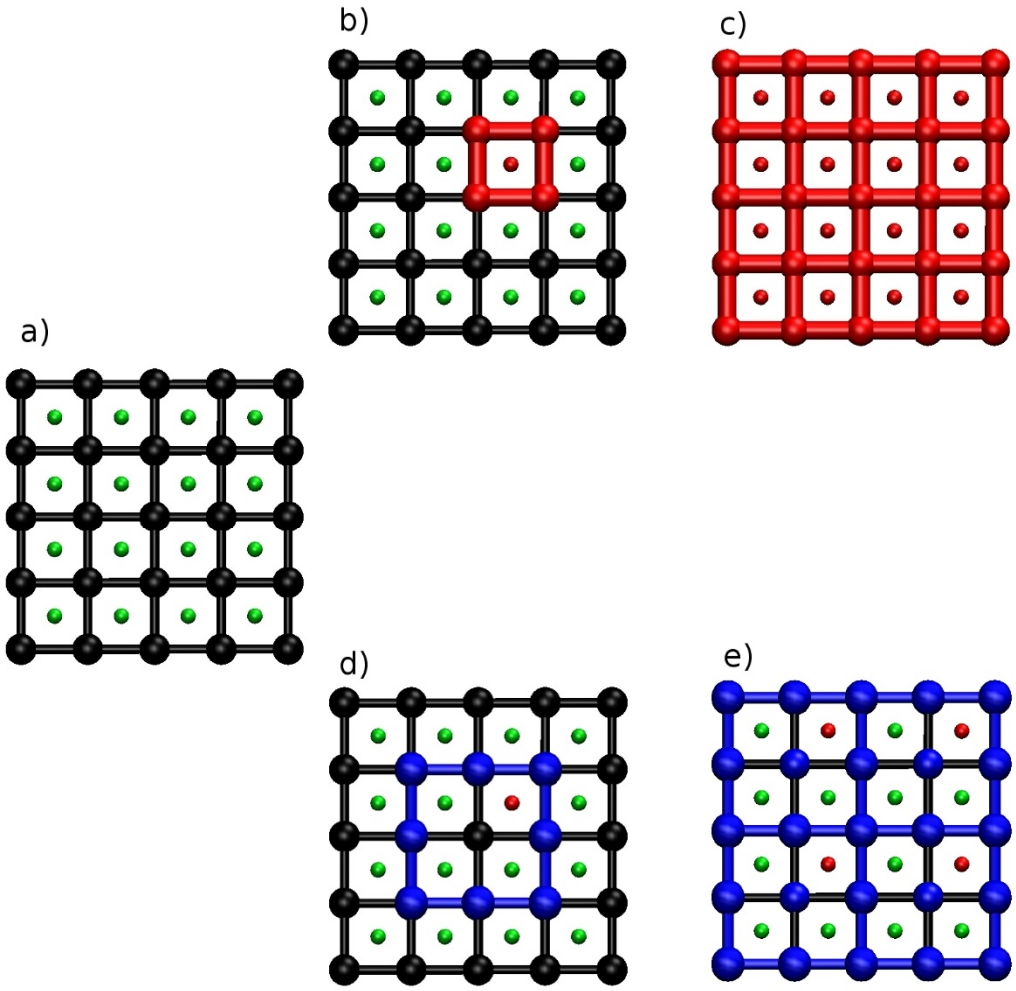

Figure 2.2. Illustration of translational symmetry loss in PBC. If the perfectly periodic system (a) loses its symmetry (red point in panels b and d), an alternative supercell needs to be defined. The choice of the size of the supercell encompassing the symmetry rupture affects the stoichiometry and nature of the system modelled (panels c and e).

The first Brillouin zone volume is calculates as:

$$\Omega_{1\text{stBZ}} = \frac{(2\pi)^3}{\Omega_{\text{cell}}} \tag{2.55}$$

where Ω_{cell} is the volume of the simulation cell. For typical LS-DFT applications on very extended systems, Ω_{cell} is usually large enough that $\Omega_{1\text{stBZ}}$ is very small and can be suitably sampled by its central Γ-point (k=0).

2.2.5. Plane-waves basis-set

To solve the Kohn-Sham equations a basis-set is necessary to compute the Hamiltonian matrix elements and express the corresponding eigenfuntions. In DFT probably the most used basis sets for practical calculations is the plane wave basis set [27]. This choice for a basis set is natural: it grants efficient evaluation of space dependent operator (potential, momentum etc.) and allows for extremely efficient Fourier transformations using FFT techniques.

The choice of a plane wave basis set looks even more suitable for the DFT when Eq. 2.54 is taken in consideration:

$$\Psi_{\mathbf{nk}}(\mathbf{r}) = e^{\mathbf{ikR}} u_{\mathbf{nk}}(\mathbf{r}) = e^{\mathbf{ikR}} \sum_{\mathbf{G}} c_{\mathbf{n,k+G}} e^{\mathbf{iGr}} \tag{2.56}$$

Here the $u_{\mathbf{nk}}(\mathbf{r})$ periodic function has been Fourier-expanded so that $\Psi_{\mathbf{nk}}(\mathbf{r})$ results in a sum of plane-waves, with expansion coefficients $c_{\mathbf{n,k+G}}$. In principle, an infinite number of plane waves is necessary to describe the wave-functions at each **k**-point. In practice, however, to make the calculation feasible, the Fourier expansion has to be truncated. Normal practice is to use a kinetic cut-off energy (E_{cut}) as parameter to truncate the sum:

$$E_{cut} \leq \frac{|\mathbf{k+G}|^2}{2} \tag{2.57}$$

The energy of the wave-functions calculated with a plane-waves basis set converges variationally with respect to the cut-off energy [27]; this represents another important advantage of using plane-waves as basis set. In spite of the many positive aspects, a plane-waves basis is not free from drawbacks. The most prominent ones are i) since plane-waves are delocalized over the whole simulation cell, increment of the size of the simulation cell leads to increase of the computational (and memory) cost even if the space is occupied by vacuum; and ii) the analytical form of the plane-waves make it difficult to reproduce the fast oscillations of the wave-functions near the atomic cores unless very high energy cutoffs are used.

2.2.6. The Pseudopotential approximation

The highly oscillatory character of the electronic wave-function near the core of the atoms makes their representation with plane-waves (or psinc functions, see below) a major numerical issue for DFT. An accurate description of the electronic wave-function close to the atom core requires an incredibly large amount of functions, or equivalently, a very large plane-wave cutoff in Eq. 2.57. A computational strategy to circumvent this issue is the so-called pseudopotential approximation. Instead of trying to solve the “real” wave-function at the atom-core, solution of the Schrödinger equation for the core-electrons of the isolated atom is used to obtain an effective core-potential (and core-electron pseudo-wave-function). Core electronic states are known to be slightly perturbed by the formation of chemical bonds

between valence electrons. Accordingly, the pseudopotential approximation is used to replace their explicit description by the mean of a fictitious fixed potential acting on the valence electrons. Elimination of the core states/electrons from the DFT problem allows use of greatly reduced basis sets.

In order to develop a pseudopotential, a set of smoother pseudo-valence orbitals can be built subtracting a linear combination of core orbitals to the valence wave-functions so that their core region is smoother than the real valence states:

$$|\Psi_{val}\rangle = |\Psi_{PS}\rangle + \sum_{v,c} C_{v,c} |\Psi_c\rangle \tag{2.58}$$

The expansion coefficients in Eq. 2.58 are determined by imposing orthogonality between the valence and core states:

$$\langle\Psi_{PS}|\Psi_C\rangle = C_{v,c} \tag{2.59}$$

The basic requirement for the pseudo-valence states is that it needs to reproduce the eigenvalues ϵ_{val} of the original valence states and the energy levels of the core state in their frozen core approximation. When the Hamiltonian is applied to $|\Psi_{PS}\rangle$:

$$\hat{H}|\Psi_{PS}\rangle = \epsilon_{val}|\Psi_{val}\rangle + \sum_{v,c} C_{v,c}\, \epsilon_c|\Psi_c\rangle \tag{2.60}$$

using Eq. 2.60, Eq. 2.58 can be re-written as:

$$\hat{H}|\Psi_{PS}\rangle = \epsilon_{val}|\Psi_{PS}\rangle + \sum_{v,c} C_{v,c}\, \{\epsilon_v - \epsilon_c\}|\Psi_c\rangle \tag{2.61}$$

Eq. 2.61 can then be expressed as the Schrödinger equation for pseudo-valence functions where:

$$\hat{H} + V_{PS}|\Psi_{PS}\rangle = \epsilon_v|\Psi_{PS}\rangle \tag{2.62}$$

with:

$$\hat{V}_{PS} = \sum_c \{\epsilon_v - \epsilon_c\}\, |\Psi_c\rangle\langle\Psi_c| \tag{2.63}$$

Eq. 2.63 represents the Kleinmann expression [28] for the construction of pseudopotentials. In this approximation, a smooth pseudopotential is obtained applying projectors to the core states weighted by the energy difference between valence and core eigenstates. Using this construction scheme, the core states vanish outside the core region and $|\Psi_{PS}\rangle$ becomes equal to $|\Psi_{val}\rangle$. Conversely, near the nucleus, the repulsive V_{PS} screens considerably the attractive potential from the nucleus. Reduction of the attractive potential makes the pseudo-wave-function much smoother, allowing for representation of the pseudo-wave-function with a small number of plane-waves. Together with the smoothness of the pseudo-function, two other properties are highly desirable when building a pseudopotential: accuracy and transferability.

These properties are usually quantified by the capability of a pseudopotential to reproduce all electron calculations results for a wide range of systems and valence electronic configurations. One of the most used approaches to obtain accurate highly transferable pseudopotentials is the generation of so-called norm-conserving pseudopotentials (NCP).

An NCP has to match the exact wave-function beyond a certain core radius ($\mathbf{r}_c$):

$$\Psi_{PS}(r) = \Psi_{PS} \quad \forall\, \mathbf{r} \geq \mathbf{r}_c \tag{2.64}$$

While any type of function can be adopted to make the pseudopotential as smooth as possible inside r_c, the charge integral over the core region must be equal to the one of the true valence wave-function:

$$\int_0^{\mathbf{r}_c} \mathbf{r}^2\, \Psi_{PS}^*(\mathbf{r})\Psi_{PS}(\mathbf{r})d\mathbf{r} = \int_0^{\mathbf{r}_c} \mathbf{r}^2\, \Psi_{val}^*(\mathbf{r})\Psi_{val}(\mathbf{r})d\mathbf{r} \tag{2.65}$$

a NCP has also (obviously) to reproduce the Ψ_{val} eigenvalues. To properly reproduce the scattering behaviour of the all-electron wave-function a NCP needs also to have the same logarithmic derivative of Ψ_{val} at $\mathbf{r}_c$:

$$\left.\frac{\partial \ln(\Psi_{val}(\mathbf{r}))}{\partial \mathbf{r}}\right|_{\mathbf{r}=\mathbf{r}_c} = \frac{1}{\Psi_{val}(\mathbf{r}_c)}\frac{\partial \Psi_{val}}{\partial \mathbf{r}}(\mathbf{r}_c) = \frac{1}{\Psi_{PS}(\mathbf{r}_c)}\frac{\partial \Psi_{PS}}{\partial \mathbf{r}}(\mathbf{r}_c) \tag{2.66}$$

The range for which the equality of the logarithmic derivatives holds is a measure of the transferability of a NCP: the longer the energy span, the better the pseudopotential transferability. A major step forward in the construction of NCPs was the strategy introduced by Bachelet, Haman and Schlüter [29]. In this scheme, the first step consists in solving an all-electron DFT calculation for a certain atomic reference configuration that is spherically symmetric. Subsequently a core radius $\mathbf{r}_c$ is assigned for each momentum channel (l) of the real wave-function Ψ_{val}. A trial potential is then chosen to continuously remove the singularity represented by the nucleus within $\mathbf{r}_c$. The pseudo-potential has also to yield the lowest eigenvalue of the corresponding valence state. In Ref. 29, the authors proposed the following function to obtain the trial potential:

$$V_t = \frac{Z_{ion}}{r}\left(1 - f(\mathbf{r}/\mathbf{r}_{c,l})\right) + V_{0,l} f(\mathbf{r}/\mathbf{r}_{c,l}) \tag{2.67}$$

where Z_{ion} is the ionic charge of the atom considered, f is a trial cutting function of choice, $\mathbf{r}_{c,l}$ are the different core radius for each angular momentum channel and $V_{0,l}$ is the depth of the trial potential. Norm-conservation is imposed by adding a correction function that rapidly decays after the $\mathbf{r}_{c,l}$ to the trail potential. The screened pseudopotential can then be found knowing V_t and solving the radial Schrödinger equation:

$$\left(\frac{\partial^2}{\partial r^2} + \frac{l(l+1)}{2r^2} + V_l(\mathbf{r})\right)\Psi_{val,l} = \epsilon_l \Psi_{val,l} \tag{2.68}$$

Hence:

$$\hat{V}_l(\mathbf{r}) = \epsilon_l - \frac{l(l+1)}{2r^2} + \frac{1}{2\Psi_{val,l}}\frac{\partial^2 \Psi_{val,l}}{\partial r^2} \tag{2.69}$$

The potential obtained by this procedure needs then to be unscreened by subtracting the XC and Hartee terms so that the V_{PS} read:

$$\hat{V}_{PS,l}(\mathbf{r}) = V_l(\mathbf{r}) - \int \frac{\rho_{val}(r')dr'}{|r-r'|} - \hat{V}_{xc}(\rho_{val}(\mathbf{r})) \tag{2.70}$$

The Bachelet, Haman, Schlüter scheme leads to angular momentum dependent pseudo-potentials. Hence, the use of angular momentum projector operators is necessary to build such NCP:

$$V_{PP} = \sum_l \hat{V}_{PS,l}(\mathbf{r}) P_{l\phi}(\mathbf{r}) \; ; \; P_{l\phi}(\mathbf{r}) = \sum_{m=-l}^{l} |Y_{l,m}\rangle\langle Y_{l,m}|\phi\rangle \tag{2.71}$$

where $Y_{l,m}$ are spherical harmonics.

Two further points need special care when constructing an accurate NCP: the pseudo-function dependence from the angular momentum just cited, and the pseudopotential applicability to spin polarised cases.

It has been shown above that the NCP formulation explicitly imposes some dependence on the angular momentum number. The pseudopotential can be then expressed as the sum of a local part independent of the channel l, and its non-local components in the different angular momentum channels following application of projector operators:

$$\hat{V}_{PS}(\mathbf{r}) = \hat{V}_{loc} + \sum_l \sum_{m=-l}^{l} |lm\rangle \hat{V}_l^{non-local} \langle lm| \tag{2.72}$$

Where $|lm\rangle$ represent the spherical harmonic Y_{lm}. This formulation of $V_{PS}(\mathbf{r})$ is still computationally impractical since it depends quadratically on the number of basis function used. A solution to this problem was offered by Kleynman and Bylander that proposed a factorisation for the NCP [30].

$$\hat{V}_{KB} = \hat{V}_{loc} + \sum_{l,m} \frac{\left|\hat{V}_l^{non-local}\Psi_{lm}\right\rangle\left\langle\Psi_{lm}\hat{V}_l^{non-local}\right|}{\left\langle\Psi_{lm}\left|\hat{V}_l^{non-local}\right|\Psi_{lm}\right\rangle} \tag{2.73}$$

In this equation, Ψ_{lm} is an eigenstate of the atomic pseudo-Hamiltonian (equation 2.61). The operator $\hat{V}_l^{non-local}$ is the same as in Eqs. 2.72 and 2.73. However, in 2.73 $\hat{V}_l^{non-local}$ is applied only once, which makes this NCP formulation scale linearly with the number of atoms. Eq. 2.73 is justified since is the first-order approximation to a complete series, whose limit yields the same results of Eq. 2.72 [31].

2.3. Linear Scaling Density Functional Theory and its implementation in ONETEP

2.3.1. Basic concepts in Linear Scaling DFT

Through the years, the increase in popularity of DFT has been driven by the increment in the numerical efficiency of its implementation and the extension of the computational power accessible for academic research. What started like a scheme used on systems of few atoms developed into sophisticated method capable of handling structures made up of thousands of atoms. As the size of the structures simulated has grown, so it has the complexity of the phenomena that can be modelled. This trend, together with the shift of interest by the scientific community toward fields of increasing complexity, such as nano-materials and biological systems, constantly pushes DFT applications to limit of their computational viability.

It is well known that the computational cost of a standard plane-wave DFT calculation scales as N^3, where N is the number of atoms. Although the computational load in standard plane-wave DFT calculations is dominated by [ln(N) scaling] Fast Fourier Transform (FFT) of the plane-waves to compute the Hamiltonian (see Section 2.2), the asymptotic scaling limit of DFT, and the current impossibility of treating systems over a few hundred atoms, is due to the (cubic-scaling) imposition of orthogonality between different Khon-Sham states. This seriously hinders the simulation of complex and large systems (over a few hundred atoms), making optimization of their geometry, and simulation of their electronic structure impractical or simply impossible.

Another extremely important factor to be considered when discussing the computational efficiency of DFT calculations is the development of modern High Performance Computing. The growth of accessible computational power is nowadays characterised by an increment in the number of processors available and the consequent possibility of differently efficient parallelisation of the algorithm. Therefore, to maximise the efficiency of the available computational power, the algorithm used to solve the DFT problem should offer the possibility of an efficient parallelisation. Unfortunately, the heavy use of FFT in standard plane-wave DFT, which requires a so called *all to all* communication of information across the processors used in the simulation, makes efficient parallelisation of the method far from immediate.

It is now almost 25 years since the computational scientific community started pouring effort in the research of more efficient, i.e. better parallelizable and scaling, approaches to DFT calculations. Particular effort has been put in the development of linear-scaling algorithms [O(N)]. The whole approach to linear-scaling calculation is based on the principle of near-sightedness of quantum mechanics [33, 34]. This principles postulates that, in a quantum

mechanical systems formed by a large number of interacting particles, the potential experienced by each particle is dominated by local interactions, with the extent of local depending on the system of interest. On this basis, fully delocalised construction of the DFT Hamiltonian by using plane-waves, and the ensuing $O(N^3)$ scaling is, effectively, redundant.

The "locality" of the interactions has been estimated for insulating, semiconducting and metallic systems. The expression of this relation is based on the density matrix formulation of DFT that will be treated in the next Section. It is known that for systems with an electronic band gap (insulators and semiconductors) the elements of the electronic density matrix $[\rho(\mathbf{r},\mathbf{r}')]$ decay exponentially with respect to the distance:

$$\rho(\mathbf{r},\mathbf{r}') \sim e^{-\gamma|\mathbf{r}-\mathbf{r}'|} \; ; \; \gamma \propto \sqrt{E_{bg}} \tag{2.74}$$

where γ is positive and E_{bg} is the band gap of the material considered. Eq. 2.74 indicates that the contributions to the electronic density from different regions of the system decay exponentially with the distance between them. This relation holds for metallic systems too. However, in metallic systems the decay of the $\rho(\mathbf{r},\mathbf{r}')$ elements is not exponential but it follows a power law.

Extensive work in the field has led to the development of different numerical approaches, of variable computational complexity and accuracy, to the linear-scaling implementation of DFT. Due to the extent of the subject, the interested reader is referred to Refs. [35, 36] for recent and extensive reviews of the field. In the remaining of this Chapter, the focus will be on the implementation of linear-scaling DFT in the ONETEP program.

2.3.2. Density matrix formulation of DFT and its implementation in ONETEP

Many LS-DFT codes use the density matrix (DM) as central variable. This is a natural choice since the DM provides a complete description of the fictitious Kohn-Sham electronic density and allows use of the nearsightedness property explicitly. The DM concept can be deduced in the following way. Let $\langle\Psi|O|\Psi\rangle$ be the expectation value of an operator O on the basis of a normalised state $|\Psi\rangle$. Then, when a complete set of states expressed in a different basis is considered:

$$\langle\Psi|O|\Psi\rangle = \sum_{i,j}\langle\Psi|i\rangle\langle i|O|j\rangle\langle j|\Psi\rangle \Longrightarrow \sum_{i,j}\langle j|\Psi\rangle\langle\Psi|i\rangle\langle i|O|j\rangle \Longrightarrow$$

$$\sum_{i,j}\langle j|\rho|i\rangle\ \langle i|O|j\rangle\ \Longrightarrow \mathrm{Tr}[\rho O] \tag{2.75}$$

Where j and i run over all the possible combination of states belonging to the system considered, and $\hat{\rho}$ is the density operator:

$$\hat{\rho} = |\Psi\rangle\langle\Psi| \tag{2.76}$$

The $\hat{\rho}$ expression in Eq. 2.76 is valid only for system with pure states. If the eigenstates of the systems are instead formed by a superposition of different states, the density operator will instead read:

$$\hat{\rho} = \sum_n p_n|\Psi_n\rangle\langle\Psi_n| \tag{2.77}$$

where p_n is the coefficient of the weight of the states used as basis for the expansion. Then the expression for the DM for mixed states is:

$$\rho_{ij} = \sum_n p_n\langle i|\Psi_n\rangle\langle\Psi_n|j\rangle = \langle i|\hat{\rho}|j\rangle \tag{2.78}$$

The DM can then be rewritten in the position representation as:

$$\rho(\mathbf{r},\mathbf{r}') = \sum_n f_n\Psi_n(\mathbf{r})\Psi_n^*(\mathbf{r}') \tag{2.79}$$

where f_n are the occupancies of the different states.

In order to find the ground state with a DM method during a DFT calculation, three constrains must be respected. First, the DM must be normalised in order to obtain the total number of electron of the system described:

$$N = \mathrm{Tr}(\rho) \tag{2.80}$$

Second, the DM must commute with the Hamiltonian:

$$[\rho, H] = 0 \tag{2.81}$$

Third, the DM must be idempotent:

$$\rho^2 = \rho \Longrightarrow \rho(\mathbf{r}, \mathbf{r}') = \int d\mathbf{r}''\rho(\mathbf{r}, \mathbf{r}'')\rho(\mathbf{r}'', \mathbf{r}') \quad (2.82)$$

Idempotency of the DM is equivalent to orthogonality of the Kohn-Sham states in standard DFT, which is needed for a pure, fermionic, spin-collinear state, and to ensure that $f_n \in \{0,1\}$ in compliance with Pauli Exclusion Principle [37].

Imposition of DM-idempotency and particle number conservation while minimising the energy of the system are the main challenge in a LS-DFT code. In the remainder of this Section, the implementation of the DM minimisation method used in ONETEP will be summarised. The interest reader is referred to Refs. [38, 39] for a more extended discussion.

The Kohn-Sham problem can be reformulated on the basis of the DM, in turn defined as the sum of the contributions from the occupied single-particle KS states (Eq. 2.56):

$$\rho(\mathbf{r}, \mathbf{r}') = \sum_n f_n \frac{V}{(2\pi)^3} \int_{1st\,BZ} \Psi_{n\mathbf{k}}(\mathbf{r})\Psi^*_{n\mathbf{k}}(\mathbf{r}')d\mathbf{k} \quad (2.83)$$

Within ONETEP, the single-particle DM is recast in a separable form [39] using atom-centred functions (Non-Orthogonal Generalized Wannier Functions, NWGFs [40]), φ_α, as the basis set:

$$\rho(\mathbf{r}, \mathbf{r}') = \sum_{\alpha\beta} |\varphi_\alpha\rangle K^{\alpha\beta} \langle\varphi_\beta| \quad (2.84)$$

where $K^{\alpha\beta}$ is known as density kernel. $K^{\alpha\beta}$ has elements which are nonzero only if $|\mathbf{r}_\alpha - \mathbf{r}_\beta| < \mathbf{r}_c$, where $\mathbf{r}_\alpha$ and $\mathbf{r}_\beta$ indicate the coordinates of the centers of the NGWFs φ_α and φ_β, and $\mathbf{r}_c$ is a real-space cut-off length.

Making use of this representation for the DM, the total energy of the non-interacting Kohn-Sham system can be written as:

$$E = Tr(\mathbf{KH}) \quad (2.85)$$

The normalization imposition takes the form:

$$N = Tr(\mathbf{KS}) \quad (2.86)$$

with the electronic density being related to the DM through the equation:

$$n(\mathbf{r}) = \rho(\mathbf{r}, \mathbf{r}') \quad (2.87)$$

and **S** being the overlap matrix defined as:

$$\mathbf{S} = \langle\varphi_\alpha|\varphi_\beta\rangle \quad (2.88)$$

To achieve linear scaling, locality of interactions needs to be imposed on the DM via truncation of the density kernel $K^{\alpha\beta}$. Such process, justified by the known exponential decay

of $\rho(\mathbf{r},\mathbf{r}')$ (Eq. 2.74) with respect to $|\mathbf{r}-\mathbf{r}'|$ for systems with an electronic band gap [41, 42, 43], leads to a sparse density matrix [$\rho(\mathbf{r},\mathbf{r}')$] and makes any insulating or semiconducting system amenable to LS-DFT simulation. As also noted above, imposition of the locality constraint on the basis set is performed on the basis of a localisation radius. Contributions to the DM from basis-functions which do not overlap are therefore neglected, being equal to zero.

Several strategies have been developed to drive the DM towards idempotency during the energy-minimisation process. A very common solution is to add a penalty term dependent on DM-idempotency to the energy functional. The best known approach to accomplish this is the purification scheme proposed by McWeeny [44]:

$$\widetilde{E}[\rho] = E[\rho] + \alpha P[\rho] \tag{2.89}$$

with:

$$P[\rho] = \mathrm{Tr}[(\rho-\rho^2)^2] \tag{2.90}$$

McWeeny's work shows that, close to idempotency, steepest descent optimisation of P leads to an iterative process that increasingly improve a trial DM:

$$\rho(\mathbf{r},\mathbf{r}')_{k+1} = 3\rho(\mathbf{r},\mathbf{r}')_k^2 - 2\rho(\mathbf{r},\mathbf{r}')_k^3 \tag{2.91}$$

This process is illustrated in Fig. 2.3.

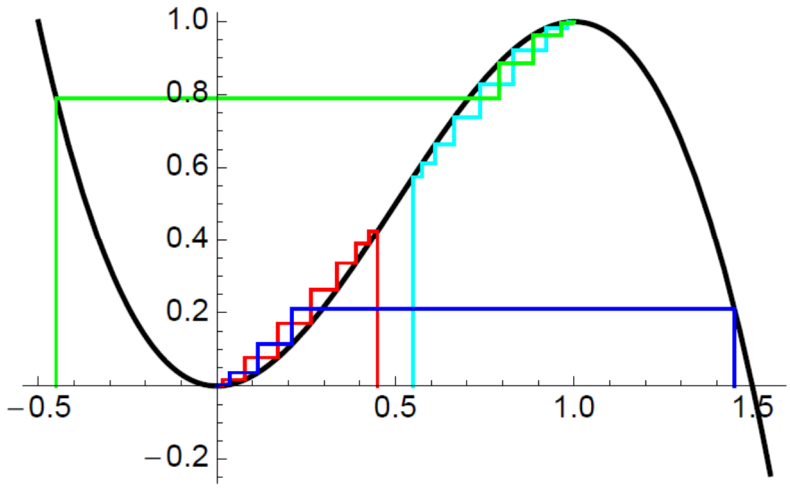

Figure 2.3. Illustration of McWeeny's purification transformation in terms of the orbital occupancies for three example cases: e.g., −0.45 (green), 0.45 (red), 0.55 (cyan) and 1.45 (blue).

This procedure can be proved to converge if the initial occupancies of the trial DM lie in the $(\frac{1-\sqrt{5}}{2}, \frac{1+\sqrt{5}}{2})$ interval If tighter bounds are used, McWeeny purification leads to even better results. When the occupancies lie in the $[-\frac{1}{2}, \frac{3}{2}]$ range, then the ρ_{k+1} DM (called purified DM) will be weakly idempotent and all its entries lie in the [0, 1] range. McWeeny purification method is used in ONETEP as the first step in the minimisation of the DFT-energy with respect to the DM.

Once an acceptable level of idempotency has been reached, the Li-Nunes-Vanderbilt (LNV) method [45, 46, 47] is used to further minimise the total energy and refine the DM towards idempotency. In this purification mechanism, the total energy is minimised with respect to an auxiliary matrix σ related to the DM by:

$$\rho = 3\sigma^2 - 2\sigma^3 \tag{2.92}$$

where:

$$\sigma(\mathbf{r}, \mathbf{r}') = \sum_{\alpha\beta} \varphi_\alpha(\mathbf{r}) L^{\alpha\beta} \varphi^*_\beta(\mathbf{r}') \tag{2.93}$$

In Eq. 2.93 $L^{\alpha\beta}$ is the matrix element of the auxiliary kernel **L** defined as:

$$\mathbf{K} = 3\mathbf{LSL} - 2\mathbf{LSLSL} \tag{2.94}$$

It is demonstrated [45, 46, 47] that minimizing $\widetilde{E}[\rho]$ with respect to σ naturally drives the DM to idempotency. As long as the entries of σ are in the $[-\frac{1}{2}, \frac{3}{2}]$ range, ρ will be weakly idempotent and the minimisation process will lead to the ground-state energy of the system. This process present various advantages, the most important of which is the lack of local minima in the potential surfaces explored. It is however important to underline the instability of the LNV method if any value of **L** stray from the $[-\frac{1}{2}, \frac{3}{2}]$ range. To overcome this limitation, a variant of the LNV algorithm is implemented in ONETEP: the Haynes, Skylaris, Mostofi and Payne (HSMP) one [48]. In this variant, σ is defined in terms of the purified and renormalized DM:

$$\rho = N \frac{3\sigma^2 - 2\sigma^3}{Tr[3\sigma^2 - 2\sigma^3]} \tag{2.95}$$

The denominator in Eq. 2.95 permits to generate terms in the search direction that project out the electron number gradient by construction and effectively self-determine the chemical potential of the system. Once the density kernel is converged to the desired tolerance, the NGWFs are updated (via an outer optimisation cycle, vide infra) and the kernel re-optimised until the total convergence in the calculation is reached.

2.3.3. Psinc basis-set

The LS-DFT approach makes it necessary to employ a localised basis set to take full advantage of the sparsity of the electronic DM for semiconductors and insulators. However, use of localised basis-set in known to create computational complications associated with the spurious Pulay forces that originate from translation of the localised basis-set when the atoms move during geometry optimisation [38].

A solution to very advantageously compromise on this dichotomy has been reached in ONETEP with the use of support functions ($D_m(\mathbf{r})$) that are formed from discrete sum of plane-waves, which makes the set of $D_m(\mathbf{r})$ independent from the nuclear coordinates and systematically improvable upon increase of the kinetic energy cut-off, retaining in this way the positive aspects of the plane-waves [27]. These support functions are called psinc functions and are defined as:

$$D_m(\mathbf{r}) = \prod_{i=1}^{3} \frac{1}{N_i} \sum_{p_i=-J_i}^{J_i} e^{i(p_i \mathbf{b}_i)\cdot(\mathbf{r}-\mathbf{r_m})} \tag{2.96}$$

with $2J_i$ being the lattice points considered in every directions. The psinc functions are approximations to the Dirac delta function at their central point $\mathbf{r}_m$. This relation is formally expressed as:

$$D_m(\mathbf{r}) \approx \delta(\mathbf{r}-\mathbf{r_m}) = \frac{\Omega_{cell}}{(2\pi)^3} \int d\mathbf{G}\ e^{i\mathbf{G}\cdot(\mathbf{r}-\mathbf{r_m})} \tag{2.97}$$

An important propriety of these functions is that in the reciprocal space they are fully equivalent to plane-wave basis truncated to a rhombohedrum with its dimension defined by the reciprocal lattice vector. The sampling fineness of this rhombohedrum can be increased until the energy is well converged. In ONETEP, the psinc functions are computed in a reciprocal space sphere having the same volume as the reciprocal lattice vector rhombohedrum. In analogy with the plane-wave case (Eq. 2.57), the sampling accuracy of this reciprocal space sphere is controlled by a kinetic cut-off. Use of the psinc functions allows solution of the DFT problem with the same accuracy of a plane-wave basis set, but with the advantage of being spatially localised around their centres $\mathbf{r}_m$, as needed to achieve linear-scaling.

2.3.4. Non Orthogonal Wannier functions and their use in ONETEP

In the previous section, the basis set used in ONETEP (Non Orthogonal Wannier Function, NGWFs [54]) was shortly mentioned. Their use is instrumental to ONETEP reaching linear scaling without any accuracy compromise with respect to standard plane-wave DFT.

Wannier functions (WFs) are a reformulation of the Bloch wave-function (Eq. 2.80) and perfectly suited for the analysis of localized properties. These functions are localised and defined within a unit cell with lattice vector **R**:

$$|w_{n\mathbf{R}}\rangle = \left(\frac{\Omega_{cell}}{(2\pi)^3}\right)^{\frac{1}{2}} \int_{1^{st}BZ} d\mathbf{k} e^{-i\mathbf{k}\cdot\mathbf{R}} |\Psi_{n\mathbf{k}}\rangle \quad (2.98)$$

where $\Psi_{n\mathbf{k}}$ (considering a general case) is a Bloch function expressed in terms of the plane-waves basis set (Eq. 2.56).

WFs are mutually orthogonal, as the Bloch wave-function, since the FFT is a unitary transformation, hence:

$$\int d\mathbf{r}\, w^*_{n\mathbf{R}}(\mathbf{r}) w_{n'\mathbf{R}'}(\mathbf{r}) = \delta_{nn'}\delta_{\mathbf{R}\mathbf{R}'} \quad (2.99)$$

Considering the occupancies to be **k**-independent (i.e. systems with a large band-gap), the DM can be written using WFs:

$$\rho(\mathbf{r}, \mathbf{r}') = \sum_n \sum_{\mathbf{R}} w^{(\sigma)}_{n'\mathbf{R}'}(\mathbf{r}) f^{(\sigma)}_n w^{(\sigma)*}_{n\mathbf{R}}(\mathbf{r}') \quad (2.100)$$

It has been shown [43] that, for insulating systems, a set of exponentially-localised WFs can be build:

$$w(\mathbf{r}) \sim \exp(-\lambda|\mathbf{r} - \mathbf{r}_0|)\,;\ \lambda \propto \sqrt{E_{bg}} \quad (2.101)$$

where E_{bg} is the band gap energy. The equality in Eq. 2.74 shows how the construction of exponentially localised WFs as in Eq. 2.101 is of paramount importance for linear scaling applications. The DM (Eq. 2.100) decays exponentially. Hence WFs represent a basis set for which, given a system with a band gap, the DM can be truncated in a physically meaningful way.

In ONETEP, however, the support functions φ_α are the NGWFs that are derived from a subspace rotation **M** of the WFs:

$$|\,\varphi_{\alpha\mathbf{R}}(\mathbf{r})\rangle = \frac{V}{(2\pi)^3} \int_{1^{st}BZ} d\mathbf{k} e^{-i\mathbf{k}\cdot\mathbf{R}} \sum_n |\Psi_{n\mathbf{k}}(\mathbf{r})\rangle \left[\mathbf{M}^{\dagger\beta}_n \mathbf{S}_{\alpha\beta}\right] d\mathbf{k} \quad (2.102)$$

Where:

$$M^{\alpha}_n(\mathbf{k}) = \int d\mathbf{r}\ \varphi_{\alpha\mathbf{R}}(\mathbf{r}) \Psi_{n\mathbf{k}}(\mathbf{r}) \quad (2.103)$$

is the transformation matrix and $\Psi_{n\mathbf{k}}(\mathbf{r})$ is a pseudoatomic orbital used as starting guess for the initial NGWFs representation:

$$\Psi_{n\mathbf{k}}(\mathbf{r}) = \sum_\nu c_{n,\nu} B_{l_n,\nu}(\mathbf{r})\, S_{l_n,m_n} \quad (2.104)$$

In Eq. 2.99 S_{l_n,m_n} represents a real spherical harmonics, $B_{l_n,v}(\mathbf{r})$ is the radial part of normalised spherical Bessel fun tions of given angular momentum l and $c_{n,v}$ are the contraction coefficients (in terms of the psinc basis-set) obtained by solving the Kohn-Sham DFT calculation performed for every pseudo-atom in the system.

The non-orthogonality of the NGWFs requires a tensorially correct formulation. Considering the dual basis [33, 34] of the NGWFs $\{|\varphi^{\alpha}\rangle\}$ defined as:

$$|\varphi^{\alpha}\rangle = \sum_{\beta}|\varphi_{\beta}\rangle S^{\beta\alpha} \tag{2.105}$$

with:

$$S^{\beta\alpha} = \langle\varphi^{\alpha}|\varphi^{\beta}\rangle = \left(S_{\alpha\beta}\right)^{-1} \tag{2.106}$$

It is important to note the contra-variant vectors can always be converted to covariant ones making use of the inverse of the superposition matrix (see Eq. 2.106). In ONETEP the NGWFs are expressed as a linear combination of psinc functions so that the same accuracy of a standard plane-wave basis approach can be reached:

$$\varphi_{\alpha\mathbf{R}}(\mathbf{r}) = \sum_{\mathrm{K}=0}^{\mathrm{N}_1-1}\sum_{\mathrm{L}=0}^{\mathrm{N}_2-1}\sum_{\mathrm{M}=0}^{\mathrm{N}_3-1} \mathrm{C}_{\mathrm{KLM},\alpha}\mathrm{D}_{\mathrm{KLM}}(\mathbf{r}) \tag{2.107}$$

With $\mathrm{C}_{\mathrm{KLM},\alpha}$ being the expansion coefficients and $\mathrm{D}_{\mathrm{KLM}}(\mathbf{r})$ the psinc functions:

$$D_{KLM}(\mathbf{r}) = \frac{1}{N_1N_2N_3}\sum_{P=-J_1}^{J_1}\sum_{Q=-J_2}^{J_2}\sum_{R=-J_3}^{J_3} e^{-i(P\mathbf{B}_1+Q\mathbf{B}_2+R\mathbf{B}_3)\cdot(\mathbf{r}-\mathbf{r}_{KLM})} \tag{2.108}$$

Being different from the WFs only by a rotation operation, the NGWFs still decay exponentially within a certain radius. However due to the loss of orthogonality, the DM has to be express as in Eq. 2.84. In the next Section the implications of this formulation of the DM on the calculation of the total energy in ONETEP are discussed.

2.3.5. Further computational details of the ONETEP method

ONETEP is a program for the LS-DFT calculation of total energies and atomic forces. It is based on the concepts previously described in this Chapter. Starting from Eq. 2.84, the electronic density can be expressed in terms of the NGWFs as:

$$\mathrm{n}(\mathbf{r}) = \rho(\mathbf{r},\mathbf{r}') = \mathrm{K}^{\alpha\beta}\rho_{\alpha\beta}(\mathbf{r}) = \sum_{\mathrm{X}=0}^{(\mathrm{N}_1-1)}\sum_{\mathrm{Y}=0}^{(2\mathrm{N}_2-1)}\sum_{\mathrm{Z}=0}^{(2\mathrm{N}_3-1)}\mathrm{K}^{\alpha\beta}\rho_{\alpha\beta}(\mathbf{r}_{\mathrm{XYZ}})\mathrm{B}_{\mathrm{XYZ}}(\mathbf{r}) \tag{2.109}$$

where $\rho_{\alpha\beta}$ is the short-notation for the expansion coefficients of the two NGWFs φ_{α} and φ_{β} and $\mathrm{B}_{\mathrm{XYZ}}(\mathbf{r})$ are the fine grid delta functions defined as $\mathrm{D}_{\mathrm{KLM}}(\mathbf{r})$ (Eq 2.108) but including twice the maximum wave-vector of $\mathrm{D}_{\mathrm{KLM}}(\mathbf{r})$ to accurately describe the linear combination representing the product of two NGWFs.

Eq. 2.109 indicates that, since the total energy is a functional of the electronic density, its minimisation depends on two main parameters: the expansions coefficients of the NGWFs and the occupations in the density kernel.

$$E^0 = \min_{n} E[n] = \min_{\rho} E[\rho] = \min_{\rho} E\left[\rho\left(\{K^{\alpha\beta}\},\{\varphi_\alpha\}\right)\right] =$$

$$\min_{\{K^{\alpha\beta}\}\{C_{KLM,\alpha}\}} E\left[\rho\left(\{K^{\alpha\beta}\},\{C_{KLM,\alpha}\}\right)\right] = \min_{\{C_{KLM,\alpha}\}} \varepsilon\left[\{C_{KLM,\alpha}\}\right] \quad (2.110)$$

with:

$$\varepsilon\left[\{C_{KLM,\alpha}\}\right] = \min_{\{K^{\alpha\beta}\}} E\left[\left(\{K^{\alpha\beta}\};\{C_{KLM,\alpha}\}\right)\right] \quad (2.111)$$

Eqs. 2.110 and 2.111 define the nested loops (one for the NWFS, φ_α, and one for the density kernel, $K^{\alpha\beta}$) optimisation strategy used to minimise the DFT-energy in ONETEP. In the outer NWGFs-optimisation loop, the density kernel is kept fixed while the NGWFs coefficients are variationally optimised to reach the minimum self-consistent energy. This process is equivalent to solve the Kohn-Sham problem for the system of interest, provided the idempotency of the DM is satisfied (through the optimisation of $K^{\alpha\beta}$). Once the NGWFs optimal coefficients are updated, the total energy is minimised in the inner cycle with respect to the elements of $K^{\alpha\beta}$ (i.e. occupancies), while the NGWFs expansions are kept fixed. This process is repeated until self-consistency of the DFT-energy with respect to both the variational parameters (the expansion coefficients for φ_α and $K^{\alpha\beta}$) is achieved.

The total DFT-energy in ONETEP is expressed in the following way:

$$E[n] = E_K[n] + E_H[n] + E_{loc}[n] + E_{nl}[n] + E_{xc}[n] \quad (2.112)$$

where $E_K[n]$ is the kinetic energy, $E_H[n]$ is the Hartree energy, $E_{loc}[n]$ is the energy contribution of the local part of the pseudopotentials, $E_{nl}[n]$ is the energy contribution of the non-local part of the pseudopotentials, and $E_{xc}[n]$ is the energy obtained the adopted approximation to the exchange-correlation functional.

The kinetic energy $E_K[n]$ in ONETEP can be calculated as the trace product of the density kernel and the matrix elements of the kinetic operator:

$$E_K[n] = K^{\alpha\beta}\langle\varphi_\beta|\hat{T}|\varphi_\alpha\rangle \quad (2.113)$$

The matrix element evaluation is straightforward in ONETEP since $\hat{T}$ can be applied to the plane-wave representation of φ_α (Eq. 2.107), and then the integral can be evaluated by discrete summation over grid points in real space. Such procedure is possible thanks to the NGWFs

psinc function representation where $\hat{T}|\varphi_\alpha\rangle$ is considered a function, whose action on the simulation grid is expressed as:

$$\int_V D_{KLM}(\mathbf{r})f(\mathbf{r})d\mathbf{r} = Wf_D(\mathbf{r}_{KLM}) \tag{2.114}$$

where W is the volume per grid point and f_D is the result of bandwidth limiting $f(\mathbf{r})$ applied to the plane-wave like component of φ_α. The same approach can be used for all the other contributions to the total DFT-energy (Eq. 2.112):

$$E_H[n] = \frac{1}{2}\int V_H\, n(\mathbf{r})d\mathbf{r} = K^{\alpha\beta}\langle\varphi_\beta|\hat{V}_H|\varphi_\alpha\rangle \tag{2.115}$$

$$E_{loc}[n] = K^{\alpha\beta}\langle\varphi_\beta|\hat{V}_{loc}|\varphi_\alpha\rangle \tag{2.116}$$

$$E_{nl}[n] = K^{\alpha\beta}\langle\varphi_\beta|\hat{V}_{nl}|\varphi_\alpha\rangle \tag{2.117}$$

The $\hat{V}_{nl}$ operator in Eq. 2.117 is the non-local pseudo-potential operator in the Kleyman-Bylander form for a norm-conserving pseudopotential. These summations are all exactly equivalent to the analytical form of the respective integral. However, an approximation is required for the exchange-correlation term, due to the high non-linear terms present in the exchange-correlation functional:

$$E_{xc}[n] = K^{\alpha\beta}\langle\varphi_\beta|\hat{V}_{xc}|\varphi_\alpha\rangle \approx \frac{V}{8N_1N_2N_3}\sum_{XYZ} F(n(\mathbf{r}_{XYZ})) \tag{2.118}$$

where $F(n(\mathbf{r}_{XYZ})$ is the result of the application of $\hat{V}_{xc}$ on the fine grid. This approximation does not affect substantially the accuracy of the calculated exchange correlation energy and is applied in almost all the plane-waves based codes.

As Eq. 2.114 shows, the evaluation of the integral to calculate the different energies has to be done on the whole simulation cell since the application of the various operators is performed in the reciprocal space on the psinc components of the NGWFs. This approach would lead to a $O(Nlog(N))$ type of scaling (owing to the log(N) scaling of the FFT technique).

To solve this issue, a very innovative strategy, known as FFTbox method [49], was developed in ONETEP to reach true linear scaling. This strategy rests on the localisation of the NGWFs in real space. Their localisation permits evaluation of the various DFT-Hamiltonian matrix elements in a cell (the FFTbox) smaller than the whole simulation cells. Provided the localisation radius of the NWGFs is kept constant, the size of the FFTbox can be left unchanged as the size of the simulation-cell increases (Fig. 2.4), making the cost of integral evaluation independent of the overall system size and allowing highly parallel linear scaling execution of DFT simulations.

During ONETEP execution, the simulation cell is divided in many “parallelepipeds” (PPDs) commensurate with the original simulation cell in order to obtain an efficient subdivision of the overall space. The FFT box is then defined. The NGWFs for which the matrix elements need to be calculated are then “extracted” from the simulation cell and “deposited” in the FFT box. This operation is performed through an operator $\widehat{P}_{(\beta\alpha)}$ that projects the different NGWFs from the simulation cell on the subspace spanned by the FFT box. Formally, $\widehat{P}_{(\beta\alpha)}$ reads:

$$\widehat{P}_{(\beta\alpha)} = \frac{1}{W}\sum_{k=0}^{(n_1-1)}\sum_{l=0}^{(n_2-1)}\sum_{m=0}^{(n_3-1)}|d_{klm}\rangle \times \left\langle D_{(k+K_{\alpha\beta})(l+L_{\alpha\beta})(m+M_{\alpha\beta})}\right| \quad (2.119)$$

where $K_{\alpha\beta}$, $L_{\alpha\beta}$ and $M_{\alpha\beta}$ are the grid points of the total simulation cells. Conversely, lowercase terms refer to the grid points contained in the FFT box. It is worth noting that the projection operator $[\widehat{P}_{(\beta\alpha)}]$ will return a null action for the points of the total simulation cell, which fall outside of the FFTbox. As an example, if the matrix elements of the kinetic operator have to be evaluated, the corresponding formula reads:

$$T \approx -K^{\alpha\beta}\left\langle \varphi_\beta \middle| \hat{P}^{\dagger}_{(\beta\alpha)}\nabla^2\hat{P}_{(\beta\alpha)} \middle| \varphi_\alpha \right\rangle \quad (2.120)$$

Once the quantities of interest are calculated, the FFT box results are then projected back into the original simulation cell. This procedure is repeated until the whole space defined by the NGWFs spatial localisation and their overlap is spanned. The procedure is graphically summarised Figs. 2.4 and 2.5.

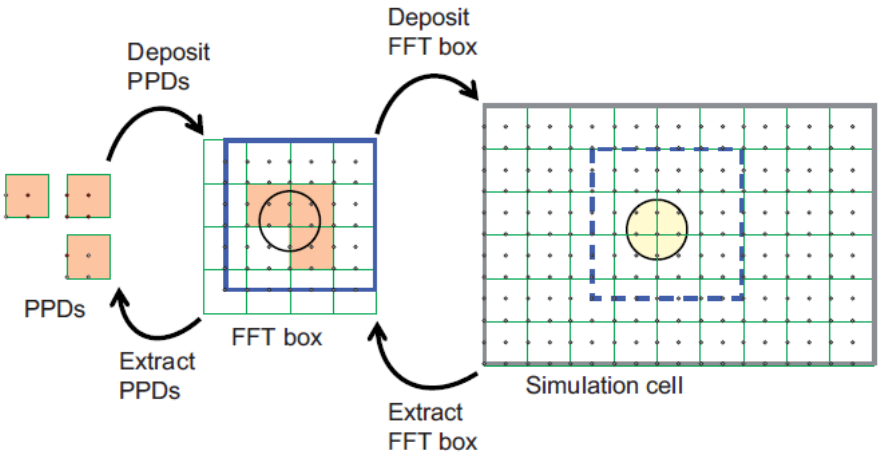

Figure 2.4. Schematic illustration of the FFTbox approach. From left to right: An NGWF can be deposited to, or extracted from, an FFTbox. The fixed-size of the FFTbox, determined by the radius of the NGWFs, makes it possible to perform operations in reciprocal space with computing cost independent of system size. The FFT box can in turn be deposited to, or extracted from, the simulation cell in real space. The localisation sphere of the NGWF is highlighted in yellow. The subdivision of the simulation cell in PPDs of the psinc grid and their relation to the FFT box is also shown.

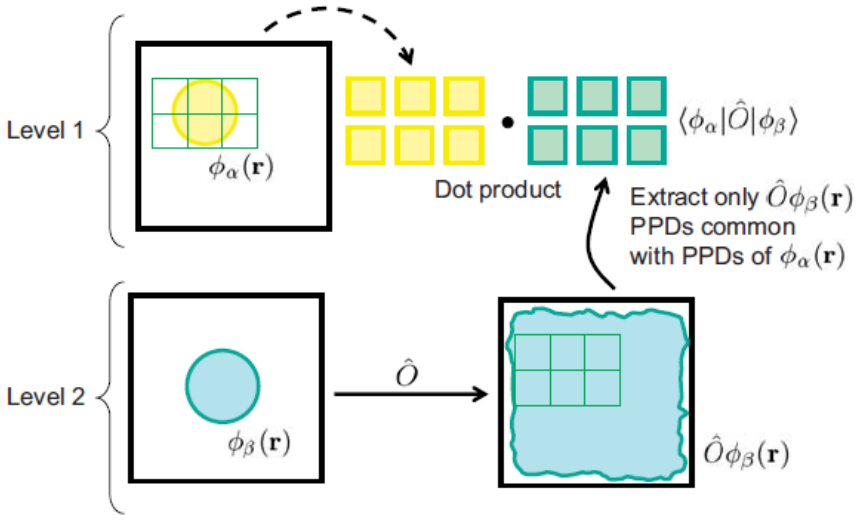

Figure 2.5. Matrix element evaluation in ONETEP. The operator is applied only once and causes the delocalisation of $\hat{O}\phi_\beta(\mathbf{r})$ over the entire volume of the FFT box. The integral is then calculated as a dot product over the PPDs that belong to the localisation region of $\phi_\alpha(\mathbf{r})$

2.3.6. Force calculations in ONETEP

In every DFT code, the calculation of atomic forces is the basis for geometry optimisation. Given an ionic configuration of the system, the force acting on an ion placed at $\mathbf{R}_{\gamma}$ is obtained as the derivative of the energy with respect to the ionic position ($\mathbf{R}_{\gamma}$):

$$\mathbf{F}_{\gamma} = \frac{\mathrm{dE}}{\mathrm{d}\mathbf{R}_{\gamma}} = -\frac{\partial \mathrm{E}}{\partial \mathbf{R}_{\gamma}} - \sum_{\alpha\beta} \frac{\partial \mathrm{E}}{\partial \mathrm{K}^{\alpha\beta}} \frac{\mathrm{dK}^{\alpha\beta}}{\mathrm{d}\mathbf{R}_{\gamma}} - \sum_{\alpha} \int \frac{\delta \mathrm{E}}{\delta \phi_{\alpha}(\mathbf{r})} \frac{\mathrm{d}\phi_{\alpha}(\mathbf{r})}{\mathrm{d}\mathbf{R}_{\gamma}} \mathrm{d}^{3}\mathbf{r} \tag{2.121}$$

where the chain rule is applied to account for the variational dependence of the total energy on the density kernel $\mathrm{K}^{\alpha\beta}$, and the psinc expansion coefficients $C_{KLM,\alpha}$ used to define the NGWFs in the psinc (DKLM(r)) basis. Since the NGWFs are expressed in terms of a psinc basis grid that is independent of the ionic configuration (i.e. $\frac{\mathrm{D}_{\mathrm{KLM}}(\mathbf{r})}{\mathrm{d}\mathbf{R}_{\gamma}} = 0$), Eq. 2.122 can be recast as:

$$\mathbf{F}_{\gamma} = \frac{\mathrm{dE}}{\mathrm{d}\mathbf{R}_{\gamma}} = -\frac{\partial \mathrm{E}}{\partial \mathbf{R}_{\gamma}} - \sum_{\alpha\beta} \frac{\partial \mathrm{E}}{\partial \mathrm{K}^{\alpha\beta}} \frac{\mathrm{dK}^{\alpha\beta}}{\mathrm{d}\mathbf{R}_{\gamma}} - \sum_{\alpha} \sum_{\mathrm{i}\in \mathrm{LR}(\alpha)} \frac{\partial \mathrm{E}}{\partial \mathrm{C}_{\mathrm{i},\alpha}} \frac{\mathrm{dC}_{\mathrm{i},\alpha}}{\mathrm{d}\mathbf{R}_{\gamma}} \mathrm{d}^{3}\mathbf{r} \tag{2.122}$$

where $\mathrm{LR}(\alpha)$ stands for the localisation region of the α NGWF, and the index i is used as a short-hand notation for the grid indexes KLM. In Eq. 2.122, the localisation region of the NGWFs moves with the atoms to which they are associated. In principle, this displacement does not affect the analytical derivative $\frac{\partial E}{\partial \mathbf{R}_{\gamma}}$ since for infinitesimal changes in $\mathbf{R}_{\gamma}$ the psinc grid points inside the localisation region $LR(\alpha)$ do not change. In ONETEP, the forces acting on the nuclei are calculated at the end of the electronic energy minimisation process so that the following conditions can be assumed to hold numerically:

$$\frac{\partial \mathrm{E}}{\partial \mathrm{K}^{\alpha\beta}} = 0 \; ; \; \frac{\partial \mathrm{E}}{\partial \mathrm{C}_{\mathrm{i},\alpha}} = 0 \tag{2.123}$$

which in turn reduce Eq. 2.122 to:

$$\mathbf{F}_{\gamma} = -\frac{\partial \mathrm{E}}{\partial \mathbf{R}_{\gamma}} \tag{2.124}$$

Thus, provided the electronic optimization process has been executed with tight convergence criteria (Eq. 2.123 is satisfied), the only contribution to the force on the atom in $\mathbf{R}_{\gamma}$ is the Hellman-Feynman term [50]. This term can be calculated using the same approach exposed in Section 2.3.5 for the various components of the total energy.

In order to work out the expression for the right term in Eq. 2.124, it has to be considered that the only components of the total energy explicitly dependent on $\mathbf{R}_{\gamma}$ are the ion-ion and electron-ion terms, hence:

$$\mathbf{F}_\gamma = \mathbf{F}_\gamma^{\mathrm{nl}} + \mathbf{F}_\gamma^{\mathrm{loc}} + \mathbf{F}_\gamma^{\mathrm{ew}} \tag{2.125}$$

where $\mathbf{F}_\gamma^{\mathrm{nl}}$ is the term due to the non-local part of the pseudopotentials, $\mathbf{F}_\gamma^{\mathrm{loc}}$ is the contribution caused by the local part of the pseudopotentials, and $\mathbf{F}_\gamma^{ew}$ is the factor obtained by the Ewald Summation [51] for long range interactions.

From Eq. 2.117, the expression of the non-local contribution to the total energy can be formulated, showing explicitly its dependence from the density kernel and the NGWFs:

$$\mathrm{E_{nl}} = \sum_{\alpha\beta}\sum_{\mathrm{i}}\langle\phi_\alpha|\chi_\mathrm{i}\rangle\,\mathrm{E_i}\langle\chi_\mathrm{i}|\phi_\beta\rangle\,\mathrm{K}^{\alpha\beta} \tag{2.126}$$

In Eq. 2.126, χ_i is the i^{th} projector, with i running over all the projectors of all the atoms and $\mathrm{E_i}$ is the correspondent Kleynman-Bylander energy term. Accordingly, $\mathbf{F}_\gamma^{\mathrm{nl}}$ can be expressed as:

$$\mathbf{F}_\gamma^{\mathrm{nl}} = -\frac{\partial \mathrm{E_{nl}}}{\partial \mathbf{R}_\gamma} = -\sum_{\alpha\beta}\sum_{\mathrm{i}}\left[\left\langle\phi_\alpha\middle|\frac{\partial\chi_\mathrm{i}}{\partial\mathbf{R}_\gamma}\right\rangle\mathrm{E_i}\langle\chi_\mathrm{i}|\phi_\beta\rangle - \langle\phi_\alpha|\chi_\mathrm{i}\rangle\mathrm{E_i}\left\langle\frac{\partial\chi_\mathrm{i}}{\partial\mathbf{R}_\gamma}\middle|\phi_\beta\right\rangle\right]\mathrm{K}^{\alpha\beta} \tag{2.127}$$

with the sum over projectors being restricted to the projectors of atom γ. Given the strict localisation of the NGWFs, the projectors/NGWFs overlap matrices are highly disperse. This allows calculation of the nonlocal contribution to the forces ($\mathbf{F}_\gamma^{nl}$) in the framework of the FFT box approximation so that its computational cost scales linearly with the dimension of the system.

The easiest way to evaluate the local contribution of the pseudopotentials to the forces involves the representation in the reciprocal space of the local part of the pseudofunction:

$$\mathbf{F}_\gamma^{\mathrm{loc}} = -\frac{\partial \mathrm{E_{LOC}}}{\partial \mathbf{R}_\gamma} = \sum_{\mathbf{G}} \mathrm{i}\mathbf{G}\mathrm{e}^{-\mathrm{i}\mathbf{G}\mathbf{R}_\gamma}\,\mathrm{V}_\gamma(\mathbf{G})\mathrm{n}^*(\mathbf{G}) \tag{2.128}$$

The evaluation of this equation poses a non-trivial problem since its computation scales as $\mathrm{O(N^2)}$. This is due to the $\mathrm{O(N)}$ scaling of the summation in the $\mathbf{G}$ vectors, that has to be evaluated for the N atoms in the system, leading to an overall $\mathrm{O(NxN)} = \mathrm{O(N^2)}$ scaling. The scaling can in principle be reduced to $\mathrm{O(NlnN)}$, but a linear-scaling cannot be achieved. However, although there is no linear-scaling for this operation, it has been numerically demonstrated that the computational pre-factor associated with the calculation of forces is so small with respect to the cost of the electronic structure calculations that a slowdown is not observed in the overall ONETEP approach for systems up to a few thousand atoms [52].

The Ewald force term is calculated as the derivative of the energy obtained by the Ewald Summation:

$$\mathbf{F}_\gamma^{\mathrm{ew}} = -\frac{\partial \mathrm{E_{ew}}}{\partial \mathbf{R}_\gamma} \tag{2.129}$$

The evaluation of this term present the same issue of the pseudopotential local term in that the Ewald summation method scales $O(NlnN)$ too. In spite of this, and in analogy to the $\mathbf{F}_\gamma^{loc}$ term, the computational overhead with respect to the electronic-structure optimisation for systems of a few thousand atoms is negligible.

In the evaluation of atomic forces, the NGWFs optimisation procedure introduce an additional term to be considered. Although the NGWFs are expressed as a linear combination of the underlying (delocalised) psinc grid, which in principle removes the necessity of calculating Pulay forces contributions [53] as the atoms move, an extra Pulay term due to the NGWFs gradient appears. As previously mentioned, this term should be zero during the force calculation. In practice, however, a tight convergence of the energy is not always inexpensively achieved with respect to psinc expansion of the NGWFs. Although the effects of partial optimisation of the NGWFs on the DFT energy can be negligible, the corresponding Pulay contribution to the forces may not be. The Pulay force originating from incomplete optimisation of the NGWFs reads:

$$\mathbf{F}_\gamma^{\mathrm{Pulay}} = \int \mathrm{d}\mathbf{r} \frac{\delta E}{\delta \phi_\alpha(\mathbf{r})} \frac{\partial \phi_\alpha(\mathbf{r})}{\partial \mathbf{R}_\gamma} \tag{2.130}$$

and the total forces are consequently defined as:

$$\mathbf{F}_\gamma = \mathbf{F}_\gamma^{\mathrm{HF}} + \mathbf{F}_\gamma^{\mathrm{Pulay}} \tag{2.131}$$

The first term in Eq. 2.130 is calculated after every SCF optimisation so that its evaluation is computationally inexpensive. Its analytical form has been derived by Soler and Miyazaky [54]:

$$\frac{\delta E}{\delta \phi_\alpha(\mathbf{r})} = 4\left[\hat{H}\phi_\beta(\mathbf{r})K^{\alpha\beta} + \phi_\beta(\mathbf{r})Q^{\alpha\beta}\right] \tag{2.132}$$

where $Q^{\alpha\beta} = -(KHS^{-1})^{\alpha\beta}$. The second term in Eq. 2.130 is calculated applying the gradient operator to the NGWFs:

$$\frac{\partial \phi_\alpha(\mathbf{r})}{\partial \mathbf{R}_\gamma} = -\nabla \phi_\alpha(\mathbf{r}) \delta_{\alpha\beta} \tag{2.133}$$

If we consider the psinc expansion of the NGWFs, and substitute it in Eq. 2.133, the resulting expression is:

$$\frac{\partial \phi_\alpha(\mathbf{r})}{\partial \mathbf{R}_\gamma} = \frac{1}{N_p} \sum_{\mathbf{G}}^{\mathbf{G}_{\max}} \tilde{\phi}_\alpha(\mathbf{G}) e^{i\mathbf{G}(\mathbf{r}-\mathbf{R}_\gamma)} \tag{2.134}$$

This evaluation takes place in the reciprocal space representation of ϕ_α and is done using the FFTbox approximation so that linear scaling is preserved.

2.3.7. Geometry Optimisation in ONETEP and BFGS implementation

Geometry optimisation in ONETEP is achieved through minimisation of the system energy on the basis of the atomic forces calculated according to the prescriptions explained in Section 2.3.5. ONETEP executes geometry optimisation using the Broyden-Fletcher-Goldfarb-Shanno quasi Newton algorithm in the variant suggested by Pfrommer et al. [55].This implementation relaxes the structure of interest with respect to the enthalpy $= \mathrm{E} + \mathrm{pV}$, in principle allowing relaxation of the simulation cell coupled with an external pressure bath.

Let us consider a crystal structure determined by the matrix of lattice vectors $\mathrm{h}\{\mathrm{a}, \mathrm{b}, \mathrm{c}\}$ and the coordinates s_i of the N atoms in the unit cell. The unit cell has volume $\Omega = \det(\mathrm{h})$ and its energy E is a function of both h and s_i's. Pfrommer et al. devised a convenient choice of variables to reduce in the stress tensor ε that has nine components and represents a change in the system from a configuration h_0 to $\mathrm{h} = (1 + \varepsilon)\,\mathrm{h}_0$. After such reduction, relaxing the crystal structure becomes equivalent to optimising the enthalpy per unit cell $\mathrm{H} = \mathrm{E} + \mathrm{p}\Omega$. This problem spans a configurational space with dimensionality $(9 + 3\mathrm{N})$.

The BFGS algorithm is implemented in such a way that a point in the configuration space is defined by the vector $\mathbf{X}$ whose first nine components are the symmetry irreducible stress tensor components: $\mathbf{X}_{3(\mathrm{i}-1)+\mathrm{j}} = \varepsilon_{\mathrm{ij}}$. The remaining elements of X are the coordinates of the atoms in the unit cell $\mathrm{X}_{(\mathrm{i}+9)} = \mathrm{s}_\mathrm{i}$.

The so force-vector in this configuration space is defined as:

$$\mathrm{F} = -\frac{\partial \mathrm{H}}{\partial \mathrm{X}}\Big|_\mathrm{p} \tag{2.135}$$

its first nine elements are the derivatives of the components of H with respect to ε:

$$\mathrm{f}^{(\varepsilon)} = -(\sigma + \mathrm{p}\Omega)\left(1 + \varepsilon^\mathrm{T}\right)^{-1} \tag{2.136}$$

with:

$$\sigma = \left(\frac{\partial \mathrm{E}\left((1+\varepsilon\prime)\mathrm{h}\right)}{\partial \varepsilon\prime}\right)_{\varepsilon=0} \tag{2.137}$$

The remaining 3N elements are the product of the forces acting on the atoms $\mathrm{f}_\mathrm{i} \ldots \mathrm{f}_\mathrm{N}$ in lattice coordinates with the metric tensor $\mathrm{g} = \mathrm{h}^\mathrm{T}\mathrm{h}$:

$$\mathrm{F} = \left(\mathrm{f}^{(\varepsilon)}, \mathrm{gf}_1, \ldots, \mathrm{gf}_\mathrm{N}\right)^\mathrm{T} \tag{2.138}$$

Once X and F are defined, the BFGS scheme is applied. When close to the minimum of the configurational space ($\mathrm{X}_{\mathrm{min}}$), the change in enthalpy can be approximately expressed as:

$$\delta H = \frac{1}{2}(X - X_{min}) \cdot A(X - X_{min}) \quad (2.139)$$

In Eq. 2.139, *A* represent the Hessian matrix. For a quadratic problem, knowing A and given F, should allow location of the minimum in one step of geometry optimisation. However, since A is unknown, and the electronic potential energy is far from quadratic, one starts with a guess that is iteratively improved as the relaxation to the minimum proceeds. In real implementations, however, is the inverse of A, $A^{-1}$to be refined during the optimisation. At each iteration, X_i is updated according to:

$$X_{i+1} = X_i + \lambda \Delta X_i \quad (2.140)$$

$$\Delta X_i = A_i^{-1} F_i \quad (2.141)$$

where λ is the step length determined by a line minimisation along ΔX_i. Given A_0^{-1}as input, the BFGS algorithm progressively improves it as:

$$A_i^{-1} = A_{i-1}^{-1} - \frac{(X_i - X_{i-1}) \otimes (X_i - X_{i-1})}{(X_i - X_{i-1}) \cdot (F_i - F_{i-1})} - \frac{\left(A_{i-1}^{-1}(F_i - F_{i-1})\right) \otimes \left(A_{i-1}^{-1}(F_i - F_{i-1})\right)}{(F_i - F_{i-1}) \cdot A_{i-1}^{-1}(F_i - F_{i-1})} +$$

$$\left[(F_i - F_{i-1}) \cdot A_{i-1}^{-1}(F_i - F_{i-1})\right] U \otimes U \quad (2.142)$$

With:

$$U = \frac{(X_i - X_{i-1})}{(X_i - X_{i-1}) \cdot (F_i - F_{i-1})} - \frac{A_{i-1}^{-1}(F_i - F_{i-1})}{(F_i - F_{i-1}) \cdot A_{i-1}^{-1}(F_i - F_{i-1})} \quad (2.143)$$

The process continues until convergence for the force vector within a numerical threshold is obtained. In principle, if the enthalpy, H, were perfectly quadratic in $X - X_{min}$, A_i^{-1} would converge to the full Hessian matrix in a number of relaxation steps equal to the degrees of freedom of the system. In reality, however, the speed of convergence is principally due to the first guess of A_i^{-1} hence a sensible choice of A_0^{-1} is of paramount importance. In order to have the best possible guess in ONETEP a preconditioning scheme of the Hessian matrix has also been implemented. The interested reader is referred to Reference [56] for further details.

2.3.8. Optimization of empty Kohn-Sham (KS) states and Fermi golden rule optical spectra in ONETEP

The nested loops optimisation of the DFT energy (Eqs. 2.110 and 2.111) allows linear-scaling solution of the Kohn-Sham DFT problem for systems with an electronic band gap without diagonalisation of the DFT Hamiltonian, as typical for standard (cubic scaling) plane-wave DFT. Although capable of accurate representation of occupied KS states (obtained from final one-shot diagonalisation of the DFT Hamiltonian), the LS-DFT ONETEP approach results in poor description of all but the lowest-lying unoccupied states. The separable

representation of the DM (Eq. 2.84) allows optimisation of the NWGFs to describe only the occupied KS states. As a result, the description of empty KS states in terms of both energy and real-space amplitude can be inaccurate [57].

In ONETEP such limitation is overcome via optimisation of a second set of atom-centred conduction NGWFs (χ_α) to accurately describe empty bound KS from the pre-optimised valence NGWFS (ϕ_α) and related DM and DFT Hamiltonian.

The so-called conduction band calculation method, described in Ref [57], optimises a selected number of empty KS states by minimising the energy of a conduction-projected Hamiltonian (H_χ^p) with respect to the conduction NGWFs (χ_α) and their associated density kernel ($M^{\alpha\beta}$):

$$E = \mathrm{Tr}\left[M^{\alpha\beta}, \chi_\alpha\right] \tag{2.144}$$

H_χ^p is obtained from the valence NGWFs (ϕ_α), density kernel $K^{\alpha\beta}$ and overlap matrix $S^{\beta\alpha}$ (Eq. 2.106) as:

$$H_\chi^p = \left(H_\chi\right)_{\alpha\beta} - \left(T^\dagger K H_\phi K T\right)_{\alpha\beta} + \sigma\left(T^\dagger K H_\phi K T\right)_{\alpha\beta} \tag{2.145}$$

In Eq. 2.145, H_χ is the unprojected conduction Hamiltonian, $T_{\alpha\beta} = \int d\mathbf{r}\, \phi_\alpha^*(\mathbf{r})\chi_\beta(\mathbf{r})$ is the cross-overlap between valence- and conduction-NGWFs, and σ is the energy shift enforced to be able to apply the procedure to initially positive eigenvalues of the (unprojected) conduction Hamiltonian.

The conduction density kernel $M^{\alpha\beta}$ can be meaningfully truncated on the basis of the conduction NGWFs radial cut-off allowing linear-scaling. The truncation of $M^{\alpha\beta}$ is physically justified whenever some degree of localization of the low-energy empty KS-states is present (i.e. occurrence of a gap in the unoccupied KS manifold) so that $M^{\alpha\beta}$ can be treated in analogy with the valence band one $K^{\alpha\beta}$. Given the more delocalised nature of empty KS with respect to occupied ones, it is good practice to use conduction NGWFs with slightly larger localisation radii.

Once the conduction NGWFs have been optimised, the KS-Hamiltonian can be computed and diagonalised in a joint basis comprising both valence (ϕ_α) and conduction (χ_α) NGWFs, yielding the KS states [57]. The procedure yields eigenvalues in very good agreement with the results from standard plane-wave DFT (for the occupied and optimized empty KS states).

The optimisation of conduction NGWFS is affected by several factors: the energy and number of the optimized conduction KS states, the similarity between valence and conduction KS states, the number of conduction NGWFs (χ_α) per atom and their localization radius.

Numerical analysis of the convergence of the empty KS states with respect to these parameters is hence good practice.

The optimised conduction KS states can be used to calculate optical spectra via Fermi's golden rule [58] or within the linear-response time-dependent DFT (LR-TDDFT) framework recently implemented in ONETEP [59].

The availability of optimized empty KS states makes it possible to approximate optical absorption spectra on the basis of the imaginary part of the dielectric function $\varepsilon_2(\omega)$ computed as [57]:

$$\varepsilon_2(\omega) = \frac{8\pi}{\Omega}\left|\langle\psi^{c}_{n,k}|\mathbf{q}\cdot\mathbf{r}|\psi^{v}_{n,k}\rangle\right|^2 \delta(E^{c}_{nk} - E^{v}_{nk} - \hbar\omega) \qquad (2.146)$$

where v and c denote valence and conduction KS-state, respectively. $|\psi_{nk}\rangle$ is the n^{th} KS-state, of energy E_{nk} at the k^{th} **k**-point. Ω is the simulation cell volume. **q** is the polarization direction of the incoming photon of energy $\hbar\omega$. **r** is the position operator. As explained in [57, 60, 61, 62], owing to the ill-undefined nature of **r** in periodic systems, $\varepsilon_2(\omega)$ needs to be computed via the momentum operator (**p**) and then related to the position (**r**) representation through corresponding commutator with the Hamiltonian.

Although limitations in the procedure are to be expected owing to the neglect of non-local electron-hole interactions and relaxations in the simulated spectra [63], the adopted procedure can be useful to initially explore the optical properties of very extended, periodic systems as considered in this thesis. The well-known limitation of the adiabatic local density approximation (ALDA) for Linear-Response Time-Dependent (LR-TDDFT) simulation of periodic semiconductors and insulators [63], further stresses the favourable trade off of between computational accuracy and feasibility of the Fermi Golden rule approach in Eq. 2.146.

2.3.9. The Coulomb cutoff method for electrostatic interactions in periodic boundary conditions

ONETEP makes use of the PBC to solve the KS equations on a plane wave related basis set (Psinc functions). The PBC/plane-waves set up has been originally developed for application to three-dimensional (3D) periodic systems such as bulk crystalline materials. Through the years this method has however evolved and PBC simulations have started to be used for a myriad of different, not just 3D, systems. In particular, PBC are used for the simulation of two-dimensional and one-dimensional systems with residual translational symmetry in two or one direction, as well as for isolated molecules with sufficiently extended vacuum buffer in the simulation cell [64]. This choice allows to take full advantage of the computational

maturity (read efficiency) of periodic plane-wave (or equivalent as in the ONETEP case) DFT implementations.

For charge neutral systems the supercell approach is a relatively well-controlled approximation. By increasing the vacuum separation between replicated images of (vacuum-padded) aperiodic systems, the isolated non-periodic limit can be rapidly approached. The most common example is represented by dipole free neutral molecules where good result can be obtained just by avoiding overlap of the charge densities between periodically repeated molecules.

The supercell approximation however loses its accuracy for systems where a monopole charge or dipoles and higher multipoles are present. A monopole charge potential decays as $1/R$, it is hence practically impossible to reach the infinite limit approximation for system with a net charge. The same problem arises when a large dipole is present in the simulated cell (dipole potential decays as $1/R^3$). For accurate simulation of these cases, the simulations cell would need to be unfeasibly large in order to reach an acceptable level of convergence of the electrostatic interactions [27].

A large (and constantly growing) number of different approximations/correction techniques has been developed trying to address this problem and eliminate PBC artefacts on the description of the electrostatics for systems with non-zero charge or multipoles [65, 66]. These techniques are based on an array of different methods: the *a posteriori approaches* add a correction term to the total energy after the SCF calculation [67, 68]. This term is usually evaluated through some fitting to the infinite limit of the electrostatic contributions to the total energy. Alternatively, the multipole expansion of the localised charge can be employed after a uniform periodic background charge is added to counter the monopole in the system considered [69, 70]. Last, the evaluation of electrostatic interaction in the real and reciprocal space can be modified in order to pre-emptively avoid interactions between periodic images [71, 72].

In ONETEP, the so-called Coulomb-cutoff technique [73, 74, 75] has been implement in order to properly account for electrostatic interactions in aperiodic charged systems. The electrostatic energy in ONETEP is composed by the Hartree term $\mathrm{E_H[n]}$ due to electron-electron repulsive interactions, the local pseudopotential term $\mathrm{E_{locps}[n]}$, which express the interaction of the electron density with the potential of the ion cores, and the ion-ion term $\mathrm{E_{ion-ion}}$ which comprises the repulsive interactions between the atomic cores.

Specifically, the Hartree energy is obtained as:

$$\mathrm{E_H} = \frac{1}{2}\int \mathrm{n}(\mathbf{r})\mathrm{V_H}(\mathbf{r})\,\mathrm{d}\mathbf{r} \tag{2.147}$$

Where $\mathrm{V_H}(\mathbf{r})$ is obtained from the electronic density $n(\mathbf{r})$ via Poisson's equation:

$$\nabla^2 \mathrm{V_H}(\mathbf{r}) = -4\pi \mathrm{n}(\mathbf{r}) \tag{2.148}$$

In Eq. 2.148 atomic units are used. This problem can be solved employing the Green function $\mathrm{G}(\mathbf{r}, \mathbf{r}') = -1/4\pi|\mathbf{r} - \mathbf{r}'|$ that produces:

$$\mathrm{V_H}(\mathbf{r}) = -\int \frac{\mathrm{n}(\mathbf{r}')}{|\mathbf{r}-\mathbf{r}'|} \mathrm{d}\mathbf{r}' \tag{2.149}$$

The integral in Eq. 2.149 is evaluated over all the space of the simulation cell. Under PBC conditions such integral is non divergent only for neutral systems. If a net charge is present in the simulation cell $\mathrm{q} = \int_\Omega \mathrm{n}(\mathbf{r})\mathrm{d}\mathbf{r} \neq 0$. Eq. 2.147 then needs to be modified as:

$$\nabla^2 V_H(\mathbf{r}) = -4\pi(n(\mathbf{r}) - \frac{q}{\Omega}) \tag{2.150}$$

where Ω is the volume of the simulation cell. In this reformulation, a uniform background charge density equal to the opposite of the net charge present in the cell is considered. Under PBC condition, $\mathrm{n}(\mathbf{r})$ and $\mathrm{V_H}(\mathbf{r})$ are periodic too so that Eq. 2.149 can be recast in terms of discrete Fourier transform:

$$V_H(\mathbf{G}) = \frac{4\pi}{\Omega \mathbf{G}}(\tilde{n}(\mathbf{G}) - q\delta_{\mathbf{G},0}) \tag{2.151}$$

The Coulomb interaction is easy to calculate in the reciprocal space from the reciprocal electronic density $\tilde{\mathrm{n}}(\mathbf{G})$. Once $\mathrm{V_H}(\mathbf{G})$ is obtained, $\mathrm{V_H}(\mathbf{r})$ can be deduced with an inverse FFT. $\mathrm{E_H} = \frac{1}{2}\int \mathrm{n}(\mathbf{r})\mathrm{V_H}(\mathbf{r})\,\mathrm{d}\mathbf{r}$ is then calculated over the original simulation cell to obtain the Hartree energy per simulation cell. This calculation, however, omits the contribution to the total energy of the infinitely repeated electronic density $\mathrm{n}(\mathbf{r})$, and neglects the interactions between the background neutralising charges and the electronic density $\mathrm{n}(\mathbf{r})$ of the simulation cell. This same issue is encountered in the calculations of $E_{locps}[n]$ and $E_{ion-ion}$. These contributions, usually calculated using the Ewald summation technique [51], are affected by the same shortcoming affecting E_H evaluation (i.e. omission of the background charges interaction with $\mathrm{n}(\mathbf{r})$, neglect of infinite periodic images contribution to the energy). As a result, the influence of the periodic neighbour will polarise the charge distribution during the SCF process leading to wrong results or in the worst cases diverging energies.

These considerations makes it evident that a posteriori approach to correct the total energy cannot fully capture (and account for) the complexity of the interactions between the periodic images, $\mathrm{n}(\mathbf{r})$ and the background of neutralising charges. Starting from this consideration, in ONETEP the Coulomb cutoff scheme has been implemented to self-consistently correct the treatment of electrostatic interactions for overall charged (non multipole-free) systems within

a PBC approach. As a result, ONETEP can calculate not only the correct electrostatic energy, but also the correct electrostatic potential.

In the Coulomb cutoff approach, a spatial cutoff is applied to the bare electrostatic interactions so that they are limited within a single simulation unit cell. This cutoff makes the integral in Eq. 2.149 non-divergent also for charged systems. This, in turn, makes the use of a neutralising background charge unnecessary.

A form that can be used to for the Coulomb potential in order to truncate the electrostatic interactions of the simulation cell with its PBC-replicated images is:

$$\mathrm{V_{CC}} = \begin{cases} \frac{1}{|\mathbf{r}-\mathbf{r}'|} & \mathbf{r}-\mathbf{r}' \in \mathrm{R_1} \\ 0 & \mathbf{r}-\mathbf{r}' \notin \mathrm{R_1} \end{cases} \tag{2.152}$$

where R_1 is a region which size and shape are defined so that when the Hartree potential at $\mathbf{r}$ is calculated, all the $\mathbf{r}'$ of interest (usually all the point with non-vanishing $n(\mathbf{r})$ or with $n(\mathbf{r})$ over a certain threshold) are included in R_1. An example of the R_1 region for a cubic cell is reported in Fig. 2.6. Given the definition of the Coulomb potential in Eq. 2.152, the Hartree potential can be calculated as the convolution of the Coulomb cutoff operator V_{CC} and the electronic density:

$$\mathrm{V_H}(\mathbf{r}) = \int_{\Omega} \mathrm{n'^{(r)}}\, \mathrm{V_{CC}}(\mathbf{r}-\mathbf{r}')\mathrm{d}\mathbf{r}' \tag{2.153}$$

Let us consider the simplest shape for $\mathrm{R_1}$ that is a sphere of radius $\mathrm{R_c}$. For this shape $\mathrm{V_{CC}}$ takes the form:

$$\mathrm{V_{CC}}(\mathbf{r}) = \Theta(|\mathbf{r}| - \mathrm{R_c})/|\mathbf{r}| \tag{2.154}$$

where Θ is the Heaviside step function [76]. The Fourier transform of Eq. 2.154 is known:

$$\tilde{V}_{\mathrm{CC}}^{sphere}(\mathbf{r}) = \frac{4\pi(1-\cos(\mathbf{G}R_c))}{\Omega\mathbf{G}^2} \tag{2.155}$$

Eq. 2.155 does not have any singularity at $\mathbf{G} = 0$. Hence, $\mathrm{V_H}(\mathbf{r})$ can be calculated via Eq. 2.151 but without considering the term $-\mathrm{q}\delta_{\mathbf{G},0}$ since the background neutralising charge is not present anymore.

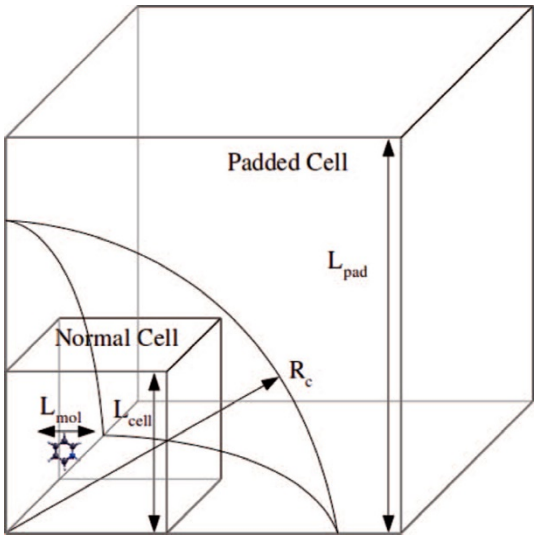

Figure 2.6. Illustration of the R_1 region for a cubic cell with dimension defined by L_{cell}, L_{pad} and cutoff radius R_c for the spherical cutoff Coulomb approach. R_c must be at least as large as the largest distance between any two non-zero charges in the system (condition met if $R_c \geq \sqrt{3}L_{cell}$). In order for the periodic densities not to influence each other, $L_{pad} \geq (L_{mol} + R_c)$ must be satisfied. L_{mol} is the extension of the system (the maximum distance between two non-zero charges) in any Cartesian direction.

In practical calculations, $n(\mathbf{r})$ of the original cell is transferred to a larger padded cell of size L_{pad}. The electronic density is then FFT-transformed in $\tilde{n}_{pad}(\mathbf{G})$. In the reciprocal space the terms of $V_{CC}(\mathbf{r})$ can be calculated and stored. These terms are then used to multiply the Fourier components of $\tilde{n}_{pad}(\mathbf{G})$ every time $V_H(\mathbf{r})$ is calculated. The reverse FFT of the multiplied $\tilde{n}_{pad}(\mathbf{G})$ components give the terms $V_{H,pad}(\mathbf{r})$. $V_H(\mathbf{r})$, localized inside the original unit cell, is then used for the solution of the DFT problem.

Since nanotubes, the systems considered in this Thesis, have a high aspect ratio, the simulation unit cell is more extended in one direction than in the remaining two others. This shape makes the use of a spherical Coulomb cutoff region impractical. The obvious choice for this type of systems is that of cylindrical shape for the R_1 region. Numerical techniques for evaluation of truncated electrostatic in a cylindrical region (as well as one-dimensional periodically repeated wires) are available in ONETEP [75] and have been used for Coulomb cutoff simulation of charged systems as presents in the defective nanotubes (Chapter 6).

References

[1] Schrödinger E. 1926 *Phys. Rev.* **28** (6) 1049.

[2] Kohn. W. *Rev. of Mod. Phys.* 1999 **71** (5) 1253.

[3] Born M., Oppenheimer. R. *Ann. d. Physik* 1927 **84** (20) 457.

[4] Yarkony DR *Rev. of Mod. Phys* 1996 **68** (4) 985.

[5] Pisana S., Lazzeri M., Cashiraghi C., Mauri F.2007 **6** 198.

[6] Wodtke A., Tully C., Auerbach J.D. *Int. Rev. in Phys. Chem.* 2007 **23** (4) 513.

[7] Antonov V., Harmon B., Yaresko. A. 2004 *Electronic Structure and Magneto-Optical Properties of Solids* (Kluwer Academic).

[8] Fermi E. Zeitschrift für Physik, 1928 **48** (1) 73.

[9] Weizsäcker. C. V. Zeitschrift für Physik 1935 **96** (7) 43.

[10] Hohenberg P., Kohn. W. *Phys. Rev.* 1964 **136** (3B) B864.

[11] Kohn W., Sham. L. J. *Phys. Rev.* 1965 **140** (4A) A1133.

[12] Levy M. *Phys. Rev. A* 1982 **26** (3) 1200

[13] Levy M. *Proc. Natl. Acad. Sci. U.S.A.* 1979 **76** (12) 6062

[14] Lieb, E., Shimony, A., Feshbach, H. *Physics as Natural Philosophy: Essays in Honor of Laszlo Tisza on His 75th Birthday* 1982 111–149. MIT Press, Cambridge

[15] Lieb, E.H. *Int. J. Quantum Chem.* 1983 **24** (3), 243

[16] Martin, R. *Electronic Structure: Basic Theory and Practical Methods. Cambridge University Press,* 2004 Cambridge MIT Press.

[17].van Leeuwen J. M. J., Groeneveld J., de Boer J. *Physica* 1959 **25** (7) 792.

[18] Jones R. O., Gunnarsson. O. *Rev. Mod. Phys.* 1989 **61** (3) 689.

[19] Capelle. K. *Braz. J. Phys* 2006 **36** 1318.

[20] Gell-Mann M., Brueckner. K. A *Phys. Rev.* 1957 **106** (2) 364.

[21] Perdew J. P., Burke K., Ernzerhof M. *Phys. Rev. Lett.* 1996 **77** (18) 3865.

[22] Kohn W., Becke A. Parr. R. *J. Phys. Chem.*1996 **100** 12974.

[23] Anisimov V. I., Zaanen J., Andersen. O. K. *Phys. Rev. B* 1991 **44** (3) 943.

[24] Zhao Y., Schultz N.E., Truhlar D. G. *J. Chem. Theory and Comp*.2006 **2** (2) 364.

[25] Novoa J.J., Sosa C *J. Phys Chem*. 1995 **99** (43) 15837.

[26] Makov G., Payne M.C. *Phys Rev B* 1995 **51** (7) 4014.

[27] Arias T. A., Payne M. C., Joannopoulos. J. D. *Phys. Rev. B* 1992 **45** (4) 1538.

[28] Phillips J.C., Kleinman L. *Phys. Rev.* 1959 **116**, 287.

[29] Hamann D.R., Schlüter M., Chiang, C. *Phys. Rev. Lett.* 1979 **43** 1494.

[30] Kleinman L., Bylander D.M. *Phys. Rev. Lett*. 1982 **48** 1425.

[31] Perdew J., Zunger A. *Phys Rev B* 1981 **23** 5048.

[32] Fuchs M., Scheffler. M. *Computer Physics Communications* 1999 **119** (1) 67.

[33] Kohn. W. *Phys. Rev. Lett.* 76 1996 **17** 3168.

[34] Prodan E., Kohn W. *Proc. Natl. Acad. Sci. U.S.A* 2005 **102** (33) 11635.

[35] Bowler D.R., Miyazaki T., Gillan M.J. *J. Phys. Condens. Matter* 2002 **14** (11) 2781.

[36] Rudberg E., Rubensson E.H. *J. Phys.: Condens. Matter* 2011 **23** (7) 075502.

[37] Pauli. W. *Phys. Rev.* 1940 **58** 716.

[38] Skylaris C.K., Haynes P.D., Mostofi A.A., Payne. M.C. *J. Chem. Phys.* 2005 **122** 084119.

[39] Hernandez E. Gillan M.J. *Phys. Rev. B* 1995 **51** (15) 10157.

[40] Skylaris C.K., Mostofi A.A., Haynes P.D., Diéguez O., *Phys. Rev. B* 2002 **66** (3) 035119.

[41] des Cloizeaux. J. *Phys. Rev.* 1964 **135** (3A), A685.

[42] He L., Vanderbilt D. *Phys. Rev. Lett.* 2001 **86** 5341.

[43] Brouder C., Panati G., Calandra M., Mourougane C., Marzari N. *Physical Review Letters* 2007 **98** (4) 046402.

[44] McWeeny R. *Rev. Mod. Phys.* 1960 **32** (2) 335.

[45] Li X.P., Nunes R. W., Vanderbilt D. *Phys. Rev. B* 1993 **47** (16) 10891.

[46] Nunes R.W., Vanderbilt D. *Phys. Rev. B* 1994 **50** (23) 17611.

[47] Daw. M. S., *Phys. Rev. B* 1993 **47** (16) 10895.

[48] Haynes P. D., Skylaris C.K., Mostofi A. A., Payne M. C. *Journal of Physics: Condensed Matter* 2008 **20** (29) 294207.

[49] Skylaris C. K., Haynes P. D., Mostofi A. A., Payne M. C. *Phys. Stat. sol. (b)* 2006 **243** (5) 973.

[50] Feynman, R. P. *Phys. Rev.*1939 **56** (4) 340.

[51] Essman U., Perera L., Berkowitz M. L. *J. Chem. Phys* 1995 **103** (19) 8577

[52] Hine N. D. M., Robinson M., Skylaris C. K., Haynes P. D., Mostofi A. A., Payne M. C. *Phys Rev B* 2011 **83** 195102

[53] Ruiz-Serrano A., Hine N. D. M., Skylaris C. K *J. Chem. Phys*. 2012 **136** 234101.

[54] Miazaky T., Bowler D. R., Choudhury R., Gillan M. J. *J. Chem. Phys*. 2004 **121** 6186

[55] Pfrommer B. G., Cote M., Louie S. G., Cohen M. L. *J. Comp. Phys* 1997 **131** 233

[56] Skylaris C. K., Haynes P. D., Mostofi A. A., Payne M. C. *J. Chem. Phys* 2003 **119** 8842

[57] Ratcliff L E, Hine N D M and Haynes D 2011 *Phys. Rev. B.* 2011 **84** 165131

[58] Dirac P. A. M *Proceedings of the Royal Society A* 1927 **114** (767) 243.

[59] Zuehlsdorff T J, Hine N D M, Spencer J S, Harrison N M, Riley D J, and Haynes P D 2013 *J. Chem. Phys.* **139** 064104.

[60] Pickard C J Ph.D. Thesis University of Cambridge 1997.

[61] Read A J and Needs R J 1991 *Phys. Rev. B* **44** 13071.

[62] Motta C, Giantomassi M, Cazzaniga M, Gal-Nagy K, and Gonze X 2010 *Comput. Mater. Sci.* **50** 698.

[63] Onida G, Reining L and Rubio A 2002 *Rev. Mod. Phys.* **74** 601.

[64] Ihm J., Zunger A., Cohen M. L. *J. Phys. C* 1979 **12** 4409.

[65] Neugebauer J., Kresse G., Janotti A., Van de Walle C. G. *Rev. Mod. Phys* 2014 **86** 253.

[66] Lany S., Zunger A. *Phys. Rev B.* 2008 **78** 235104.

[67] Leslie M., Gillan M. J. *J. Phys. C* 1985 **18** 973.

[68] Makov G., Payne M. C. *Phys. Rev. B* 1995 **51**, 4014.

[69] Bengtsson L. *Phys. Rev. B* 1999 **59** 12301.

[70] Nozaki H., Itoh S. *Phys. Rev. E* 2000 **62** 1390.

[71] Kantorovich L. N. *Phys. Rev. B* 1999 **60** 15476.

[72] Genovese L., Deutsch T., Goedecker S. *J. Chem. Phys*.2007 **127** 054704

[73] Jarvis M. R., White I. D., Godby R. W., Payne M. C. *Phys. Rev. B* 1997 **56** 14972.

[74] Rozzi C. A., Varsano D., Marini A., Gross E. K. U., A. Rubio, *Phys. Rev. B* 2006 **73** 205119.

[75] Hine N. D., Dziedzic J., Skylaris C. K., Haynes P. D. J.Chem.Phys 2011 **135** 204103.

[76] Ernst Julius Berg *Heaviside's Operational Calculus, as applied to Engineering and Physics* 1936 McGraw-Hill Education.

Chapter 3

Imogolite aluminosilicate nanotubes: a brief review

Abstract

In this chapter a small literature review on the Imogolite nanotubes (Imo-NTs) is presented. The use of the Imo-NTs as potential photo-catalyst is proposed on the basis of recent separate observations of the beneficial role of one-dimensional (1D) nanostructuring, permanent polarizations in photo-ferroelectrics, and reactant nanoconfinement for photo-catalysis. The available experimental results regarding Imo-NTs composition, structure, synthesis, functionalisation and doping are summarised to highlight how Imo-NTs integrate 1D structuring, permanent polarization and the possibility of reactant nano-confinement (separation) in one material, which is believed to hold great promise for photo-catalytic applications. The chapter comprises also a short report regarding the state of the art in electronic structure simulation of the Imo-NTs. The results presented are then discussed with respect to the potential of the materials as photo-catalyst, which drives the original research presented in this Thesis.

3.1. Imogolite Nanotubes as photo-catalyst

As extendedly discussed in Chapter 1, the efficiency and viability of a given photo-catalyst (PC) is jointly determined by the following elements:

i) The PC needs to be able to absorb light via electronic excitation. For sunlight and artificial visible light to be used, the energy gap between occupied and empty electronic states of the PC need to match the visible light spectrum (1.6-3.1 eV), and ideally the sun radiance peak (1.6-2.1 eV) [1].

ii) The nature of the electronic excitation, or its decay, needs to lead to effective separation of the excited electron (e*) and hole (h), preventing their recombination.

iii) The separated e* and h must diffuse efficiently and independently to the surface of the PC (or the current collectors for photovoltaics application [1]).

iv) For photo-catalytic applications, the photo-generated excited e* and h need to be transferred to reactants with high efficiency. Efficient transfer of e* (photo-reduction) or h (photo-oxidation) rests on suitable alignment between the PC and reactant electronic energy levels as well as electron-transfer kinetics faster than any competitive e*-h recombination process.

v) The transfer of photo-generated e* or h needs to lead to the desired product(s).

vi) Ideally, the ratio of absorbed photons to e* (h) transferred and generated product (Quantum Yield) should be as high as possible [2-14].

vii) The selectivity of a given PC towards a specific reactant or product in a multi-component medium should be controllable and tuneable [15].

Over one century of research in the field [2-14,16-19] has firmly established that, besides being a formidable challenge, simultaneous fulfilment of conditions (i)-(vii) intimately depends on the atomic composition, structure and dynamics of the PC, reactants and their interfaces in a given medium. Given the remarkable extension and variety of the literature on photo-catalysis a complete account of the state of the art techniques and findings is beyond the scope of this thesis. The interested reader is referred to recent review articles [2-14, 17-19].

The increased aspect-ratio (the ratio of length to diameter or surface to volume) of 1D nanostructures has been recently shown to be linked to increased photo-catalytic performances. Such increment in the photo-catalytic activity is a result of the highly anisotropic diffusion of separated e*-h pairs. Various examples can be found in the literature regarding CdS, ZnO and GaN nanorods [20-22]. As discussed in Chapter 1, 1D nanomaterials offer the possibility of nano-engineering the exposed surfaces (micro-facets) of the material considered. This type of solution has been recently tested on 1D TiO_2 and Zn_2GeO_4 systems, revealing clear benefits with respect to bulk or thin-film phases [23-25]. Coating or asymmetric functionalization of 1D nanostructures has also being studied, with findings offering appealing prospects for the development of enhanced photo-catalytic strategies [19, 26-35].

The central role of effective e*-h separation for any viable photo-catalytic strategy has led to a growing interest in the development of photo-active ferroelectric (photo-ferroelectric) substrates. Their intrinsic permanent polarizations is capable of influencing the e*-h relaxation leading to efficient separation and diffusion to the PC surfaces. Reports on the beneficial role that permanent polarization can play for efficient e*-h separation have started to appear in the literature [36-42]. To the best of our knowledge, the use of 1D ferroelectric materials for photo-catalysis is yet to be explored, although the specialised literature presents growing

characterisation of 1D ferroeletric nanotubes (NTs) and nanorods for multi-ferroics applications [43-58].

Together with efficiency, cost and scalability, selectivity of the PC is another pivotal element in order to obtain selective synthesis and subsequent control over the conversion of reactants in fine-chemicals and feedstock. Pioneering work on highly selective methane activation by microporous beta-zeolite via deep-UV photo-catalysis [15] has attracted interest from the scientific community due to the novelty of the concept of nano-confinement-assisted photo-catalysis [59-64].

While the development of photo-catalytic strategies based on 1D nanostructures [19,20-26], ferroelectric substrates [36-42] and porous PCs [59-64] is separately progressing, to the best of our knowledge, these concept are yet to be integrated in one hybrid solution. The possible integration of these three concepts in one solution based on cheap and abundant materials is the central to the research presented in this Thesis. In addition, we also speculate on whether local polarization of overall dipole-free nanostructures, rather than macroscopic polarizations present in ferroelectrics, could be as effective in promoting e*-h separation and enhance photo-catalytic activity.

Towards the exploration of these concepts, in this Thesis we have started to turn to an emerging class of 1D nanomaterials, Imogolite (Imo) NTs, which has been receiving growing interest by the experimental and theoretical community [65-107].

3.2. Imogolite Nanotubes: synthesis, functionalization and properties

3.2.1. Imo NTs structure

Imogolite aluminosilicate (AlSi) and aluminogermanate (AlGe) NTs are structurally analogous to the naturally occurring hydrous-aluminosilicate imogolite [73-75]. Imogolite nanotubes (NTs) are constituted by a curved gibbsite $Al(OH)_3$ sheet with orthosilicate groups O_3SiOH attached to the inner wall, resulting in a $(Al_2SiO_7H_4)_N$ stoichiometry. The structural repeat unit along the NT-axis is composed of six aluminium oxide octahedra arranged in a hexagonal ring, and coordinated to one silicate tetrahedron via three oxygen bridges. The average radii of the tubes measures (11.5 ± 3.0 Å [75, 77]). The Al-O octahedra are linked by hydroxyl μ_2-OH groups at the shared edges (Fig 3.1). The labelling μ_2 indicates that the hydroxyl is connected to two metal (Al) atoms.

The curvature of the nanotubes originates from attachment of the orthosilicate groups (O_3SiOH) to the inner wall. This attachment causes a shortening of the O-O distances (2.7 Å),

with respect to those found in gibbsite (3.2 Å), favouring edge-sharing with a SiO_4 tetrahedron. Hence, a mismatch between the Al-O bond lengths in the inner and the outer wall of the nanotube is created, which causes the gibbsite sheet to warp.

Analogous considerations hold also for the Al-Ge tubes. As reported by Konduri *et al.* [76], the substitution of Si with Ge leads to an increment in the system radius (13 ± 3 nm [79]), without altering the tubular shape [70]. The increase in diameter is due to the fact that the Ge-O bonds (in the GeO_4 tetrahedron) are weaker than the Si-O ones. This leads to a reduced mismatch between the bonds in the inner and outer parts of the tube, and to an increase of its radius of curvature.

Al-Ge NTs exits not only as single-wall (SW). The creation of double-walled (DW) AlGe NTs has also been recently achieved [78]. Depending by the initial concentration of the reactant, SW or DW NTs can be selectively synthesised. The DW NTs have larger radii of (15 ± 3 Å [79]) due to the presence of an external NTs. Experimental investigation has shown that the two co-axial NTs are not covalently bonded and that an average distance of 2.7 Å is present between the internal and external cylinder.

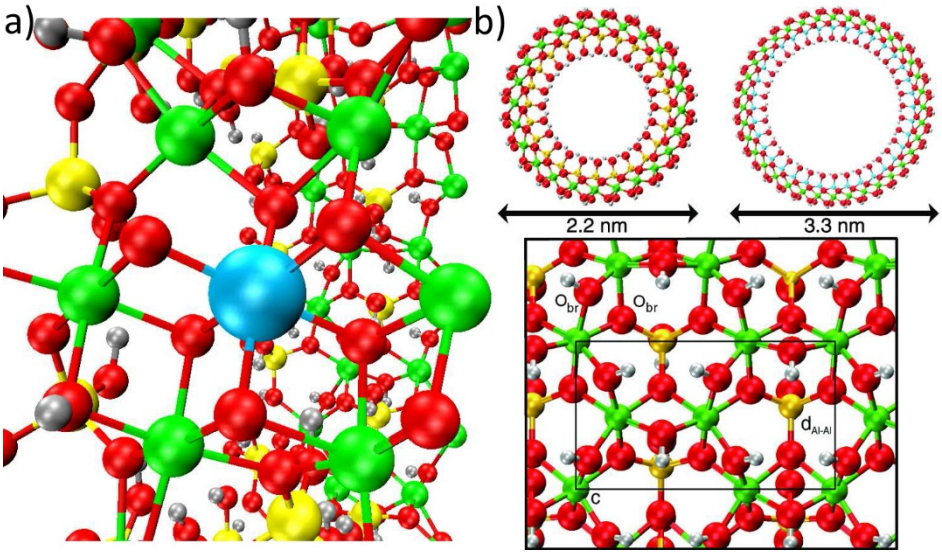

Figure 3.1. Perspective view of the octahedral coordination of Al-atoms in Al-Si (Al-Ge) nanotubes (a). b) Optimized structure of $(Al_2SiO_7H_4)_{24}$ (left) and $(Al_2GeO_7H_4)_{36}$ (right) NTs together with a close up on the NTs local coordination (bottom). O: red; H: grey; Al: green; Si: yellow Ge: cyan.

AlSi, AlGe and DW-AlGe differ not only by the dimension of their radii but in their length too. The three structures measure around 100 nm (AlSi), 200 nm (AlGe) and up to 1 µm (DW

AlGe), respectively. X-Ray diffraction (XRD) and dynamic light scattering (DLS) measurements [67] give an experimental length of 0.851 nm for the repetitive unit cell of both the AlSi and AlGe NTs.

The structural similarity between Al-Si and Al-Ge tubes leads to another very appealing feature. By varying the ratio between Si and Ge atoms in the tubes, it is possible to control the diameter and length of the systems [70]. This introduces the possibility of controlling the tube radius of curvature and, accordingly, both the shape selectivity and micropolarity of the tube cavity.

3.2.2. Imo NTs synthesis

The synthesis of the Al-Si and Al-Ge (DW Al-Ge) nanotubes is a water-solution process. The synthesis of the nanotubes requires five steps [67]:

1. Hydrolysis i.e. dissolution of aluminium and silicon (germanium) precursors in water at pH 3.5.
2. Basification i.e. slow ramping of the pH to 5.0 by addition of sodium hydroxide (NaOH).
3. Partial re-acidification to pH to 4.5 by addition of an acid.
4. Equilibration at room temperature.
5. Heating above room temperature under reflux.

Imo-NTs synthesis has been object of various studies [67, 68, 70, 71, 76]. A definitive synthetic mechanism was not identified until the study of Yucelen *at al.* [71]. The authors showed that initial hydrolysis of the reactants leads to the formation of precursors with curved structures. These precursors display chemical coordination (i.e. bond lengths, angles) similar to that of the nanotubes. The formed precursors are both ionic sub-nanoparticles (Keggin ions like, with formula $[AlO_4Al_{12}(OH)_{24}(H_2O)]^{7+}$ and monomeric, polymeric aluminate and aluminosilicate species ($Al_1Si_x - Al_{13}Si_x$).

In their work, Yucelen *at al.* [71] developed also a model according to which the tube synthesis is divided into 2 steps: (i) initial condensation of the proto-nanotubes precursors and (ii) rearrangement of the condensed systems (Fig 3.2). This work is important because it ended the uncertainty regarding the assembling process of the Imo-NTs [71] by clarifying the structures of the NT-precursors and their connection to the final product. The condensation of the precursors is driven by the conversion of their tetrahedral coordinated end-groups into fully octahedral configuration as they condense together. The formation of the tubes from assembling and rearrangement of curved precursors suggests that the key to effective

doping/functionalization of the NTs may reside in the possibility of forming doped curved precursors capable of self-assembling.

Recently, Mallet et al. [78] have shown that AlGe NTs can be synthesised also as DW-NTs depending by the concentration of the initial reactants. If the initial concentration of aluminium perchlorate (step 1 in the scheme reported before) is around 0.25 mol·dm^{-3}, only AlGe DW-NTs are formed. Conversely, if the aluminium perchlorate concentration is increased to values around 0.5 mol·dm^{-3}, only AlGe SW-NTs are formed. The physico-chemical mechanism behind this behaviour is still unclear and being debated.

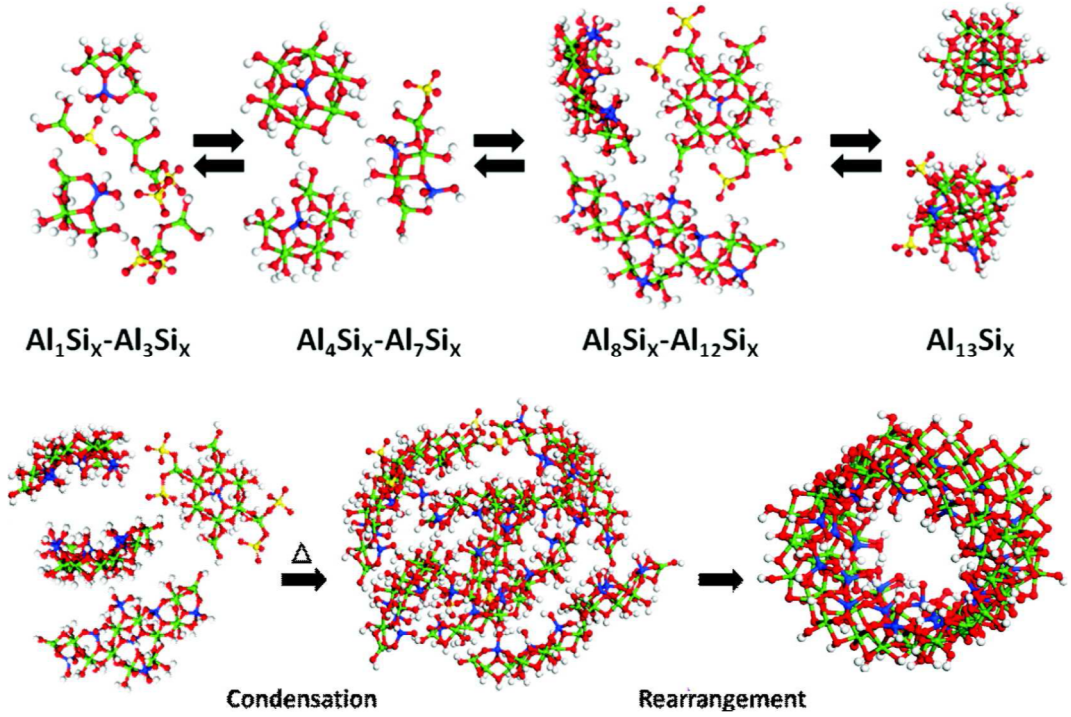

Figure 3.2. Proposed formation mechanism for Imo-NTs (from Ref. [71]).

3.2.3 Synthetic and Post synthetic Functionalisation of the Imo-NTs

An intriguing characteristic of the Imo-NTs is the flexibility in selective functionalization of either sides of the NT-cavity by organic groups [82-87]. Important advances have been recently made in this direction. Nair et al. [82] developed an approach to modify the interior of the AlSi NTs by covalent bonding of different organic species (i.e. $HSiCl_3$, $CH_3Si(OCH_3)_3$, $ClCOCH_3$). Although the percentage of inner substituted silanols is only up to 35%, it is sufficient to alter the water uptake inside the NT-cavity. These results illustrate the potential and tuneability of Imo-NTs as selective gas-adsorbent, ion adsorbent, humidity sensor or inorganic support for biomolecules.

In the same line of work, Bottero et al. [86] described a synthetic route to obtain NTs with the interior of the cavity completely methylated (AlSi-Me NTs). This new material presents larger pores and higher specific surface than pristine Imo-NTs. In the same original study it was demonstrated that organic functionalization of the NT-interior leads to larger adsorption of methane (CH_4) with respect to pristine AlSi NTs. The coexistence of a hydrophobic inner surface and of an outer hydrophilic one holds great promise for use of the AlSi-Me NTs in gas separation processes.

Imo-NTs functionalisation was also investigated by Zanzottera et al. [83, 84]. Following Ref. [86], they synthesised AlSi-Me NTs. However, through post-synthesis grafting, the external walls of the NTs were further functionalised with amine groups (Am-AlSi-Me NTs). This process led to a limited loss in micro-porosity. In spite of this, no loss in the specific surface area was observed. It is reported in [83,84] that the presence of amine groups should turn the functionalized NTs more soluble in organic solvent, expanding even further the range of potential applications.

Another notable example of the flexibility offered by the Imo-NTs functionalization is the work of Kang et al. [87]. In their study, the direct synthesis of amine-methyl functionalised NTs was reported. The resulting NTs structure was observed to enhance molecular adsorption selectivity. The internal amino methyl groups largely enhanced the NTs uptake of CO_2 but suppressed the adsorption of N_2 and CH_4.

The work of Avellan et al. [94] is of extreme relevance for the prospect of engineering Imo-NTs structure. In this study, the incorporation of iron (Fe) atoms into the AlGe NTs was achieved. Although the concentration of Fe inserted in the NTs is only around 1%, this type of doping should reduce, according to DFT calculations [103], the band gap (BG) of the AlGe NTs, leading to absorption of the visible part of the light spectrum. If confirmed, this modification would be highly significant for the possible use of AlGe NTs as visible-light photo-catalyst.

These studies represent just an initial exploration of the possibility offered by modification of Imo-NTs. Imo-NTs can be functionalised and doped under mild condition while their structural conformations remain almost unaffected. It is hence possible to change the properties of both the outer and the inner surface without loss in porosity or degradation of the material. Altogether, the NTs structural stability and chemical flexibility suggest use for a rather vast range of appealing applications.

3.3. Theoretical studies on Imogolite Nanotubes

Although Density Functional Theory (DFT) modelling and derived Tight-Binding approximations (TB-DFT) have assisted research in the growth mechanism of AlSi NTs [71, 72], in the properties of periodic defect-free (SW and DW) AlSi and AlGe NTs models [95-101], and in possible phosphorous- and arsenic-based functionalization [102], the recent experimental progress in the field of Imo-NTs has yet to be completely matched by the materials modelling community. With the exception of a very limited number of DFT studies of point-defects and Fe-doping in AlSi and AlGe NTs [97, 98, 103], the structural and electronic characterization of defects, dopant, functionalization and termination effects in Imo-NTs and their role in tuning the NT electronic and spectroscopic properties as well as its chemical reactivity is to date unexplored. Before focusing on these unexplored aspects in the next Chapters, here we provide a contained review of the published theoretical work on Imo-NTs to provide the current state of the art in the field and to comment on the challenges in the simulations of these systems. .

AlSi NTs present different structures depending on their crystallization conditions. Synthetic and natural tubes have a different number of Al atoms in their circumference. Experimental investigations [71,72] suggest structures with N=10 and N=12 Al atoms in the tube circumference as the most plausible geometries for natural and synthetic AlSi NTs, respectively.

Unambiguous determination of the nanotubes structure is a fundamental step to understand the properties of these materials. To this end, several theoretical studies have targeted the origin of different radii for natural and synthetic AlSi NTs. The existence of two stable structures suggests the likely presence of two different minima in the ground state potential energy surface of the tubes. These minima may be differently populated by different synthetic routes. Interestingly, Zhao *et al.* [99] found two energy minima corresponding to structures with 9 (N=18 Al atoms) and 12 (N=24 Al atoms) gibbsite units in the circumference. Consistent with the smaller (larger) diameter measured for natural (synthetic) imogolite [75, 77], the N=18 and N=24 minima were assigned to natural and synthetic tubes, respectively.

Conversely, Demichelis *at al.* [100] found different values for the lowest energy structure of imogolite nanotubes. The authors found only one minima of the imogolite nanotube structure corresponding to a geometry with 10 gibbsite units (N=20 Al atoms) in the circumference. In this work, the authors suggested that the differences from the results of Zhao *et al.* [99] may be due to the different DFT functionals used for the calculations (B3LYP by Demichelis *et al.* in [100], PBE by Zhao *et al.* in [99]). However, in their work Demichelis et al. [100] could not reproduce the local minimum at N=12 with the PBE functional. The minimum at N=12 was

instead recovered by Guimaraes et al. [96] using a Tight Binding DFT (TB-DFT) approach. In the conclusion of their work, the authors stated that the presence of a second minima at N=10 could not be excluded, due to the intrinsic limitations of the parameterized TB-DFT method. Additional controversy was added by the work of Lee at al. [107]. Their PBE simulations resulted in a minimum energy structure of the AlSi NTs composed by N=8 gibbsite units. Finally, the most recent study by Laurenco et al. [101] reports TB-DFT simulations of the AlSi NTs resulting in single minima for the structure formed by N=11 (22 Al atoms) gibbsite units.

To date, the effort to determine the structure of the Al-Ge and DW AlGe NT is not as extensive as in the AlSi case. Although a larger amount of experimental data is available [78-81], the experimental investigations have so far provided a less clear picture of the number of units forming the AlGe NTs. Ref. [101] reports a comprehensive TB-DFT study of the dimension of the Al-Ge and DW AlGe NTs. In the AlGe case, the lowest-energy structure was computed for N=28. The calculations on the DW AlGe NTs resulted in the most stable structure being for an inner N=24 and outer N=42 NT. In this case, the simulations have also shown the stabilising effect of the external tube on the internal one, leading to a minimum of the energy for inner tubes of reduced dimensions (N=24) with respect to the single wall AlGe NT (N=28).

Although the available results from theoretical investigations of Imo-NTs are relatively close to the experimental data, a definitive agreement has still to be reached. Despite the lack of consistency between the different simulations of the Imo-NTs, few important structural characteristic have been consistently found. Imo-NTs (similarly to the carbon NTs case) can present different types of symmetries in their structures (i.e. armchair or zig-zag [107]). In all the studies where this aspect was considered [96, 100, 101, 107], the (achiral) zig-zag symmetry was found to be energetically preferred.

The stabilisation of the zig-zag NTs structures has been linked to the formation of different hydrogen-bonding (HB) networks depending by the chirality of the NT [107]. Lee et al. have shown that HB plays an important role in the formation of Imo-NTs and for their structural stability. It was found that the HB on the outer surface significantly affects the Al-O distances and consequently the potential energy surface of the NTs. The HB on the inner cavity exhibited an even more important role. Whereas the relaxation of inner and outer Al-O and Si-O bond distances is the driving force for the Imo-NTs formation, it was proved that the origin in the strain energy minimum determining the NTs geometrical structure depends by the inner HB network. The presence of this inner HB network, leading to a well-defined energy minimum, is thence suggested to be the origin of the high experimental mono-dispersity of Imo-NTs.

Moving to the analysis of the Imo-NTs' electronic properties, despite differences in the calculated band-gap (BG), all the theoretical studies published so far agree in modelling Imo-NTs as wide band gap insulators with a direct gap. This means that the lowest energy state in the conduction band (CB) and the maximum energy state in the valence band (VB) have the same crystal momentum, a condition favourable to the optical excitation of electrons from the valence to the conduction band [108].

Considering the AlSi case, the NTs band gap was calculated by Zhao, Li, and Alvarez-Ramirez [99, 95] using a Generalised Gradient Approximation (GGA) DFT-approach and employing the PBE [108] functional, well known to underestimate the BG values of semiconductors and insulators [108]. Their results lie in the 3.7-5.3 eV range. Guimaraes *et al.* [96] and Laurenco et al. [101] used a tight binding DFT (TB-DFT) method that usually overestimates the BG, obtaining a value of roughly 10 eV. Teobaldi *et al.* [98] used the PW91-GGA functional (that underestimates BGs [108]) and obtained a 4.1 eV value. Finally, Demichelis *et al.* [100] used the hybrid functional B3LYP, well known to overestimate BGs [108], and obtained a gap of 7.2 eV. The differences between the values obtained in these studies are mainly due to the use of different DFT functionals and basis sets used in the calculations. Regardless of these deviations, the true electrostatic band gap of imogolite Al-Si NTs is expected to be in between the underestimated GGA values and the overestimated B3LYP results [108].

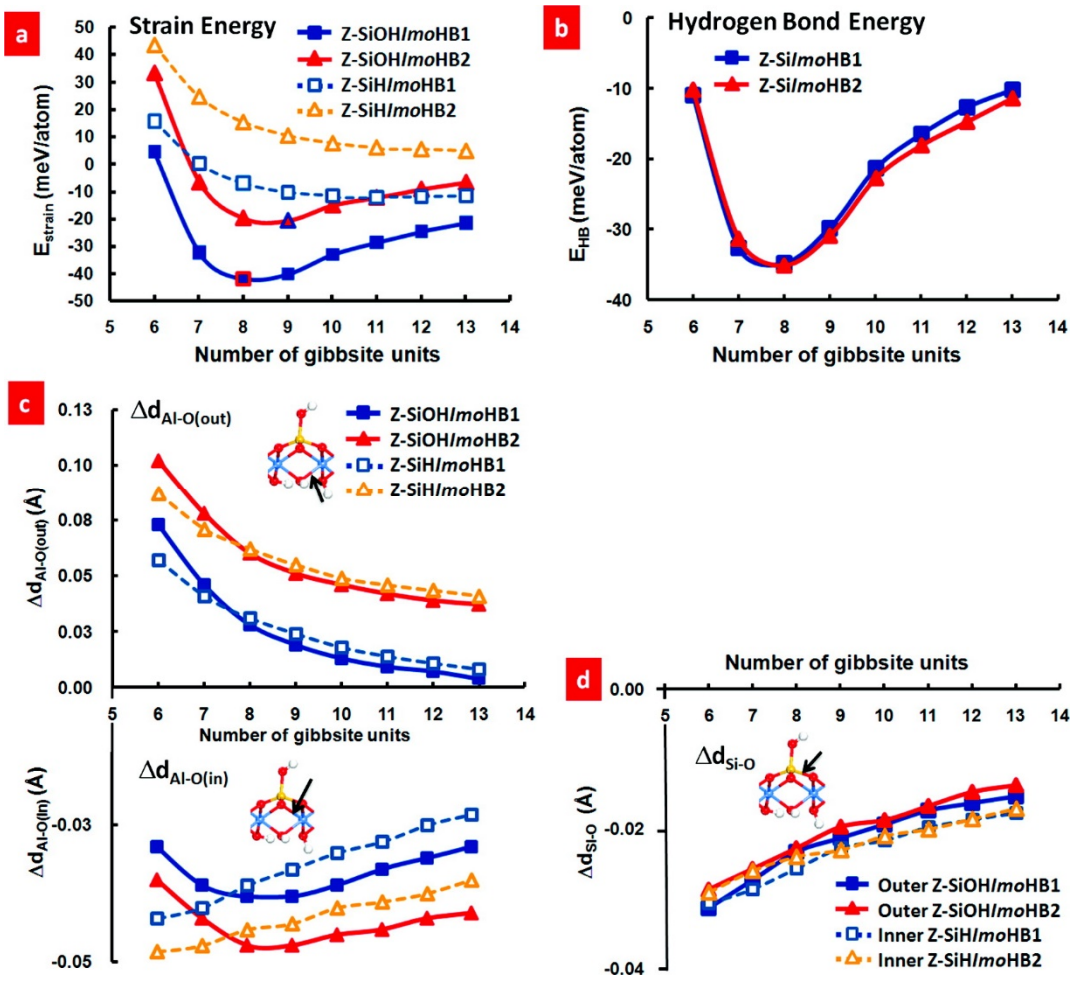

Figure 3.3. Calculated energies and structural parameters as a function of the number of gibbsite units(N) for zigzag imogolite nanotubes. (a) Strain energy, E_{strain}, and (b) inner HB energy, EHB, and the variations of outer and inner Al-O and Si-O bond distances compared to those of gibbsitelike imogolite sheet, (c) ΔdAl-O(out) and ΔdAl-O(in), and (d) ΔdSi-O. (from Ref. [107]).

As for the geometrical analysis, the study of the electronic properties of AlGe and DW AlGe NTs has received less attention. To the best of our knowledge, the only BG values reported in literature for these systems have been obtained at TB-DFT level and reported in Ref [101]. Both AlGe and DW AlGe NTs are computed to present BG-narrowing with respect to the AlSi case. Specifically, the calculated BGs for AlGe and DW AlGe were 9.6 eV and 8.5 eV, respectively. (AlSi BG at the same level of theory: ~10 eV) [96-101]).

A fascinating property of the Imo-NTs was unveiled by analysis of the real-space distribution of the VB and CB edges for AlSi NTs. It was found that while the top of the VB is localised

on the inner part of the tubes, the bottom of the CB is localised on the outer wall of the tube (Fig. 3.4). This result was independently confirmed by Zhao *et al.* [99].

Another notable peculiarity of Imo NTs is the polarization of the tube wall. Gustaffson first suggested [43] that the chemical reactivity of Imo-NTs depends on a delicate balance between local geometrical deformations associated with the tube bending and charges accumulation on the inner/outer surfaces. The polarization of the NT-wall calculated by Teobaldi [98], Guimaraes [96] and Gustaffson [104] are all in qualitative accord and suggest a dipole density across the wall consistent with positive (negative) charge accumulation at the outer (inner) surface of the tube (Fig 3.4).

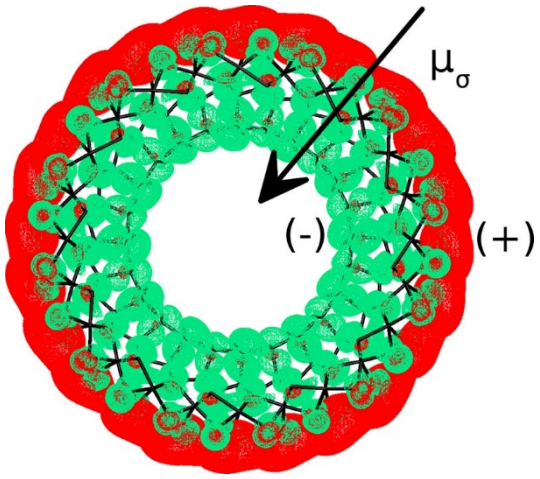

Figure 3.4. Front view of the real space separation between high-energy VB-edge (green) and low-energy CB-edge (red) in AlSi-NTs. The black arrow marks the direction of the permanent surface dipole density ($\boldsymbol{\mu_\sigma}$) of the NT-wall, with negative (positive) charge accumulation on the inner (outer) surface.

Given the real-space localisation of the VB and the CB edges, a photo-excitation is expected to produce a separated e*-h pair, with the electron (e*) situated on the outer wall of the tube (CB-edge) and the hole (h) facing the cavity (VB-edge). On this basis, it can be hypothesised that given the orientation of the wall-dipole opposite to the VB-CB recombination path, and in analogy with the effects in photo-ferroelectrics [36-42], the photo-generated e*-h recombination process will be slowed down, increasing the possibility of selective photo-reactions at the NTs surfaces (oxidation on the inside, reduction on the outside).

Very few computational studies focused on the investigation of non-pristine Imo-NTs. As important as conclusively determining the lowest energy structure for pristine Imo NTs, understanding the role of chemical functionalization [82-87], doping [94] and presence of defects [105] for the structural and electronic properties of Imo NTs is needed to fully develop the potential of the material for innovative chemical separation and photo-catalytic applications.

To this end, Teobaldi *et al.* analysed the electronic structure of hydroxyl (OH) vacancies in the tube [98]. It was found that the presence of OH-vacancies introduces both occupied and unoccupied states in the band-gap, resulting in a reduction of the BG from 3.9 to 1.1 eV for the Al-Ge NTs and from 4.1 to 1.8 eV for the Al-Si ones [98]. The reduction of the tube BG by introduction of defect states is an important result because of the ensuing possibility of having optical excitation by absorption of lower energy (longer wavelength) light than required by the defect free NTs. Thus, visible sunlight, instead of UV-light, could be used to photo-excite the defective NTs.

Alvarez-Ramirez explored the effect of Fe-doping on the Imo-NTs electronic properties [103]. The incorporation of the hetero-metal dopant (Fe) in the NTs was calculated to lead to the appearance of both occupied and unoccupied states in the pristine BG. The NT BG was calculated to reduce from 4.6 to 2.6 eV due to the appearance of highly-localised dopant-induced electronic states. These results suggest that, together with the introduction of defects, also doping of the NTs could be used to promote absorption of visible-light by the NTs and make them potentially significant for visible sunlight photo-catalysis.

Overall, this short recap underlines how DFT-based research in the field of Imo-NTs has so far been of limited support in exploring the appealing properties of this rapidly growing class of materials. The support of the computational community has been hindered by the severe accuracy-viability compromises, which need to be faced when modelling this class of systems on academically available hardware, even on Tier-1 High Performance Computing systems. With a periodic unit cell containing over 300 atoms for the smallest member of the Imo-NT family, the AlSi (N=24) NT with 336 atoms [98], the computational effort required for standard plane-wave or atomic basis-set simulation of these systems is, at the very least, challenging. Although reduction of the computational cost of the simulations can be obtained by using a minimal (fixed) atomic-basis set [95, 97, 99, 103], exploiting symmetry [100], or relying on the transferability of TB-DFT parameterizations for analogous systems [96, 101], best practice for accurate simulation of these systems in the presence of defects, dopants, termination effects, electronic excitations and solvation by media of non-negligible ionic-strength is far from being established.

The well-known limitations of standard local and semi-local exchange-correlation functionals in accurate simulation of BGs, electronic localization and polaronic distortions in metal-oxide materials [109, 110, 111] further increase the range of challenges and accuracy compromises to be faced for realistic modelling of Imo-NTs at standard DFT-level. However, such compromises can be ameliorated by realisation of the remarkable progress made in linear-scaling implementations of DFT (LS-DFT), which have made it possible to simulate systems up to several thousand atoms at DFT-level on academically available hardware [112].

On the basis of these consideration, a primary interest in the photo-catalytic capabilities of the NTs rather than in contributing to the debate about the Imo-NTs structure, and in the absence of atomically resolved X-ray scattering or Atomic Force Microscopy results on Imo NTs structure (to the best of our knowledge not available in the literature), our focus is the initial exploration of the relationships between Imo NTs composition, structure, polarization and bands alignment as well as the sensitivity of the results on the adopted DFT functional.

Accordingly, in the following Chapters we present an exploration using LS-DFT of the relationships between the composition of Imo NTs and their electronic and optical properties as well as their potential as model systems for the development of novel photo-catalytic strategies based on inorganic nanotubes.

References

[1] Hagfeldt A and Gratzel M Molecular photovoltaics 2000 *Acc. Chem. Res.* 33 269

[2] Hoffmann M R, Martin S T, Choi W Y, Bahnemann D W 1995 *Chem. Rev.* **95** 69

[3] Hagfeldt A and Grätzel M 1995 *Chem. Rev.* **95** 49

[4] Fox M A and Dulay M T 1993 *Chem. Rev.* **93** 341.

[5] Yang Y, Zhong H and Tian C X *Res.* 2011 *Chem. Intermediat.* **37** 91

[6] Rauf M A and Ashraf S S 2009 *Chem. Eng. J.* **151** 10

[7] Fujishima A, Zhang X T and Tryk D A 2008 *Surf. Sci. Rep.* **63** 515

[8] Chong M N, Jin B, Chow C W K and Saint C 2010 *Water Research* **44** 2997

[9] Ahmed S, Rasul M G, Martens W N, Brown R and Hashib M A 2010 *Desalination* **261** 3

[10] Maeda K and Domen K 2010 *J. Phys. Chem. Lett.* **1** 2655

[11] Kitano M and Hara M 2010 *J. Mater. Chem.* **20** 627

[12] Ji P F, Takeuchi M, Cuong T M, Zhang J L, Matsuoka M and Anpo M 2010 *Res. Chem. Intermediat.* **36** 327

[13] Hernandez-Alonso M D, Fresno F, Suarez S and Coronado J M 2009 *Energ. Environ. Sci.* **2** 1231

[14] Morris A J, Meyer G J and Fujita E 2009 *Accounts Chem. Res.* **42** 1983

[15] Sastre F, Fornes V, Corma A, and García H Selective 2011 *J. Am. Chem. Soc.* **133** 17257

[16] Ciamician G The Photochemistry of the Future 1912 *Science* **36** 385

[17] Tong H, Ouyang S, Bi Y, Umezawa N, Oshikiri M, and Ye J 2012 *Adv. Mater.* **24** 229

[18] Djurišić A B, Leunga Y H and Ng A M C 2014 *Mater. Horiz.* **1** 400

[19] Weng B, Liu S, Tang Z-R and Xu Y-J 2014 *RSC Adv.* **4** 12685

[20] Jung H S, Hong Y J, Li Y, Cho J, Kim Y J and Yi G C 2008 *ACS Nano* **2** 637

[21] Jang J S, Joshi U A and Lee J S 2007 *J. Phys. Chem. C* **111** 13280

[22] Kenanakis G and Katsarakis N 2010 *Appl. Catal. A-Gen.* **378** 227

[23] Wu N Q, Wang J, Tafen D, Wang H, Zheng J G, Lewis J P, Liu X G, Leonard S S and Manivannan A 2010 *J. Am. Chem. Soc.* **132** 6679

[24] Liu Q, Zhou Y, Kou J H, Chen X Y, Tian Z P, Gao J, Yan S C and Zou Z G 2010 *J. Am. Chem. Soc.* **132** 14385

[25] Huang J, Ding K, Hou Y, Wang X and Fu X 2008 *ChemSusChem* **1** 1011

[26] Bi Y P and Ye J H 2009 *Chem. Commun.* 6551

[27] Wang L, Wei H W, Fan Y J, Liu X Z and Zhan J H 2009 *Nanoscale Res. Lett.* **4** 558

[28] Shahid M, Shakir I, Yang S J and Kang D J 2010 *Mater. Chem. Phys.* **124** 619

[29] Berr M, Vaneski A, Susha A S, Rodríguez-Fernández J, Döblinger M, Jäckel F, Rogach A L and Feldmann J 2010 *Appl. Phys. Lett.* **97** 093108

[30] Vaneski A, Susha A S, Rodriguez-Fernandez J, Berr M, Jäckel F, Feldmann J and Rogach A L 2011 *Adv. Funct. Mater.* **21** 1547

[31] Berr M J, Wagner P, Fischbach S, Vaneski A, Schneider J, Susha A S, Rogach A L, Jäckel F and Feldmann J 2012 *Appl. Phys. Lett.* **100** 223903.

[32] Berr M J, Vaneski A, Mauser C, Fischbach S, Susha A S, Rogach A L, Jäckel F and Feldmann J 2012 *Small* **8** 291

[33] Berr M, Schweinberger F, Döblinger M, Sanwald K, Wolff C, Breimeier J, Crampton A, Ridge C, Tschurl M, Heiz U, Jäckel F and Feldmann J 2012 *Nano Lett.* **12** 5903

[34] Schweinberger F F, Berr M J, Döblinger M, Wolff C, Sanwald K E, Crampton A S, Ridge C J, Jäckel F, Feldmann J, Tschurl M and Heiz U 2013 *J. Am. Chem. Soc.* **135** 2013 13262

[35] Simon T, Bouchonville N, Berr M J, Vaneski A, Adrović A, Volbers D, Wyrwich R, Döblinger M, Susha A S, Rogach A L, Jäckel F, Stolarczyk J K and Feldmann J 2014 *Nat. Mater.* **13** 1013

[36] Choi T, Lee S, Choi Y J, Kiryukhin V and Cheong S-W 2009 *Science* **3** 63

[37] Grinberg I, West D V, Torres M, Gou1 G, Stein D M, Wu L, Chen G, Gallo E M, Akbashev A R, Davies P K, Spanier J E and Rappe A M 2013 *Nature* **503** 509

[38] Li H, Sang Y, Chang S, Huang X, Zhang Y, Yang R, Jiang H, Liu H, and Wang Z L 2015 *Nano Lett.* **15** 2372

[39] Su R, Shen Y, Li L, Zhang D, Yang G, Gao C, and Yang Y 2015 *Small* **11** 202

[40] Cui Y, Briscoe J, and Dunn S 2013 *Chem. Mater.* **25** 4215

[41] Kirchartz T, Bisquert J, Mora-Seroc I and Garcia-Belmonte G 2015 *Phys. Chem. Chem. Phys.* **17** 4007

[42] Chen Y, Zhao H, Liu B and Yang H 2015 *Applied Catalysis B: Environmental* **163** 189

[43] Venkateswarlu Bhavanasi, Damar Yoga Kusuma and Pooi See Lee 2014 *Adv. Energy Mater*. **4** 1400723

[44] Jeon C H, Lee Y S, Yee K J, Han J K and Bu S.D 2015 *Curr. Appl. Phys.* **15** 115

[45] Liew W H, Mirshekarloo M S, Chen S, Yao K and Tay F E H 2015 *Sci. Rep.* **5** 9790

[46] Liu M and Wang J 2015 *Sci. Rep.* **5** 7728

[47] Li H F, Zhang G H, Zheng, Y, Wang B and Chen W J 2014 *Acta Mater.* **76** 472

[48] Wang J, Xu T, Shimada T, Wang X and Zhang T Y 2014 *Phys. Rev. B.* **89** 144102

[49] Yoo H, Bae C, Kim M, Hong S, No K, Kim Y, and Shin H 2013 *Appl. Phys. Lett.* **103** 022902

[50] Zhao Y, Miao J, Meng X B, Weng F, Xu X G, Jiang Y, and Wang S G 2013 *J. Mater. Sci.* **24** 1439

[51] Evarestov, R A, Bandura, A V and Kuruch, D D 2013 *J. Comput. Chem.* **34** 175

[52] Han J K, Choi Y C, Kwak J H and Bu S D 2013 *Ferroelectrics* **454** 29

[53] Nuraje N and Su K 2013 *Nanoscale* **5** 8752

[54] Shimada T, Wang X, Kondo Y and Kitamura T 2012 *Phys. Rev. Lett.* **108** 067601

[55] Alexe M and Hesse D 2012 *Ferroelectrics* **433** 53

[56] Rorvik P M, Grande T and Einarsrud M A 2011 *Adv. Mater.* **23** 4007

[57] Wang C D, Lu Z Z, Yuan W X, Kwok S Y and Teng B H 2011 *Phys. Lett. A* **375** 3405

[58] Luo Y, Szafraniak I, Zakharov N D, Nagarajan V, Steinhart M, Wehrspohn R B, Wendorff J H, Ramesh R and Alexe M 2003 *Appl. Phys. Lett.* **83** 440

[59] Sastre F, Fornés V, Corma A and García H 2012 *Chemistry - A European Journal* **18** 1820

[60] Sastre F, Corma A and García H, 2012 *J. Am. Chem. Soc.* **134** 14137.

[61] Sastre F, Corma A and García H 2012 *Appl. Catal. B: Environ.* **128** 84

[62] Dietl N, Schlangen M, and Schwarz H 2012 *Angewandte Chemie International Edition* **51** 23

[63] Fresno F, Portela R, Suárez S and M. Coronado J 2014 *J. Mater. Chem. A* **2** 2863

[64] Baltrusaitis J, Jansen I and Schuttlefield Christus J D 2014 *Catalysis Science & Technology* **4** 2397

[65] Wada S I, Eto A and Wada K 1979 *J. Soil Sci.* **30** 347

[66] Barron P F, Wilson M A, Campbell A S and Frost R L 1982 *Nature* **299** 616

[67] Mukherjee S, Bartlow V M and Nair S 2005 *Chem. Mater.* **17** 4900

[68] Kang D Y, Zang J, Wright E R, McCanna A L, Jones C W and Nair S 2010 *ACS Nano* **4** 4897

[69] Theng B K G, Russell M, Churchman G J and Parfitt R L 1982 *Clays Clay Miner.* **30** 143

[70] Mukherjee S, Kim K and Nair S 2007 *J. Am. Chem. Soc.* **129** 6820

[71] Yucelen G I, Choudhury R P, Vyalikh A, Scheler U, Beckham H W and Nair S 2011 *J. Am. Chem. Soc.*, **133** 5397

[72] Yucelen G I, Kang D Y, Guerrero-Ferreira R C, Wright E R, Beckham H W and Nair S 2012 *Nano. Lett.* **12** 827

[73] Cradwick P D, Wada K, Russell J D, Yoshinaga N, Masson C R and Farmer V C 1972 *Nature Phys. Sci.* **240** 187

[74] Bursill L A, Peng J L and Bourgeois L N 2000 *Phil. Mag. A* **80** 105

[75] Levard C, Rose J, Masion A, Doelsch E, Borschneck D, Olivi L, Dominici C, Grauby O, Woicik J C and Bottero J-Y 2008 *J. Am. Chem. Soc.* **130** 5862

[76] Konduri S, Mukherjee S and Nair S 2006 *Phys. Rev. B* **74** 033401

[77] Levard C, Rose J, Thill A, Masion A, Doelsch E, Maillet P, Spalla O, Olivi L, Cognigni A, Ziarelli F and Bottero J Y 2010 *Chem. Mater.* **22** 2466

[78] Maillet P, Levard C, Larquet E, Mariet C, Spalla O, Menguy N, Masion A, Doelsch E, Rose J and Thill A. 2010 *J. Am. Chem. Soc.* **132** 1208

[79] Maillet P, Levard C, Spalla O, Masion A, Rose J and Thill A 2011 *Phys. Chem. Chem. Phys.* **13** 2682

[80] Thill A, Maillet P, Guiose B, Spalla O, Belloni L, Chaurand P, Auffan M, Olivi L, and Rose J. 2012 *J. Am. Chem. Soc.* **134** 3780

[81] Amara M-S, Paineau E, Bacia-Verloop M, Krapf M-E M, Davidson P, Belloni L, Levard C, Rose J, Launois P and Thill A 2013 *Chem. Comm.* **49** 11284

[82] Kang D Y, Zang J, Jones C W, Nair S 2011 *J. Phys. Chem. C.*, **115** 7676

[83] Zanzottera C, Armandi M, Esposito S, Gorrone E and Bonelli B 2012 *J. Phys. Chem. C.* **116** 20417

[84] Zanzottera C, Vicente A, Celasco E, Fernandez C, Garrone E and Bonelli B 2012 *J. Phys. Chem. C.*, **116** 7499

[85] Bonelli B, Armandi M, and Garrone E 2013 *Phys. Chem. Chem. Phys.* **15** 13381

[86] Bottero I, Bonelli B, Ashbrook S E, Wright, P A, Zhou W, Tagliabue M, Armandi M and Garrone E 2011 *Phys. Chem. Chem. Phys.* **13** 744

[87] Kang D Y, Brunelli N A,. Yucelen G I, Venkatasubramanian A, Zang J, Leisen J, Hesketh P J, Jones C W and Nair S 2014 *Nature Comm.* **5** 3342

[88] Amara M S, Paineau E, Rouzière S, Guiose B, Krapf M-E M, Taché O, Launois P, and Thill A 2015 *Chem. Mater*. **27** 1488

[89] Katsumata K, Hou X, Sakai M, Nakajima A, Fujishima A, Matsushita N, MacKenzie K J D and Okada K 2013 *Appl. Catal B-Environ.* **138** 243

[90] Marzan L L and Philipse A P 1994 *Colloid Surface A* **90** 95

[91] Ma W, Yah W O, Otsuka H and Takahara A 2012 *J. Mater. Chem.* **22** 11887

[92] M. Ookawa, in Clay Minerals in Nature – Their Characterization, Modification and Application, ed. M. Valaskova, InTech, 2012, p. 2708.

[93] Arancibia-Miranda N, Escudey M, Pizarro C, Denardin J C, García-González M T, Fabris J D and Charlet L 2014 *Mater. Res. Bull.* **51** 145

[94] Avellan A, Levard C, Kumar N, Rose J, Olivi L, Thill A, Chaurand P, Borschneck D and Masion A 2014 *RSC Adv.* **4** 49827

[95] Alvarez-Ramírez F 2007 *Phys. Rev. B.* **76** 125421

[96] Guimarães L, Enyashin A N, Frenzel J, Heine T, Duarte H A and Seifert G 2007 *ACS Nano* **1** 362

[97] Li L, Xia Y, Zhao M, Song C, Li J and Liu X 2008 *Nanotechnology* **19** 175702

[98] Teobaldi G, Beglitis N S, Fisher A J, Zerbetto F and Hofer W A 2009 *J. Phys. Condens. Matter*. **21** 195301

[99] Zhao M, Xia Y and Mei L 2009 *J. Phys. Chem. C.* **113** 14834

[100] Demichelis R, Noël Y, D'Arco P, Maschio L, Orlando R and Dovesi R 2010 *J. Mater. Chem.* **20** 10417

[101] Lourenço M P, Guimarães L, da Silva M C, de Oliveira C, Heine T, and Duarte H A 2014 *J. Phys. Chem. C* **118** 5945

[102] Guimarães L, Pinto Y N, Lourenço M P and Duarte H A 2013 *Phys. Chem. Chem. Phys.* **15** 4303

[103] Alvarez-Ramírez F 2009 *J. Chem. Theory Comput.* **5** 3224

[104] Gustafsson J P 2001 *Clays Clay Miner.* **49** 73

[105] Yucelen G I, Choudhury R P, Leisen J, Nair S and Beckham H W 2012 *J. Phys. Chem. C.* **116** 17149

[106] Poli E, Elliott J D, Hine N D M, Mostofi A A and Teobaldi G 2015 *Mater. Res. Innov.* **19** S272.

[107] Lee U. S, Chol Y. C., Youm G. S, Shom D. 2011 *J.Phys. Chem. C.* **115** 5226

[108] J. Perdew, M. Levy, 1983 *Phys. Rev. Letter.* **51** 1884

[109] Pacchioni G, Frigoli F, Ricci D and Weil J A 2000 *Phys. Rev. B.* **63** 054102.

[110] Stoneham A M, Gavartin J, Shluger A L, Kimmel1 A V, Muñoz Ramo1 D, Rønnow H M, Aeppli G, and Renner C 2007 *J. Phys.: Condens. Matter Vol.* **19** 255208

[111] Lany S and Zunger A 2009 *Phys. Rev. B.* **80** 085202

[112] Bowler D.R., Miyazaki T. 2012 *Rep. Prog. Phys.*, **75** (3) 036503-036547

Chapter 4

Large scale Density Functional Theory simulation of inorganic nanotubes: a case study on Imogolite nanotubes

Abstract

Investigation of the electronic and spectroscopic properties for Imogolite naotubes (Imo-NTs) has so far been hampered by the large size of the systems repeat unit (+300 atoms). The large unit cells pose severe challenges and accuracy-viability compromises for standard plane-wave (fixed atomic basis-set) Density Functional Theory (DFT) simulations on academically available hardware. These challenges can however be met by linear-scaling DFT approaches based on *in situ* optimisation of minimal basis-sets. In this Chapter, we report on the applicability of linear-scaling DFT to Imo-NTs by illustrating the structural and electronic characterization of periodic and finite models of aluminosilicate (AlSi) and methylated-aluminosilicate (AlSi-Me) Imo-NTs. We discuss the dependence of the results on key parameters of the simulation set-up as well as the size of the simulated systems. These results should be useful for future linear-scaling DFT investigation of Imo-NTs and other aluminosilicate-based functional materials.

4.1 Introduction

Density Functional Theory (DFT) modelling and derived Tight-Binding approximations (TB-DFT) have assisted research in the growth mechanisms of AlSi NTs [1,2], been used to elucidate the properties of periodic defect-free AlSi and AlGe NTs models [3-8], and to investigate possible phosphorous- and arsenic-based functionalization [9], nonetheless the recent experimental progress in the field of Imo-NTs has yet to be matched by the materials modelling community. With the exception of three DFT contributions focused on point-defects and Fe-doping in AlSi and AlGe NTs [5,6,10], the structural and electronic characterization of defects, dopant and termination effects in Imo-NTs and their role in tuning the NT electronic and spectroscopic properties as well as its chemical reactivity is to date unexplored. In

addition, AlSi NTs walls are experimentally known to develop an intrinsic polarization [11], with accumulation of negative (positive) charges on the interior (exterior) of the NT-cavity (Fig.4.2). Recent DFT simulations have shown this polarization to be linked with a separation in real space of the edges of the NT Valence (VB) and Conduction Bands (CB) [6,7] and to be independent of the substitution of Si–OH by Ge–OH in the tube interior [6]. The extent to which these peculiar AlSi and AlGe NTs properties are affected by functionalization of the tube walls [12-17], the encapsulation of NTs of different radii in double-walled AlGe NTs [18-20], cation-vacancy induced defects [21] or by the ionic strength of the solvent is currently unknown, which motivates our interest in this class of materials.

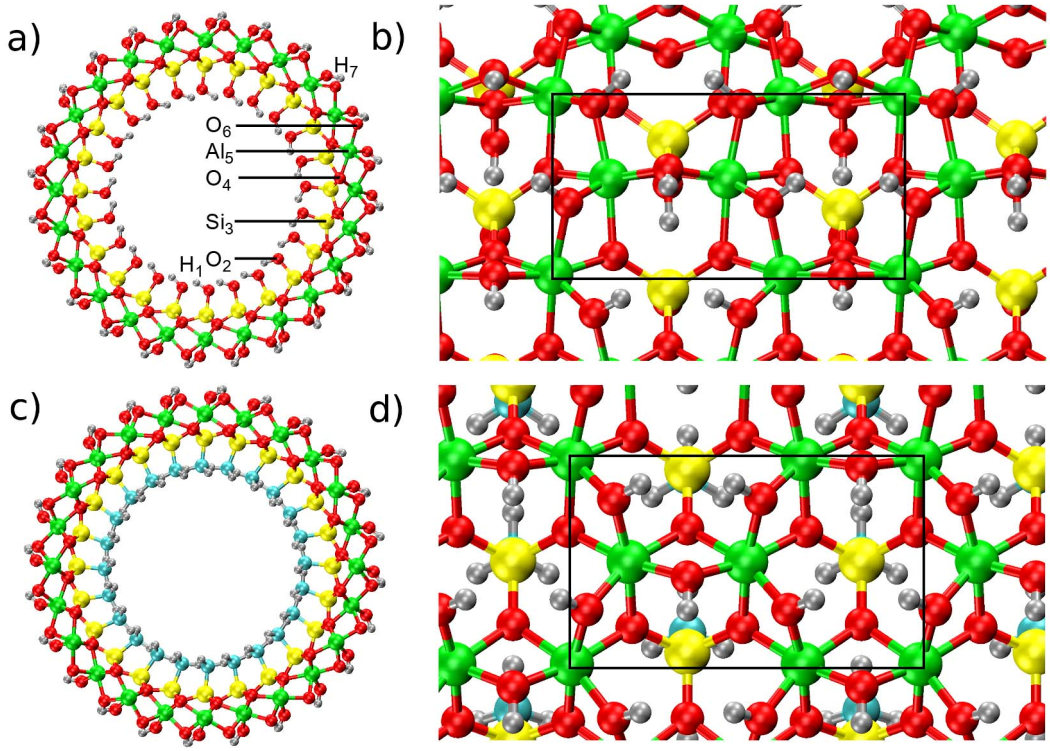

Figure 4.1. a) Front view of the AlSi NT (N=24) structure with the adopted, layer-resolved, radial atomic labelling. b) The AlSi wall structural motif together with the zig-zag periodic unit (black line) along the nanotube axis as seen from outside the NT-cavity. c) Front-view of the AlSiMe NT (N=24) with substitution of the inner hydroxyls (–OH) by methyl groups ($–CH_3$). The AlSiMe NT wall structure is displayed in d). Al: green, Si: yellow, O: red, H: silver, C: cyan.

DFT-based research in the field of Imo-NTs has so far been hindered by the severe accuracy-viability compromises, which need to be faced when modelling this class of systems on

academically available hardware. With a periodic unit cell containing over 300 atoms for the smallest system of the Imo-NT family, the AlSi (N = 24) NT: 336 atoms [22], the computational efforts required for standard plane-wave or atomic basis-set simulation of these systems are, at the very least, challenging. As a result, DFT investigations of Imo-NTs have been limited to periodically repeated models of no more than one periodic ring [3-9] or fractions of the Imo-NTs [1,2]. Although reduction of the computational cost of the simulations can be obtained by using minimal (fixed) atomic-basis set [3,5,7,10], exploiting the system symmetry [8], or resting on the transferability of TB-DFT parameterizations for analogous systems [5,9], best practice for accurate simulation of these systems in the presence of defects, dopants, termination effects, electronic excitations and solvation by media of non-negligible ionic-strength is far from being established.

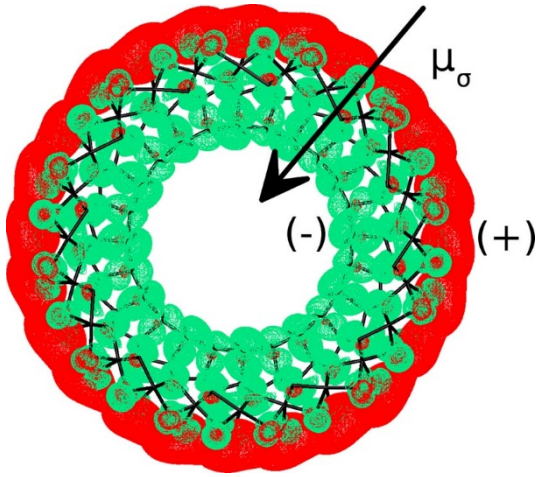

Figure 4.2. Front view of the real space separation between high-energy VB-edge (green) and low-energy CB-edge (red) in AlSi-NTs. The black arrow marks the direction of the permanent surface dipole density ($\boldsymbol{\mu}_\sigma$) of the NT-wall with negative (positive) charge accumulation on the inner (outer) surface.

The well-known limitations of standard local and semi-local exchange-correlation functionals in accurate simulation of band gaps, electronic localization and polaronic distortions in metal-oxide materials [23-25] further increase the range of challenges and accuracy-viability compromises to be faced for realistic modelling of Imo-NTs at standard DFT-level. Such compromises can however be ameliorated by realization of the remarkable progress made in linear-scaling implementations of DFT (LS-DFT), which have made it possible to simulate systems up to several thousand atoms at DFT-level on academically available hardware [26].

Extensive work in the development of LS-DFT implementations has produced several codes capable of LS-DFT simulation, such as for instance ONETEP [27-30], CONQUEST [31,32], SIESTA [33], OPENMX [34], and highly efficient modelling of large-scale systems as possible with BIGDFT [35], FHI-AIMS [36], and CP2K [37]. In spite of their proved maturity and applicability, these advances have not yet benefited research in Imo-NTs and other inorganic nanotubes. With the aim of introducing LS-DFT in the field of Imo-NTs, in this Chapter we illustrate the applicability of LS-DFT as implemented in the ONETEP program [27-30] to this class of materials, detailing the existing accuracy-viability compromises, and introducing practices to maximize the efficiency of the simulations without affecting their accuracy. We believe our results should be useful for future LS-DFT investigation of Imo-NTs and other nanostructured aluminosilicate (germanate) functional materials, such as zeolites or inorganic glasses.

The Chapter is organized as follows: after a brief introduction to the computational procedures used we present and discuss results on the convergence of the Imo-NTs simulation with respect to key computational parameters such as the kinetic energy cutoff, the localization radius of the basis set, and the convergence threshold for geometry optimisation. We then examine the procedure for optimisation of the Imo-NTs CB towards computation of converged band-gaps. Finally, we establish the size of the smallest possible model capable of capturing relaxation of the Imo-NTs ends in the presence of a core bulk-like region.

4.2 Methods

All the simulations where performed with the PBE functional [38] and separable (Kleinman-Bylander) norm-conserving pseudopotentials [39], constructed with the opium code [40]. Unless specified otherwise, the adopted kinetic energy cutoff was 1,000 eV and 4 (9) valence or conduction NGWFs were used for O (Al,Si) atoms. 1 NGWF was used for H atoms. In all cases, no truncation of the density kernel ($K^{\alpha\beta}$) was enforced. Based on the reported convergence tests (below), the localization radius for all the NGWFs was 8 Bohr, unless stated otherwise. All simulations were performed with periodic boundary conditions ensuring at least 15 Å vacuum separation between replicated images along the non-periodic directions.

Geometry-relaxations where executed via the quasi-Newton optimisation scheme based on the Broyden-Fletcher-Goldfarb-Shanno (BFGS) algorithm [41]. In all cases, Pulay corrections due to residual optimisation of the valence NGWFs [42] were included in the geometry optimisation.

All the simulations made use of the hybrid MPI-OpenMP parallelism recently implemented in the ONETEP program [43].

4.3 Results and Discussion

4.3.1 Convergence with respect to kinetic energy cutoff and NGWFs localization radius

The numerical precision of the ONETEP approach in solving the KS problem depend on the number and localization radius ($\mathbf{r}_c$) of the NGWFs used to represent $\rho(\mathbf{r},\mathbf{r'})$:

$$\rho(\mathbf{r},\mathbf{r}') = \sum_{\alpha\beta} \varphi_\alpha(\mathbf{r}) K^{\alpha\beta} \varphi^*_\beta(\mathbf{r}') \quad (4.1)$$

where $K^{\alpha\beta}$ is the density kernel. $K^{\alpha\beta}$ has elements which are nonzero only if $|\mathbf{r}-\mathbf{r}'| < \mathbf{r}_c$, where $\mathbf{r}$ and $\mathbf{r}'$ indicate the coordinates of the centers of the NGWFs φ_α and φ_β, and $\mathbf{r}_c$ is a real-space cut-off length. Calculation precision also depends on the kinetic energy cutoff, which is used to set up the real-space grid for the psinc expansion of the NGWFs [44,45,46]:

$$\varphi_{\alpha\mathbf{R}}(\mathbf{r}) = \sum_{K=0}^{N_1-1} \sum_{L=0}^{N_2-1} \sum_{M=0}^{N_3-1} C_{KLM,\alpha} D_{KLM}(\mathbf{r}) \quad (4.2)$$

with $C_{KLM,\alpha}$ being the expansion coefficients and $D_{KLM}(\mathbf{r})$ the psinc functions. To fine-tune the balance between simulation accuracy and costs, it is thus necessary to study the convergence of the DFT-energy with respect to these computational parameters. This is especially important when modelling a material with ONETEP for the first time, as in the case of the Imo-NTs considered here.

Our tests were performed on the basis of two models. The first one was a reduced 1D-periodic model system of $Al_{12}Si_6O_{52}H_{44}$ stoichiometry, extracted from the plane-wave DFT optimised AlSi structure in [6], and kept fixed to preserve the pristine curvature of the NT structure (Fig.4.3). Peripheral hydroxyls were replaced by H_2O molecules to maintain the overall electro-neutrality of the system. The second model was the periodic AlSiMe (N = 24) NT displayed in Fig.4.1.

Starting with the NT-fragment, use of a 1,000 eV kinetic energy cutoff and of 8 Bohr (a_0) localization radius ($\mathbf{r}_c$) for the NGWFs yields a final DFT-energy converged to within 1 meV/atom with respect to the results for a 1,400 eV cutoff (Table 4.1). Although tighter levels of convergence are achievable, they are obtained at the cost of increased computation time so that on balance 1,000 eV cutoff emerges as a reasonable compromise.

A similar convergence rate is found for the DFT-energy for $\mathbf{r}_c$ in the 8-10 a_0 range. Owing to the use of 4 (9) NGWFs on each of O (Al,Si) atom in the system, increase of $\mathbf{r}_c$ impacts on

the simulation time more heavily than the kinetic energy cutoff due to the larger number of psinc grid-points included in the NGWF localization region (Eq.4.2), and the ensuing increase in the number of steps required to optimize the coefficients of the NGWFs. Based on these results, use of 8 Bohr NGWFs localization radius ($\mathbf{r_c}$) and a kinetic energy cutoff of 1,000 eV appear to provide the optimal tradeoff between precision of the DFT-solution and computation time. On a more specialist note, timings were measured for simulations run with 12 MPI processes and 2 OpenMP threads per MPI-process on two 2.7 GHz, 12-core E5-2697-v2 (Ivy Bridge) series processors (no hyper-threading), and different performances may be obtained by further, hardware-dependent, fine-tuning of the MPI-OpenMP parallelism [94] on other HPC systems.

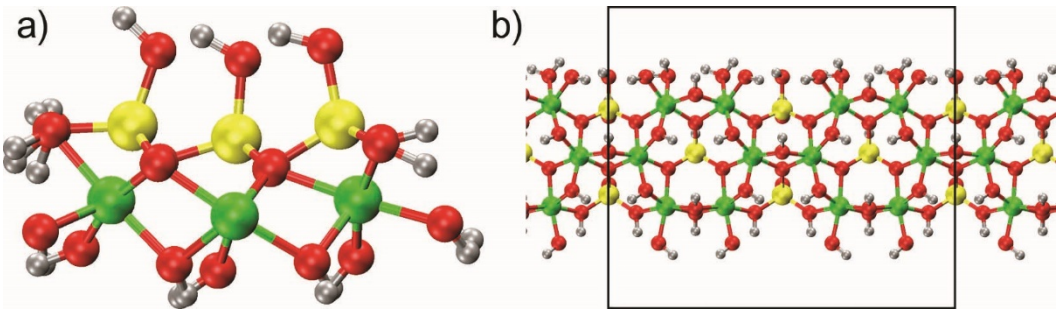

Figure 4.3. Front (a) and top (b) view of the 1D-periodic $Al_{12}Si_6O_{52}H_{44}$ AlSi-NT warped fragment used for the NGWFs-convergence tests. The black rectangle in b) indicates the periodic unit cell. Same atom-colour labelling as in Fig.4.1.

We also considered the dependence of the computed DFT-energy on the kinetic energy cutoff for a whole-NT model. Fig.4.4 shows the convergence of the DFT-energy with respect to the kinetic energy cutoff for the AlSiMe NT with 24 Al-atoms in the tube circumference (Fig.4.1) and $\mathbf{r_c}$ = 8 a_0. Also in this case, comparison between the results for 1,000, 1,300 and 1,500 eV cut-off indicates an acceptable level of convergence (~2 meV/atom) for 1,000 eV. Noticeably tighter convergence (less than 0.5 meV/atom) can be attained for moderate increase of the kinetic energy cutoff over 1,200 eV, which however leads to increase of the computation time. On the basis of these results, we adopted a kinetic energy cutoff of 1,000 eV and $\mathbf{r_c}$ = 8 a_0 for the following benchmarks.

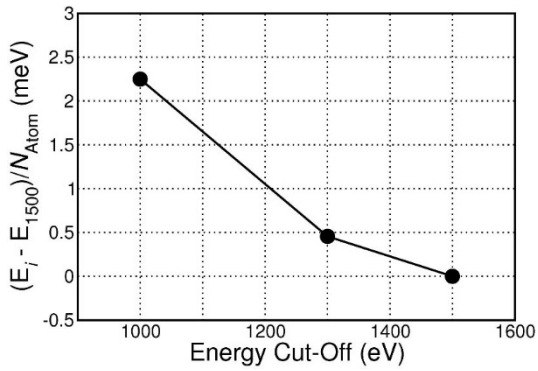

Figure 4.4. The convergence of the AlSiMe NT (N = 24) DFT-energy with respect to the adopted kinetic energy cutoff.

Cutoff (eV); r_c (a_0)	**ΔE (meV/atom)**	**N_{it}**	**Δt**
800; 8	26.16	19	-50%
1,000; 8	1.09	18	-26%
1,200; 8	0.72	17	-17%
1,400; 8	0.	15	0.
1,000; 8	0.91	19	-69%
1,000; 9	0.03	20	-58%
1,000; 10	0.	32	0

Table 4.1. The convergence of the DFT energy for the 1D-periodic $Al_{12}Si_6O_{52}H_{44}$ fragment as a function of the kinetic energy cutoff (eV) and the NGWFs-localization radius ($\mathbf{r_c}$, a_0). ΔE is the relative energy (meV/atom) with respect the adopted energy reference (ΔE = 0). N_{it} refers to the number of NGWFs-optimisation required to converge the DFT-solution to less than 10^{-4} eV/atom. Δt is the percent computational speed-up with respect to the adopted reference.

4.3.2 Optimisation of the NT periodic unit

We now illustrate the procedure for optimisation of the NT repeat unit length with ONETEP, focusing on the AlSiMe NT (N=24) displayed in Fig.4.1. Based on earlier plane-wave DFT reports regarding weak dependence of this parameter on the reciprocal-space sampling in the simulations, with optimal convergence obtained for 2 k-points along the NT periodic direction [3], in our tests we adopted an equivalent set up based on a x2 supercell of the AlSiMe NT along the tube axis. The localization radius of the NGWFs was set to 8 a_0, on the basis of the good convergence of the DFT-energy tested in Table 4.1.

In order to maintain the translational invariance of the system with respect to the discretized psinc grid (avoiding the emergence of the "egg-box" effect [47,48]), and following [49], the unit cell length along the tube axis (c, Fig.4.1) was expanded and contracted in multiple of the psinc-spacing. In each case, all the atomic positions were optimised to within a 0.05 eV/Å convergence threshold.

The energy for the optimised geometries are plotted in Fig.4.5 as a function of c. Quadratic fitting of the calculated values suggests an energy minimum for c = 8.64 ± 0.01 Å, which is very close to the optimised c-value for the N = 24 AlSi-NT (8.68 ± 0.01 Å) [6], suggesting a predominant role of the aluminium-hydroxide backbone, rather than the inter-silanol hydrogen bonding network or methyl pending groups, in controlling the optimised length of the tube, at least at PBE level. In line with experimental results [14], optimisation of the c-parameter and atomic position for AlSiMe NTs of different diameter (N) reveals the occurrence of a shallow energy minimum for diameters larger ($28 < N < 32$, depending on the adopted functional and ensuing treatment of dispersion interactions) than for the AlSi NT (N = 24). These results will be reported elsewhere [50].

Finally, on a more technical note, we report that in out tests the energy of the 0.1 eV/Å optimised systems were found to be converged within less than 10^{-5} eV/atom with respect to the results of the 0.05 eV/Å optimisation, suggesting an 0.1 eV/Å optimisation threshold as viable for Imo-NTs.

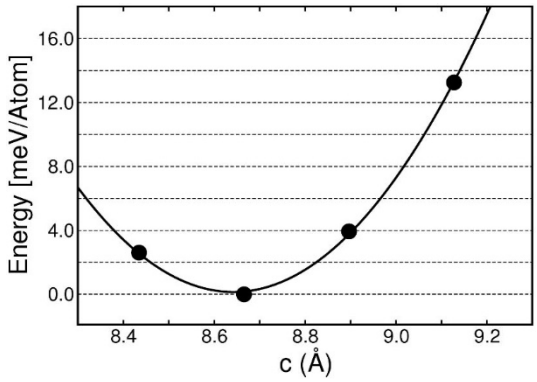

Figure 4.5. The energy of the optimised AlSiMe NT (N=24) as a function of the tube repeat unit length, c. The continuous line shows the results of a quadratic fitting to the DFT energies (points).

4.3.3 Optimisation of the NT Conduction Band and band gap

The optimisation of empty KS states in ONETEP is achieved via dedicated post-processing of the optimised (valence) density matrix and KS energy (as reported in Chapter 2.3.8). The user has control over the number of empty KS states to be optimised as well as the number and localization radius of the conduction-NGWFs (χ_α) used to represent them, with fewer states and (more compact) NGWFs requiring less computational resources at the potential cost of accuracy [50]. Here, we present results on the convergence of the AlSiMe (N = 24, Fig.4.1) band gap with respect to the number of empty KS optimised for an x1 supercell at the minimum-energy c-value (Fig.4.5).

We tested the convergence of the band gap computed on the joint φ_α and χ_α representation (see Chapter 2.3.8) following optimisation of 10, 20, 30 and 40 empty KS states. The results are displayed in Fig.4.6. The low-energy edge of the Conduction Band (CB) obtained with 30 optimised KS is found to deviate by less than 9 meV with respect to the results for 40 optimised empty KS states. Optimisation of 20 (10) empty KS leads to a poorer convergence of 18 eV (32 meV) for the computed CB-edge. The converged band gap for the AlSiMe NT, calculated as energy difference between the low-energy CB-edge and high-energy VB-edge with 40 optimised conduction KS states is 4.75 eV, 0.18 eV wider than for the pristine AlSi NTs (N = 24) at the same level of theory. Thus, the methylation of AlSi NTs leads to an increase of the NT band-gap with respect to the hydroxylated case. Electrostatic alignment between AlSi and AlSiMe NTs reveals a negative shift of -0.34 eV (-0.16 eV) for the AlSiMe NT VB (CB) with respect to the AlSi results, suggesting methylation of Imo-NTs as an effective strategy towards engineering of band-gaps and band-alignments for these materials [51].

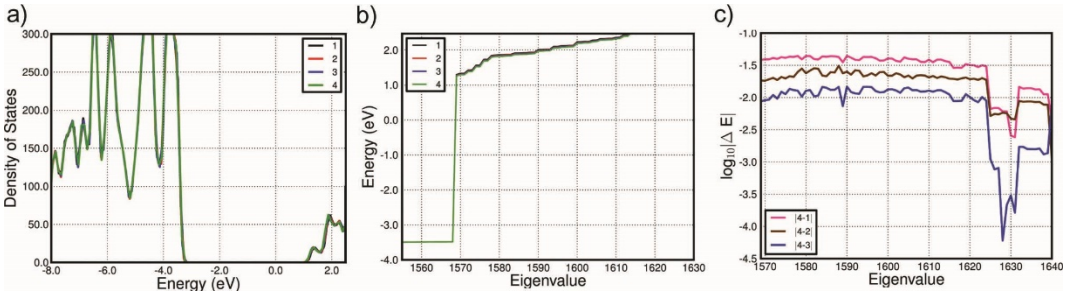

Figure 4.6. The calculated Density of States for the AlSiMe NT (N = 24, Fig.4.1) following optimisation of different numbers of conduction-KS (a). 1-4 labels indicate the results for 10 (1), 20 (2), 30 (3), 40 (4) optimised conduction-KS. The energy of each KS eigenvalue is reported in (b). Panel (c) displays, on a logarithmic scale, the eigenvalue energy differences between datasets 1-3 and 4.

4.3.4 NT-end relaxation and its dependence on the size of the model

With the exception of the (non-atomically resolved) Transmission Electron Microscopy images for AlSi and AlGe NT thin-films reported in [52], very little is currently known on the structure of the tube open-ended extremities. As a result, the available insight into termination-induced effects on the NTs electronic properties and chemical reactivity or into the possible segregation of point-defects [21] at the tube extremities is effectively non-existent.

Although the atomic structure and electronic properties of Imo-NT extremities could in principle be elucidated via DFT modelling, the size of the models to realistically capture the tube extremities in vacuo or, even more challenging, in solvent-phase, has so far prevented any advance along these lines. However, as we demonstrate below, DFT-modelling of the tube-terminations can be viably and accurately performed by exploiting the ONETEP approach. For this illustrative application we consider the AlSi (N = 24) NT.

Owing the composition of the structural unit, $(Al_2SiO_7H_4)_N$ (Fig.4.1), two neutral terminations are possible for the AlSi NTs (Fig.4.7). In one case, referred to as the $AlOH_2$–termination from here onwards, the aluminium hydroxide network of the NT is truncated and the terminal under-coordinated Al-atoms saturated with one H_2O molecule (instead of one hydroxyl, –OH) to maintain electro-neutrality. In the other, referred to as the SiOH–termination, the NT ends with two hydroxyls connected to the 4-fold coordinated terminal Si-atom, resulting in a $Si–(OH)_2$ termination. Also in this case, the second hydroxyl is needed to maintain electro-neutrality.

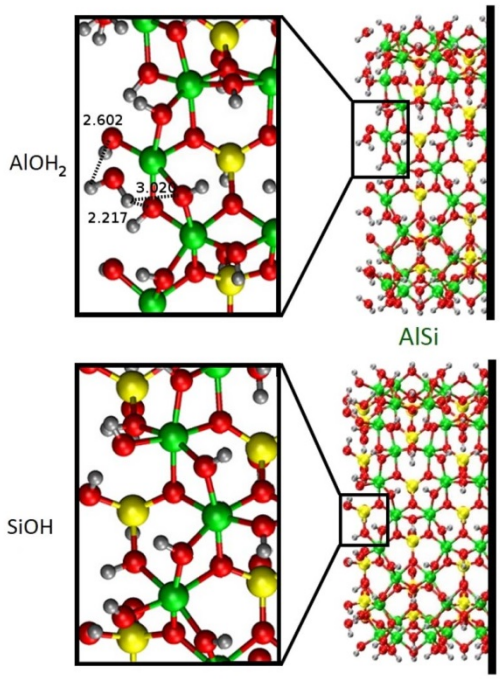

Figure 4.7. Side-view of the two optimised electro-neutral truncations of the AlSi NT: $AlOH_2$-termination (top) and SiOH-termination (bottom). The insets display a close up of the coordination of the terminal Al (top) and Si (bottom) atoms. For the $AlOH_2$-termination, the shortest distances (Å) between the H-atoms of the coordination-H_2O and the bridging hydroxyls (Al–OH–Al) have been marked as dotted lines. Same atom colour labelling as in Fig.4.1

In order to simulate NT-ends, a suitable model should be clearly finite (i.e. not 1D-periodic as used so far for Imo-NTs [3-10]) and large enough to allow accurate description of both the *core* and *terminal* regions of the NT-model. Although real Imo-NTs are 20-100 nm long depending on their composition [52], it is reasonable to expect the relaxation of the tube terminations to involve no more than a few nm from the tube-end. Accordingly, rather than attempting simulation of 20+ nm models, it is desirable to define the smallest possible system capable of simultaneous description of both the *core* and *terminal* regions of the NTs. To this end, several models were set up on the basis of the periodically optimised NT-structure. As shown in Fig.4.8, for both the $AlOH_2$ and SiOH terminations, we considered models of increasing size measured by the number of complete Al-hexagons (Fig.4.8) present along the structure-axis, which we accordingly labelled *hex-3,5* and *7*. Their overall stoichiometry and number of atoms is reported in Table 4.2. To prevent the occurrence of large longitudinal polarizations [53] which may affect the geometry optimisation of the systems, all the finite NTs model were symmetric with respect to a plane containing the innermost Si-ring (Ring 0 in Fig.4.1).

	$AlOH_2$-terminated	**SIOH-terminated**
hex-3	$Al_{96}Si_{36}O_{348}H_{264}$ (744)	$Al_{96}Si_{60}O_{396}H_{264}$ (816)
hex-5	$Al_{144}Si_{60}O_{516}H_{360}$ (1080)	$Al_{144}Si_{84}O_{564}H_{360}$ (1152)
hex-7	$Al_{192}Si_{84}O_{684}H_{456}$ (1416)	$Al_{192}Si_{108}O_{732}H_{456}$ (1488)

Table 4.2. The stoichiometry of the considered models of the $AlOH_2$- and SiOH-terminations of the AlSi NTs (N = 24). The total number of atom is reported within brackets.

The geometry of the AlSi NT finite-models was optimised relaxing all the atoms of the models, apart from the Si-atoms in the central ring (R = 0 in Fig.4.8). The latter were kept fixed at the periodically optimised geometry and used as reference for measuring the distortion of the tube along its axis.

The NT-relaxation was monitored according to three geometrical descriptors. The first one is the average ring-displacement, $< \Delta r(R) >$, defined as:

$$< \Delta r(R) > = N^{-1} \sum_i^N \left| \mathbf{r_i}(R) - \mathbf{r_i^b}(R) \right| \qquad (4.3)$$

where $\mathbf{r_i}$ is the position of the i^{th} atom of the R^{th} ring (Fig.4.8) in the finite NT-model, and $\mathbf{r_i^b}$ is the position of the same atom in the periodically repeated NT-model. N refers to the number of atoms in a given ring. A ring is defined as the group of longitudinally equivalent Si (Al) atoms and bridging hydroxyls (OH) plus the closest hydroxyl groups facing the tube ends. For the central ring (R = 0 in Fig.4.8), only longitudinally equivalent Si-atoms and bridging OH were considered in computing $< \Delta r(0) >$. For $AlOH_2$–terminated NTs, terminal H_2O molecules were not considered in the calculation of the average ring-displacement. Negligible $< \Delta r >$ values correspond to negligible relaxation of the ring-structure from the periodically optimised geometry, and are used to identify the separation between core and terminal regions of the NT-model.

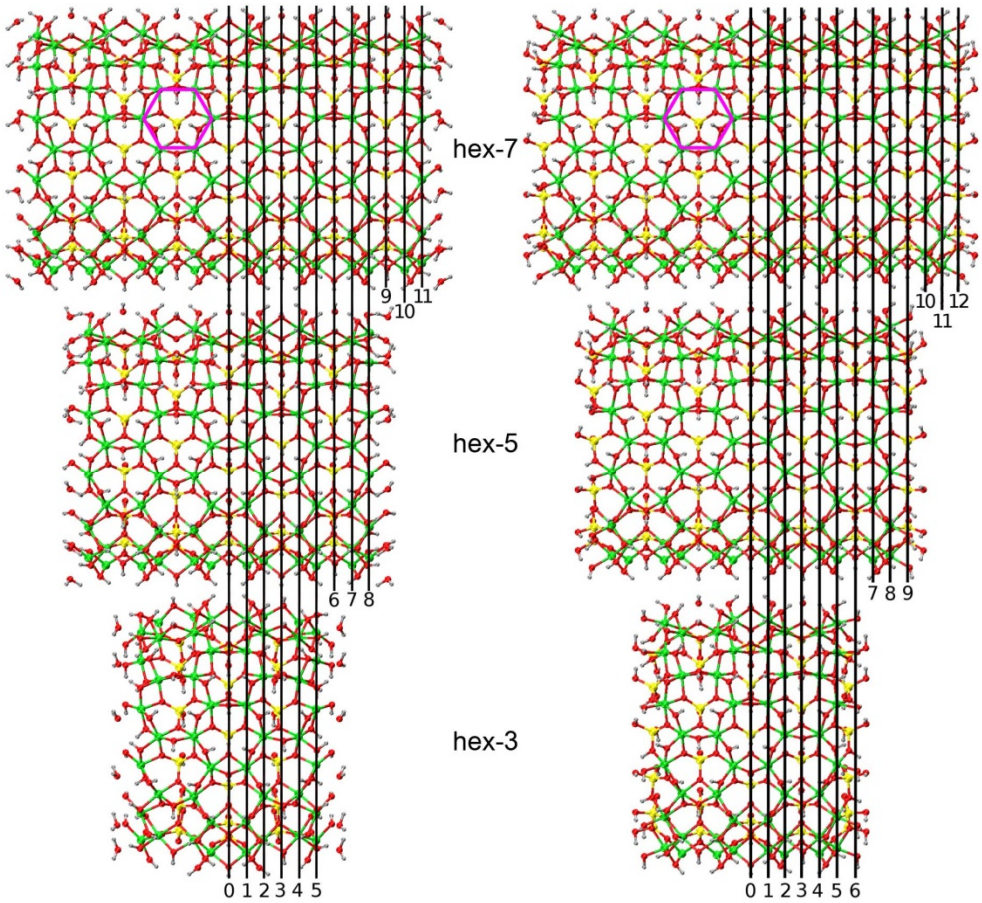

Figure 4.8. The optimised atomic structure of the considered finite models for the $AlOH_2$ (left) and SiOH (right) terminations. The models are labelled (hex-3,5,7) according to the number of complete Al-hexagons present along the structure-axis. In the top panels, one Al-hexagon has been highlighted in pink. Black vertical lines marks the position of the tube-rings (R=-12,…,0,…,12 from left to right) with R=0 corresponding to the innermost Si-ring. Marks for negative rings have been omitted for clarity. Same atom-colour labelling as in Fig.4.1.

The second geometrical descriptor to quantify the cross-section distortion of the NT, leading to changes in the diameter of the NT-rings, is the average radial-resolved (Fig.4.1) ring-diameter $< D(j,R) >$, calculated as:

$$< D(j,R) >= M^{-1} \sum_i^M d_i(j,R) \qquad (4.4)$$

where $d_i(j,R)$ indicates the layer-resolved (j: H_1, O_2,…H_7, see Fig.4.1) diameter for the i^{th} pair of atoms in the R^{th} ring. Each $d_i(j,R)$ was in turn calculated as the distance between opposite atoms in the j^{th} layer of the R^{th} ring. M = N/2 is the number of layer-equivalent atom-pairs in a given ring.

The third geometrical descriptor used to measure the overall longitudinal relaxation of the NT-models was the tube length (L) along its axis (parallel to the z-direction) calculated as the difference in the z-coordinate between the terminal Al (Si) rings of the $AlOH_2$- (SiOH-) terminations:

$$L = n^{-1} \sum_i^n [z_i(R_{max}) - z_i(R_{min})] \quad (4.5)$$

with n referring to the number of atoms in the Al(Si) terminal rings (12 for the considered systems).

With an average ring displacement ($< \Delta r >$, Fig.4.9) larger than 0.1 Å for the innermost rings, the hex-3 models turns out to be too small to accommodate for converged relaxation of the tube-extremities in the presence of a structurally unperturbed core-region. This conclusion holds regardless of the $AlOH_2$ or $Si(OH)_2$ termination. Conversely, the negligible average ring displacement ($\leq 10^{-3}$ Å) for at least the 3 (5) innermost rings of the hex-5 (hex-7) models demonstrates that these larger models are indeed suitable for describing relaxation of the tube-ends in the presence of a bulk-like core. It is interesting to note that, both for the hex-5 and hex-7 models, the $AlOH_2$-termination is calculated to induce larger structural relaxation than the $Si(OH)_2$ termination, due to the larger disruption to the aluminum hydroxide network and NT-valence band [6].

Radial- and ring-resolved analysis of the relaxed diameters ($< D(j, R) >$, Fig.4.10) reveals an overall tendency for the NT-ends to relax inwards, making the cavity narrower at the NT-extremities. The simulations for the larger hex-5 (7) models suggest the tube-end relaxation mechanism to be affected by the specific ($AlOH_2$ or SiOH) termination, leading to different changes for radially-different atoms. Whereas relaxation of the (hex-7) $AlOH_2$-termination proceeds via major contraction of the O_2, Si_3, O_4 diameters, geometry-optimisation of the SiOH-termination is found to affect mainly the Al_5 and O_6 layers.

In line with the calculated $< \Delta r >$, also the calculated $< D(j, R) >$ points out severe biases in the optimisation of the smallest hex-3 models. With deviations up to more than 2 Å (O_4-layer) from the hex-5 (7) optimised terminal diameters, the hex-3 model turns out to be clearly too small to accurately capture the cavity narrowing at the tube extremities. These results strengthen the conclusion that, if interested in modelling termination effects in AlSi NTs in the presence of a core bulk-like region of the tube, the smallest viable model should be at least as long as the hex-5. Work is currently underway to assess whether the same conclusion holds also for other members of the Imo-NTs family such as AlSiMe or AlGeMe [54].

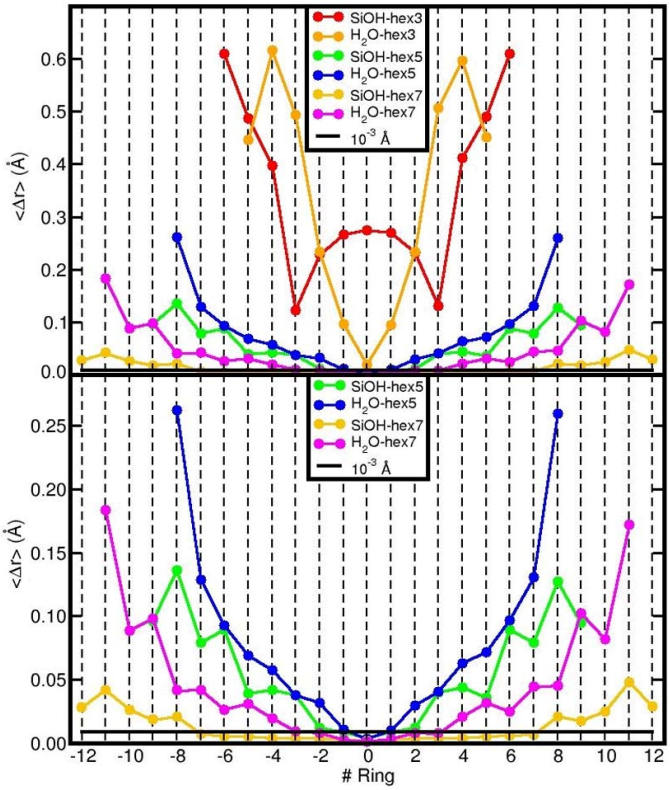

Figure 4.9. The ring-resolved average displacement (< Δr >, Å) for the finite (hex-3,5,7) models of the $AlOH_2$ and SiOH NT-terminations (top). The bottom panel reports a close up of the data for hex-5 and hex-7 terminations. The black horizontal line marks the 10^{-3} Å displacement threshold. Same ring labelling as in Fig.4.8.

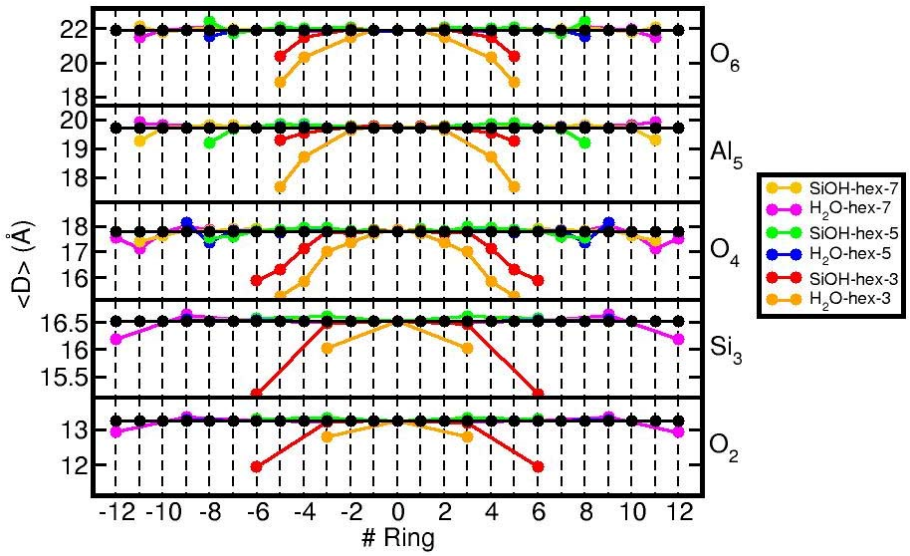

Figure 4.10. The layer-resolved ($O_{2,4,6}$, Si_3, and Al_5, see Fig.4.1) average ring-diameter (< D >, Å) for the finite (hex-3,5,7) models of the $AlOH_2$ and SiOH NT-terminations. Results for the periodically optimised NT are displayed has black circles. Same ring labelling as in Fig.4.8.

Turning to the variation in the NT length (L) following relaxation of its extremities, Table 4.3 shows the difference in the tube length between the optimised finite models and the periodically repeated counterparts (ΔL). With ΔL values smaller than 0.05 Å, we find the relaxation of the tube terminations to negligibly affect the length (Eq.4.5) of hex-5 and hex-7 models, regardless of the $AlOH_2$ or SiOH-termination. These results are in qualitative agreement with the regular appearance imaged for the termination of AlSi thin-films by TEM in [52], although the resolution of the experimental images does not allow quantitative comparison between experiment and simulations.

Contrary to the hex-5 and hex-7 cases, the simulations suggest the specific termination of the hex-3 models to more strongly affect the relaxed NT-length. Whereas the calculated ΔL for the $AlOH_2$-terminated hex-3 model is negligibly small (ΔL = +0.01 Å), the axial-distortion for the SiOH-termination is substantially larger (ΔL = +1.16 Å) as a consequence of the displacement induced on the terminal Si-atoms by reorganization of the silanol H-bonding network at the tube-extremities (Fig.4.11).

Overall, these results indicate that hex-5 models are sufficiently extended to suitably account for the termination-induced relaxations in AlSi NT in the presence of a bulk-like region at the core of the model. They also demonstrate that smaller models, such as the hex-3, can severely bias the simulation. Further work, currently in progress, will explore the effects of terminal

relaxations on the AlSi NTs electronic structure and wall-polarization and similarities and analogies between end-relaxations in AlSi, AlGe and AlSiMe NTs. These results will be reported elsewhere [54].

	$AlOH_2$-terminated	**SiOH-terminated**
hex-3	14.40 (+0.01)	16.15 (+1.16)
hex-5	23.07 (+0.01)	26.00 (+0.00)
hex-7	31.68 (+0.05)	34.35 (+0.02)

Table 4.3. The optimised length (L, Å) of the finite (hex-3,5,7) models of the $AlOH_2$ and SiOH NT-terminations. The change with respect to the length of the corresponding periodic models (ΔL, Å) is reported in brackets. Axial NT-contraction (expansion) corresponds to positive (negative) values of ΔL. Same model- and termination-labelling as in Fig.4.8.

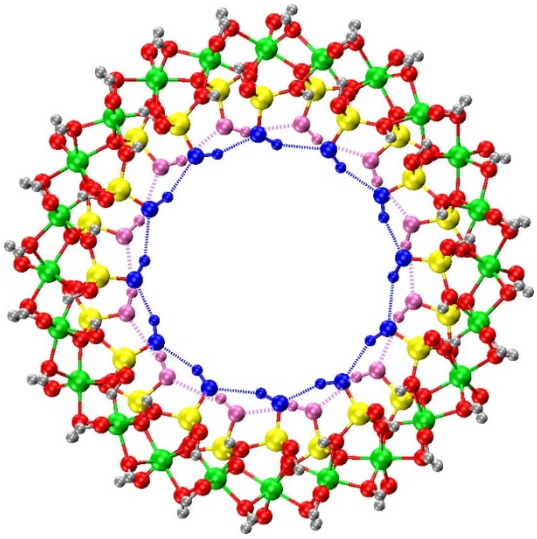

Figure 4.11. Front view of the relaxed SiOH-termination of the hex-3 model. The outermost (blue) and 2nd outermost (pink) H-bonding networks between pending silanol groups have been marked by dotted lines. Same atom colour labelling as in Figs.4.1 and 4.8 apart from the terminal (blue) and next to terminal (pink) hydroxyl groups.

4.4 Conclusions

We have illustrated the applicability of the linear-scaling, in situ optimised basis-set, ONETEP approach to the emerging class of inorganic open-ended aluminosilicate-based Imo-NTs. Study of accuracy-viability tradeoffs for representative systems of the Imo-NTs family suggests the use of 1,000 eV kinetic energy cutoff and 8 Bohr localization spheres for the optimised basis-set to provide optimal accuracy-viability compromises for geometrical relaxation of these systems. We find optimisation of at least 30 empty Kohn Sham states to be needed for convergence of the calculated band gap to less than 10 meV. Analysis of the optimised structure for differently-sized models of the tube extremities reveals heavy biases in the simulation for systems shorter than 2 nm (~1,100 atoms), making use of highly efficient DFT implementations a requirement for accurate simulation of the NT-terminations. Overall, we find the NT extremities to relax inwards leading to a narrower cavity at the tube extremities, with minimal effects on the NT-length.

References

[1] G.I. Yucelen, R.P. Choudhury, A. Vyalikh, U. Scheler, H.W. Beckham and S. Nair: *J. Am. Chem. Soc.*, 2011, **133**, (14), 5397-5412.

[2] G.I. Yucelen, D.Y. Kang, R.C. Guerrero-Ferreira, E.R. Wright, H.W. Beckham and S. Nair: *Nano. Lett.*, 2012, **12**, (2), 827-832.

[3] F. Alvarez-Ramírez: *Phys. Rev. B.*, 2007, **76**, (12), 125421.

[4] L. Guimarães, A.N. Enyashin, J. Frenzel, T. Heine, H.A. Duarte and G. Seifert: *ACS Nano*, 2007, **1**, (4), 362-368.

[5]. L. Li, Y. Xia, M. Zhao, C. Song, J. Li and X. Liu: *Nanotechnology*, 2008, **19**, (17), 175702-175711.

[6] G. Teobaldi, N.S. Beglitis, A.J. Fisher, F. Zerbetto and W.A. Hofer: *J. Phys. Condens. Matter*., 2009, **21**, (19), 195301-195310.

[7] M. Zhao Y. Xia and L. Mei: *J. Phys. Chem. C.*, 2009, **113**, (33), 14834-14837.

[8] R. Demichelis Y. Noël, P. D'Arco, L. Maschio, R. Orlando and R. Dovesi: *J. Mater. Chem.*, 2010, **20**, (46), 10417-10425.

[9] L. Guimarães, Y.N. Pinto, M.P. Lourenço and H.A. Duarte: *Phys. Chem. Chem. Phys.*, 2013, **15**, (12), 4303-4309.

[10] F. Alvarez-Ramírez: *J. Chem. Theory Comput.*, 2009, **5** (12), 3224-3231.

[11] J.P. Gustafsson: *Clays Clay Miner.*, 2001, **49**, (1), 73-80.

[12] D.Y. Kang, J. Zang, C.W. Jones, S. Nair: *J. Phys. Chem. C.*, 2011, **115**, (15), 7676-7685.

[13] C. Zanzottera, M. Armandi S. Esposito, E. Gorrone and B. Bonelli: *J. Phys. Chem. C.*, 2012, **116**, (38), 20417-20425.

[14] C. Zanzottera, A. Vicente, E. Celasco, C. Fernandez, E. Garrone and B. Bonelli: *J. Phys. Chem. C.*, 2012, **116**, (25), 7499-7508.

[15] B. Bonelli, M. Armandi, and E. Garrone: *Phys. Chem. Chem. Phys.*, 2013, **15**, (32), 13381-13390.

[16] I. Bottero, B. Bonelli, S.E. Ashbrook, P.A. Wright, W. Zhou, M. Tagliabue, M. Armandi and E. Garrone: *Phys. Chem. Chem. Phys.*, 2011, **13**, (2), 744-750.

[17] D.Y. Kang, N.A. Brunelli, G.I. Yucelen, A. Venkatasubramanian, J. Zang, J. Leisen, P.J. Hesketh, C.W. Jones, S. Nair: *Nature Comm.*, 2014, **5**, 3342-3351.

[18] P. Maillet, C. Levard, O. Spalla, A. Masion, J. Rose and A. Thill: *Phys. Chem. Chem. Phys.*, 2011, **13**, (7), 2682-2689.

[19] A. Thill, P. Maillet, B. Guiose, O. Spalla, L. Belloni, P. Chaurand, M. Auffan, L. Olivi, and J. Rose: *J. Am. Chem. Soc.*, 2012, **134**, (8), 3780-3786.

[20] M.-S. Amara, E. Paineau, M. Bacia-Verloop, M.-E. M. Krapf, P. Davidson, L. Belloni, C. Levard, J. Rose, P. Launois and A. Thill: *Chem. Comm.* 2013, **49**, (96), 11284-11286.

[21] G.I. Yucelen, R.P. Choudhury, J. Leisen, S. Nair and H.W. Beckham: *J. Phys. Chem. C.*, 2012, **116**, (32), 17149-17157.

[22] S. Konduri, S. Mukherjee and S. Nair: *Phys. Rev. B*, 2006, **74**, (3), 033401.

[23] G. Pacchioni, F. Frigoli, D. Ricci and J.A. Weil: *Phys. Rev. B.*, 2000, **63**, (1), 054102.

[24] A. M. Stoneham, J. Gavartin, A.L. Shluger, A.V. Kimmel1, D. Muñoz Ramo1, H.M. Rønnow, G. Aeppli, and C. Renner: *J. Phys.: Condens. Matter Vol.*, 2007, **19**, (25), 255208-255230.

[25] S. Lany and A. Zunger: *Phys. Rev. B.*, 2009, **80**, (8), 085202.

[26] D.R. Bowler and T. Miyazaki: *Rep. Prog. Phys.*, 2012, **75**, (3), 036503-036547.

[27] C.K. Skylaris, P.D. Haynes, A.A. Mostofi, and M.C. Payne: *J. Chem. Phys.*, 2005, **122**, (8), 084119.

[28] P.D. Haynes, C.K. Skylaris, A.A. Mostofi, and M.C. Payne: *Phys. Status Solidi B*, 2006, **243** (11), 2489-2499.

[29] N.D.M. Hine, P.D. Haynes, A.A. Mostofi, K. Skylaris, and M.C. Payne: *Comput. Phys. Commun.*, 2009, **180**, (7), 1041-1053.

[30] N.D.M. Hine, M. Robinson, P.D. Haynes, C.K. Skylaris, M.C. Payne and A.A. Mostofi: *Phys. Rev. B.*, 2011, **83**, (19), 195102.

[31] D.R. Bowler, R. Choudhury, M.J. Gillan, and T. Miyazaki: *Phys. Status Solidi B*, 2006, **243**, (5), 989-1000.

[32] M.J. Gillan, D.R. Bowler, A.S. Torralba, and T. Miyazaki: *Comput. Phys. Commun.*, 2007, **177**, (1-2), 14-18.

[33] J. M. Soler, E. Artacho, J. D. Gale, A. Garcia, J. Junquera, Ordejon, and D. Sanchez-Portal: *J. Phys.: Condens. Matter*, 2002, **14**, (11), 2745-2779.

[34] T. Ozaki and H. Kino: *Phys. Rev. B*, 2005, **72**, (4), 045121.

[35] S. Mohr, L. E. Ratcliff, Boulanger, L. Genovese, D. Caliste, T. Deutsch, and S. Goedecker: J. *Chem. Phys.*, 2014, **140**, (20), 204110.

[36]. V. Blum, R. Gehrke, F. Hanke, Havu, V. Havu, X. Ren, K. Reuter, and M. Scheffler: *Comput. Phys. Commun.*, 2009, **180**, (11), 2175-2196.

[37] J. Hutter, M. Iannuzzi, F. Schiffmann and J. VandeVondele: *WIREs Comput. Mol. Sci*, 2014, **4**, (1), 15-25.

[38] J. Perdew, K. Burke, and M. Ernzerhof: *Phys. Rev. Lett.*, 1996, **77**, (18), 3865-3868.

[39] X. Gonze, R. Stumpf, M. Scheffler: *Phys. Rev. B*, 1991, **44**, (16), 8503-8513.

[40] http://opium.sourceforge.net/sci.html

[41] B. G. Pfrommer, M. Côté, S. G. Louie, and M. L. Cohen: *J. Comput. Phys.*, 1997, **131**, (1), 233-240.

[42] A. Ruiz-Serrano, N. D. M. Hine, and C. K. Skylaris: *J. Chem. Phys.*, 2012, **136**, (23), 234101.

[43] K. A. Wilkinson, N. D. M. Hine, and C. K. Skylaris: *J. Chem. Theory Comput.*, 2014, **10**, (11), 4782-4794.

[44] M. C. Payne, M. Teter, D. C. Allan, T. A. Arias, and J. D. Joannopoulos: *Rev. Mod. Phys.*, 1992, **64**, (4), 1045-1097.

[45] E. Hernandez and M. J. Gillan: *Phys. Rev. B*, 1995, **51**, (15), 10157-10160.

[46] P. D. Haynes, C. K. Skylaris, A. A. Mostofi, and M. C. Payne: *Chem. Phys. Lett.*, 2006, **422**, (4-6), 345-349.

[47] J. Bernholc, E. L. Briggs, D. J. Sullivan, C. J. Brabec, M. B. Nardelli, K. Rapcewicz, C. Roland, and M. Wensell: *Int. J. Quantum Chem.*, 1997, **65**, (5), 531-543.

[48] E. Artacho, E. Anglada, O. Dieguez, J. D. Gale, A. Garcia, J. Junquera, R. M. Martin, Ordejon, J. M. Pruneda, D. Sanchez-Portal, and J. M. Soler: *J. Phys.: Condens. Matter*, 2008, **20**, (3), 064208.

[49] C. K. Skylaris and D. Haynes: *J. Chem. Phys.*, 2007, **127**, (16), 164712.

[50] L. E. Ratcliff, N. D. M. Hine, and D. Haynes: *Phys. Rev. B.*, 2011, **84**, (16), 165131.

[51] J. D. Elliott, N. D. M. Hine, A. A. Mostofi and G. Teobaldi: to be submitted.

[52] S. Mukherjee, V.M. Bartlow and S. Nair: *Chem. Mater.*, 2005, **17**, (20), 4900-4909.

[53] N. D. M. Hine, W. Avraam, Tangney and D. Haynes: *J. Phys.: Conf. Ser.*, 2012, **367**, 012002.

[54] E. Poli, J. D. Elliott, N. D. M. Hine, A. A. Mostofi and G. Teobaldi: to be submitted.

Chapter 5

The potential of Imogolite nanotubes as (co-) photocatalyst: a linear-scaling Density Functional Theory study

Abstract

In this Chapter, we report a linear-scaling Density Functional Theory (DFT) study of the structure, wall-polarization absolute band-alignment and optical absorption of several, recently synthesized, open-ended Imogolite (Imo) nanotubes (NTs), namely single-walled (SW) aluminosilicate (AlSi), SW aluminogermanate (AlGe) , SW methylated aluminosilicate (AlSi-Me), and double-walled (DW) AlGe NTs. Simulations with three different semi-local and dispersion-corrected DFT-functionals reveal that the NT wall-polarization can be increased by nearly a factor of four going from SW-AlSi-Me to DW-AlGe. Absolute vacuum alignment of the NT electronic bands and comparison with those of rutile and anatase TiO_2 suggest that the NTs may exhibit marked propensity to both photo-reduction and hole-scavenging. Characterization of the NTs' band-separation and optical properties reveal the occurrence of (near-)UV inside-outside charge-transfer excitations, which may be effective for electron-hole separation and enhanced photocatalytic activity. Finally, the effects of the NTs' wall-polarization on the absolute alignment of electron and hole acceptor states of interacting water (H_2O) molecules are quantified and discussed.

5.1 Introduction

The efficiency of a photo-catalyst (PC) is depends on the atomic composition, structure and dynamics of the PC, reactants and their interfaces in a given medium. In spite of this, the current understanding of the atomistic requirements to maximise the efficiency of a given PC for a given reaction is far from exhaustive. As a result, great efforts are now directed towards atomically- and time-resolved characterization of PCs and their interfaces with reactants in different media. Improved atomistic understanding of PCs would greatly expedite the development of novel photocatalytic solutions [1-19].

in this context, the increased aspect ratio (the ratio of length to diameter or surface to volume) of 1D nanostructures has been recently shown to be linked to an increased photo-catalytic activity as a result of the highly anisotropic diffusion of separated e*-h pairs in CdS, ZnO and GaN nanorods [20-22]. The possibilities offered by nano-engineering the micro-facets exposed by 1D TiO_2 and Zn_2GeO_4 substrates have been recently explored, revealing clear benefits with respect to bulk or thin-film phases [23-25]. Coating or asymmetric functionalization of 1D nanostructured substrates has also started to be studied, with findings offering appealing prospects for development of enhanced photo-catalytic strategies [19,26-35].

The pivotal role of effective e*-h separation for any viable photo-catalytic strategy has led to a growing interest in the development of photo-active ferroelectric substrates. These possess intrinsic permanent polarizations, which are capable of biasing the e*-h relaxation leading to efficient separation and diffusion to the PC surfaces. Reports on the beneficial role that permanent polarizations can play for efficient e*-h separation have started to appear in the literature [36-42], prompting growing interest in this field. To the best of our knowledge, the use of 1D ferroelectrics for photo-catalysis is yet to be explored, although several studies of 1D ferroeletric nanotubes (NTs) and nanorods are present in the literature [43-58].

Together with efficiency, cost and scalability, selectivity of the PC is another critical element for controlled, industrially viable synthesis and conversion of fine-chemicals and feedstock. Stimulated by pioneering work on highly selective methane activation by microporous beta-zeolite via deep-UV photo-catalysis [15], the concept of nanoconfinement-assisted photo-catalysis has started to receive attention from both experimental and theoretical communities [59-64].

As briefly discussed in Chapter 3, the fast progress in development of photo-catalytic strategies based on 1D nanostructures [19,20-26], ferroelectric substrates [36-42] and porous PCs [59-64] has led us to question whether these three concepts could be integrated in one solution, ideally based on cheap and abundant materials. Our interest is also focused on whether local polarization of overall dipole-free nanostructures, rather than macroscopic polarizations present in ferroelectrics, could be as effective in promoting e*-h separation and enhance photo-catalytic activity. To this end, atomically resolved insight into the relationships that exist between the local electrostatics of a porous photo-catalyst, its local polarizations, the vacuum-alignment and real-space distribution of electron bands, as well as the ensuing perturbations to the reactant electronic states would be a highly beneficial complement to research in the field.

Imogolite NTs (Imo-NTs) are a class of material that perfectly fit our interests. They can be cheaply synthesised in water solution, present extreme structural and compositional flexibility and can be easily functionalised in both sides of their cavity [65-73]. Adding to this appealing properties AlSi NTs walls are known from experiments to develop intrinsic polarisation [74] with accumulation of negative (positive) charges on the interior (exterior) of the NTs cavity. DFT simulations have shown this polarization to be linked with a separation in real space of the NT VB and CB edges [72-73], and to be independent of the substitution of Si–OH by Ge–OH in the tube interior [72]. The extent to which these appealing AlSi and AlGe NT properties are affected by functionalization of the tube walls [65-71],or the encapsulation of NTs of different radii in double-walled AlGe NTs is currently unknown, which motivates our interest in this class of materials.

Following the initial computational benchmark exposed in Chapter 4, here we present an exploration, using LS-DFT, of the relationships between the composition of Imo NTs and their electronic and optical properties as well as their potential as model systems for the development of novel photo-catalytic strategies based on inorganic nanotubes.

The Chapter is organized as follows: after a brief introduction to computational methods adopted (Section 5.2), in Section 5.3 we present and discuss results on the structural and electronic characterization, absolute band alignment and wall-polarization for pristine SW AlSi NTs as well as SW AlSi-Me, SW AlSiGe and DW AlGe NTs for different DFT functionals and treatment of dispersion interactions. We then analyse the optical absorption properties of the systems considered and discuss them against available experimental data. Finally, we investigate and quantify the effects of the (different) NT wall-polarization on the absolute alignment of H_2O electron acceptor and donor states for model NT/H_2O interfaces.

5.2 Methods

Simulation of the SW AlSi and SW/DW AlGe NTs were performed with the PBE functional [75]. Owing to the presence of highly polarisable methyl groups, and to test possible deficiencies of the PBE functional, SW AlSi-Me NTs were simulated with PBE, PBE with empirical dispersion corrections according to Grimme's D2 parameterization [76] (PBE-D2) and via the self-consistent dispersion functional OPTB88, chosen for the reported optimal performance in simultaneous treatment of H-bonding and methyl-group dispersion interactions [77]. In all cases, separable (Kleinman-Bylander) norm-conserving pseudopotentials [78], constructed with the opium code [79], were used.

As in Chapter 4, the adopted kinetic energy cutoff was 1000 eV and 4 (9) valence and conduction NGWFs were used for O (Al,Si) atoms. 1 NGWF was used for H atoms. In all cases, no truncation of the density kernel ($K^{\alpha\beta}$) was enforced. The localization radius for the valence (conduction) NGWFs was 8 Bohr (15 Bohr). All simulations were performed with periodic boundary conditions ensuring at least 15 Å vacuum separation between replicated images along the non-periodic directions. The conduction NGWFs optimization was performed on x2 super-cells along the tube-axis (i.e. two-fold replicas of the original minimal simulation cell) to accommodate the extended localization radius, which, together with optimization of 100 empty Kohn-Sham states, was necessary for sub-meV convergence of BGs and CB edges. The periodic unit for the SW-AlSi, SW-AlSi-Me, SW-AlGe and DW-AlGe NTs was the PBE-optimized one [72] (SW-AlSi: 8.666 Å, SW-AlSi-Me: 8.666 Å, SW-AlGe: 8.627 Å, DW-AlGe: 8.627 Å).

Geometry-relaxations where performed via the quasi-Newton optimization scheme based on the Broyden-Fletcher-Goldfarb-Shanno (BFGS) algorithm [80].

To prevent biases due to the asymmetric distribution of the H_2O molecules inside and outside the NTs (end ensuing dipoles), vacuum-aligned KS-states were obtained from 1D-periodic simulations with truncated electrostatics in the two directions perpendicular to the tube axis [81] (see also Chapter 2). The adopted truncation radii (SW-AlSi: 57.2 Å, SW-AlSi-Me: 77.9 Å, SW-AlGe: 76.2 Å, DW-AlGe: 102.7 Å) were numerically checked to yield sub-meV convergence of the results. All the simulations made use of the hybrid MPI-OpenMP parallelism available in ONETEP [82].

Local Density of States was calculated as [83]:

$$D_I(\epsilon) = \sum_n \delta(\varepsilon - \varepsilon_n)\langle\psi_n|\sum_{\alpha\in I}(|\phi^\alpha\rangle\langle\phi_\alpha|)\,|\psi_n\rangle) \quad (5.1)$$

with Ψ_n and ϕ_α (ϕ^α) being the Kohn-Sham states and the covariant (contravariant) representation of the NGWFs, respectively.

5.3. Results and discussion

5.3.1 Structural characterization of the Imo NT-models

Investigation of Imo NTs energy and internal strain as a function of the number of units in the Imo NTs circumference has been the subject of intense computational and experimental research with often contrasting results [73,84-95], due to the use of different computational approximations (bulk-parameterized hamiltonians or force fields, minimal fixed atomic basis sets, strongly reduced plane-wave energy cutoffs, semi-local or hybrid DFT functionals,

neglect of solvent, fixed-cavity implicit solvation) and synthetic experimental protocols. An organized collection of the results previously published on the matter can be found in Table 1 of Ref. [95].

Rather than contributing to this debate, in the absence of atomically resolved X-ray scattering or Atomic Force Microscopy results on Imo NTs structure (to the best of our knowledge not available in the literature), our focus is the initial exploration of the relationships between Imo NTs composition, structure, polarization and bands alignment as well as the sensitivity of the results on the adopted DFT functional. To this end, we consider five archetypal systems of the Imo NTs family, namely i) SW AlSi (N =24, **$AlSi_{24}$** from now), ii) SW AlSi-Me (N = 28, **$AlSi_{28}$-Me** in the following), iii) SW AlSi-Me (N = 34, **$AlSi_{34}$-Me**), iv) SW-AlGe (N = 36, **$AlGe_{36}$**), and v) DW-AlGe (N_{in} = 36, N_{out} = 54, **DW-$AlGe_{36,54}$**). They are shown in Fig.5.1.

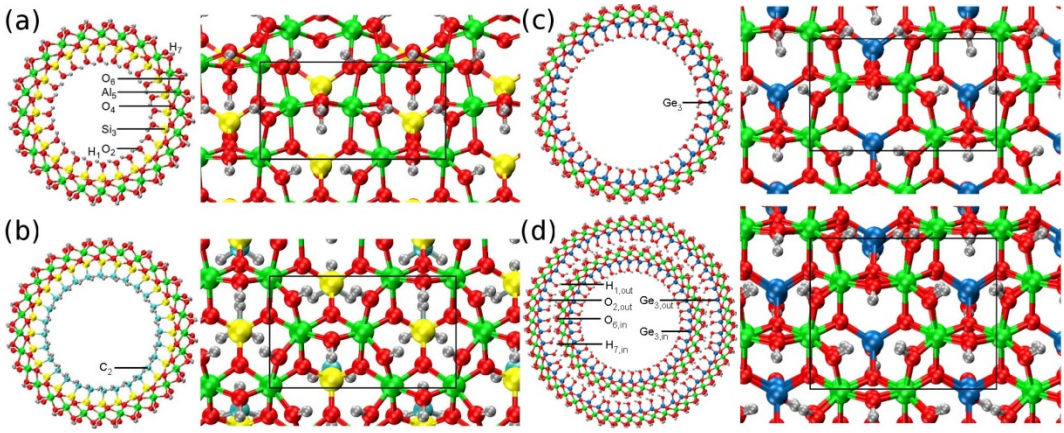

Figure 5.1. Top and side view of the optimized (a) SW-$AlSi_{24}$, (b) SW-$AlSi_{28}$-Me, (c) SW-$AlGe_{36}$ and (d) DW-$AlGe_{36,54}$ Imo NTs. The zig-zag periodic unit along the nanotube axis is marked by the black rectangle. The adopted radial labelling is displayed in panel (a), with O_2 being substituted by C_2 in (b). Si_3 is substituted by Ge_3 in (c), and by $Ge_{3,in}$ and $Ge_{3,out}$ in (d). Al: green, Si: yellow, Ge: blue, O: red, H: silver, C: cyan.

The $AlSi_{24}$ and $AlGe_{36}$ were chosen following earlier results on minimization of the (SW) AlSi (AlGe) NT-strain for 24 (36) units in the tube circumference [85,87,93]. $AlSi_{28}$-Me and $AlSi_{34}$-Me were selected since their optimized diameters (Table 5.1) brackets the peak in the experimental pore-size distribution [69]. DW-$AlGe_{36,54}$ was chosen after a minimal energy screening of different DW-AlGe NTs with smaller and larger outer NT (Fig. 5.2). It is interesting to note that, at PBE level, the energy favoured DW-$AlGe_{36,54}$ presents an 18-unit

(9-unit according to the labelling in [95]) difference between the inner and outer tubes in line with recent TB-DFT suggestions for zig-zag DW AlSi and AlGe NTs [95].

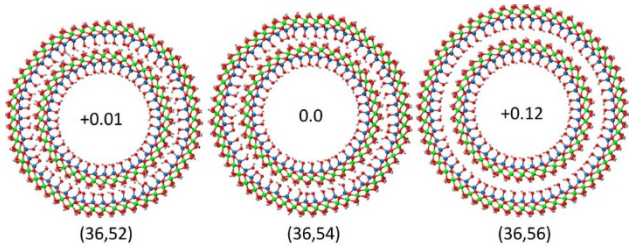

Figure 5.2. Front view of the optimized DW AlGe (N_{in}, N_{out}) NT models screened. The relative energy per ($Al_2GeO_7H_4$) unit (eV) is shown inside each NT-model.

For the interested reader, Table 5.1 reports a layer-resolved (see also Fig.5.1) analysis of the calculated diameters for the optimized NT-models. In line with earlier ultrasoft pseudopotential plane-wave PBE-DFT results [72], the optimized outer (H_7, Fig. 5.1) diameter for the $AlSi_{24}$ (23.11 Å) and $AlGe_{36}$ (33.18 Å) NTs is in good agreement with the experimental reported values of 23 Å [84] and 30-38 Å [84,86-92,95], respectively. The optimized outer diameter for DW-$AlGe_{36,54}$ ($O_{6,out}$: 45.37 Å, $H_{7,out}$: 46.38 Å) also lies reasonably close to experimentally reported values for DW-AlGe NTs (40-43 Å [89,91,95]). DW-$AlGe_{36,54}$ is not expected to be an energy minimum for DW-AlGe NTs [95], which explains the larger deviations from the experimentally derived diameter-range.

For the interested reader we report that the average inter-tube H-bonding distance (taking into account both $H_{7,in}$-$O_{2,out}$ and $O_{6,in}$-$H_{1,out}$ bonding patterns) is 2.23±0.46 Å, with the larger standard deviation originating from a non-perfectly circular section of the NTs to maximise to the inter-tube interactions. Change from circular to hexagonal cross-section has been previously observed for SW-AlGe NTs organised in bundles [96], showing that inter-tube interactions can majorly affect the cross-sectional symmetry of SW and DW AlGe NTs.

The optimized inner diameters for the $AlSi_{28}$-Me (15.39 Å) and $AlSi_{34}$-Me (20.25 Å) are found to bracket the peak in the experimental pore distribution measured by N_2 adsorption experiments (15-20 Å [69]). Notably, the deviations between PBE, PBE-D2 and OPTB88 results of the optimized H_1-O_7 diameters for the $AlSi_{28,34}$-Me NTs are found to be less than 0.02 Å. This result clearly indicates that the neglect (PBE) or inclusion (PBE-D2 and OPTB88) of dispersion interactions is effectively irrelevant for geometrical optimization of methylated Imo NTs because of the dominant contribution of the covalently bonded aluminosilicate framework to the NT diameter.

In spite of the overall acceptable agreement between computed and experimentally reported diameters, it is worth recalling that the ionic strength of the solution used for the NT synthesis is known to strongly affect the diameter of Imo AlSi NTs [97]. This makes comparison of experimental and vacuum-computed results far from conclusive. To this end, atomically resolved X-ray scattering or Atomic Force Microscopy would be extremely beneficial and timely for the communities with interest in Imo NTs.

5.3.2 Imo NTs' wall-polarization

Accumulation of negative (positive) charge on the inner (outer) tube surface, leading to a wall-polarisation of surface dipole density μ_σ, for SW AlSi and AlGe NTs has been previously considered in [72,74]. We now analyse the extent to which μ_σ is affected by the different tube composition, diameter and number of tube walls.

Following [72], we compute μ_σ from the difference (ΔV) between the plateaus of the angularly and longitudinally averaged electrostatic (ionic plus Hartree) potential inside and outside the NT-cavity:

$$\Delta V = -4\pi\mu_\sigma \frac{R_{in}}{\Delta R} \ln\left(\frac{R_{in}}{R_{out}}\right) \tag{5.2}$$

where the inner (R_{in}) and outer (R_{out}) radii of the tube are obtained from the onset of the vacuum-electrostatic plateaus, defined as the radii at which the vacuum oscillations of the local potential (V) are smaller than an arbitrary ($5x10^{-3}$ eV) threshold. For the adopted sign convention, positive μ_σ values indicate accumulation of negative (positive) charge-density at the inner (outer) surface of the NTs.

	H_1	O_2 (C_2)	Si_3 (Ge_3)	O_4	Al_5	O_6	H_7
$AlSi_{24}$ (PBE)	12.37±0.02	13.25±0.01	16.52 ±0.01	17.81±0.04	19.73±0.02	21.91±0.06	23.11±0.04
$AlSi_{28}$-Me (PBE)	15.33±0.03	16.10 ±0.02	19.77±0.01	21.04 ±0.04	22.97±0.01	25.15±0.05	26.33±0.02
$AlSi_{28}$-Me (PBE-D2)	15.35 ±0.01	16.11±0.01	19.78±0.01	21.04±0.04	22.97±0.01	25.14±0.04	26.32±0.02
$AlSi_{28}$-Me (OPTB88)	15.34 ±0.02	16.11±0.01	19.78±0.01	21.04±0.04	22.96±0.01	25.13±0.04	26.33±0.02
$AlSi_{34}$-Me (PBE)	20.25±0.02	20.79±0.01	24.45±0.01	25.82±0.01	27.77±0.01	29.89±0.01	30.92±0.01
$AlSi_{34}$-Me (PBE-D2)	20.25±0.02	20.78±0.01	24.45±0.01	25.82±0.01	27.77±0.01	29.89±0.01	30.92±0.01
$AlSi_{34}$-Me (OPTB88)	20.25±0.02	20.80±0.03	24.45±0.01	25.82±0.01	27.76±0.01	29.88±0.01	30.92±0.01
$AlGe_{36}$ (PBE)	22.01±0.02	22.79±0.03	26.40±0.03	27.80±0.05	29.79±0.02	31.95±0.04	33.18±0.02
DW-$AlGe_{36,54}$ (PBE)	22.08±0.05 (35.09±0.06)	22.87±0.06 (36.19±0.12)	26.46±0.06 (39.69±0.10)	27.83±0.09 (41.25±0.11)	29.81±0.06 (43.24±0.11)	31.94±0.13 (45.37±0.11)	33.02 ±0.38 (46.38±0.55)

Table 5.1. Average atom-resolved diameters and corresponding standard deviation (Å) for the optimized NT-models and considered DFT-functionals. The adopted radial labelling is reported in Fig. 5.1. For DW-$AlGe_{36,54}$ the results for the outer (N=54) tube are reported in brackets.

Encapsulation of two AlGe NTs in DW-$AlGe_{36,54}$ is computed to more than double (2.14 fold increase), μ_σ with respect to the SW-$AlGe_{36}$ value. Overall these results indicate that by tuning Imo NTs composition and diameter (i.e. curvature), control of the wall-polarization (thence affinity for electro-positive and negative species) can be readily achieved. Whereas methylation of Imo NTs is found to decrease the wall-polarization, creation of DW systems results in larger μ_σ.

	μ_σ (mD Å^{-2})	ΔV (eV)	R_{in} (Å)	R_{out} (Å)
$AlSi_{24}$ (PBE)	67.53	1.40	4.52	13.45
$AlSi_{28}$-Me (PBE)	35.68	0.78	5.59	15.11
$AlSi_{28}$-Me (PBE-D2)	36.69	0.81	5.59	14.99
$AlSi_{28}$-Me (OPTB88)	38.64	0.85	5.59	15.11
$AlSi_{34}$-Me (PBE)	32.75	0.82	8.09	17.37
$AlSi_{34}$-Me (PBE-D2)	32.23	0.81	8.09	17.37
$AlSi_{34}$-Me (OPTB88)	33.90	0.85	8.09	17.49
$AlGe_{36}$ (PBE)	63.64	1.62	8.73	18.28
DW-$AlGe_{36,54}$ (PBE)	136.11	2.89	8.79	25.29

Table 5.2. Computed surface dipole density (μ_σ, mD Å^{-2}), vacuum-plateau difference (ΔV, eV), and electrostatically-derived inner (R_{in}, Å) and outer (R_{out}, Å) radii for the considered NT-models and DFT functionals.

5.3.3 Imo NTs' electronic structure and absolute band alignment

For an insulator to be viable as PC for a given reaction, the position of its VB and CB edges with respect to the h and e-acceptor levels of the reactants, and effective e*-h separation, are of utmost importance [1-14]. To begin assessing the potential of Imo NTs as possible photo-catalysts, here we investigate the absolute vacuum alignment of the isolated NTs' VB and CB edges and their real-space distribution. Furthermore, the vacuum-aligned Imo NTs band edges are discussed with respect to recent combined X-ray photoemission spectroscopy, optical spectroscopy and electrostatically embedded DFT results for the bulk-phases of two archetypal photo-catalysts, namely anatase and rutile TiO_2 [98].

We recall that, qualitatively, for energetically viable transfer of excited e* from a PC to a reactant, the empty e-acceptor state of the reactant needs to be *lower* in energy than the CB-edge of the PC. Conversely, for energetically viable h-transfer from a PC to a reactant, the highest-energy occupied h-acceptor state of the reactant needs to be *higher* in energy than the VB-edge of the PC [1-13].

We also note that, owing to the use of semi-local approximations to the exchange component of the adopted PBE(-D2) and OPTB88 DFT-functionals [75,77], overestimation (underestimation) of the computed energy of the VB (CB) edge, leading to an overall underestimation of the BG, is to be expected [99-104]. Accordingly, the computed Imo NTs VB and CB edges should be taken as upper and lower boundary of the Imo NTs band edges, respectively. The following analysis neglects also the role of PC-reactants (medium) interfacial relaxations, which may affect the combined system electrostatics and, accordingly, the band alignment. These effects will be considered in the next section for model NT-H_2O interfaces.

Fig.5.3 reports the vacuum-aligned Density of States (DOS) for the considered Imo NTs. The computed band edges and BGs are collected in Table 5.3. We start noting that the computed BG for $AlSi_{28}$-Me and $AlSi_{34}$-Me (4.67-4.75 eV depending on the adopted functional) is 0.23-0.31 eV larger than for $AlSi_{24}$. Thus, in spite of substitution of more polar hydroxyls by less polar methyl units, the Imo NT BG increases upon methylation of the cavity. Mulliken population analysis [105] for $AlSi_{28/34}$-Me indicates that the modelled BG opening is accompanied by a non-negligible charge transfer of 0.30±0.01 e/CH_3, depending on the adopted functional, from the gibbsite (aluminium hydroxide) backbone to the methyl groups. Thus, we compute the methyl groups in the Imo NTs to be negatively charged. On a more specialist note, the marginal deviations (<0.08 eV) between the computed BG of $AlSi_{28/34}$-Me for the different DFT-functionals, highlights the negligible role played by dispersion interactions in the simulation of methylated Imo NT BGs.

In line with previous PBE results [72,106] $AlGe_{36}$ is also computed to be an insulator with a 4.35 eV BG. Notably, the DW-$AlGe_{36,54}$ BG (2.81 eV) is substantially smaller (-1.54 eV) than for $AlGe_{36}$. As indicated by the inner- and outer-tube resolved local DOS (LDOS [83]) in Fig. 5.3, this result stems from the mutual polarization of the inner and outer tubes, leading to an upward (downward) shift of the inner (outer) tube electronic bands. Although the calculated BG for DW-$AlGe_{36,54}$ is likely underestimated due the limitations of the PBE functional, the computed reduction in BG going from $AlGe_{36}$ to DW-$AlGe_{36,54}$ should be, at least qualitatively, significant.

Turning to the vacuum band alignment for the Imo NTs, at PBE-level the lowest (-5.97 eV) and highest (-4.30) VB edge is found for $AlSi_{28/36}$-Me and DW-$AlGe_{36,54}$, respectively. Instead, the lowest (-1.49 eV) and highest (-1.22/-1.23) CB edge is found for DW-$AlGe_{36,54}$ and $AlSi_{28/34}$-Me, respectively. Charge depletion by the methyl group (0.3 e/CH_3) leads to nearly 0.2 eV lowering (0.15 eV increase) of the $AlSi_{28/36}$-Me VB (CB) edge with respect to $AlSi_{24}$. Work is in progress to investigate whether this mechanism is present also in methylated hybrid Si/Ge Imo NTs [71].

Comparison between the band edges of SW-$AlGe_{36}$ and DW-$AlGe_{36,54}$ reveals that encapsulation of AlGe NTs causes a large (1.44 eV) upward shift of the VB-edge with simultaneous, but smaller, lowering (0.1 eV) of the CB-edge, leading to a marked narrowing (-1.54 eV) of the computed BG.

On a specialist note, and in contrast with the results for the optimized geometries and BGs, the inclusion of dispersion interactions in the functional is found to affect (up to nearly 0.3 eV) the absolute alignment of the VB and CB edges. It thus turns out that some care should be exerted when comparing vacuum-aligned band edges obtained with non-local (PBE) or self-consistent dispersion corrected (OPTB88) DFT-functionals.

Previous DFT simulation of AlSi and AlGe Imo NTs have revealed an intriguing real-space separation of the VB and CB edges [72-73], which may be beneficial for e*-h separation. The extent to which this peculiar property is affected by methylation or creation of DW-AlGe NTs has to date not been investigated. Our simulations suggest that the separation in real-space between the VB and CB-edges is qualitatively unaffected by methylation or the choice of the DFT-functional (Fig. 5.4). Notably, and in line with the tube-projected and layer-resolved results for DW-$AlGe_{36,54}$ (Fig.5.3 and Appendix A), the VB and CB edge of the DW-$AlGe_{36,54}$ are found to be localised on different tubes, with the VB (CB) edge on the inner (outer) tube, leading to the intriguing possibility of e*-h relaxation on different faces of different AlGe NTs.

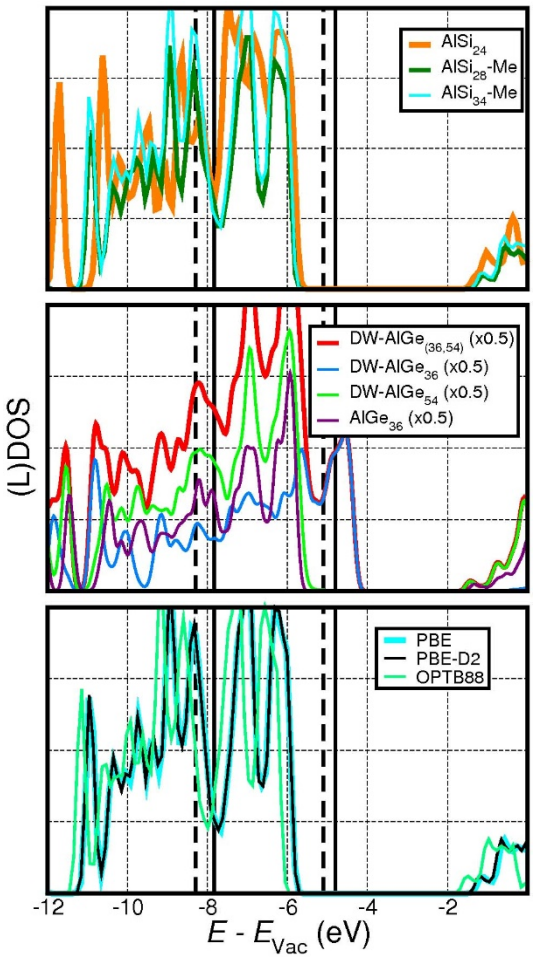

Figure 5.3. Vacuum-aligned DOS and tube-projected LDOS for the considered Imo NTs and DFT-functionals. The VB and CB edges for bulk anatase (dotted) and rutile (continuous) TiO_2, obtained from addition of the experimental optical gap to the computed ionization potential [98], are marked with black vertical lines.

Consistent with the real-space distribution of the VB and CB edges in Fig.5 4, layer-resolved, NGWF-projected [83], analysis of the computed DOS (LDOS, see Appendix A) indicates major contributions of the O_2/O_4 (H_7) layers to the VB (CB) edge of $AlSi_{24}$. Similarly, the VB (CB) edge of $AlSi_{28,34}$-Me is found to be dominated by C_2/O_4 (H_7) layers. DW-$AlGe_{36,54}$ is more peculiar with leading contributions to the CB and VB edges from inner O_2/O_4 and outer Al_5/H_7 layers, respectively. With larger contributions from the Ge_3 (O_6) layer to the CB (VB) band edges, the real-space separation of the latter for $AlGe_{36}$ is found to be less pronounced than for the other NTs.

	VB (eV)	CB (eV)	BG (eV)
$AlSi_{24}$ (PBE)	-5.80	-1.36	4.44
$AlSi_{28}$-Me (PBE)	-5.97	-1.22	4.75
$AlSi_{28}$-Me (PBE-D2)	-5.96	-1.24	4.72
$AlSi_{28}$-Me (OPTB88)	-6.21	-1.54	4.67
$AlSi_{34}$-Me (PBE)	-5.97	-1.23	4.74
$AlSi_{34}$-Me (PBE-D2)	-5.97	-1.26	4.71
$AlSi_{34}$-Me (OPTB88)	-6.24	-1.56	4.68
$AlGe_{36}$ (PBE)	-5.74	-1.39	4.35
DW-$AlGe_{36,54}$ (PBE)	-4.30	-1.49	2.81
DW-$AlGe_{36,54}$ (inner NT)	-4.30	-0.93	3.37
DW-$AlGe_{36,54}$ (outer NT)	-4.92	-1.49	3.43
Rutile TiO_2[a]	-7.83	-4.80	3.03
Anatase TiO_2[a]	-8.30	-5.10	3.20

[a] Ref. [98]

Table 5.3. Vacuum-aligned VB and CB edges (eV), and computed BG (eV) for the considered Imo NTs and DFT-functionals.

Finally, we note that the PBE, PBE-D2 and OPTB88 layer-resolved LDOS for $AlSi_{28}$-Me and $AlSi_{34}$-Me are effectively undistinguishable (see Appendix A), which demonstrates a marginal role of inclusion of dispersion corrections for the modelled LDOS in methylated AlSi-Me NTs.

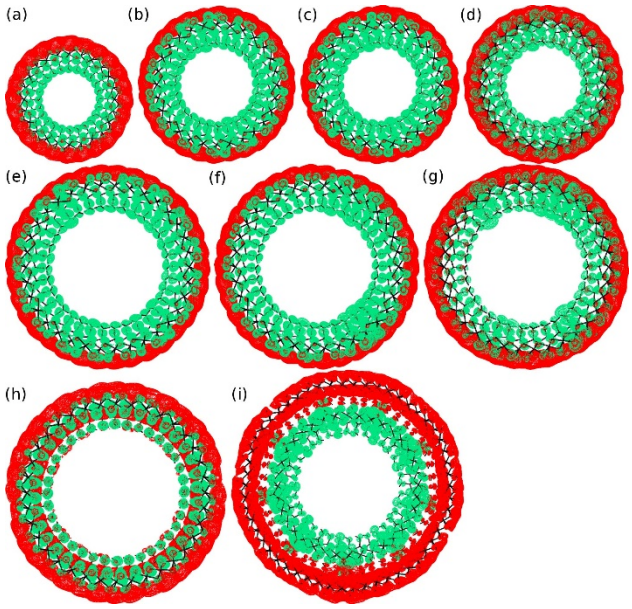

Figure 5.4. Front view of the VB (green) and CB edge (red) separation for the considered Imo NTs and DFT functionals. (a) $AlSi_{24}$ (PBE), (b) $AlSi_{28}$-Me (PBE), (c) $AlSi_{28}$-Me (PBE-D2), (d) $AlSi_{28}$-Me (OPTB88), (e) $AlSi_{34}$-Me (PBE), (f) $AlSi_{34}$-Me (PBE-D2), (g) $AlSi_{34}$-Me (OPTB88), (h) $AlGe_{36}$ (PBE), (i) DW-$AlGe_{36,54}$ (PBE). The structures in (a)-(h) are displayed according to their relative size (Table 5.1). For more compact representation, the structure in (i) has been scaled down by a factor 1.5. The six lowest-energy occupied and highest-energy empty KS-states have been plotted for the VB and CB edge in (a)-(h), respectively. For DW-$AlGe_{36,54}$, thirty two (sixteen occupied, sixteen empty) frontier KS-states have been used.

5.3.4 Comparison between Imo NTs and TiO_2 vacuum-aligned band edges

To better put these results into wider context, Fig. 5.3 and Table 3 report vacuum-aligned band edges also for rutile and anatase TiO_2 [98], whose mixture is known to lead to effective water photolysis [107]. By comparing the relative energy of TiO_2 and the Imo NTs band edges, we begin to estimate the NTs possible increased or reduced drive towards H_2O reduction or oxidation, neglecting any interfacial effects.

The vacuum-aligned VB-edges of the Imo NTs are at least 1.86 eV (2.33 eV) higher than rutile (anatase) VB-edge. Neglecting any electron transfer kinetics consideration, this result suggests a lower H_2O photo-oxidation propensity for Imo NTs with respect to TiO_2. Additionally, the CB-edge for the Imo NTs is at least +3.31 eV and +3.61 eV higher in energy than the rutile and anatase, respectively. Again neglecting any kinetics consideration, this suggests a higher drive for H_2O photo-reduction by Imo NTs in comparison to TiO_2. This

analysis rests on the assumption that the NT wall-polarization has a negligible role in shifting the H_2O acceptor and donor states. In the next section we explore this assumption and the extent to which the NT wall-polarisation shifts the electronic states of interacting molecules.

Finally, while detrimental to their possible use as photo-oxidant, the rather high-energy VB-edges of the Imo NTs, lying between -5.97 eV ($AlSi_{28/34}$-Me) and -4.30 eV (DW-$AlGe_{36,54}$), suggest that grafting a molecular or nanoparticle PC to Imo-NTs may result in a rewarding strategy towards enhanced e*-h separation by promoting h-transfer and relaxation from the grafted PC onto the NT.

5.3.5 Imo NTs' optical absorption

In spite of the growing research interests in Imo NTs, to date their optical absorption properties have not been very extensively studied. To the best of our knowledge, the only published UV-visible absorption spectrum for Imo NTs is the one reported in Ref. [85], obtained for the synthetic solution into which AlGe NTs were made, that is, without any previous separation of the Imo NTs from the unreacted precursors and possible photoactive side-products.

We now present simulated optical spectra of the (isolated and neutral) Imo-NTs in an attempt to contribute to characterization of their optical properties. Fig. 5.5 shows the computed imaginary component of the dielectric function (ε_2, see Chapter 2 Eq. 2.144) for the considered NT models. Larger values of ε_2 indicate a larger absorbance of the system. Owing to our interest in assessing possible differences between the different Imo NTs, and in order to maintain reasonable the computational cost, all the spectra were simulated at PBE level. We recall that given the limitations of the adopted DFT-functional and approximations for the evaluation of optical spectra (Section 5.2) expectations are that the energy of the optical transitions will be underestimated.

The experimental spectra for the AlGe NTs synthetic solution show a main absorbance peak at 6.2 eV with a broad shoulder in the 5-5.4 eV range, and a well-defined secondary peak at 3.9 eV [85]. Given the expected underestimation of the $AlGe_{36}$ BG (Section 5.3.3) we associate the simulated main 5 eV peak (Fig. 5.5) to the experimental 6.2 eV signature. Analysis of the optical matrix elements (Fig 5.6) indicates that transition involving deep VB and CB KS-states are optically active and contribute significantly to the modelled spectrum. The lower energy absorbance shoulder (associated to the 5-5.4 eV experimental feature) is seen to originate from transitions involving the VB and CB edges, which, as shown in Fig.5.4, are separated on different sides of the NT cavity. We speculate that these optically active inside-outside charge-transfer excitations may be beneficial for effective e*-h separation because recombination would have to occur in the direction against the wall-polarization (Table 5.2).

The simulations for the defect-free $AlGe_{36}$ model do not present any secondary absorbance peak detached from the main one. Being at lower energy than the underestimated PBE-gap (4.35 eV, Table 5.3), it has been suggested that experimental 3.9 eV peak may be due to excitonic effects in AlGe NTs [72,85], which cannot be captured by single-electron approximations to the optical spectra [108] as used here. Besides obvious limitations of Eq. 2.144, the disagreement between experiment and simulations could also stem from the fact that the experimental 3.6 eV peak is due to absorbance by point-defects (known to exist in AlSi NTs [109]), the tube-terminations (which have not been accounted for in this work) or to the presence of unreacted precursors, photoactive side-products or NT-aggregates in the synthetic solution monitored in [85]. Work is in progress to investigate these aspects.

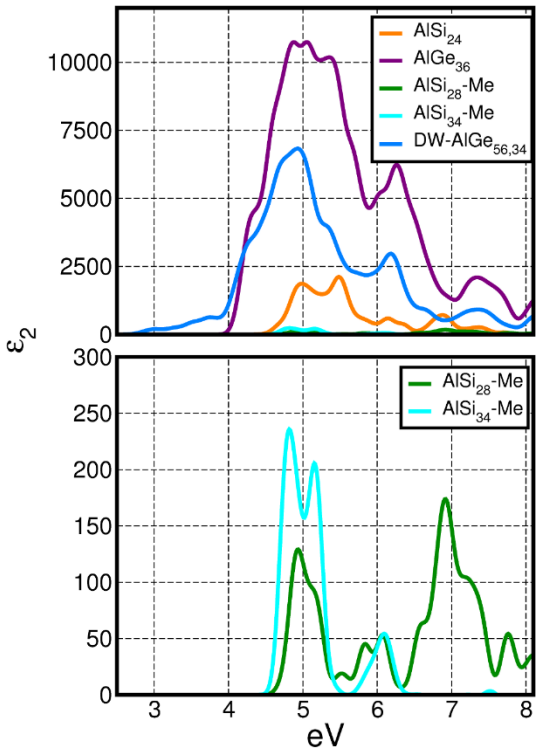

Figure 5.5. Top: calculated imaginary component of the dielectric function (ε_2) for the considered Imo NTs. To facilitate comparison, each spectrum has been normalized to the total number of Imo units (N) present in the NT-models. Bottom: close up on the $AlSi_{28}$-Me and $AlSi_{34}$-Me results.

Comparison of the calculated spectra, normalized by the number of Imo units present in the NT, indicates that optical absorbance of $AlGe_{36}$ (DW-$AlGe_{36,54}$) is nearly six (four) times larger than $AlSi_{24}$, with the absorbance of methylated $AlSi_{28}$-Me and $AlSi_{34}$-Me being the lowest (over forty five times smaller than $AlGe_{36}$). That is, the modelled absorbance per Imo unit is found to decrease going from SW $AlGe_{36}$ to DW-$AlGe_{36,54}$,SW $AlSi_{24}$, and methylated $AlSi_{28}$-

Me and $AlSi_{34}$-Me NTs. Although, the low-energy ε_2 peak is found to weakly depend on the NT composition, being bracketed between 4.83 eV ($AlSi_{34}$-Me) and 4.94 eV ($AlSi_{24}$), the appearance of an absorbance shoulder in the 3-4 eV range for DW-$AlGe_{36,54}$ indicates the creation of DW NTs is effective in introducing lower-energy (near-UV) absorption. Notably, the lower-energy absorbance shoulder of DW-$AlGe_{36,54}$ is dominated by inter-tube charge-transfer excitations (Fig5.6), which may be extremely effective for e*-h separation because of the larger separation between inner and outer NTs ($H_{7,in}$-$H_{1,out}$: 2.07 Å, $H_{1,in}$-$H_{7,out}$: 24.03 Å, see Table 5.1).

Finally, the optical matrix elements for transitions involving states at the VB and CB edges of the methylated $AlSi_{28,34}$-Me NTs are found to dominate the main absorbance peak (Fig. 5.6). Thus, contrary to $AlSi_{24}$ and $AlGe_{36}$ (DW-$AlGe_{36,54}$), the optical absorbance of the AlSi-Me NTs turns out to be primarily due to transitions between states localised on different sides of the NT cavity.

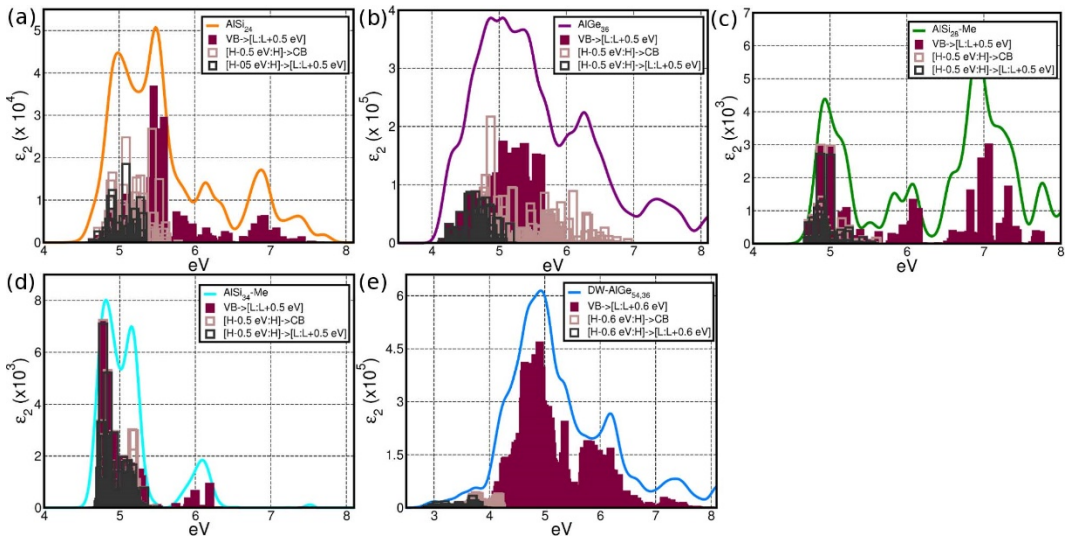

Figure 5.6. KS-state resolved analysis of the largest contributions to the low-energy values of ε_2 for (a) $AlSi_{24}$, (b) $AlGe_{36}$, (c) $AlSi_{28}$-Me, (d) $AlSi_{34}$-Me, (e) DW-$AlGe_{36,54}$. H (HOMO) and L (LUMO) indicate the highest-energy occupied and lowest-energy empty KS-state, respectively. The VB and CB edges include the KS-states within 0.5 eV (0.6 eV for DW-$AlGe_{36,54}$) from H (VB) and L (CB), respectively. Excitations between VB and CB edges are marked as "[H-0.5 eV:H]→[L:L+0.5 eV]". Excitations from the VB-edge to the whole CB and from the whole VB to the CB-edge are marked as "[H-0.5 eV:H]→CB" and "VB→[L:L+0.5 eV]", respectively.

5.3.6 H_2O at IMO NTs

Suitable electronic alignment between the PC band-edges and the reactant e (h) acceptor state(s) is crucial for viable photo-induced e (h) transfer from the PC to the reactant. As a result, PC band engineering to match a given reactant e (h) acceptor states continues to be the subject of intense research [1-14].

Two concepts, to the best of our knowledge substantially less explored, are whether by engineering of the electrostatics of nano-cavities i) reactants can be forced to match the band edge of a (polarizing) PC and ii) nano-confinement of PCs and reactants of expectedly different polarizability in a polarizing environment can be used to tailor electronic line-ups between a prospect PC and a given reactant. With inner diameters ranging from 12 Å up to 22 Å (Table 5.1), and markedly different electrostatic environments on either sides of the NT cavity (Table 5.2), Imo NTs emerge as an ideal system to start exploring these concepts. To this end, we investigate the effect of the NTs wall-polarization on H_2O molecules interacting with inner and outer surface of the considered Imo NTs (Fig. 5.7).

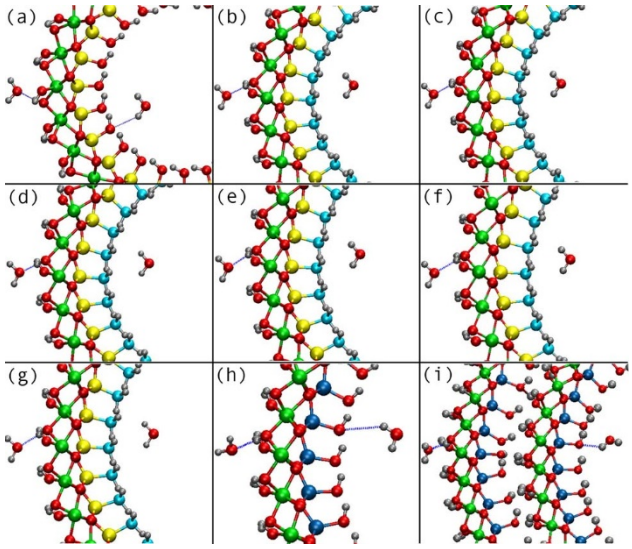

Figure 5.7. Close up of the optimized geometry of the considered $2H_2O$@Imo NTs models for the DFT-functionals used. (a) $AlSi_{24}$ (PBE), (b) $AlSi_{28}$-Me (PBE), (c) $AlSi_{28}$-Me (PBE-D2), (d) $AlSi_{28}$-Me (OPTB88), (e) $AlSi_{34}$-Me (PBE), (f) $AlSi_{34}$-Me (PBE-D2), (g) $AlSi_{34}$-Me (OPTB88), (h) $AlGe_{36}$ (PBE), (i) DW-$AlGe_{36,54}$ (PBE). The shortest H_2O-NT H-bonding distances (see also table 4) are highlighted by dotted lines. Same atom-colour labelling as in Fig.5.1.

Table 5.4 reports the optimized shortest distances between the H_2O molecule and the NT hosts, together with the computed Mulliken [105] charges. The noticeably longer ($\geq$ +0.29 Å) distances of the inner H_2O with respect to the outer H_2O for the SW hydroxylated $AlSi_{24}$ and $AlGe_{34}$ NTs indicate weaker H-bonding at the electronegative (Table 5.2) NT-cavity. Conversely, the deviations between outer and inner H-bonding for the DW-$AlGe_{36,54}$ NT (0.02 Å) are found to be negligible. Thus, H-bonding of H_2O at the NT cavity turns out to be governed by a subtle interplay between the NT-polarization and curvature, with smaller inside/outside differences for less curved (DW-$AlGe_{36,54}$) substrates.

Methylation of the NT-cavity for $AlSi_{28,34}$-Me is found to minimally affect (±0.01 Å) the outer H-bonding distance. Not unexpectedly given the different treatment of dispersion interactions, the inner H_2O-NT distance is found to be sensitive (up to ±0.08 Å differences) to the adopted DFT-functional. It is interesting to note that the deviations between PBE, PBE-D2 and OPTB88 results are different for $AlSi_{28}$-Me and $AlSi_{34}$-Me, indicating that both the cavity polarization (Table 5.2) and dispersion interactions jointly affect the adsorption of H_2O on the NT inner methylated surface.

In all cases, interaction of the H_2O molecule with the outer hydroxylated surface is found to be accompanied by small, yet non-negligible, electronic charge depletion, leading to a partially positive (+0.02/+0.07 e) adsorbed H_2O. Conversely, negligible charge transfer ($\leq$0.01 e) is modelled for the inner H_2O molecule.

H_2O adsorption on the outer surface of a carbon nanotube (CNT) has been recently shown to lead to negligible ($<10^{-4}$ e/molecule) electron transfer from H_2O to the CNT [109]. Thus, contrary to this CNT case, and likely due to the presence of H-bonding not offered by the CNT, we find the interactions of H_2O and Imo-NTs to be instead accompanied by a small charge transfer. Although simulation of periodically repeated small H_2O/NT rings (as considered here) may lead to overestimation of the charge-transferred [109], the trends among the Imo NTs considered should be robust.

Turning to the effect of NT wall-polarization on interacting H_2O molecules, Fig.5.8 reports vacuum-aligned LDOS for the considered H_2O@Imo NT systems. Consistent with the more electronegative (positive) potential at the inner (outer) surface of the NTs, and regardless of the NT composition and adopted DFT-functional, the HOMO of the inner H_2O molecule is invariably shifted (by up to roughly 3 eV for $AlSi_{24}$ and DW-$AlGe_{36,54}$) to higher energies with respect to the outer H_2O molecule. Upward (downward) shift is computed also for the LUMO of the inner (outer) H_2O molecule. These results demonstrate that the NT wall-polarization can induce major changes in the electronic alignment of adsorbed H_2O. We speculate that qualitatively similar results may be found also for other adsorbates.

	d (Å)	q (e)
$AlSi_{24}$ (PBE)	2.38 (2.09)	-0.01 (+0.05)
$AlSi_{28}$-Me (PBE)	2.32 (2.08)	+0.01 (+0.05)
$AlSi_{28}$-Me (PBE-D2)	2.32 (2.08)	+0.01 (+0.05)
$AlSi_{28}$-Me (OPTB88)	2.40 (2.00)	0.00 (+0.07)
$AlSi_{34}$-Me (PBE)	2.34 (2.10)	+0.01 (+0.04)
$AlSi_{34}$-Me (PBE-D2)	2.28 (2.20)	+0.01 (+0.04)
$AlSi_{34}$-Me (OPTB88)	2.31 (2.13)	0.00 (+0.05)
$AlGe_{36}$ (PBE)	2.49 (2.09)	0.00 (+0.02)
$AlGe_{36,54}$ (PBE)	2.09 (2.11)	-0.01 (+0.05)

Table 5.4. The shortest H_2O-NT (H-bond) distances (d, Å) and Mulliken charges (q, e) for the H_2O molecule inside (outside) the considered NT-models for the different DFT-functionals used.

Comparison of the HOMO-energy between the adsorbed molecules and one isolated H_2O molecule in vacuo (Fig. 5.8) indicates that, depending on the adsorption side, and neglecting any electron transfer kinetics consideration, oxidation of the inner (outer) H_2O should be energetically favoured (disfavoured) over the same process in vacuo because of the higher (lower) HOMO. Interestingly, owing to the NT wall-polarization and outer electropositive environment, the LUMO-level of the outer H_2O molecule is brought below the vacuum-level (0 eV), leading to a positive electron affinity (EA) for the adsorbed H_2O molecule in stark contrast with the negative EA for isolated H_2O [110].

The PBE alignment between the inner H_2O HOMO (outer H_2O LUMO) and the NT top VB (bottom CB) edge is compatible with photo-oxidation (photo-reduction) of the inner (outer) H_2O by $AlSi_{24}$. With a HOMO-energy higher than the NT top VB-edge, energetically viable photo-oxidation of the inner H_2O molecule by the NT is modelled also for $AlGe_{36}$ and DW-$AlGe_{36,54}$. Conversely, owing to a LUMO-energy higher than the NT bottom CB-edge, photo-reduction of the outer H_2O molecule by the $AlGe_{36}$ ($AlGe_{36,54}$) lowest-energy CB-states is computed to be energetically unviable. However, population of deep (higher energy) CB-states via active (Fig. 5.6) optical excitations could be energetically compatible with photo-reduction

of the outer H_2O molecule. The competition between kinetics of CB e*-relaxation and NT→H_2O e*-transfer will be the subject of future investigations.

Regardless of the adopted functional, electronic alignment suitable to photo-reduction of the outer H_2O molecule (LUMO energy lower than bottom CB-edge) is computed also for $AlSi_{28,34}$-Me. Conversely, the alignment between the inner H_2O HOMO and the $AlSi_{28,34}$-Me top VB-edge is less favourable than for non-methylated $AlSi_{24}$, at least for the considered optimized geometries. In spite of this, optically active (Fig. 5 6) excitations from deep VB-states and creation of holes deep in the VB could nevertheless promote photo-oxidation of the inner H_2O molecule by the methylated $AlSi_{28,34}$-Me NTs. Future work will consider the competition between kinetics of VB h-relaxation and NT→H_2O h-transfer.

Several notes of cautions are in place. First, the present analysis neglects any consideration of the electron (hole) transfer kinetics [111]. Thus, even if the modelled electronic alignments are appealing, the electron (hole) transfer kinetics may be impractically slow. Second, the analysis is based on the optimized geometries of highly idealised models in vacuo, which may not fully capture the real photo-electro-chemistry of the defective and solvated NTs. Depending on the polar nature of the medium interacting with the NTs [112-115], the wall-polarization may be differently screened, leading to non-negligible deviations from the computed shifts for the H_2O HOMO and LUMO levels. Third, the role of temperature-induced fluctuations [116-119] for the dynamic NTs-H_2O electronic line-ups, which may well be non-negligible, has also been neglected. Fourth, the discussion presented is based on the use of KS-states which, apart from the highest-energy occupied one and neglecting functional limitations, ultimately do not have strong physical significance in terms of molecular acceptor and donor states [120-123].Work is in progress to advance along these lines. In spite of these objective limitations, partially or completely shared with most of the current DFT-based theoretical production on PC materials [124-131], we hope this initial contribution will be effective in stimulating further input by the scientific community with interest in photo-catalysis and photo-catalytic materials.

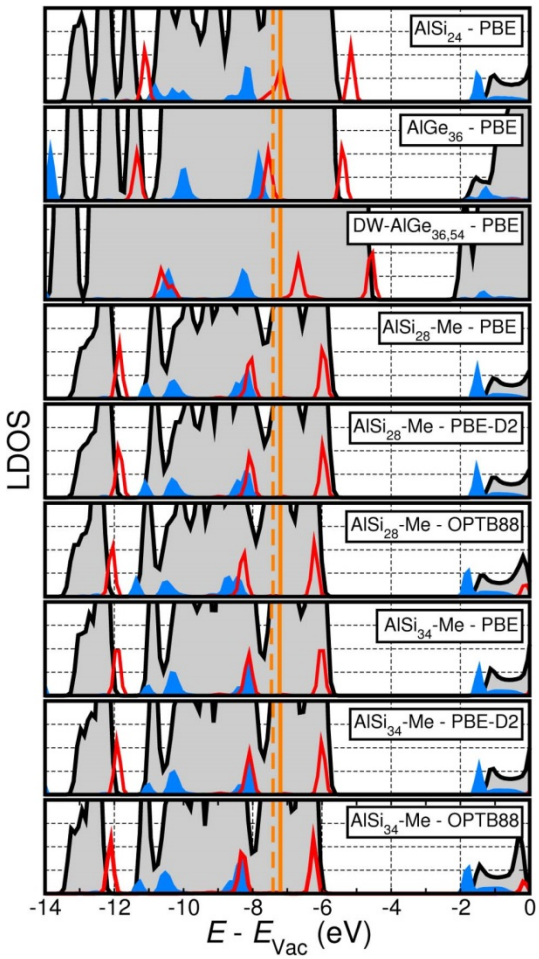

Figure 5.8. NT (filled grey) and H_2O-resolved, vacuum-aligned, LDOS for the optimized $2H_2O$@Imo NT systems and adopted DFT-functionals. The inner H_2O and outer H_2O PDOS are displayed in red and blue, respectively. The energy of the HOMO level of one isolated H_2O molecule according to PBE and PBE-D2 (-7.200 eV), and OPTB88 (-7.413 eV) are marked by orange vertical continuous (PBE, PBE-D2) and dotted (OPTB88) lines, respectively. In accordance with the literature [110], the PBE (PBE-D2) and OPTB88 LUMO-level for one isolated H_2O molecule is above the 0 eV vacuum-level [PBE(-D2): +0.629 eV, OPTB88: +0.262 eV, not shown in the graph].

5.4. Conclusion

Simulation with three different DFT-functionals (PBE, PBE-D2, OPTB88) of SW-$AlSi_{24}$, SW-$AlSi_{28}$-Me, SW-$AlSi_{34}$-Me, SW-$AlGe_{36}$ and DW-$AlGe_{36,54}$ Imo NTs either isolated or interacting with two H_2O molecules indicates that:

i) by controlling the Imo NTs composition and curvature, the NT wall-polarization can be changed by nearly a factor of four with the lowest value (20.95 mD $Å^{-2}$) for SW $AlSi_{28}$-Me

and the largest value for DW-$AlGe_{36,54}$ (72.51 mD $Å^{-2}$). Regardless of the NT composition and SW or DW nature, the NT inner surface is always more electronegative than the outer surface. The computed wall-polarization for methylated $AlSi_{28}$-Me and $AlSi_{34}$-Me NTs is found to be weakly (~8%) affected by the adopted DFT-functional.

ii) All the considered NTs are insulators with computed (likely underestimated by the functionals used) BGs ranging from 2.81 eV (DW-$AlGe_{36,54}$) to 4.75 eV ($AlSi_{28}$-Me). Use of PBE, PBE-D2 or OPTB88 is found to minimally (≤0.08 eV) affect the computed BGs for the methylated NTs.

iii) Regardless of the NT composition and curvature, SW or DW nature, and adopted DFT-functional, the VB (CB) edge is consistently modelled to be mostly localised at the NT inner (outer) surface.

iv) The absolutely vacuum-aligned NT VB edges are noticeably high in energy (> -5.97 eV), which suggests possible strong hole-scavenging propensity. DW-$AlGe_{36,54}$ is found to have the highest VB-edge (-4.30 eV).

v) The absolutely vacuum-aligned NT CB edges are also found to be remarkably high in energy (> -1.49 eV), which anticipates possible marked photo-reduction propensity. SW $AlSi_{28}$–Me is found to have the highest CB-edge (-1.22 eV).

vi) By comparison to rutile and anatase TiO_2, the Imo NTs have noticeably higher VB (up to +4.0 eV) and CB-edges (up to +3.6 eV).

vii) Contrary to the results for the wall-polarization and BGs, the absolute band-alignment of the $AlSi_{28,34}$-Me NTs is found to be non-negligibly (~0.3 eV) affected by the choice of the functional, with OPTB88 yielding lower VB-edges than PBE and PBE-D2. Accordingly, care should be exerted when comparing vacuum-aligned band edges obtained with non-local (PBE) or self-consistent dispersion (OPTB88) DFT-functionals.

viii) The optical activity of SW-$AlGe_{36}$ and DW-$AlGe_{36,54}$ NTs is noticeably (nearly six- and four-fold, respectively) larger than SW-$AlSi_{24}$ NTs, which in turn have substantially (nearly eight-fold) larger UV absorbance than methylated SW-$AlSi_{28,34}$-Me NTs. This analysis has been performed for isolated, neutral NT-models.

ix) The NT wall-polarization is found to markedly affect the electronic alignment of H_2O molecules interacting with either surface of the NTs. The computed alignment of the CB bottom edges suggests energetically viable photo-reduction of H_2O at the outer surface of all the considered NT models apart from DW-$AlGe_{36,54}$. Photo-oxidation of H_2O inside the NT-cavity by the top VB edge is modelled to be energetically favoured for all the non-methylated

NTs (SW $AlSi_{24}$, SW $AlGe_{36}$, DW-$AlGe_{36,54}$). This analysis neglects any electron transfer kinetics consideration and the role of solvent and temperature effects in altering the H_2O-NT relative band-alignment.

References

[1] Hoffmann M R, Martin S T, Choi W Y, Bahnemann D W 1995 *Chem. Rev.* **95** 69

[2] Hagfeldt A and Grätzel M 1995 *Chem. Rev.* **95** 49

[3] Fox M A and Dulay M T 1993 *Chem. Rev.* **93** 341.

[4] Yang Y, Zhong H and Tian C X *Res.* 2011 *Chem. Intermediat.* **37** 91

[5] Rauf M A and Ashraf S S 2009 *Chem. Eng. J.* **151** 10

[6] Fujishima A, Zhang X T and Tryk D A 2008 *Surf. Sci. Rep.* **63** 515

[7] Chong M N, Jin B, Chow C W K and Saint C 2010 *Water Research* **44** 2997

[8] Ahmed S, Rasul M G, Martens W N, Brown R and Hashib M A 2010 *Desalination* **261** 3

[9] Maeda K and Domen K 2010 *J. Phys. Chem. Lett.* **1** 2655

[10] Kitano M and Hara M 2010 *J. Mater. Chem.* **20** 627

[11] Ji P F, Takeuchi M, Cuong T M, Zhang J L, Matsuoka M and Anpo M 2010 *Res. Chem. Intermediat.* **36** 327

[12] Hernandez-Alonso M D, Fresno F, Suarez S and Coronado J M 2009 *Energ. Environ. Sci.* **2** 1231

[13] Morris A J, Meyer G J and Fujita E 2009 *Accounts Chem. Res.* **42** 1983

[14] Hagfeldt A and Gratzel M Molecular photovoltaics 2000 *Acc. Chem. Res.* **33** 269

[15] Sastre F, Fornes V, Corma A, and García H Selective 2011 *J. Am. Chem. Soc.* **133** 17257

[16] Ciamician G The Photochemistry of the Future 1912 *Science* **36** 385

[17] Tong H, Ouyang S, Bi Y, Umezawa N, Oshikiri M, and Ye J 2012 *Adv. Mater.* **24** 229

[18] Djurišić A B, Leunga Y H and Ng A M C 2014 *Mater. Horiz.* **1** 400

[19] Weng B, Liu S, Tang Z-R and Xu Y-J 2014 *RSC Adv.* **4** 12685

[20] Jung H S, Hong Y J, Li Y, Cho J, Kim Y J and Yi G C 2008 *ACS Nano* **2** 637

[21] Jang J S, Joshi U A and Lee J S 2007 *J. Phys. Chem. C* **111** 13280

[22] Kenanakis G and Katsarakis N 2010 *Appl. Catal. A-Gen.* **378** 227

[23] Wu N Q, Wang J, Tafen D, Wang H, Zheng J G, Lewis J P, Liu X G, Leonard S S and Manivannan A 2010 *J. Am. Chem. Soc.* **132** 6679

[24] Liu Q, Zhou Y, Kou J H, Chen X Y, Tian Z P, Gao J, Yan S C and Zou Z G 2010 *J. Am. Chem. Soc.* **132** 14385

[25] Huang J, Ding K, Hou Y, Wang X and Fu X 2008 *ChemSusChem* **1** 1011

[26] Bi Y P and Ye J H 2009 *Chem. Commun.* 6551

[27] Wang L, Wei H W, Fan Y J, Liu X Z and Zhan J H 2009 *Nanoscale Res. Lett.* **4** 558

[28] Shahid M, Shakir I, Yang S J and Kang D J 2010 *Mater. Chem. Phys.* **124** 619

[29] Berr M, Vaneski A, Susha A S, Rodríguez-Fernández J, Döblinger M, Jäckel F, Rogach A L and Feldmann J 2010 *Appl. Phys. Lett.* **97** 093108

[30] Vaneski A, Susha A S, Rodriguez-Fernandez J, Berr M, Jäckel F, Feldmann J and Rogach A L 2011 *Adv. Funct. Mater.* **21** 1547

[31] Berr M J, Wagner P, Fischbach S, Vaneski A, Schneider J, Susha A S, Rogach A L, Jäckel F and Feldmann J 2012 *Appl. Phys. Lett.* **100** 223903.

[32] Berr M J, Vaneski A, Mauser C, Fischbach S, Susha A S, Rogach A L, Jäckel F and Feldmann J 2012 *Small* **8** 291

[33] Berr M, Schweinberger F, Döblinger M, Sanwald K, Wolff C, Breimeier J, Crampton A, Ridge C, Tschurl M, Heiz U, Jäckel F and Feldmann J 2012 *Nano Lett.* **12** 5903

[34] Schweinberger F F, Berr M J, Döblinger M, Wolff C, Sanwald K E, Crampton A S, Ridge C J, Jäckel F, Feldmann J, Tschurl M and Heiz U 2013 *J. Am. Chem. Soc.* **135** 2013 13262

[35] Simon T, Bouchonville N, Berr M J, Vaneski A, Adrović A, Volbers D, Wyrwich R, Döblinger M, Susha A S, Rogach A L, Jäckel F, Stolarczyk J K and Feldmann J 2014 *Nat. Mater.* **13** 1013

[36] Choi T, Lee S, Choi Y J, Kiryukhin V and Cheong S-W 2009 *Science* **3** 63

[37] Grinberg I, West D V, Torres M, Gou1 G, Stein D M, Wu L, Chen G, Gallo E M, Akbashev A R, Davies P K, Spanier J E and Rappe A M 2013 *Nature* **503** 509

[38] Li H, Sang Y, Chang S, Huang X, Zhang Y, Yang R, Jiang H, Liu H, and Wang Z L 2015 *Nano Lett.* **15** 2372

[39] Su R, Shen Y, Li L, Zhang D, Yang G, Gao C, and Yang Y 2015 *Small* **11** 202

[40] Cui Y, Briscoe J, and Dunn S 2013 *Chem. Mater.* **25** 4215

[41] Kirchartz T, Bisquert J, Mora-Seroc I and Garcia-Belmonte G 2015 *Phys. Chem. Chem. Phys.* **17** 4007

[42] Chen Y, Zhao H, Liu B and Yang H 2015 *Applied Catalysis B: Environmental* **163** 189

[43] Venkateswarlu Bhavanasi, Damar Yoga Kusuma and Pooi See Lee 2014 *Adv. Energy Mater*. **4** 1400723

[44] Jeon C H, Lee Y S, Yee K J, Han J K and Bu S.D 2015 *Curr. Appl. Phys.* **15** 115

[45] Liew W H, Mirshekarloo M S, Chen S, Yao K and Tay F E H 2015 *Sci. Rep.* **5** 9790

[46] Liu M and Wang J 2015 *Sci. Rep.* **5** 7728

[47] Li H F, Zhang G H, Zheng, Y, Wang B and Chen W J 2014 *Acta Mater.* **76** 472

[48] Wang J, Xu T, Shimada T, Wang X and Zhang T Y 2014 *Phys. Rev. B.* **89** 144102

[49] Yoo H, Bae C, Kim M, Hong S, No K, Kim Y, and Shin H 2013 *Appl. Phys. Lett.* **103** 022902

[50] Zhao Y, Miao J, Meng X B, Weng F, Xu X G, Jiang Y, and Wang S G 2013 *J. Mater. Sci.* **24** 1439

[51] Evarestov, R A, Bandura, A V and Kuruch, D D 2013 *J. Comput. Chem.* **34** 175

[52] Han J K, Choi Y C, Kwak J H and Bu S D 2013 *Ferroelectrics* **454** 29

[53] Nuraje N and Su K 2013 *Nanoscale* **5** 8752

[54] Shimada T, Wang X, Kondo Y and Kitamura T 2012 *Phys. Rev. Lett.* **108** 067601

[55] Alexe M and Hesse D 2012 *Ferroelectrics* **433** 53

[56] Rorvik P M, Grande T and Einarsrud M A 2011 *Adv. Mater.* **23** 4007

[57] Wang C D, Lu Z Z, Yuan W X, Kwok S Y and Teng B H 2011 *Phys. Lett. A* **375** 3405

[58] Luo Y, Szafraniak I, Zakharov N D, Nagarajan V, Steinhart M, Wehrspohn R B, Wendorff J H, Ramesh R and Alexe M 2003 *Appl. Phys. Lett.* **83** 440

[59] Sastre F, Fornés V, Corma A and García H 2012 *Chemistry - A European Journal* **18** 1820

[60] Sastre F, Corma A and García H, 2012 *J. Am. Chem. Soc.* **134** 14137.

[61] Sastre F, Corma A and García H 2012 *Appl. Catal. B: Environ.* **128** 84

[62] Dietl N, Schlangen M, and Schwarz H 2012 *Angewandte Chemie International Edition* **51** 23

[63] Fresno F, Portela R, Suárez S and M. Coronado J 2014 *J. Mater. Chem. A* **2** 2863

[64] Baltrusaitis J, Jansen I and Schuttlefield Christus J D 2014 *Catalysis Science & Technology* **4** 2397

[65] Kang D Y, Zang J, Jones C W, Nair S 2011 *J. Phys. Chem. C.*, **115** 7676

[66] Zanzottera C, Armandi M, Esposito S, Gorrone E and Bonelli B 2012 *J. Phys. Chem. C.* **116** 20417

[67] Zanzottera C, Vicente A, Celasco E, Fernandez C, Garrone E and Bonelli B 2012 *J. Phys. Chem. C.*, **116** 7499

[68] Bonelli B, Armandi M, and Garrone E 2013 *Phys. Chem. Chem. Phys.* **15** 13381

[69] Bottero I, Bonelli B, Ashbrook S E, Wright, P A, Zhou W, Tagliabue M, Armandi M and Garrone E 2011 *Phys. Chem. Chem. Phys.* **13** 744

[70] Kang D Y, Brunelli N A,. Yucelen G I, Venkatasubramanian A, Zang J, Leisen J, Hesketh P J, Jones C W and Nair S 2014 *Nature Comm.* **5** 3342

[71] Amara M S, Paineau E, Rouzière S, Guiose B, Krapf M-E M, Taché O, Launois P, and Thill A 2015 *Chem. Mater*. **27** 1488

[72] Teobaldi G, Beglitis N S, Fisher A J, Zerbetto F and Hofer W A 2009 *J. Phys. Condens. Matter*. **21** 195301

[73] Zhao M, Xia Y and Mei L 2009 *J. Phys. Chem. C*. **113** 14834

[74] Gustafsson J P 2001 *Clays Clay Miner*. **49** 73

[75] Perdew J, Burke K, and Ernzerhof M 1996 *Phys. Rev. Lett.* **77** 3865

[76] Grimme S 2006 *J. Comput. Chem.* **27** 1787

[77] Klimeš J, Bowler D R, Michaelides A 2010 *Journal of Physics: Condensed Matter* **22** 022201

[78] Gonze X, Stumpf R, Scheffler M 1991 *Phys. Rev. B* **44** 8503

[79] http://opium.sourceforge.net/sci.html

[80] Pfrommer B G, Côté M, Louie S G, and Cohen M. L 1997 *J. Comput. Phys.* **131** 233

[81] Hine N D M, Dziedzic J, Haynes P. D, Skylaris C-K. 2011 *J. Chem. Phys.* **135** 204103

[82] Wilkinson K A, Hine N D M, and Skylaris C-K 2014 *J. Chem. Theory Comput.* **10** 4782

[83] Hine N D M, Avraam P W, Tangney P, Haynes P D 2012 *J. Phys. Conf. Ser* **367** 012002

[84] Mukherjee S, Bartlow V M and Nair S 2005 *Chem. Mater.* **17** 4900

[85] Mukherjee S, Kim K and Nair S 2007 *J. Am. Chem. Soc.* **129** 6820

[86] Levard C, Rose J, Masion A, Doelsch E, Borschneck D, Olivi L, Dominici C, Grauby O, Woicik J C and Bottero J-Y 2008 *J. Am. Chem. Soc.* **130** 5862

[87] Konduri S, Mukherjee S and Nair S 2006 *Phys. Rev. B* **74** 033401

[88] Levard C, Rose J, Thill A, Masion A, Doelsch E, Maillet P, Spalla O, Olivi L, Cognigni A, Ziarelli F and Bottero J Y 2010 *Chem. Mater.* **22** 2466

[89] Maillet P, Levard C, Larquet E, Mariet C, Spalla O, Menguy N, Masion A, Doelsch E, Rose J and Thill A. 2010 *J. Am. Chem. Soc.* **132** 1208

[90] Maillet P, Levard C, Spalla O, Masion A, Rose J and Thill A 2011 *Phys. Chem. Chem. Phys.* **13** 2682

[91] Thill A, Maillet P, Guiose B, Spalla O, Belloni L, Chaurand P, Auffan M, Olivi L, and Rose J. 2012 *J. Am. Chem. Soc.* **134** 3780

[92] Amara M-S, Paineau E, Bacia-Verloop M, Krapf M-E M, Davidson P, Belloni L, Levard C, Rose J, Launois P and Thill A 2013 *Chem. Comm.* **49** 11284

[93] Guimarães L, Enyashin A N, Frenzel J, Heine T, Duarte H A and Seifert G 2007 *ACS Nano* **1** 362

[94] Demichelis R, Noël Y, D'Arco P, Maschio L, Orlando R and Dovesi R 2010 *J. Mater. Chem.* **20** 10417

[95] Lourenço M P, Guimarães L, da Silva M C, de Oliveira C, Heine T, and Duarte H A 2014 *J. Phys. Chem. C* **118** 5945

[96] Amara M S, Rouzière S, Paineau E, Bacia-Verloop M, Thill A and Launois P 2014 *J. Phys. Chem C* **118** 9299.

[97] Yucelen G I, Kang D Y, Guerrero-Ferreira R C, Wright E R, Beckham H W and Nair S 2012 *Nano. Lett.* **12** 827

[98] Scanlon D O, Dunnill C W, Buckeridge J, Shevlin S A, Logsdail A J, Woodley S M, Catlow C R A, Powell M J, Palgrave R G, Parkin I P, Watson G W, Keal T W, Sherwood P, Walsh A and Sokol A A 2013 *Nat. Mater.* **12** 798

[99] Perdew J P, Parr R G, Levy M, and Balduz J L 1982 *Phys. Rev. Lett.* **49** 1691

[100] Sham L J and Schlüter M 1983 *Phys. Rev. Lett.* **51** 1888

[101] Heyd J, Peralta J E, Scuseria G E and Martin R L 2005 *J. Chem. Phys.* **123** 174101

[102] Paier J, Marsman M, Hummer K, Kresse G, Gerber I C and A´ngya´n J G 2006 *J. Chem. Phys.* **124** 154709

[103] Paier J, Marsman M, Hummer K, Kresse G, Gerber I C and A´ngya´n J G 2006 *J. Chem. Phys.* **125** 249901

[104] Tran F and Blaha P 2009 *Phys. Rev. Lett.* **102** 226401

[105] Mulliken R S 1955 *The Journal of Chemical Physics* **23** 1833

[106] Alvarez-Ramírez F 2007 *Phys. Rev. B.* **76** 125421

[107] Li G H and Gray K A 2007 *Chem. Phys.* **339** 173

[108] Onida G, Reining L and Rubio A 2002 *Rev. Mod. Phys.* **74** 601

[109] Yucelen G I, Choudhury R P, Leisen J, Nair S and Beckham H W 2012 *J. Phys. Chem. C.* **116** 17149

[110] Jonathan C. Rienstra-Kiracofe, Gregory S. Tschumper, and Henry F. Schaefer III. *Chem. Rev.* **2002,** *102,* 231-282.

[111] Nitzan A, *Chemical Dynamics in Condensed Phases: Relaxation, Transfer and Reactions in Condensed Molecular Systems.* 2006, Oxford University Press.

[112] Lever G, Cole D J, Hine N D M, Haynes P D, and Payne M C 2013 *J. Phys.: Condens. Matter* **25** 152101

[113] Cheng J and M. Sprik M 2012 *Phys. Chem. Chem. Phys.* **14**, 11245.

[114] Cheng J and M. Sprik M 2014 **26**, 11245.

[115] Nielsen M, Björketun M E, Hansen M H and Rossmeisl J 2015 *Surf. Sci.* **631** 2.

[116] Gavartin J L and Shluger A L *Phys. Rev. B* **64** 245111

[117] Troisi A, Orlandi G 2006 *Phys. Rev. Lett.* **96** 086601

[118] Sleigh J P, McMahon D P, Troisi A 2009 *App. Phys. A* **95** 147

[119] Liu T and Troisi A. 2014 *Adv. Funct. Mater.* **24** 925

[120] Janak J. F. 1978 *Phys. Rev. B* **18** 7165

[121] Perdew J P, Parr R G, Levy M and Balduz J L 1982 *Phys. Rev. Lett.* **49** 1691

[122] Perdew J P and Levy M 1983 *Phys. Rev. Lett.* **51** 1884

[123] Sau, J D, Neaton J B, Choi H J, Louie S G, and Cohen M L 2008 *Phys. Rev. Lett.* **101** 026804

[124] Sato J, Kobayashi H, and Inoue Y 2003 *J. Phys. Chem. B* **107** 7970

[125] Tong H, Ouyang S, Bi Y, Umezawa N, Oshikiri M and Ye J H 2012 *Adv. Mater.* **24** 229

[126] Nashed R, Ismail Y and Allam, N K 2013 *J. Renew. Sus. Chem.* **5** 022701

[127] Liu L-M, Crawford P and Hu P 2009 *Progr. Surf. Sci.* **84** 155

[128] Li Y-F, Aschauer U, Chen J and Selloni A 2014 *Acc. Chem. Res.* **47** 3361

[129] Di Valentin C and Pacchioni G *Acc.* 2014 *Chem. Res.* **47** 3233

[130] Dong S, Feng J, Fan M, Pi Y Q, Hu L M, Han X, Liu M L, Sun J Y and Sun J H 2015 *RCS Adv.* **5** 14610

[131] Bhatt M D and Lee J S 2015 *J. Mater. Chem. A* **3** 10632

Chapter 6

Cation-vacancies and hole relaxation in aluminosilicate Imogolite nanotubes: a linear-scaling DFT study.

Abstract

In this Chapter we report a linear-scaling Density Functional Theory (LS-DFT) investigation of the cation-vacancy related defects in single-walled open-ended aluminosilicate nanotubes (AlSi NTs) proposed in a recent solid-state Nuclear Magnetic Resonance study [1]. Optimisation of the defect structures leads to water condensation and profound modifications to the AlSi NT hydrogen network near the defect sites, leaving no dangling bond. Electronic structure analysis suggests that defect-states are highly localized in real-space and energy with predominant contributions to the high-energy edge of the valence band (VB). Despite a large reduction (up to 1.5 eV) of the band gap (BG), there are no defect states found within the BG. Electrostatic alignment of the defective NTs band structure reveals considerable shifts (up to 1 eV) of the VB and Conduction Band (CB) edges. Comparison between the calculated VB and CB edges suggests energetically favourable relaxation of photo-generated electrons and holes via diffusion to different defect-sites, and the ensuing possibility of defect-centred photo-redox reactivity in AlSi NTs. This conclusion holds regardless of the protonation of the defect sites. Finally, the effects of the defect relaxation on the permanent polarization of the NT-wall are investigated based on the absolute alignment and relative shifts of electron and hole acceptor states of interacting water (H_2O) molecules.

6.1. Introduction

The results presented in Chapters 4 and 5 support the idea of testing Imogolite nanotubes (Imo-NTs) as photo-catalyst. The computed synergy between the NTs wall polarisation, Band Gaps (BGs), band-alignment, and simulated optical activity suggest strong potential for photo-catalysis.

These results call for further study of the Imo-NTs and their properties. All the results presented so far have been obtained for extremely idealised periodic models in vacuum. To move towards more realistic simulations of the Imo-NTs, other factors, such as defects, terminations and solvent effects, need to be accounted for in the simulations.

A step in this direction is naturally prompted by the recent findings of Nair et al. [1]. In their solid NMR study of AlSi NTs dried samples, they estimated that 16% of the Si atoms on the NTs inner wall are involved in a defect structure. Following their spectroscopic analysis Nair et al. proposed five structures for the cation vacancy-induced defects present in the NTs. However, solid state Al and Si NMR presents several limitations such as the impossibility to give direct information about the hydrogen and oxygen atoms positions and their conformation around the defect sites. Furthermore solid state Al and Si NMR analysis does not provide any information about the effects that the structural defects have on the NTs electronic structure. The computational study of these defective structures is thence the obvious choice to further study the AlSi NTs, moving towards a more realistic representation of this material. This study assumes further significance when considering the role that defects are known to potentially have for the reactivity of micro(nano)porous aluminosilicate [2].

This Chapter is organised as follows: after a brief outline of the computational methods used (Section 6.2) the supercell approach adopted through this study will be presented and discussed in Section 6.3.1 The analysis of the defect-induced structural and electronic changes will be presented in Sections 6.3.2 and 6.3.3, followed by study of the defect optical absorption properties (Section 6.3.4). Finally, the investigation of the role of defects for the AlSi NTs wall-polarisation is considered and discussed against the results obtained in Chapter 5 for the ideal defect-free systems (Section 6.3.5).

6.2. Methods

Since the general theoretical framework behind LS-DFT has already been explained (Chapter 2), here we limit to the description of the computational set up used in this study.

All the simulation of the defective NTs structures were performed using the PBE functional [3] and separable (Kleinman-Bylander) norm-conserving pseudopotentials [4], constructed with the opium code [5].

As in Chapters 4 and 5, the adopted kinetic energy cutoff was 1000 eV and 4 (9) valence and conduction NGWFs were used for O (Al,Si) atoms. 1 NGWF was used for H atoms. In all cases, no truncation of the density kernel ($K^{\alpha\beta}$) was enforced. The localization radius for the valence (conduction) NGWFs was 8 Bohr (15 Bohr). All simulations were performed with

periodic boundary conditions ensuring at least 15 Å vacuum separation between replicated images along the non-periodic directions. Along the periodic direction, the simulation cell contained three-fold (x3) replicas of the NT along its axis (8.665 Å NTs axis length x1 cell). This choice will be extensively discussed and motivated in Section 6.3.1. This cell length, together with the optimization of 100 empty Kohn-Sham states, was found to be necessary for sub-meV convergence of the computed BGs and CB-edges.

Geometry-relaxations where performed via the quasi-Newton optimization scheme based on the Broyden-Fletcher-Goldfarb-Shanno (BFGS) algorithm [6]. All the atoms of the different systems studied were left free to relax. The geometry optimization threshold for the atomic forces was 0.05 eV/Å.

To prevent biases due to spurious electrostatic interactions in the simulation of the charged structures (see below) or asymmetric distribution of the H_2O molecules inside and outside the NTs, vacuum-aligned KS-states were obtained from 1D-periodic simulations with truncated electrostatics in the two directions perpendicular to the tube axis [7].To this end, the Coulomb cutoff technique in the wire approximation (described in Section 2.3.9) was used. The adopted truncation radii (i.e. dimension of the padded cell) of 57.2 Å, was numerically checked to yield sub-meV convergence of the results. All the simulations made use of the hybrid MPI-OpenMP parallelism available in ONETEP [8].

6.3. Results and discussion

6.3.1 The Supercell approach and the determination of the supercell size

The supercell approach to simulation of defects in crystals consists in surrounding the defect-site with a finite number of atoms, at least originally, with the same positions as in the pristine perfectly crystalline system. The supercell is then infinitely periodically repeated through the PBC approach [9] (see also Fig. 2.2).

Employing supercells has the following advantages: (1) it allows the use of the PBC framework to perform calculations. (2) The band structure of the host crystal is well described unlike other approaches such as the cluster one, where the host is modelled by a finite number of atoms terminated at a surface, typically hydrogenated or embedded in point charges [9]. Even in large clusters sizable quantum confinement effects significantly affect the band structure, biasing the results. (3) The results obtained are straightforward to interpret and compare with those for defect-free systems, since they are obtained in the same DFT framework.

However, a considerable number of issues arise when adopting of the supercell approach. The most relevant one is the fact that an isolated defect is replaced by a repetitive array so that an artificial high concentration of defects is obtained if the simulation cell is not larger enough (see Fig. 2.2). In this case, the interaction between the periodic images of the same defect-site cannot be neglected. In particular, quantum mechanics, electrostatic and magnetic interactions between the periodic images tend to lead to wrong descriptions of the system properties. This issue is in principle solvable by enlarging the supercell until the absolute convergence of the energy with respect to the cell size is obtained. However, this solution may be computationally unfeasible for low defect-concentrations.

In this study, the Coulomb cutoff technique is adopted to correctly describe the electrostatic interaction between the periodically repeated images of the defect. The 1D periodicity of the AlSi NTs and the consequent 1D symmetry Coulomb cutoff require nonetheless a careful analysis of the effect of the dimension of the 1D-periodic supercell on the results.

When the defective structures are relaxed to their ground state geometry within a supercell approach, it is common practice to keep the atoms further than a certain threshold distance from the defect side fixed to their ideal crystalline positions [10, 11, 12, 13]. This approximation is used so that the band structure of the host crystal is well represented in the simulations. Even pushing the capability of modern DFT codes to their limit, the tractable dimension of a supercell usually does not permit a full relaxation of the structure and the consequent recovery, within the simulation cell, of regions with the pristine crystalline structure. In this respect, the use of LS-DFT, and the possibility of modelling larger simulation cells, permits more flexibility than standard DFT.

To explore the convergence of the results with respect to the size of the simulation cell and determine the smallest supercell capable of recovering of bulk-like regions in the model, we focused on the first (D1) of the five defective structures proposed by Nair et al. (Fig. 6.3). The D1 structure of D1 was initially created in the pristine AlSi unit cell (336 atoms, 24 Al atoms in the NT circumference) described in Ref [14]. The D1 structure was created also in two other supercells of two (672 atoms) and three (1008 atoms) NTs repeat untis, respectively.

These three systems were relaxed to their ground state geometries. In order to investigate the effect of the defect relaxations on the NTs, and make an informed choice about the supercell dimension, we analysed the defect-induced atomic-displacements as a function of the distance from the defect site (Fig. 6.1 a). Besides providing useful insight into the effects of defects on the overall structure of the NTs, this analysis permits also to verify if spurious effects between the images of the NTs were present in the simulations. For a suitably converged calculation, it

is expected that the regions furthest from the defect site, even when allowed to fully relax, should maintain the same atomic structure as in the perfect, defect-free, system.

To facilitate analysis of the defect-induced structural changes in the NT, the NT atoms were divided in groups (Fig. 6.1b). The atoms directly bonded to a missing atom in the defect structures are referred to as nearest neighbours (NN). The atoms separated by one bond from the NN atoms are tagged second nearest neighbours (SNN). The atoms within a 10 Å distance from the defect-sites (but further than the SNN atoms) have been inserted in a group called first shell (FS). Accordingly, the FS group does not include NN and SNN atoms. The same approach has been used for atoms within 15 (second shell, SS), 20 (third shell, TS), and 25 (fourth shell, FS) Å distance from the defect-site.

The atoms further from the defect site and belonging to the SS and TS groups are subject to minimal relaxations of 10-2 Å in the simulation-cell comprising two NT repeat units. Conversely, simulation of the D1 defect in the simulation cell with three NT repeat units shows negligible displacements ($\leq 10^{-3}$ Å) for all the atoms further than the SNN group. This extremely small displacements for the TS atoms clearly indicates that the simulation cell with three NT repeat units suffer from very limited (i.e. non-relevant) finite size effects.

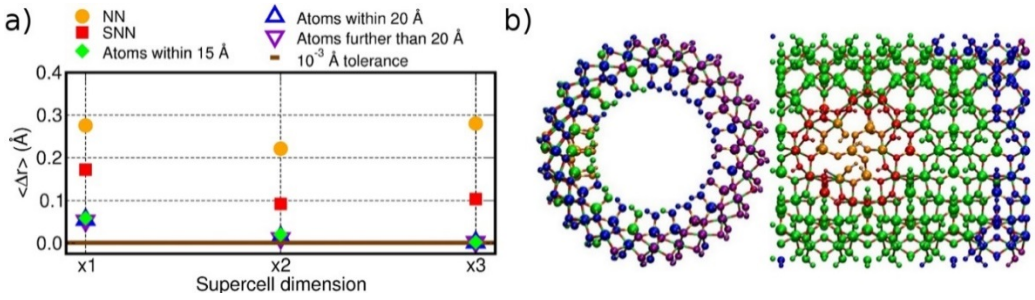

Figure 6.1. a) Computed average relaxation-displacements from the bulk-like positions for the atoms at different distances from the D1 defect-site (NN, SNN, FS, SS, TS, see text for definition) as a function of the number of NT-repeat units in the simulation cell. b) Front and side view of the AlSi NT. The different sets of atoms considered in the analysis of the defect-induced relaxation are highlighted using the same colour code adopted in (a).

The same test was repeated for all the others defect-structure using the largest x3 simulation cell. The results are shown in Fig. 6.2.

Exception made for defect three (D3), the average relaxation-displacements for the atoms further than the SNN (i.e. >15 Å away from the defect site) are in the order of 10^{-2} Å or less

for all the other (D2, D4, D5) structures. D3 larger average relaxation-displacement can be ascribed to its more extended structure (Figs. 6.3 and 6.4). The < 10^{-2} Å relaxation of the TS atoms (further than 20 Å from the defect site) for D3 , indicate both a less local rearrangement of the overall NTs defective structure and very contained finite size biases due to the dimension of the simulation cell.

Fig. 6.2 demonstrates that, for atoms belonging to the TS groups (hence furthest from the defect-site within the periodic simulation cell), the defect-induced perturbation are very effectively screened, leading to negligible displacements from bulk-like positions. On the basis of these results, an x3 simulation cell with three NT repeat untis was used for the electronic structure characterization.

This choice also permits to simulate the defect-concentrations (the considered defects involve ~10% of the Si-atoms in the cell) similar to or, unprecedented to the best of our knowledge, underestimated with respect to the experimental reported value (~16%). Accordingly, and pending limitations of the adopted PBE DFT-functional, the considered models should provide a very sound representation of the defects in AlSi NTs.

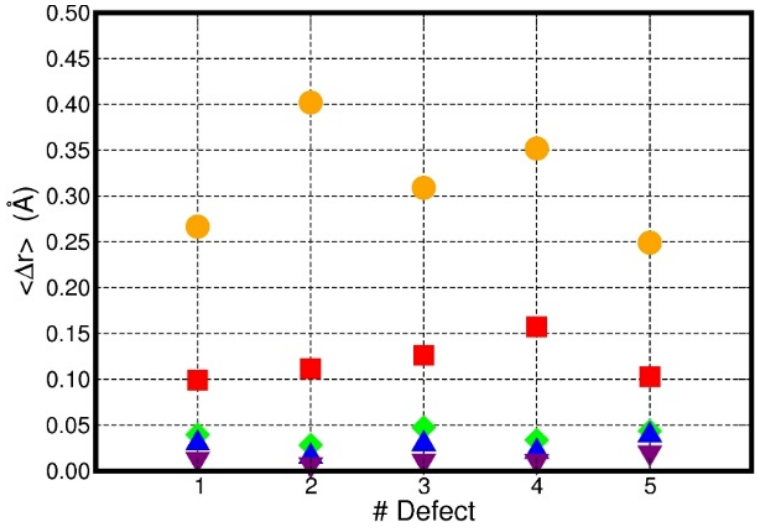

Figure 6.2. Computed average relaxation-displacements from the bulk-like positions for the NT-atoms at different distance from the defect site (NN, SNN, FS, SS, TS, same colour labelling as in Fig. 6.1) for all the five (D1-5) structures proposed in Ref. [1] (see also Fig. 6.3 and 6.4).

6.3.2. Structural characterization of the defective NT-systems

As starting point of our study we used the five defect structures proposed in [1] from analysis of solid-state NMR results. Following Nair et al. [1], these are (see Fig. 6.3):

- Defect one (D1). It is a simple Al vacancy. This vacancy introduces Al-OH dangling groups in the NTs framework, which would otherwise not be present in the defect-free NTs.
- Defect two (D2). This structure presents an additional Si-atom in the inner wall of the NTs. This additional Si-atom leads to the formation of a Si-O-Si bridge in the inner wall of the NTs.
- Defect three (D3). It involves the absence of two Al atoms (Al vacancies) in the outer gibbsite layer of the NT. NMR data [1] suggests the condensation of two silanol groups with formation of an elongated Si-O-Si bridge inside the NT-cavity.
- Defect four (D4). It comprises one Al vacancy in the outer wall, and one extra Si-atom in the inner wall of the NTs. As for D2 and D3, also D4 contains an additional Si-O-Si bridge.
- Defect five (D5). It consists of two neighbouring Al atoms vacancies. In this case, Si-OH groups around the vacancy do not form any Si-O-Si bridge and are left dangling.

All these structures are due to cation vacancy (vacancies) in the NTs framework so no positively charged structures are formed due to the presence of defects. The respective net charges of the structures are reported in Table 6.1.

#Defect	Model Stoichiometry	Net Charge
D1	$(Al_2SiO_7H_4)_{71}SiAlO_7H_7$	0
D2	$(Al_2SiO_7H_4)_{71}Si_2AlO_8H_5$	0
D3	$(Al_2SiO_7H_4)_{71}SiO_5H_2$	-4
D4	$(Al_2SiO_7H_4)_{71}Si_2O_7H_4$	-2
D5	$(Al_2SiO_7H_4)_{71}SiO_6H_4$	-4
h-D3	$(Al_2SiO_7H_4)_{71}SiO_5H_6$	0
h-D4	$(Al_2SiO_7H_4)_{71}Si_2O_7H_6$	0
h-D5	$(Al_2SiO_7H_4)_{71}SiO_6H_8$	0

Table 6.1. Stoichiometric formula and net charge for each considered defect structure.

Given the water-phase synthesis of the NTs [15-18], it is plausible that the negative charge D3, D4 and D5 will be compensated by counter-cations or protons (in the water solution). These considerations prompted us to model three additional structures, one for each negatively charged defect, where the initial structure was modified in order to neutralise the excess of charge via protonation of the defect sites.

These structures, labelled h-D3, h-D4 and h-D5 are also displayed in Fig. 6.3. These additional systems have been modelled to investigate two possible conditions (negatively charged or neutral) in which the D3-5 defects could be found are considered. Inclusion in the simulation of counter-cations (possibly Keggins ions [19]) was not considered due to the prohibitive computational cost of this approach. A more in depth realistic study on the charged states of the different defects depending on their formation energies and the overall Fermi energy of the systems [9, 20] was also not possible owing to the impossibility of modelling pH-variable solvation of the NTs in the presence of dissolved ions. In spite of this, it is worth stressing that their NMR signature has been experimentally detected, which vouches for their occurrence in the NTs, regardless of considerations on computed formation energy for vacuum-exposed models.

The optimised structures for the D1-5 and h-D3-5 defects are shown in Fig. 6.4. The D1 optimised structure presents a water molecule coordinated to an Al adjacent to the defect site. The condensation of one Al-coordinated water molecule is due to the transfer of one H-atom from a dangling –OH group to an adjacent one.

The optimised D2 geometry presents the occurrence of a local hydrogen-bond network near the defect site with different orientation with respect to the pristine NTs pattern. The pristine NTs hydrogen-bond pattern is disrupted both inside and outside the NTs cavity.

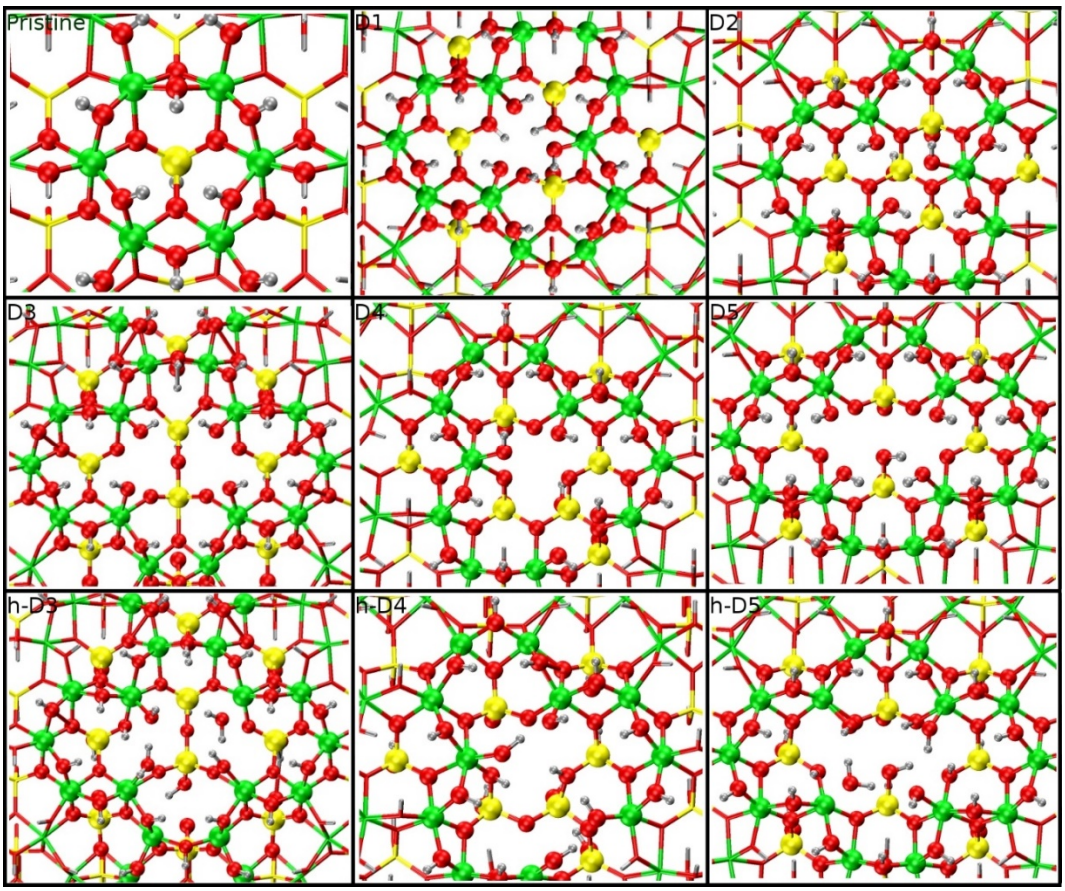

Figure 6.3. Close up of the starting geometries of the D1-5 defect-structures proposed in Ref. [1]. The pristine NTs local bonding geometry is shown in the top-left panel as reference. The hydrogenated h-D3-5 neutral defects are reported in the bottommost panels. Al: green, Si: yellow, O: red, H: silver.

D3 optimised geometry presents substantial differences with respect to the NMR proposed structure [1]. Upon DFT-relaxation, the stretched Si-O-Si bridge breaks and the O-atom relaxes towards the closest Si-atom leaving a negatively charged deprotonated O-atom. This bond rupture, caused by the rigidity of the silica tetrahedron, induces extensive reorganisation of the AlO_6 octahedron closest to the defect site. This relaxation permits the condensation of a H_2O molecule, which remains coordinated to one of the two Al atoms.

D4 optimised geometry has qualitative resemblance to the D2 optimised structure in that it also leads a rearrangement of the inner and outer NT hydrogen-bond patterns with no H_2O condensation.

D5 optimised structure resembles the D1 one. D5 undergoes the same H_2O condensation process as D1. The water molecule remains coordinated to one of the Al atoms of the the defect-site.

The final structure for the protonated defects (h-D3, h-D4, h-D5) are relaively similar to their charged correspondent. However, the presence of additional hydrogen atoms around the defect sites leads to condensation of an additional water molecule. These water molecules are in all the cases coordinated to the nearest Al atom.

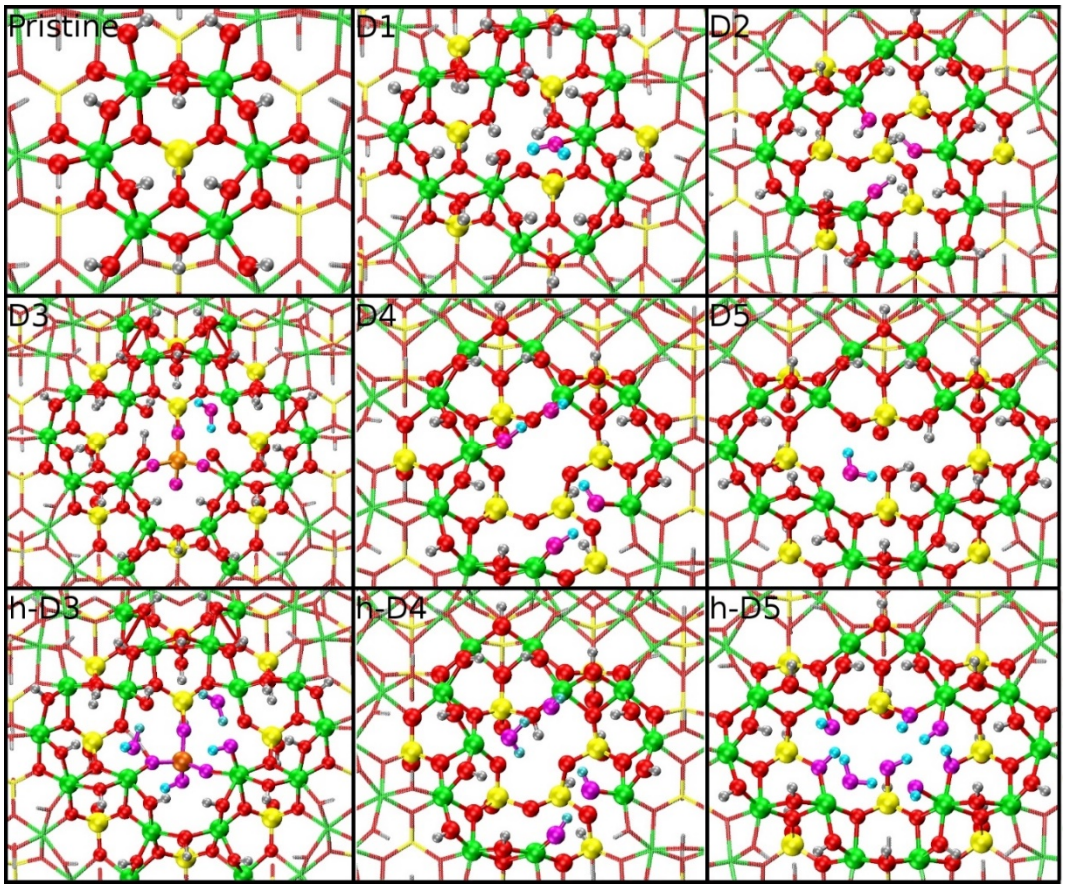

Figure 6.4. Close up of the optimised geometries of the D1-5 defect- structures proposed in Ref. [1]. The pristine NTs local bonding geometry is shown in the top-left panel as reference. The dangling hydroxyls (-OH) closest to the defect sites, the condensed water (H_2O) molecules, the defect-induced alternative hydrogen-bonding patterns, and the Si-O-Si bridge in D3 are highlighted in different colour (O: magenta, H: cyan, Si: tangerine) to highlight the changes from the starting structures.

Few remarks can be made after analysis of the optimised structures. The average bond lengths for the three types of bond present in the AlSi NTs (i.e. Si-O, Al-O, O-H) have been calculated for the NN and SNN atoms in all the defects (Table C.1, Appendix C) and then compared with respect to the pristine NTs average bond lengths (Fig. 6.5).

The presence of cation vacancies in the AlSi NTs framework causes changes in the NT-structure prevalently in the external Al-O octahedral layer. The change in length of the Al-O bonds for the NN, SNN atoms varies from case to case. However, the computed deviations from the NTs Al-O bond-length lie in the 3-10% range ($\sim 0.02 - 0.15$ Å). The rigid silica tetrahedron frame in the interior part of the NTs is negligibly distorted by the presence of defects.

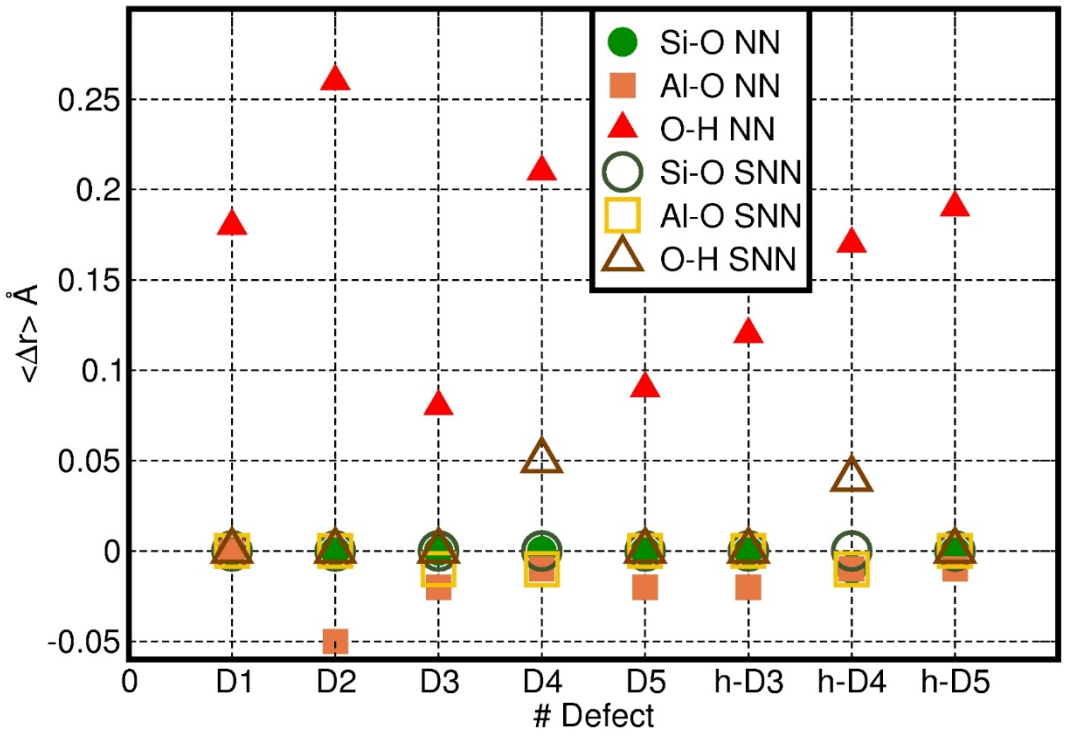

Figure 6.5. Computed change in average bond-lengths (<Δr>) of the three bond types Al-O, Si-O, O-H for the NN (filled symbols) and SNN (empty symbols) atoms for all the considered defect structures. The adopted reference for each bond type is its average length in the pristine NTs (Si-O: 1.65 ± 0.09 Å, Al-O: 1.92 ± 0.10 Å, O-H: 0.96 ± 0.08 Å).

The rearrangements due to disruption of the NT pristine hydrogen bonding network and condensation of water molecules are the most relevant effects of the presence of cation vacancies. Especially in the cases where the dangling Al-OH groups create a local hydrogen bonding pattern (D2, D4, h-D4. h-D5), the displacement and changes in O-H bonds lengths are very noticeable (>0.15 Å). These effects are especially evident in D2, D4 and h-D4.

Turning to the modelled barrier-less water condensation, this process happens only in defect structures where an Al-OH dangling group is near enough to other Al-OH groups of the NTs framework. In D2, D4 and h-D4 the presence of an extra Si atom increases the distances between the closest dangling Al-OH groups, preventing a barrier-less condensation of a water

molecule, and leading to even larger reorganisation of the atomic structure around the defect sites (Fig. 6.5).

Consistent with the absence of any dangling bonds, all the optimised defect structures have a closed-shell electronic configuration. These (closed-shell) non-magnetic solutions were explicitly tested to be energetically favoured over alternative spin-polarised ones.

6.3.3. Electronic structure and absolute band alignment for the defective NTs

Understanding the role of defects for the electronic properties of AlSi NTs is critical to assess the actual viability of these systems as photo-catalyst. By altering the local potential in a material, the presence of defects usually affects the alignment of the Valence (VB) and Conduction (CB) bands as well as the mobility of the charge carriers [21]. Furthermore, defective semiconducting or insulating structures can introduce either shallow (close to the band edges) or deep (mid gap) defect-states in the system. Especially the latter can act as charge traps and favour electron hole recombination.

Ahead of the following discussion, it is important to note that while the use of the PBE functional is well-known to underestimate computed band gaps (BGs), the relative alignment of band edges and defect-states for the considered defective structures should be, at least qualitatively, significant. Like in the previous studies presented in this thesis, the role of the medium and NT-medium, interface has not been initially considered. This aspect will be partially accounted for in Section 6.3.5. The main focus of this initial screening is to unveil the main changes caused to the electronic structure of the AlSi NTs by the presence of defects. To this end, in the following we consider the calculated electronic structure, band-alignment for the defective NT models together with the extent to which possible defect-states are localised around the defect site.

Analysis of the total Density of States (DOS) and defect-site resolved local DOS (LDOS), displayed in Fig. 6.6, indicates that, depending on the defect structure composition and hydrogenation, shallow (D4 and D5) or deep occupied states (D1, D2, D3, h-D3, h-D4 and h-D5) are introduced in the NTs band gap.

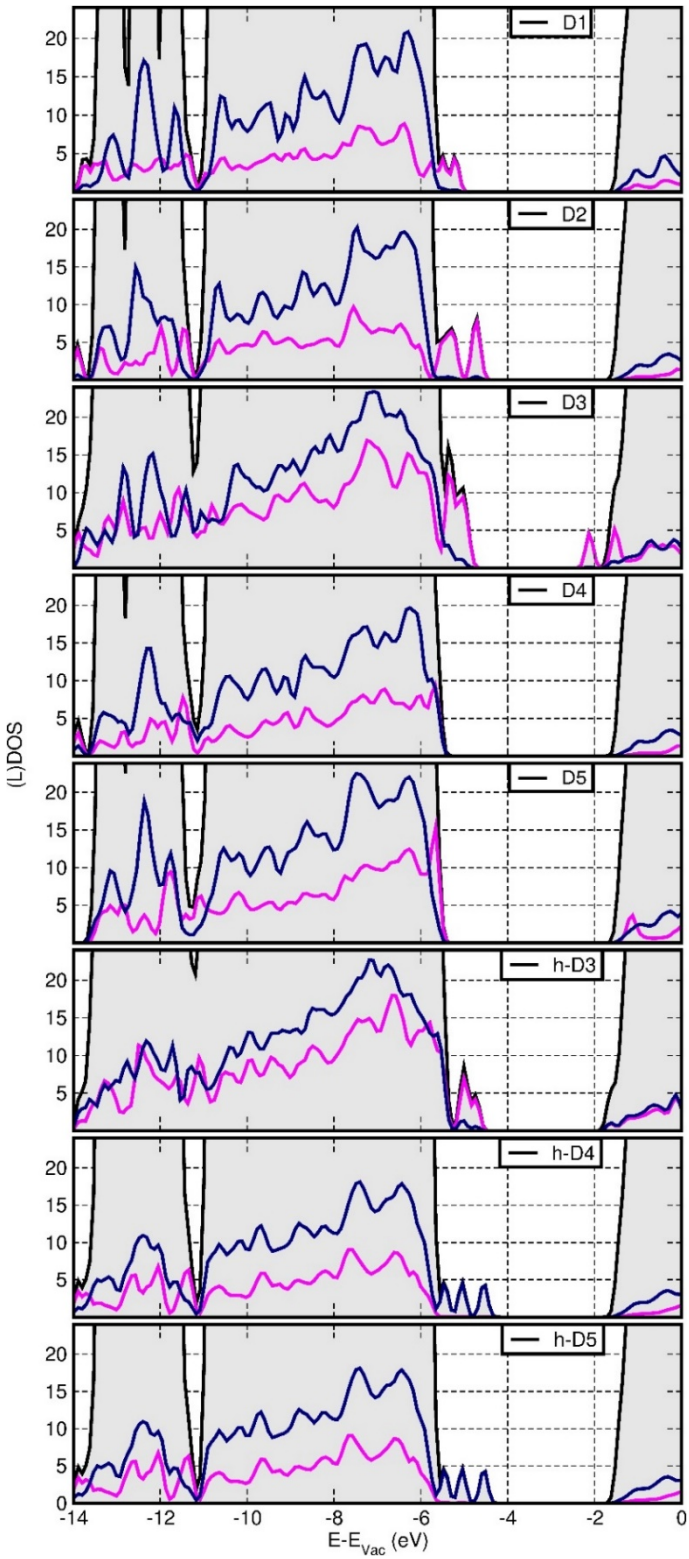

Figure 6.6. Vacuum aligned DOS, and NN (magenta) and SNN atoms (navy) local DOS (LDOS) for all the defects simulated.

Comparison between the results for the D3-5 defects and the hydrogenated counterparts (h-D3-5) indicates that hydrogenation is effective in changing the shallow defect-states (D3-5) into deep defect-states, with changes as large as nearly 1.5 eV [(h)-D3-4]. This result suggests the possibility of tuning the NTs electronic structure (BG and energy-positioning of defect-states in the gap) by altering the pH of the solution the NTs are dissolved in.

The computed LDOS indicates major contribution to the occupied defect-states from the NN and SNN atoms around the defect site. Thus, as shown in Fig. 6.7, the occupied defect-states turn out to be highly localised at the defect site.

In line with the computed (L)DOS, and contrary to the occupied defect-states, the edge of the CB maintains its delocalised character in all the cases but D3, which present deep empty defects states roughly 0.5 eV below the CB edge (Figure C.1 in Appendix C).

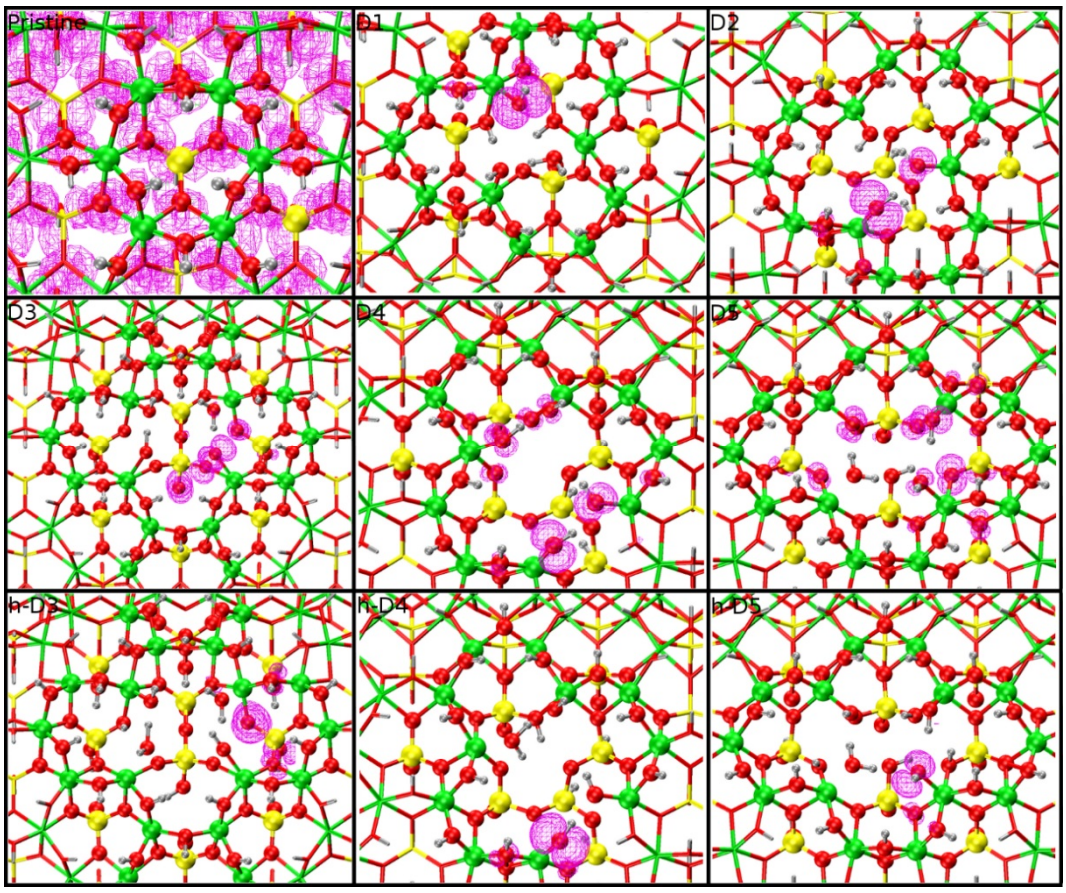

Figure 6.7. Close up of the optimised defect geometries (see also Fig. 6.4) together with the contour-plot for the highest energy occupied KS states (magenta).

Fig. 6.8 summarise the results on the absolute band-alignment for the defective NTs models (see also Fig. 6.5). Owing to their different composition and relaxation, different defects lead to profoundly different absolute energy for the highest-energy occupied and lowest-energy unoccupied KS. The highest-energy occupied states are found for the D2, h-D3 and D4 defects (-4.69/-4.46 eV). Conversely, the lowest-energy unoccupied states are found for the D3 defect. Given the strong localisation of these defect-states (Figs. 6.6, 6.7, and C.2 in the Appendix C), these results suggest the possibility of defect-mediated e*-h separation via energetically advantageous relaxation to different defect-sites in the NTs, with the ensuing creation, pending electron (hole) transfer kinetics considerations, of highly localised oxidising (reducing) centres at the defective centres receiving the hole (electron) i.e. D2 or h-D4 (D3 or h-D4).

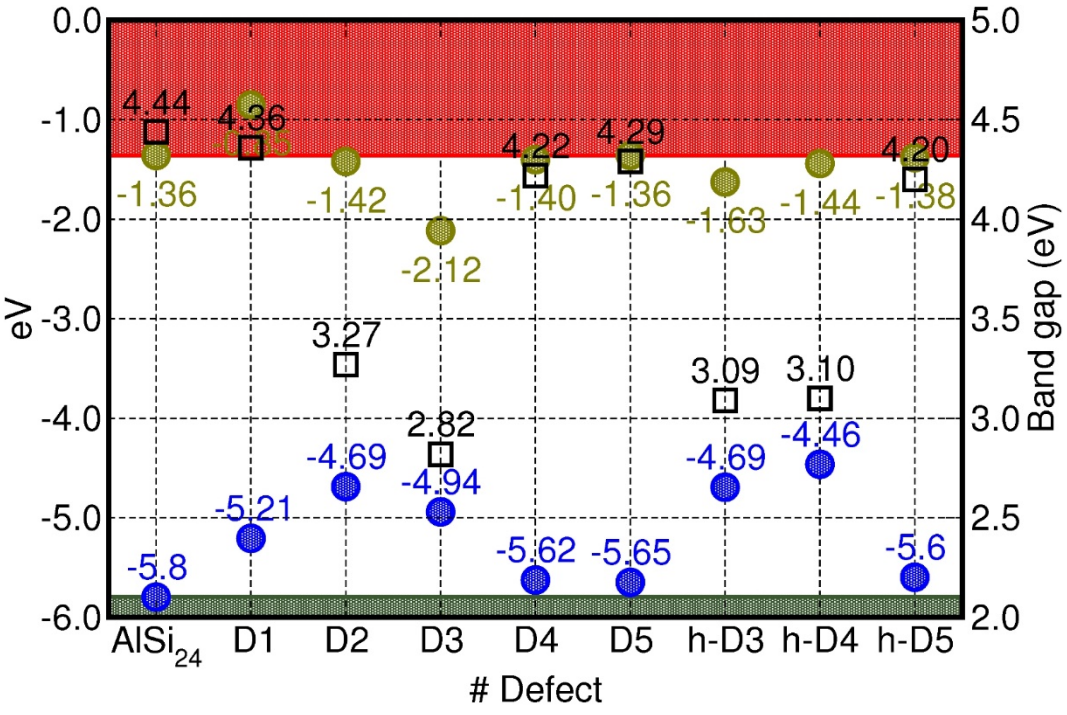

Figure 6.8. Computed vacuum-aligned VB (blue) and CB edges (ochre) for the considered defective NTs and the pristine AlSi NTs. The pristine NT VB and CB edges are marked by the green (-5.80 eV, see Table 5.3) and red (-1.36 eV, see Table 5.3) continuous lines, respectively. The calculated BG of the different defective structures is reported as black squares.

6.3.4 Optical absorption of $AlSi_{24}$ defects

As commented in Chapters 5 and 6, despite the increasing interest in AlSi and other Imogolite NTs, characterization of their optical properties and the extent to which they are affected by defects has not been published yet. To start filling to this knowledge gap, here we consider the optical properties of the considered defects and discuss their role in altering the optical absorbance of the pristine AlSi NTs.

The calculated spectra for the pristine NT and all the considered defective structures are presented in Fig. 6.9. The procedure to compute the imaginary part of the dielectric function $\varepsilon_2(\omega)$ is detailed in Chapter 2 (Section 2.3.8). We recall that large values of $\varepsilon_2(\omega)$ indicate large optical absorbance. The choice of approximating the optical absorption spectra via $\varepsilon_2(\omega)$ stems from the limitations of the adiabatic local density approximation (ALDA) for LR-TDDFT simulations of periodic semiconductor [22].

In spite of limitations due to the neglect of non-local e*-h interaction and relaxation in the simulated spectra, this approach can conveniently provide information on the role of the considered defects for the optical properties of the AlSi NTs. All the spectra were simulated at PBE level. Hence, and due to the PBE underestimation of BGs (overestimation of VB-edges, underestimation of CB-edges) the optical transition energies are expected to be underestimated.

All the simulated spectra present a main peak at ~ 5.5 eV and a low energy absorbance shoulder at $\sim 4.9 - 5.0$ eV. The secondary shoulder is particularly evident in the spectrum for the pristine defect-free NTs. Of extreme interest from a photo-catalytic standpoint is the feature in the D3 spectrum that extends from ~ 2.9 eV to ~ 4.0 eV. In principle, the presence of this tail suggests the possibility of visible light photo-excitation in the AlSi NTs. Such possibility could further increase the interest in the potential of the AlSi NTs as photo-catalyst.

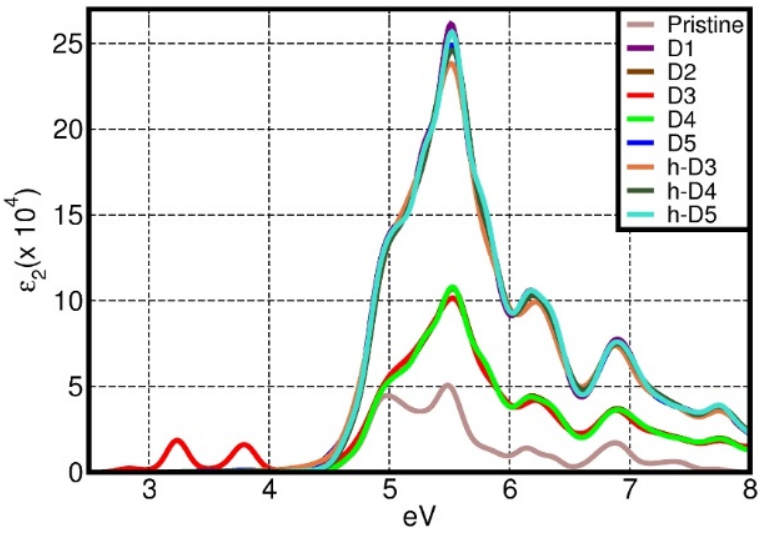

Figure 6.9. Calculated imaginary component of the dielectric function [$\varepsilon_2\hbar\omega$)] for the defective structures and the pristine NTs.

Comparison between the calculated spectra suggests a larger optical absorbance with respect to the pristine NTs for all the defective structures. Thus, defective NTs absorb more light than defect-free one. The magnitude of $\varepsilon_2(\hbar\omega)$ for D1, D5, h-D3, h-D4, h-D5 is five time larger than for the defect-free NTs. For D2, D3, and D4 $\varepsilon_2(\hbar\omega)$ is twice the value obtained for the original NTs. While a clear connection trend between the local bonding of defect and the value of $\varepsilon_2(\omega)$ cannot be easily drawn it is interesting to note the extremely similar shapes of the defects spectra (exception made for the tail in the D3 case) and the fact that protonation of D3 and D4 defects (likely for the defective NTs in water solution) results in increased optical absorbance.

Analysis of the optical matrix elements (Fig. 6.10) indicates that the defects states dominate the low energy shoulder of the absorbance peak with different secondary contributions to the main absorbance peak at 5.5 eV, D5 being the system with the largest contribution to the main peak. Given the overwhelming number of transitions between non defect-localised states, the overall shape of the main 5.5 eV peak is found not to strongly depend on the specific defect.

With the exception of D3, whose protonation into h-D3 leads to disappearance of the absorbance peaks below 4eV, protonation of D4 and D5 into h-D4 and h-D5 is found to qualitatively not affect the predominance of defect-centred transitions for the low-energy shoulder of the absorption peak. It is worth noting that the absolute absorbance of h-D3-5 is increased by roughly a factor two with respect to the deprotonated counterparts (D3-5). Thus, protonation of the negatively charged defects, likely to happen in aqueous environment, is computed to boost the optical properties of defective NTs. On this basis, alteration of synthetic protocols to try to minimize the defect-concentration may be counterproductive if interested

in NTs with strong optical absorbance. Whether the same holds also for other aluminogermanate and chemically functionalized Imo-NTs deserve further dedicated investigations.

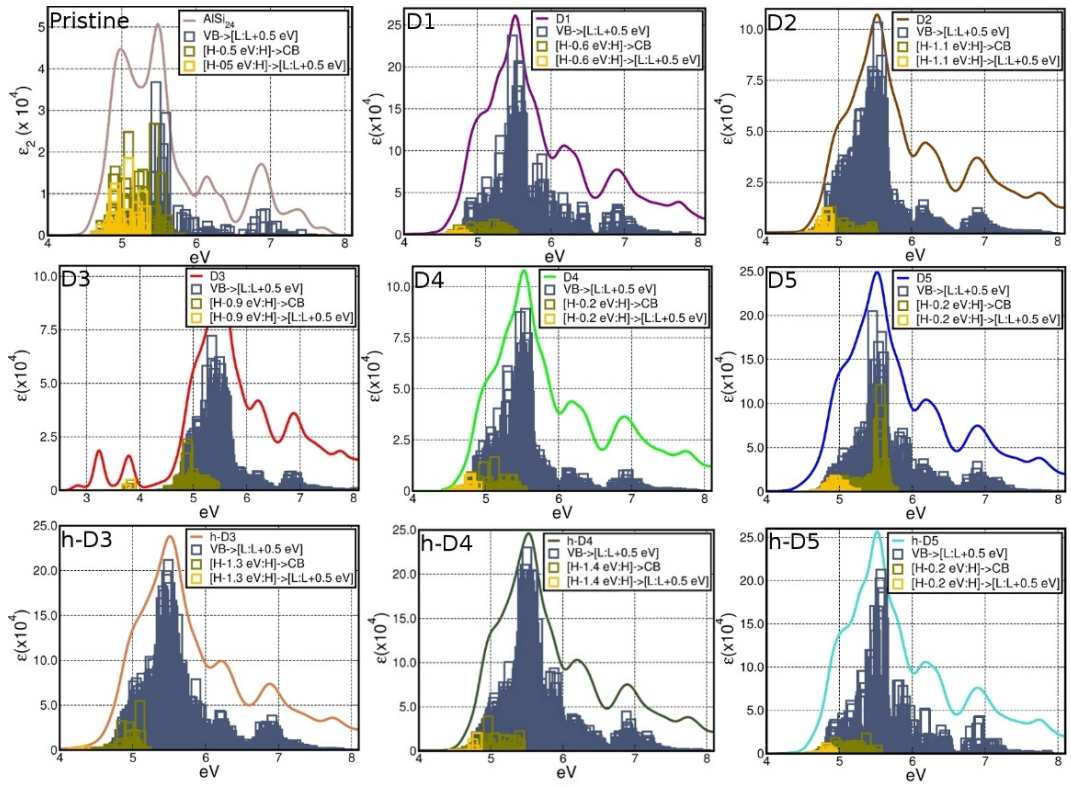

Figure 6.10. KS-resolved analysis of the largest contributions to the low energy values of $\varepsilon_2(\omega)$ for the defects simulated. H (HOMO) and L (LUMO) indicate the highest-energy occupied and lowest-energy empty KS-state, respectively. The CB edges include the KS-states within 0.5 eV from L. The VB edge comprises the defect KS-states at the top of the VB. Excitations between VB and CB edges are marked as "[H-X.X eV:H]→[L:L+0.5 eV]" (X.X depends by the energy position of the last defect state and is reported in each panel separately). Excitations from the VB-edge to the whole CB and from the whole VB to the CB-edge are marked as "[H-X.X eV:H]→CB" and "VB→[L:L+0.5 eV]", respectively.

6.3.5. H_2O at defective $AlSi_{24}$ NTs

In Chapter 5 we focused on the effects of the AlSi NT-wall polarisation on adsorbed reactants. The NTs wall-polarisation is of particular interest because, besides possibly enhancing e*-h separation, it may allow strategies to force reactants to match the band-edges of the polarising photo-catalyst. Furthermore, the NT-wall polarisation could also be used to

alter the electronic line-ups of differently polarizable photo-catalysts and reactants inside the NT-cavity.

In Chapter 5, the effects of the NT-wall dipole density on two water molecules placed on opposite sides of the NT-cavity has been analysed and discussed. As result of the interaction with the polarised and polarising NT-wall, the water HOMO (LUMO) levels were shifted up (down) in energy inside (outside) the NTs cavity. These results suggest the possibility of tailoring the electronic line-ups between reactants and photo-catalysts via use of polarising photo-catalysts.

The presence of defects alters the structure and spatial charge distribution in the NT-walls. As a result, it can locally change the NT-polarisation. Given the loss of cylindrical symmetry due to the presence of defects, the approach used in Chapter 5 to calculate the NT-wall dipole density cannot be meaningfully applied to the defective structures. Nonetheless, an indirect estimate of the dipole density of the NT-wall can be obtained from the alignment of H_2O molecules interacting with the defects on either sides of the defective NT-wall. The occurrence and extent of the induced energy-shifts for the adsorbed water molecules can be taken as indicative of the existence of polarisations across the NT-wall and his changes from the defect-free NTs.

This approach was tested on three different structures representative of the three types of defect analysed in this work: a neutral defect (D2), a charge defect (D3) and its hydrogenated correspondent (h-D3). Table 6.2 reports the shortest distance between the H_2O molecules and the defective NTs frame (Fig. 6.11), together with the computed Mulliken charges for the H_2O molecule. The strength of the H-bonding, quantified by the H-bond distance, between the H_2O molecules and the NTs varies from case to case depending on the local arrangement of the atoms in the defective structures. Depending on the considered defect, adsorption of H_2O molecules inside or outside the NT-cavity leads to longer (D2-3, inner and outer adsorption) or shorter (D3, outer adsorption and h-D3 inner and outer adsorption) H-bond lengths.

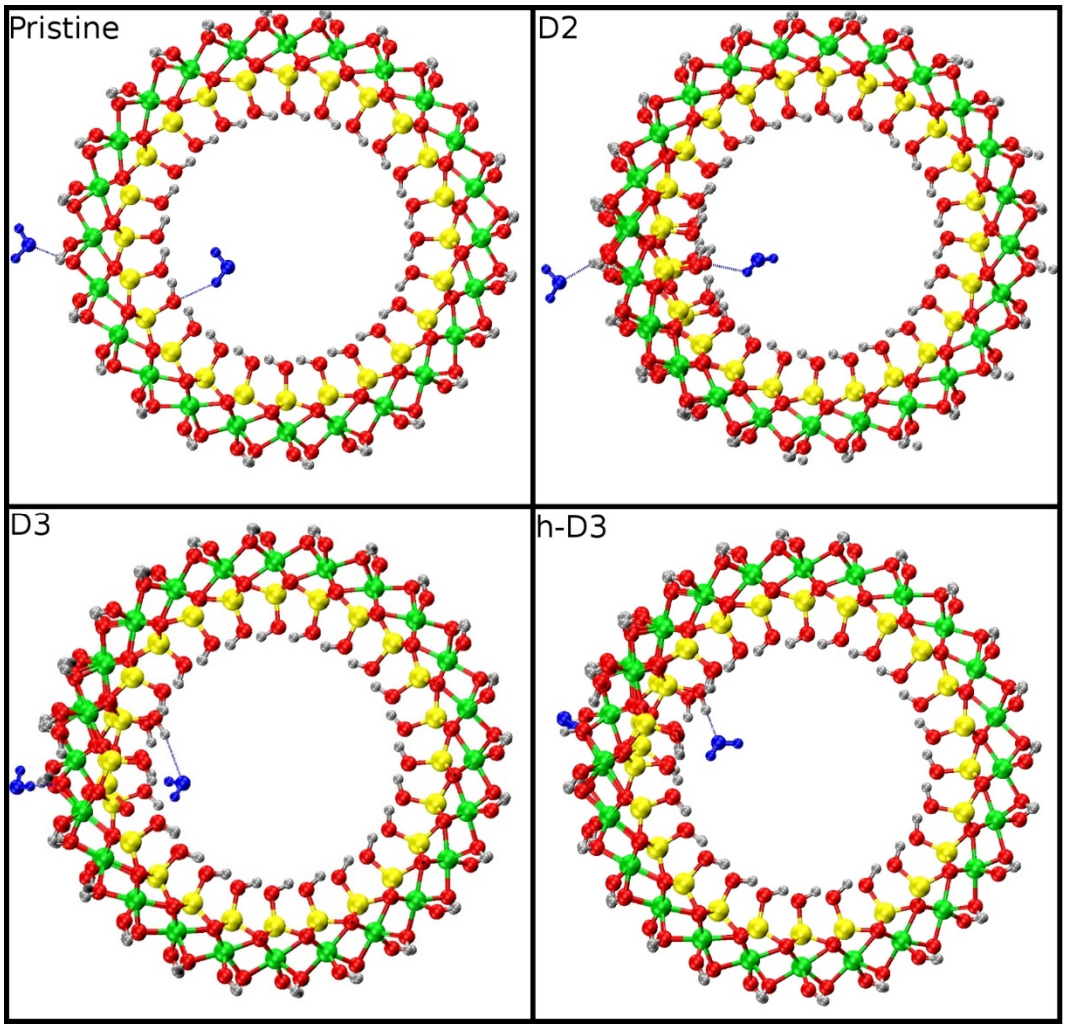

Figure 6.11. Close up of the optimised geometry of the considered $2H_2O$@Imo NTs models for D2-3 and h-D3. The shortest H_2O-NT H-bonding distances (see also Table 6.2) are highlighted by dotted lines. The adsorbed H_2O molecules are highlighted in blue. Same atom-colour labelling as in Fig.6.3.

As for the pristine NT (Chapter 5, Table 5.4), H_2O adsorption on the outer defective NT-wall leads to H-bond distances shorter than for H_2O molecules inside the NT-cavity. This result anticipates that, even in the presence of defects, the NT-wall retains residual polarisation and accumulation of negative (positive) charge inside (outside) the NT-cavity.

The charge transfer between the defective NT-wall and the adsorbed H_2O molecules does not present a clear trend, and appears to be dominated by the local defect structure rather than the NT-wall polarisation (Table 6.2).

	d (Å)	q (e)
Pristine	2.38 (2.09)	-0.01 (+0.05)
D1	2.61 (2.21)	-0.04 (-0.02)
D2	2.41 (2.43)	-0.01 (+0.01)
D3	2.54 (1.95)	+0.00 (-0.04)
h-D3	1.97 (1.88)	+0.06 (-0.10)

Table 6.2. The shortest H_2O-NT (H-bond) distances (d, Å) and Mulliken charges (q, e) for the H_2O molecule inside (outside) the considered defective structures.

The vacuum aligned LDOS for $H_2O@AlSi_{24}$ NTs (Fig. 6.12) readily shows the effects that the defects have on the dipole density of the NT-walls. Clearly indicating a more electronegative (positive) potential at the inner (outer) defective surface of the NTs, the HOMO and LUMO of the inner water molecule are shifted to higher energies with respect to the outer H_2O molecule. Equivalently, a downward shift of the HOMO and LUMO of the outer H_2O molecule is observed. The relative energy shift between the HOMO and LUMO of the inner and outer H_2O molecules are however smaller ($\sim$1.8 eV for D2, $\sim$2.3 eV for D3) with respect to the original NT ($\sim$3.0 eV) and markedly dependant on the specific defect geometry.

The h-D3 defect shows properties different from those of the D2 and D3 systems. Specifically, due to the profoundly different local bonding of the H_2O molecules on the protonated h-D3 site (Fig. 6.11), the HOMO of the inner molecules is now down-shifted in energy by roughly 1 eV with respect to the HOMO of the outer molecule. The LUMO of the inner molecule is also shifted downwards, with the LUMO of the outer molecule remaining above the vacuum-level (0 eV, thence with a negative EA [23]), in stark contrast with the results for H_2O molecules adsorbed at D1, D2 and D3 sites. These results indicate that, owing to the different atomic structure, relaxation and HB pattern of the interacting H_2O molecules, the NT-wall polarisation is inverted with accumulation of overall negative (positive) charge outside (inside) the defective NT-wall.

As shown in Table 6.2, the calculated inversion of the NT-dipole density stems from the substantially stronger HB of the H_2O molecules with the h-D3 site, leading to noticeably shorter HB distances and larger transfer of charge. It is worth recalling that the dipole-density is an interface properties involving charge re-distribution across the whole H_2O/NT-wall/H_2O interface. Accordingly, it cannot be completely described by considering H_2O Mulliken

charges alone. In spite of this, the computed downshifting of the HOMO and LUMO states for the inner H_2O molecule with respect to the outer one, conclusively indicate an inversion of the NT-wall dipole density with respect to the pristine NTs and the D2 and D3 defects.

Thus, apart from the h-D2 case, the presence of defects is found to generally decrease the NT-wall dipole density, albeit not cancelling it. The residual polarisation in the D2-3 cases is calculated to be large enough to bias the electronic alignment of H_2O molecules adsorbed inside and outside the NT cavity. When combined with results from the absolutely aligned VB-edges (Fig. 6.8), it turns out that the occurrence of cation-vacancy defects in AlSi NTs should be compatible with selective oxidation, inside the NT-cavity, of adsorbates at the defect-sites.

As in the previous Chapter, some notes of caution are in place. In spite of the favourable alignment, the defective NT→H_2O hole-transfer kinetics, which could be extremely slow making the process unviable, has not been considered in our analysis. The results presented refer to defective models in vacuum, which cannot capture solvent related screening of the NT-wall polarisation [24, 25]. Accordingly, the models may not provide an accurate description of the real photo-chemistry of the solvated system. Last, but not least, the calculated electronic alignment is based on the use of KS states which, apart from the highest energy occupied one, do not have strong physical meaning in terms of the photo-catalytic acceptor and donor states [26, 27]. Although these limitations do not permit a thoroughly realistic description of the defective NTs, the simulations presented undoubtedly represent a first step in this direction.

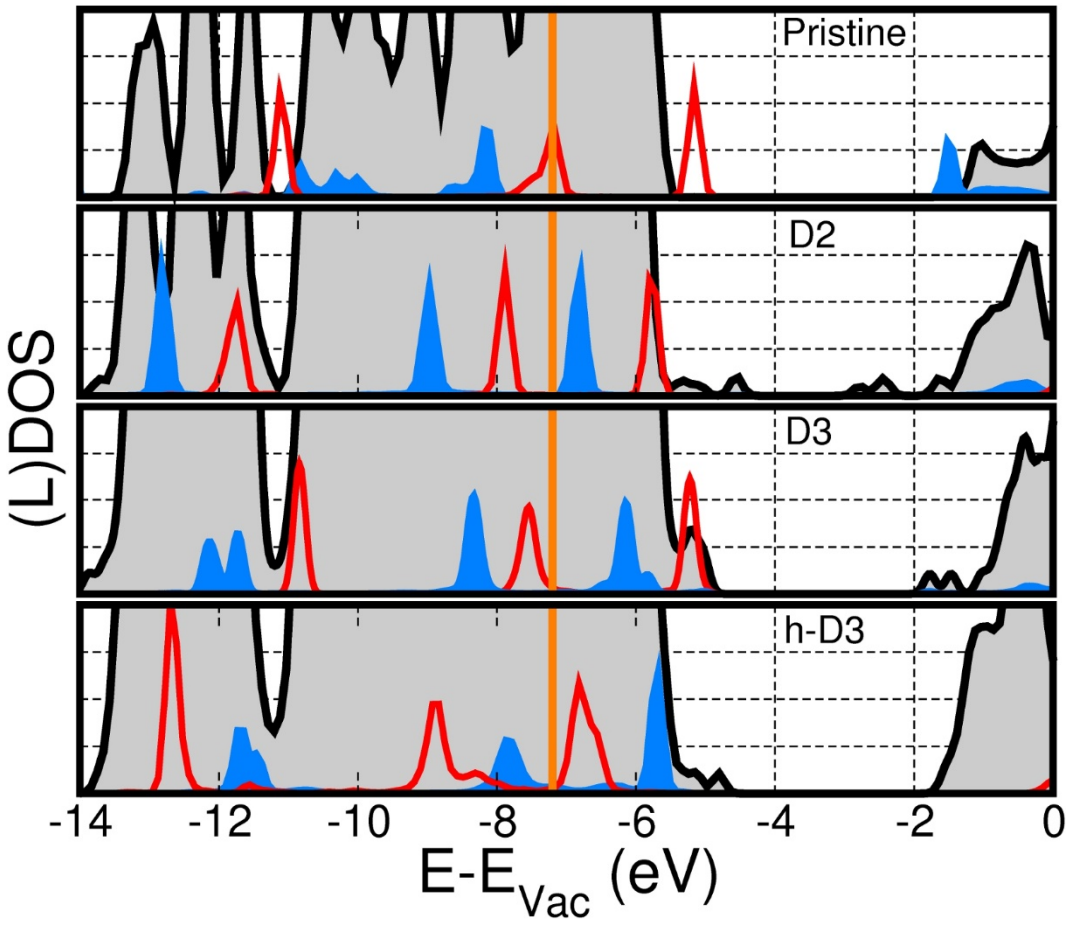

Figure 6.12. NT (filled grey) and H_2O-resolved, vacuum-aligned, LDOS for H_2O molecules adsorbed on the defective NT-walls (same defect labelling as in Fig. 6.6). The inner H_2O and outer H_2O LDOS are displayed in red and blue, respectively. The PBE-DFT HOMO energy of one isolated H_2O molecule (-7.2 eV) is marked by the orange vertical continuous line. In accordance with results from the literature [23], the PBE-DFT LUMO energy for one isolated H_2O molecule is above the vacuum-level (0 eV) and not shown in the graph (+0.629 eV).

6.4. Conclusions

Simulation of the five defect structures (D1-5) proposed in Ref. [1], and the hydrogenated counterparts for D3-D5 defects with an overall net charge, either isolated or interacting with two H_2O molecules indicates that:

i) The presence of defects induces local deformations to the NT structure. These deformations involve almost exclusively the outer Al-O octahedrons and the external O-H bonding.

ii) All the defects leads to appearance of defect-states localised in energy at the top of the VB. Apart from D3 the CB is generally unaltered. The occupied defect states are found to be highly localised around the defect site.

iii) Vacuum alignment of the VB and CB edges for the considered defects suggests the possibility of defect-mediated separation of photo-generated e*-h pairs via preferential diffusion of e* and h to different defects (e*: D3; h: D2 or h-D4).

iv) The optical absorbance of the defective NTs is notably larger with respect to the pristine NTs (two or five-fold increase depending on the defect). The low-energy shoulder of the absorbance peak for the D3 defect lies below 3 eV i.e. in the visible in the visible-region of the light-spectrum.

v) The NT wall polarisation is affected by the presence of defects. Although damped by the defect reconstruction, the direction of NT-wall dipole density is found to be maintained for the D2 and D3 defects. Conversely, and due to the profoundly different relaxation of the defects, h-D3 is computed to lead to inversion of NT-wall dipole density.

vi) As a result of iii) and v), photo-oxidation of adsorbates on the inner NT-wall is predicted to be energetically viable for D2 and D3. Conversely, photo-oxidation on the outer surface of h-D3 should be energetically preferred. Further research is needed to uncover the hole-transfer kinetics at the defective NTs.

References

[1] Yucelen G I, Choudhury R P, Leisen J, Nair S and Beckham H W 2012 *J. Phys. Chem. C.* **116** 17149.

[2] Barrer, R. M. *Hydrothermal Chemistry of Zeolites.* Academic Press, New York, 1982.

[3] Perdew J, Burke K, and Ernzerhof M 1996 *Phys. Rev. Lett.* **77** 3865.

[4] Gonze X, Stumpf R, Scheffler M 1991 *Phys. Rev. B* **44** 8503.

[5] http://opium.sourceforge.net/sci.html.

[6] Pfrommer B G, Côté M, Louie S G, and Cohen M. L 1997 *J. Comput. Phys.* **131** 233

[7] Hine N. D., Dziedzic J., Skylaris C. K., Haynes P. D. J.Chem.Phys 2011 **135** 204103

[8] Wilkinson K A, Hine N D M, and Skylaris C-K 2014 *J. Chem. Theory Comput.* **10** 4782

[9] Neugebauer J., Kresse G., Janotti A., Van de Walle C. G. *Rev. Mod. Phys* 2014 **86** 253.

[10] Limpijumnong S.,Van de Walle C. G. *Phys. Rev. B* 2004 **69**, 035207.

[11] Del Vitto A., Pachioni G., Delbecq F., Sautet P. *J. Phys. Chem. B* 2005 **109** (16) 8040.

[12] Wendt S., Schaub R., Matthiensen J. *Surf. Science* 2005 **1** (3) 226.

[13] Wörz A. S., Heiz U., Cinquini F., Pacchioni G. *J. Phys. Chem. B* 2005 **109** (39) 18418.

[14] Teobaldi G, Beglitis N S, Fisher A J, Zerbetto F and Hofer W A 2009 *J. Phys. Condens. Matter*. **21** 195301.

[15] Mukherjee S, Bartlow V M and Nair S 2005 *Chem. Mater*. **17** 4900.

[16] Kang D Y, Zang J, Wright E R, McCanna A L, Jones C W and Nair S 2010 *ACS Nano* **4** 4897.

[17] Mukherjee S, Kim K and Nair S 2007 *J. Am. Chem. Soc.* **129** 6820.

[18] Yucelen G I, Choudhury R P, Vyalikh A, Scheler U, Beckham H W and Nair S 2011 *J. Am. Chem. Soc.*, **133** 5397.

[19] Casey W. H. *Chem. Rev*. 2006 **106** (1) 1.

[20] Lany S., Zunger A. *Phys. Rev B.* 2008 **78** 235104.

[21] Pantelides S. T. *Rev. Mod. Phys*. 1978 **50** 797.

[22] Onida G, Reining L and Rubio A 2002 *Rev. Mod. Phys.* **74** 601.

[23] Jonathan C. Rienstra-Kiracofe, Gregory S. Tschumper, and Henry F. Schaefer III. *Chem. Rev.* **2002,** *102*, 231-282.

[24] Lever G, Cole D J, Hine N D M, Haynes P D, and Payne M C 2013 *J. Phys.: Condens. Matter* **25** 152101

[25] Cheng J and M. Sprik M 2012 *Phys. Chem. Chem. Phys.* **14**, 11245.

[26] Janak J. F. 1978 *Phys. Rev. B* **18** 7165.

[27] Sau, J D, Neaton J B, Choi H J, Louie S G, and Cohen M L 2008 *Phys. Rev. Lett.* **101** 026804.

Chapter 7

Terminations effects in Imogolite NTs

Abstract

In this Chapter termination-induced effects in finite aluminosilicate (AlSi), methylated aluminosilicate (AlSi-Me) and aluminogermanate (AlGe) NTs are investigated. The Chapter begins with exploration of the smallest finite-model capable of simultaneous description of the NT-ends and bulk-like NT-core. Following identification of such critical size, the energy, electronic properties and optical absorption of different NT-terminations are presented and discussed. Besides the previously presented localisation of the Valence Band (VB) and Conduction Band (CB) edges on different sides of the NT-cavity, the simulations uncover the presence of longitudinal band-bending in the NT-models brought about by structural relaxation of the NT-ends. This longitudinal band-bending is accompanied by occurrence of appealing core-periphery VB ad CB edge separations, which in turn suggest energetically advantageous mechanisms for separation of photo-generated e*-h pairs along the NT. The competition between longitudinal e*-h relaxation and defect trapping is finally analysed and discussed.

7.1 Introduction

As previously noted (Chapters 4 and 5), with the exception of the (non-atomically resolved) Transmission Electron Microscopy images for AlSi and AlGe NT thin-films reported in [1], very little is currently known on the structure of the Imo NTs' open-ended extremities with effectively non-existing insight into termination-induced effects on the NTs electronic and optical properties as well as their chemical reactivity [2-32].

Given the crucial role of termination-induced relaxation and reconstruction effects for the properties and reactivity of metal-oxide surfaces [33, 34, 35], it is reasonable to suspect that end-relaxation in open-ended Imo NTs may also lead to properties noticeably different from the bulk-like core regions of the tubes. This motivates our interest in the matter and this final, computationally very demanding, Chapter.

As shown in Chapter 4, by fully exploiting the potential of linear-scaling DFT in the ONETEP program, simulations of finite models of AlSi NTs can be effectively carried out on academically available hardware. In this Chapter we push the possibility of ONETEP (and of the hardware accessible to the group) to its very limit by exploring the termination of larger AlSi-Me and AlGe (NTs). Following Chapter 5, we limited our study at AlSi-Me and AlGe NTs with 28 and 36 Al-atoms, respectively.

The Chapter is organized as follows. After presentation of the computational details of this study (Section 7.2) we investigate the relaxation and convergence of the results for different sizes of the finite NT-models and different terminations (7.3.1 and 7.3.2). The electronic structure and optical properties of the optimised models is then presented and discussed in Sections 7.3.3 and 7.3.4, respectively. The Chapter ends with a discussion of the photo-generated e*-h relaxation mechanism uncovered by the simulations, also in relation to its possible competition with trapping processes at the defect-sites presented in Chapter 6. The Chapter is briefly concluded by highlighting the main conclusions, which can be drawn from our, to best of our knowledge unprecedented for size and ambition, DFT investigation.

7.2 Methods

In all cases, the PBE functional [36] and separable (Kleinman-Bylander) norm-conserving pseudopotentials [37] were used. The adopted kinetic energy cutoff was 1000 eV and 4 (9) valence and conduction NGWFs were used for O (Al,Si) atoms. 1 NGWF was used for H atoms. In all cases, no truncation of the valence and conduction density kernel (see Chapter 2) was enforced. The localization radius for the valence (conduction) NGWFs was 8 Bohr (15 Bohr). The conduction NGWFs optimization was performed for 100 empty Kohn-Sham (KS) states, which was numerically tested to yield sub-meV convergence of band gaps (BGs) and CB edges. The procedure for conduction NGWFs is explained in Chapter 2 (Section 2.3.8).

All simulations were performed with periodic boundary conditions ensuring at least 15 Å vacuum separation between replicated images of the finite periodic tube models. Geometry-relaxations where performed via the quasi-Newton optimization scheme based on the Broyden-Fletcher-Goldfarb-Shanno (BFGS) algorithm [38]. Grand canonical formation energies, E_{form}, were computed as [39]:

$$E_{form} = E_{tot} - NE_N - n_i\mu_i \quad (7.1)$$

where E_{tot} is the total energy of the finite NT-model. N is the (integer) number of NT building blocks of energy E_N (calculated from the periodically repeated NT) present in the model. n_i is the number of extra atoms of species i in the system, of chemical potential μ_i , that need to be added to the N NT-building blocks to recover the stoichiometry of the finite-NT model. μ_i was approximated via the (PBE) DFT energy of the bulk or molecular reference for the given atom (bulk Ge and Si in diamond structure, bulk hpc Al, C in graphite, isolated singlet H_2 molecule, isolated triplet O_2 molecule.

Vacuum-aligned KS-states were obtained from simulation with cylindrically truncated electrostatics [40] (see also Chapter 2.3.9). The truncation radii were numerically checked to yield sub-meV convergence of the results.

The optical spectra were approximated by mean of the imaginary part of the system dielectric function (ε_2) as explained in Chapter (Section 2.3.8).

7.3 Results and discussion

7.3.1 Models of AlSi, AlSi-Me and AlGe NTs terminations

As previously noted in Chapter 4, due to the structure of AlSi, AlSi-Me and AlGe-NTs, two neutral terminations are possible (Fig. 7.1). In one case, referred to as the H_2O- termination, the aluminium hydroxide network of the NT is truncated and the terminal under-coordinated Al-atoms saturated with one H_2O molecule (instead of one hydroxyl, –OH) to maintain electro-neutrality. In the other, referred to as the OH-termination, the NT terminal Si (Ge) atoms maintain a 4-fold coordination by addition of one extra hydroxyl (OH) group (instead of a dangling Si-O or Ge-O bond). Also in this case, this additional hydroxyl is needed to maintain electro-neutrality. Although in reality the NTs may well present less idealised terminations, with electroneutrality maintained by mean of defects and counterions (see Chapter 6), the considered models represent the first step ever towards exploration of the properties of NTs terminations and their characterization is expected to be valuable to the experimental community as well as to stimulate further computational research in the topic.

In order to identify the smallest possible model capable of simultaneously accounting for both the *core* and *terminal* regions of the NTs, different systems were created based on the periodically optimised structure for the AlSi (24 Al atoms), AlSi-Me (28 Al atoms) and AlGe (36 Ge atoms) NTs. We studied finite models of increasing longitudinal size measured by the number of complete Al-hexagons (Figs. 7.1 and 7.2) present along the NT-axis. For consistency with Chapter 4, these models will be referred to as hex-3 (3 hexagons), hex-5 (5 hexagons) and hex-7 (7 hexagons). Their overall stoichiometry and number of atoms is

reported in Table 7.1. To prevent the occurrence of large longitudinal polarizations [41] which may affect the geometry optimization of the systems, all the finite NTs model were symmetric with respect to a plane containing the innermost Si-ring (Si_0 in Fig. 7.1).

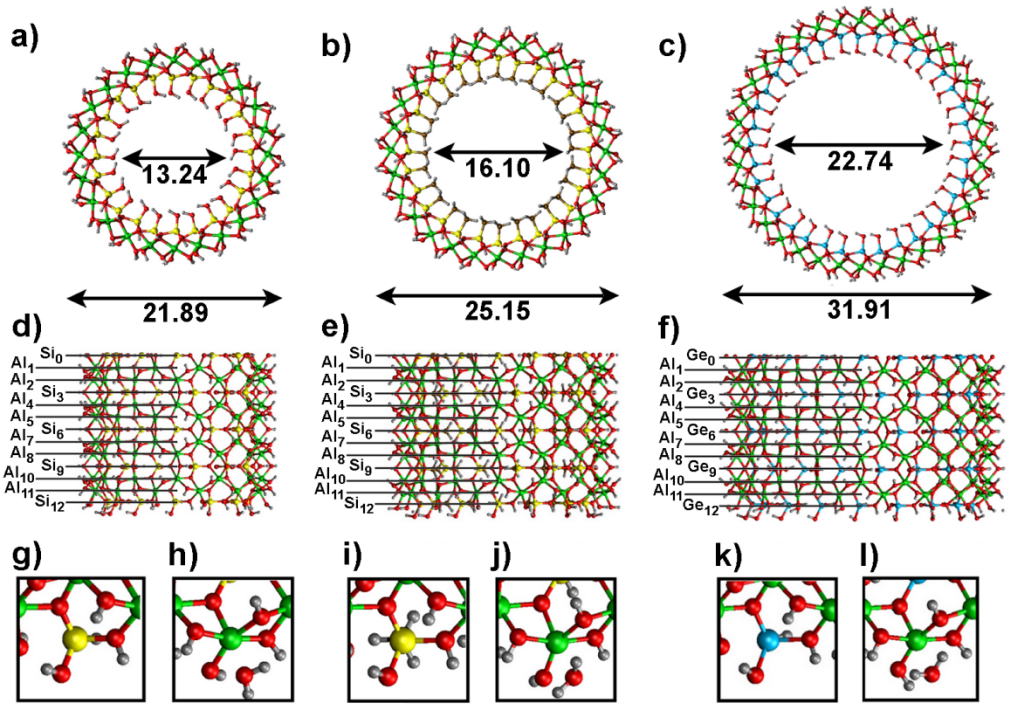

Figure 7.1. Front view of the optimised AlSi (a), AlSi-Me (b) and AlGe (c) finite tube models. Side view of *half* of the hex-7 models for AlSi (d), AlSi-Me (e) and AlGe (f), together with the adopted ring labelling. Close up of the atomic structure of the OH-termination of the AlSi (g), AlSi-Me (i) and AlGe (k) NT-models, together with the H_2O-termination of the AlSi (h), AlSi-Me (j) and AlGe (l) NTs. Al: green, Si: yellow, Ge: cyan, H: gray, O: red, C: brown. The optimised diameter of the NT-models (marked by arrows) is reported in Å.

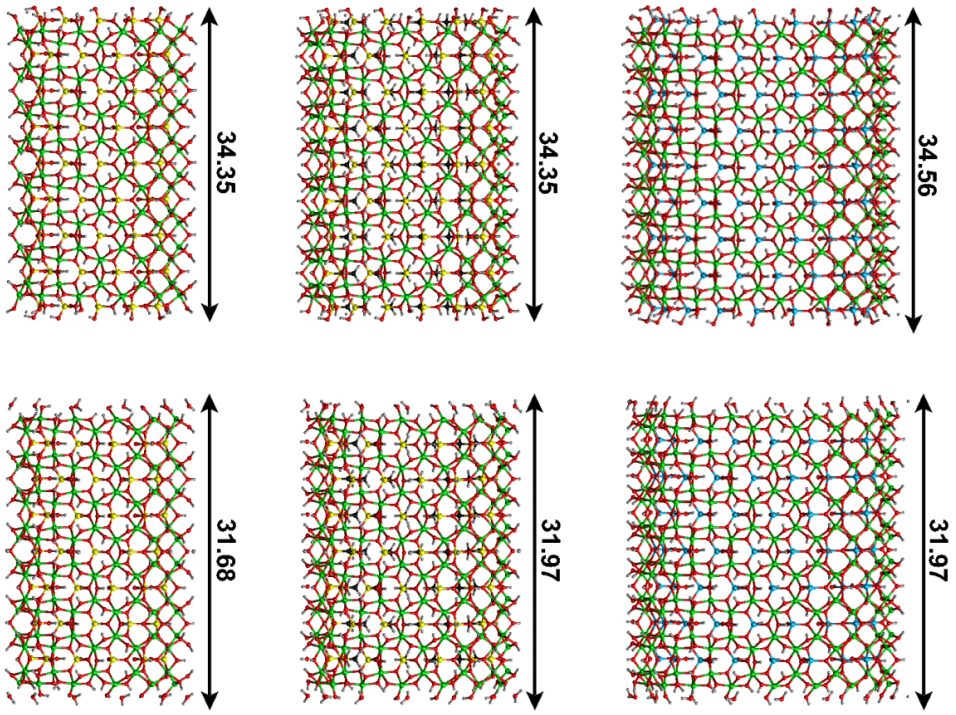

Figure 7.2. Side view of the complete hex-7 models for the AlSi (left), AlSi-Me (middle) and AlGe (right) NTs. OH and H_2O terminations are displayed in the top and bottom panels, respectively. Same colour labelling as in Fig. 7.1. The optimised length of the NT-models (marked by arrows) is reported in Å.

Model	**OH terminated**	**H_2O terminated**
AlSi hex-3	$Al_{96}Si_{60}O_{396}H_{264}$ (816)	$Al_{96}Si_{36}O_{348}H_{264}$ (744)
AlSi hex-5	$Al_{144}Si_{84}O_{564}H_{360}$ (1152)	$Al_{144}Si_{60}O_{516}H_{360}$ (1080)
AlSi hex-7	$Al_{192}Si_{108}O_{732}H_{456}$ (1488)	$Al_{192}Si_{84}O_{684}H_{456}$ (1416)
AlSi-Me hex-3	$Al_{112}Si_{70}O_{392}H_{448}C_{70}$ (1092)	$Al_{112}Si_{42}O_{364}H_{392}C_{42}$ (952)
AlSi-Me hex-5	$Al_{168}Si_{98}O_{560}H_{616}C_{98}$ (1540)	$Al_{168}Si_{70}O_{532}H_{560}C_{70}$ (1400)
AlSi-Me hex-7	$Al_{224}Si_{126}O_{728}H_{782}C_{126}$ (1986)	$Al_{224}Si_{98}O_{714}H_{742}C_{98}$ (1848)
AlGe hex-3	$Al_{144}Ge_{90}O_{594}H_{396}$ (1224)	$Al_{144}Ge_{54}O_{522}H_{396}$ (1116)
AlGe hex-5	$Al_{216}Ge_{126}O_{846}H_{540}$ (1728)	$Al_{216}Ge_{90}O_{774}H_{540}$ (1620)
AlGe hex-7	$Al_{288}Ge_{162}O_{1098}H_{684}$ (2232)	$Al_{288}Ge_{126}O_{1026}H_{684}$ (2124)

Table 7.1. Hex-3, hex-5, and hex-7 model stoichiometry of the OH and H_2O terminations of the AlSi, AlSi-Me and AlGe NTs. The total number of atoms in the simulation cell is reported in brackets.

7.3.2 Structural relaxation of the finite AlSi, AlSi-Me and AlGe NT-models

Based on the results on termination of the AlSi NTs (Chapter 4, Table 4.3), analysis of the relaxation for the (AlSi) AlSi-Me and AlGe NTs was carried out based on the ring-resolved average displacement (<Δr>) and layer-resolved average ring-diameter (<D>). The evaluation of these geometrical descriptors is detailed in Section 4.3.4 and is not repeated here. The computed <Δr> and <D> for the hex-3, hex-5 and hex-7 models of the finite NT-models are displayed in Fig. 7.3 (AlSi), 7.4 (AlSi-Me) and 7.5 (AlGe). In keeping with the convention so far used in this Thesis, the NT radial layers are labelled from the inside to the outside as H_1, O_2 (C_2), Si_3 (Ge_3), O_4, Al_5, O_6, H_7 (see Figs. 4.1 and 5.1).

With an average ring displacement (<Δr>) larger than 0.1 Å for the innermost rings, the hex-3 models turns out to be too small to accommodate relaxation of the tube-extremities in the presence of a structurally unperturbed core-region. This conclusion holds regardless of the composition of the NT (AlSi, AlSi-Me or AlGe) and the H_2O or OH termination.

In contrast to the AlSi case ($<\Delta r>\leq 10^{-3}$ Å for the innermost rings, Fig. 7.3), the computed $<\Delta r>10^{-2}$ Å for the hex-5 models of the AlSi-Me (Fig. 7.4) and AlGe (Fig. 7.5) NTs indicate that the size of these systems is not sufficiently extended to allow simulation of a bulk-like region at the core of the NT. To this end, use of hex-7 models, leading to ($<\Delta r>\leq 10^{-3}$ Å) is necessary.

Comparison between the layer-resolved average ring-diameter (<D>) for the finite and periodically repeated models (Figs. 7.3-7.5) reveal a tendency to relax inwards for the AlSi (Fig. 7.3) and AlGe (Fig. 7.5) NTs. Owing to the presence of the methyl (CH_3) group, such inward relaxation is noticeably hindered for the AlSi-Me NTs (Fig. 7.4) regardless of the termination. The presence of CH_3 groups, as well as the number of Al atoms in the circumference of the NTs is found to affect the details of the radial relaxations with different layers undergoing differently extended relaxations at the NT extremities.

To investigate the relative energies of the OH and H_2O termination, we computed grand canonical formation energies (E_{form}) for the finite models of the AlSi, AlSi-Me and AlGe NTs. Given the indications that hex-7 models are needed for simultaneous converged description of end-relaxation and bulk-like NT-core, this analysis was carried out only on the hex-7 models. The results are displayed in Table 7.2. Owing to the lower disruption to the $Al(OH)_3$ gibbsite layer, the H_2O termination (with an additional H_2O molecule saturating the octahedral coordination of the terminal Al atoms, Fig. 7.1) is computed to be consistently favoured over the OH termination (additional OH saturation of the terminal Si or Ge atoms). The increased E_{form} differences between the H_2O and OH terminations for the AlSi (24 Al-atoms in the circumference), AlSi-Me (28 Al atoms) and AlGe (36 Al atoms) indicates that

the as the NT-diameter increases (Figs. 7.1 and 7.3-7.5) the possibility of stabilising the OH termination via the inner hydrogen-bonding network is partially lost. It is worth recalling that this analysis has been conducting neglecting the role of solvent, which may profoundly alter the computed trends. The study of the role of solvent in altering the NT-relaxation is left to future research.

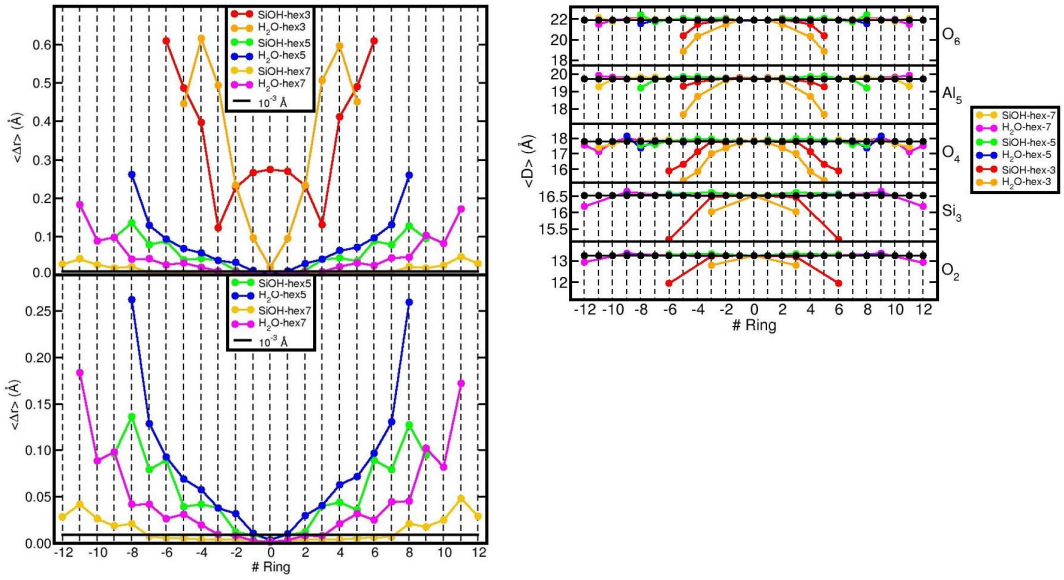

Figure 7.3. Left: ring-resolved average displacement (<Δr>, Å) for the hex-3,5,7 models of the OH and H_2O terminations of the **AlSi NT**. The bottom panel reports a close up of the data for hex-5 and hex-7 models. The black horizontal line marks the 10^{-3} Å displacement threshold. Right: layer-resolved ($O_{2,4,6}$, Si_3, and Al_5, see Fig. 5.1) average ring-diameter (<D>, Å) for the hex-3,5,7 models of the OH and H_2O terminations of the AlSi NT. Results for the periodically optimized NT are displayed has black circles. The adopted ring labelling is displayed in Fig. 7.1.

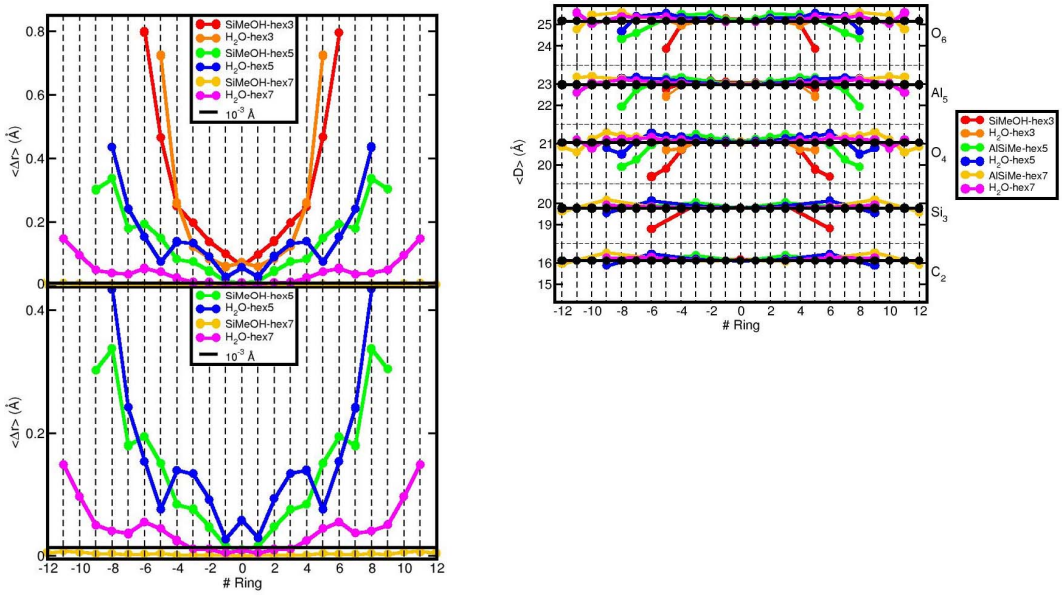

Figure 7.4. Left: ring-resolved average displacement (<Δr>, Å) for the hex-3,5,7 models of the OH and H_2O terminations of the **AlSi-Me NT**. The bottom panel reports a close up of the data for hex-5 and hex-7 models. The black horizontal line marks the 10^{-3} Å displacement threshold. Right: layer-resolved ($O_{2,4,6}$, Si_3, and Al_5, see Fig. 5.1) average ring-diameter (<D>, Å) for the hex-3,5,7 models of the OH and H_2O terminations of the AlSi NT. Results for the periodically optimized NT are displayed has black circles. The adopted ring labelling is displayed in Fig. 7.1.

Model	**OH terminated**	**H_2O terminated**
AlSi hex-7	-95.923	-185.958
AlSi-Me hex-7	-52.531	-203.132
AlGe hex-7	-75.729	-275.15

Table 7.2. Computed formation energy (E_{form}, eV) for the the OH and H_2O terminations of the AlSi, AlSi-Me and AlGe hex-7 NT-models.

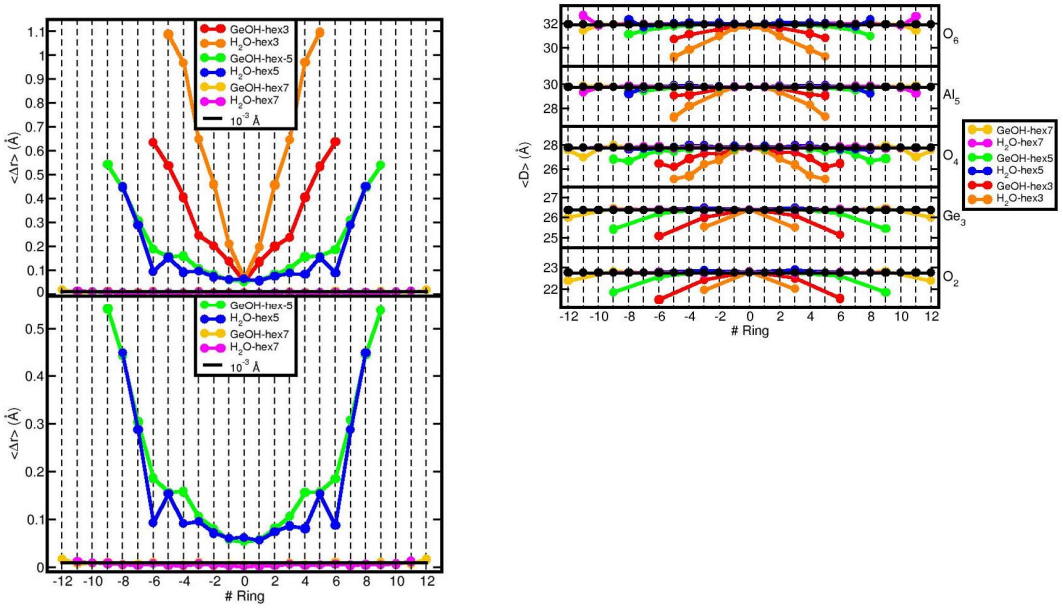

Figure 7.5. Left: ring-resolved average displacement (<Δr>, Å) for the hex-3,5,7 models of the OH and H_2O terminations of the **AlGe NT**. The bottom panel reports a close up of the data for hex-5 and hex-7 models. The black horizontal line marks the 10^{-3} Å displacement threshold. Right: layer-resolved ($O_{2,4,6}$, Si_3, and Al_5, see Fig. 5.1) average ring-diameter (<D>, Å) for the hex-3,5,7 models of the OH and H_2O terminations of the AlSi NT. Results for the periodically optimized NT are displayed has black circles. The adopted ring labelling is displayed in Fig. 7.1.

7.3.3 Electronic structure characterization

In this section we start exploring the role of end-relaxation for the electronic properties of the AlSi, AlSi-Me and AlGe NTs. Given the potentially major influence of the interactions with the solvent in (de)stabilising the two considered terminations, and the impossibility of directly addressing this uncertainty due to the prohibitive computational cost, we considered both the OH and H_2O termination for the hex-7 models.

The vacuum-aligned Density of States (DOS) and layer-resolved local DOS (LDOS) is displayed in Figs 7.6 (AlSi), 7.7 (AlSi-Me) and 7.8 (AlGe). For more compact representation and discussion, the calculated VB and CB edges and BGs have been collected in Fig. 7.9.

The simulations indicate that, regardless of the NT composition, the OH terminations leads to lower VB edges than the H_2O termination. The difference in the VB-edge for the two terminations is largest (0.7 eV) for the AlSi-Me NTs and smallest (0.2 eV) for the AlSi NTs.

The OH-termination is computed to induce also lowering of the CB-edge with respect to the results for the H_2O termination. In this case, however, the changes are reduced with smallest (largest) differences of 0.09 eV (0.13 eV) for AlSi-Me (AlGe) NTs. Accordingly, also the computed BG depends on the NT-termination with the OH termination leading to larger BGs than the H_2O one.

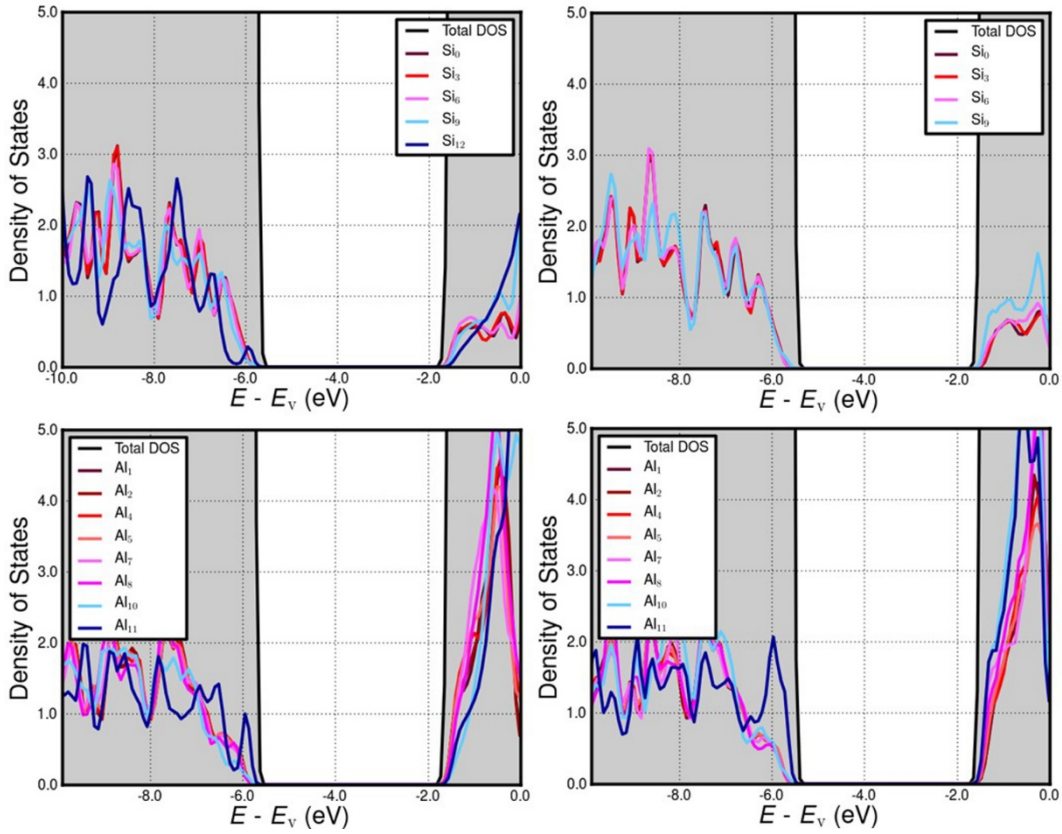

Figure 7.6. Vacuum-aligned total Density of States (DOS) with Al and Si resolved local Density of States (LDOS) for the OH (left) and H_2O (right) terminations of the **AlSi** hex-7 model.

Comparison between the computed BG for the periodic (Table 5.3) and finite NT models (Fig. 7.9) indicate that, apart from the AlSi NTs, the finite models of the AlSi-Me and AlGe NTs can have substantially lower (up to -0.86 eV) BG than the periodically repeated ones. Inspection of the vacuum-aligned VB and CB edges for the finite models (Fig. 7.9) and periodic ones (Table 5.3) reveals that the BG narrowing is mostly due to the termination-induced upshift of the VB edge in the finite models. This result stems from the higher electrostatic potential at the NT-ends with respect to the NT-core (Fig. 7.10), which progressively shift (to higher energies) the termination-centred Kohn-Sham states. Further evidence of this effect can be found in the ring-resolved LDOS analysis shown in Figs. 7.6,

7.7 and 7.8: the further the Al and Si (Ge) atom from the NT-core, the larger its contributions the high-energy edge of the VB.

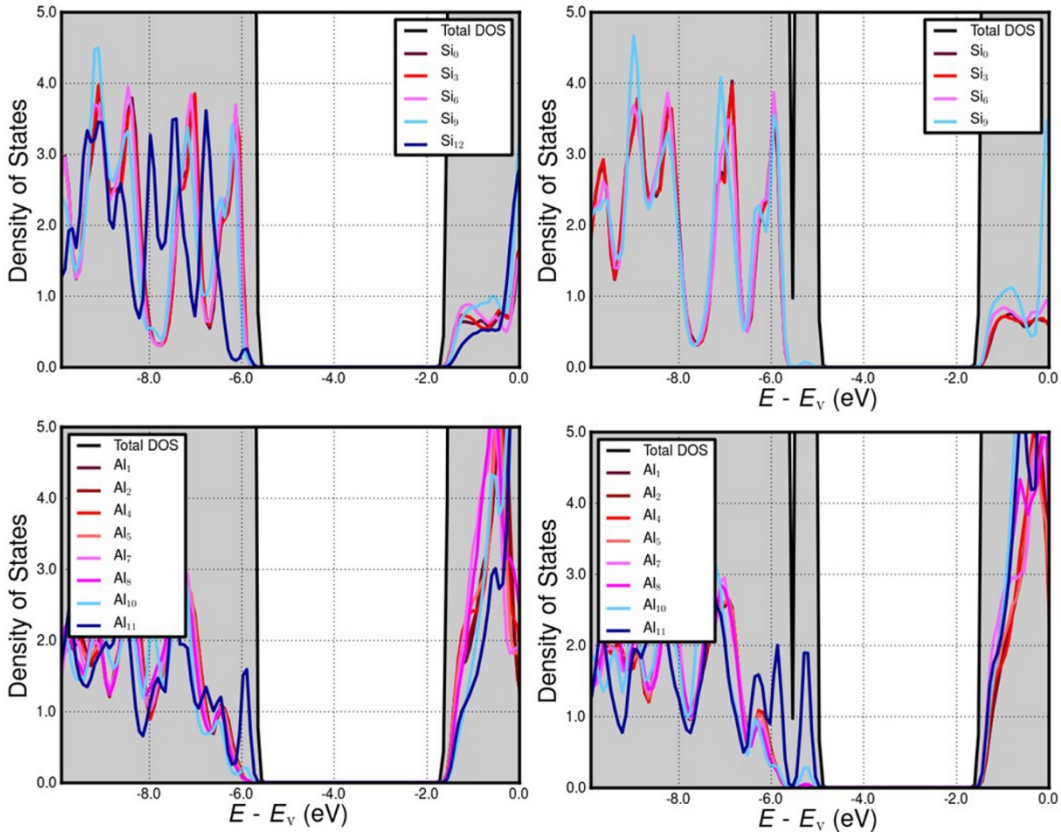

Figure 7.7. Vacuum-aligned total Density of States (DOS) with Al and Si resolved local Density of States (LDOS) for the OH (left) and H_2O (right) terminations of the **AlSi-Me** hex-7 model.

It is worth noting that, contrary to the VB case, comparison between the CB edges for the periodically repeated and finite NT-models (Table 5.3) indicates the latter to have lower VB edges (AlSi and AlSi-Me: ≤-0.2 eV, AlGe: ≤-0.43 eV).In the next Sections, we will consider the significance of these results for possible photo-catalytic application of the NTs.

In Chapter 5, it was found that, associated with a permanent polarization of the NT-wall, the periodically repeated AlSi, AlSi-Me and AlGe NTs consistently present a separation in real-space of the VB and CB edge, with the CB (VB) being localised mostly outside (inside) the NT cavity. Here, we investigate whether the same applies also to the finite models of the NTs. Fig. 7.11 shows the computed real-space distribution of the VB and CB edges for the optimised hex-7 models of the AlSi, AlSi-Me and AlGe NTs.

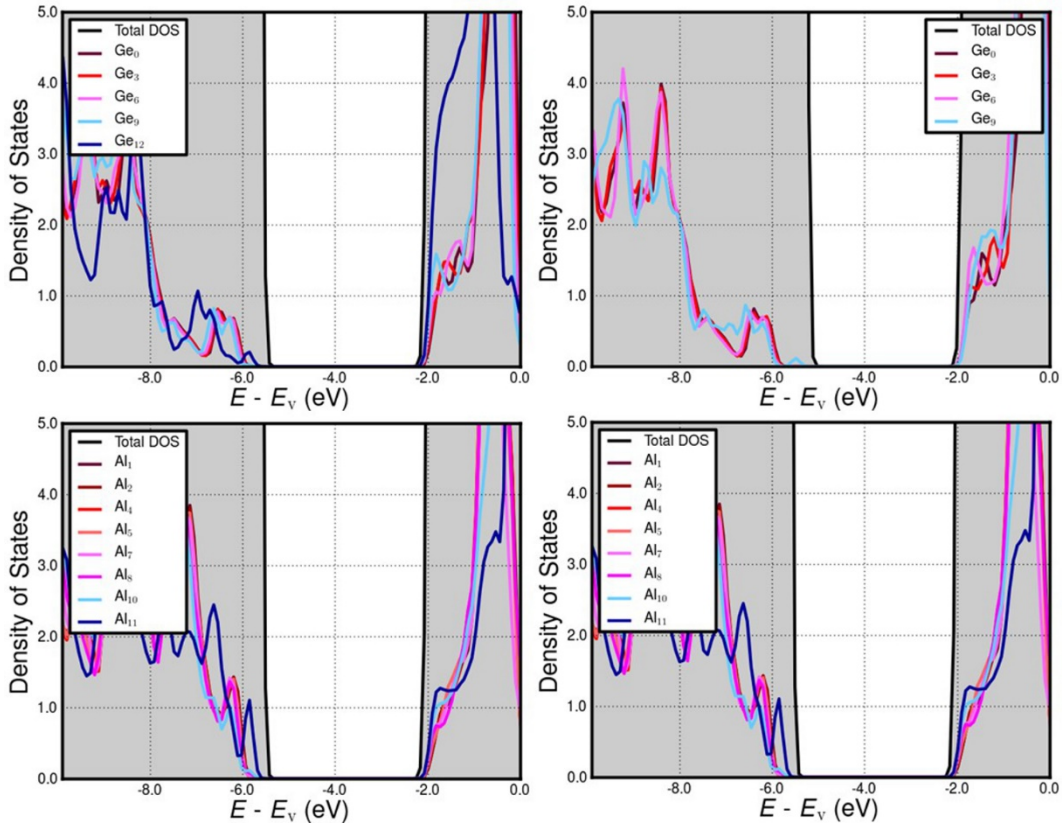

Figure 7.8. Vacuum-aligned total Density of States (DOS) with Al and Ge resolved local Density of States (LDOS) for the OH (left) and H_2O (right) terminations of the **AlGe** hex-7 model.

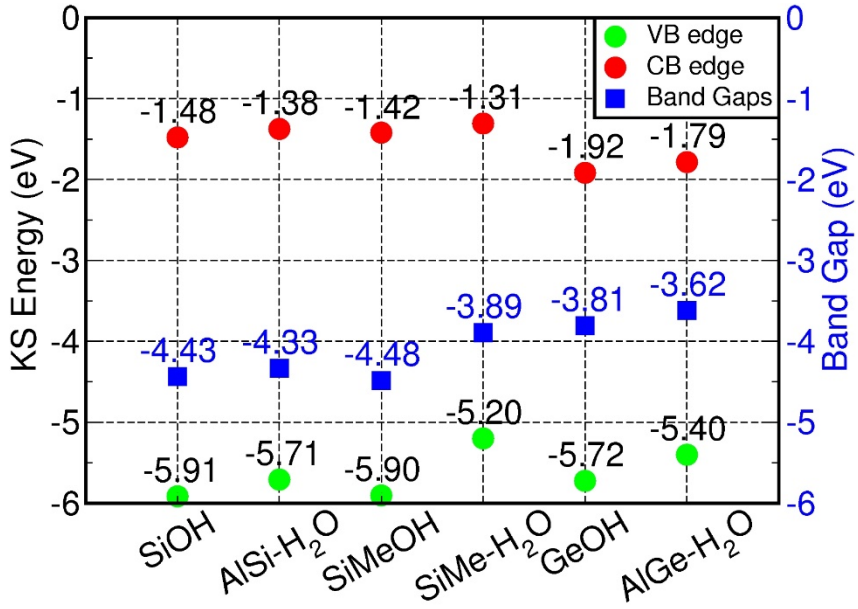

Figure 7.9. Vacuum-aligned HOMO and LUMO energy for the OH and H_2O terminated hex-7 models of the AlSi, AlSi-Me and AlGe NTs together with the computed BGs. The computed BGs for the periodic models (Table 5.3) are 4.44 eV (AlSi), 4.75 eV (AlSi-Me) and 4.35 eV (AlGe).

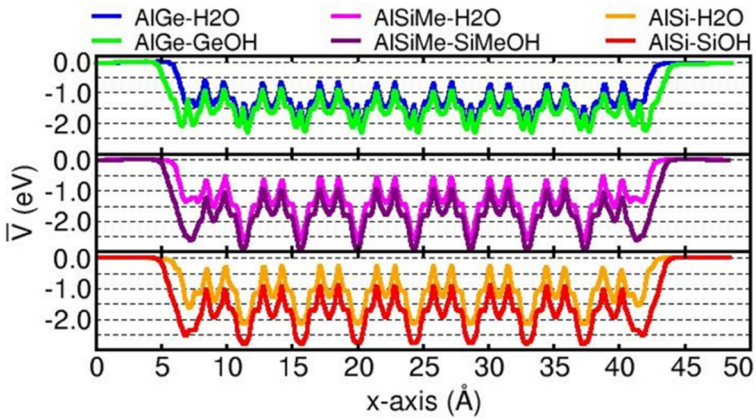

Figure 7.10. Planar average of the electrostatic potential along the tube-axis for the OH and H_2O terminated hex-7 AlSi, AlSi-Me and AlGe NT-models. The NT-axis is parallel to the x-axis.

The simulations indicate that, regardless of the (OH or H_2O) termination, the in-out separation between the VB and CB edges is not affected by truncation of the AlSi and AlSi-Me NTs. The AlGe NTs slightly deviate from this trend with (partial) presence of the CB-edge inside the NT-cavity for the (H_2O) OH-terminated model.

Turning the longitudinal VB and CB-edge localisation, apart for the H_2O termination of the AlSi NTs, in all cases the simulations indicate accumulation of the VB (CB) edge at the NT-extremities (core). This result is consistent with the modelled upward band-bending due to the end-relaxation (Figs. 7.6, 7.7, 7.8, and 7.10). As noted above, the H_2O termination deviates from this trend with accumulation of the CB-edge at the NT-ends, and spread of the CB-edge across the whole NTs. It thus turns out that depending on the NT-composition, diameters and details of the end-relaxation, different in-out and core-end band bending can be present in finite NT-models. In the remainder of the Chapter we analyse the relationship between the electronic structure of the finite NT-models and their optical properties, also in relation to possible e*-h separation and relaxation mechanism presents in the finite systems.

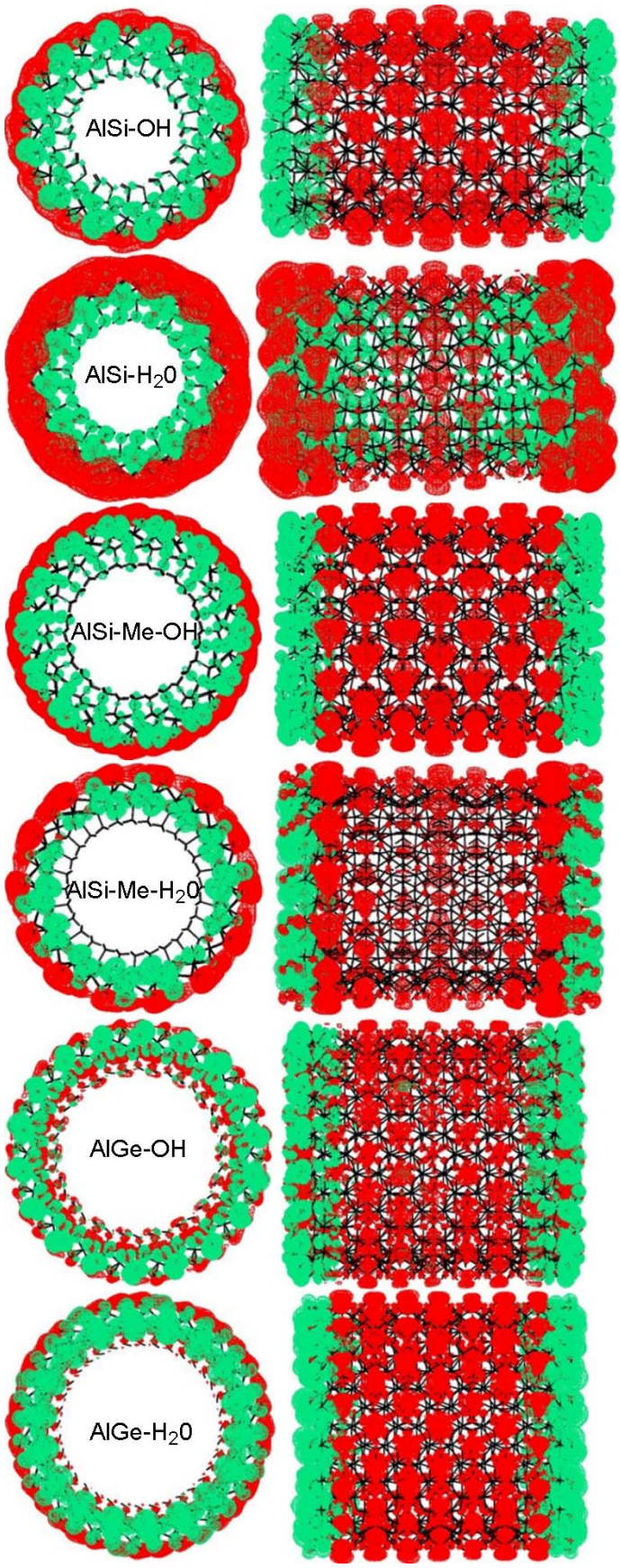

Figure 7.11. Real-space localisation of VB (green) and CB-edges for the OH (left) and H_2O terminated (right) hex-7 models of the AlSi (top), AlSi-Me (middle) and AlGe (bottom) NTs.

7.3.4 Optical properties

As previously commented in Chapter 5, apart from optical characterization of the synthetic solution for AlGe NTs [42], to date no optical study of the Imo NTs is available in the literature. To start bridging this gap, in the following we investigate the optical properties of the NT finite-models and discuss them with respect to the results for the periodic models (Section 5.3.5).

Fig. 7.12 displays the computed imaginary component of the dielectric function (ε_2, see Eq. 2.144) for the all the finite hex-7 NT-models considered. Larger values of ε_2 indicate a larger optical absorbance of the system. We recall that, because of the limitations of the adopted PBE functional and approximations for the evaluation of optical spectra (Section 2.3.8), expectations are that the energy of the optical transitions will be underestimated and possible excitonic relaxations missed.

As previously found for the periodically repeated NT-models (Chapter 5, Fig. 5.5), the computed ε_2 peaks at around 5 eV with non-negligible shifts (±0.3 eV) depending on the NT composition and (OH or H_2O) termination. The simulations place the ε_2 peak at slightly lower energies (4.7 eV) for the AlGe NTs with respect to the AlSi NTs (5.2-5.3 eV). The latter is the system with the largest energy absorbance peak. The computed trend for the finite NTs deviates from the small dependence of the absorption peak energy on the NT composition found for the periodically repeated NT-models (Fig. 5.5). These results strengthen the indication that periodically repeated NTs have electronic (and optical) properties noticeably different from finite NT-models (with a converged core-region). Therefore, results on periodically repeated NT-models may not be rigidly transferable to real Imo NTs, which are finite.

Given the separation in real-space of the VB and CB edges (Fig. 7.11) for the finite NT-models, it is relevant to investigate the contribution from end-localised states to the main absorbance peak. This analysis is also displayed in Fig. 7.12, where the contributions from excitation of the VB-edge are compared to those from excitations involving states deeper in the VB. We recall that, apart from the H_2O termination of the AlSi NT, all the systems display accumulation of the VB-edge and CB edge at the NT-terminations and core, respectively (Fig. 7.11). As a result, optical excitations from the VB-edge to the CB-edge should result in an end→core charge transfer, which in turn may be extremely beneficial for effective e-h separation and photo-catalytic reactivity.

In all cases, we find the main absorbance peak to be dominated by excitations from states deep in the VB rather than from the VB-edge. Thus, optical end→core charge transfer excitations,

albeit optically active, are not as strong as other excitations involving less localised (VB) occupied states.

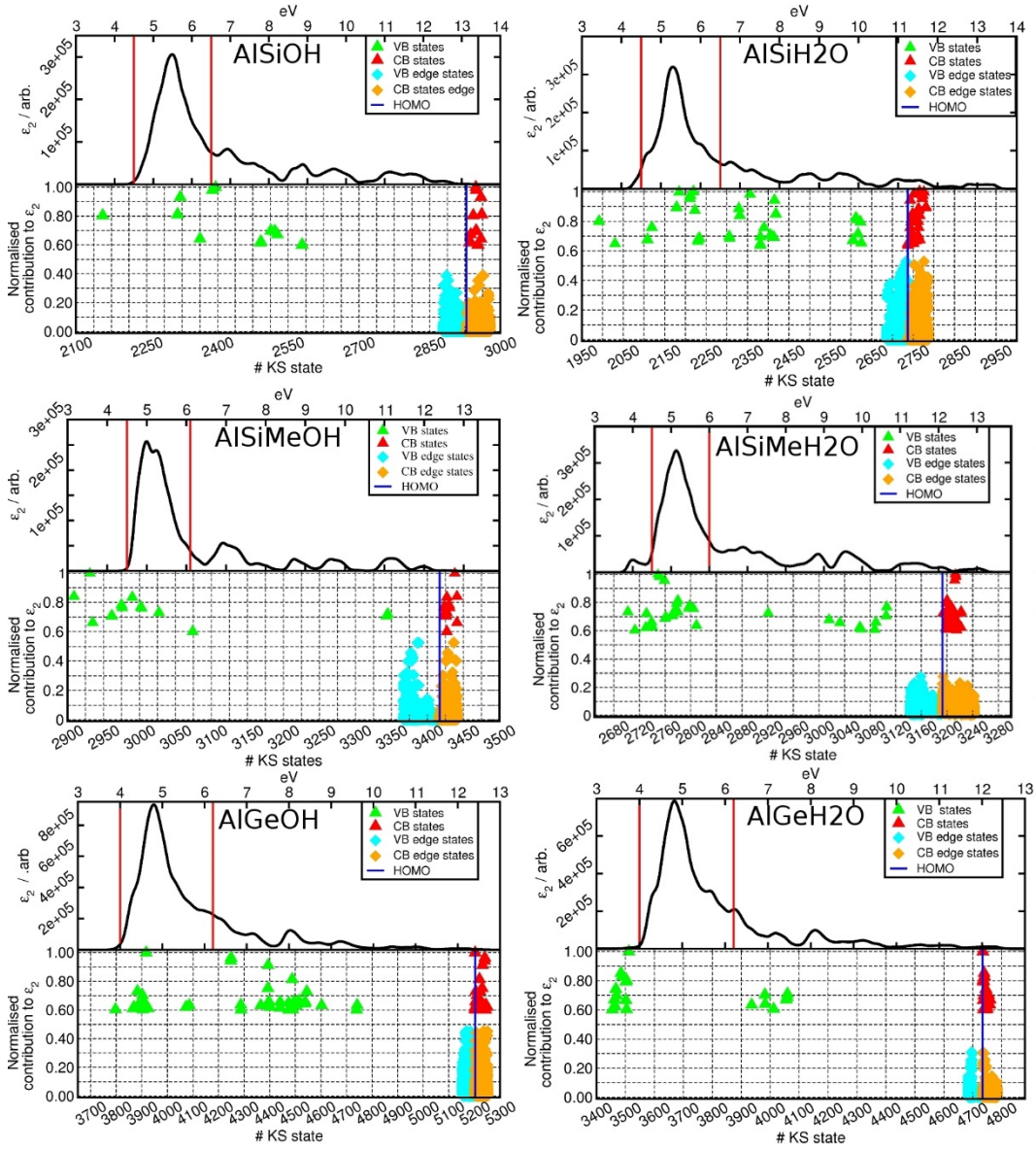

Figure 7.12. Computed ε_2 and transition-resolved analysis of the largest contributions to ε_2 peak for the OH (left) and H_2O terminated (right) hex-7 models of the AlSi (top), AlSi-Me (middle) and AlGe (bottom) NTs. The considered ε_2 peak is contained by the two red-vertical lines. The real-space distribution of the VB and CB edges is shown in Fig. 7.11. The magnitude of the state-resolved transitions has been normalized to the largest computed value. Transition not involving VB and CB states, and with normalized contribution smaller than 0.6, have been omitted for clarity.

7.3.5 Core-end electron-hole separation in finite NTs

Although the NT optical absorbance is computed to be dominated by excitation of core-region VB-states to the CB-edge, with secondary contributions from end→core charge transfer excitations, the presence of longitudinal band-bending in the finite NTs (Figs. 7.6-7.11) suggests alternative energetically viable e*-h separation mechanisms in the NTs.

As schematically depicted in Fig. 7.13, the majority NT-core excitations will leave holes in deep VB-states. Such holes will tend to relax towards the VB-edge. Being the VB-edge localised on the NT-ends (apart from the H_2O termination of AlSi, Fig. 7.11), the hole-relaxation process will move it apart from the excited e*, whose permanence in the NT-core is energetically favoured. As a result, the h and e* will tend to relax towards different regions of the NTs. A secondary mechanism, leading to relaxation of the excited e* towards the NT-core, leaving the hole on the VB-edge, can be also envisaged based on the non-zero, yet lower, absorbance (Fig. 7.12) of the VB-edge localised on the NT-ends (Fig. 7.11). Neglecting possible e-h trapping and recombination at defects centres (vide infra), and considering that Imo NTs can be as long as 20-100 nm [1], the final core-end separation in Imo NTs could be larger than 10 nm (100 Å), offering appealing prospects of photo-catalytic reactivity.

We conclude this section by discussing the competition between longitudinal e*-h relaxation (Fig. 7.13) and e*-h trapping and recombination at defect sites. Comparison between the vacuum-aligned defect-states in AlSi-NTs (Fig. 6.8) and the VB and CB edges for the H_2O and OH terminated AlSi NTs (Fig. 7.9) indicates that, being the finite-NT VB-edge (-5.91/-5.71 eV, Fig. 7.9) lower than the occupied defect states (D1-5, h-D3-5: -4.69/-4.46 eV, Fig. 6.8), and being the NT CB-edge (-1.48/-1.38 eV, Fig. 7.9) higher than the empty defect-state (D2,h-D3: -2.12 /-1.63 eV, Fig. 6.8), relaxation of the e* and h to defect-sites (rather than to the NT-core and NT-end, respectively) should be energetically favoured. However, as also noted in Section 6.3.3, based on the vacuum-alignment of the defect-states, the excited e* and h should relax to different defects (e*: D3 or h-D3, h: D2 or h-D4) with the net result of e*-h separation, albeit with different mechanism (longitudinal relaxation vs. trapping on different defect sites). Future work will have to address whether defects in AlSi NT-core (Chapter 6) and at the NT-ends have similar or different properties, and how these can affect the competitions between e*-h longitudinal relaxation and defect trapping

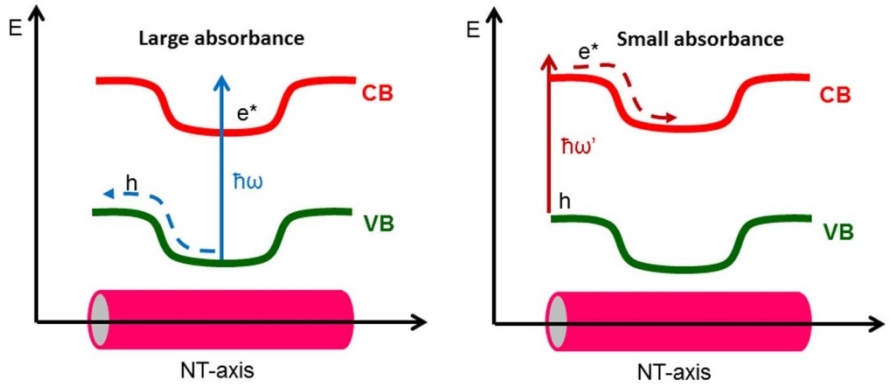

Figure 7.13. Schematic representation of the energetically viable e*-h separation and relaxation processes in finite AlSi (OH termination), AlSi-Me (OH and H_2O termination) and AlGe (OH and H_2O termination) NTs. Transition-resolved analysis of the computed optical spectra (Fig. 7.12) suggests that core→periphery h-relaxation, following optical excitation of the NT-core, should be more populated (by the larger optical absorbance) than periphery→core e*-relaxation, following optical excitation of the NT-ends.

7.4 Conclusions

Simulations of differently extended finite-models of AlSi (24 Al atoms in the circumference), AlSi-Me (28 Al atoms) and AlGe (36 Al atoms) NTs with two alternative (H_2O and OH) terminations indicate that:

i) Use of models longer than 30 Å (1,416-2,232 atoms depending on the NT composition and termination) are necessary to account for relaxation of the NT-ends in systems with a bulk-like core-region.

ii) Al-truncation of the NT, with dangling Al atoms coordinated by an additional H_2O molecule, is energetically favoured over Si-truncation with coordination of extra hydroxyls at the Si-terminated NT-ends.

iii) Physical truncation of the AlSi, AlSi-Me and AlGe NTs is found to consistently narrow the calculated band gap with respect to the results for periodically repeated NT-models. Following vacuum-alignment, the NT finite-models present higher VB and lower CB edges than the periodic counterparts.

iv) In all cases, the separation between VB and CB edges on opposite sides of the NT-cavity (VB: inside, CB: outside), typical of the periodic NTs, is maintained. With the exception of the H_2O termination of the AlSi NT, the VB-edge of the finite NTs is found to be localised at the NT-ends. Conversely, the CB-edge resides mostly at the NT-core.

v) Physical truncation of the AlSi, AlSi-Me and AlGe NTs leads to small, yet non-negligible shifts (±0.3 eV) of the main optical absorbance peak at about 5 eV. Although optical excitation of the VB-edge at the NT-ends is computed to be active, the main absorbance peak is dominated by optical excitations from deep VB-states at the NT-core.

vi) The computed longitudinal band-bending (iv) suggests energetically advantageous relaxation of photo-generated e* (h) towards the NT-core (periphery), which should be beneficial for possible photo-catalytic reactivity. In spite of this, separate relaxation of e* and h at different defect-states in the NT-core should be energetically favoured. Further research is needed to understand the competition between longitudinal band-bending and e*-h trapping at defective NT-ends as well as the extent to which such competition is affected by the solvent.

References

[1] Mukherjee S., Bartlow V.M., Nair S. *Chem. Mater.*, 2005, **17**, (20) 4900.

[2] Wada S I, Eto A and Wada K 1979 *J. Soil Sci.* **30** 347

[3] Barron P F, Wilson M A, Campbell A S and Frost R L 1982 *Nature* **299** 616

[4] Mukherjee S, Bartlow V M and Nair S 2005 *Chem. Mater.* **17** 4900

[5] Kang D Y, Zang J, Wright E R, McCanna A L, Jones C W and Nair S 2010 *ACS Nano* **4** 4897

[6] Theng B K G, Russell M, Churchman G J and Parfitt R L 1982 *Clays Clay Miner.* **30** 143

[7] Mukherjee S, Kim K and Nair S 2007 *J. Am. Chem. Soc.* **129** 6820

[8] Yucelen G I, Choudhury R P, Vyalikh A, Scheler U, Beckham H W and Nair S 2011 *J. Am. Chem. Soc.*, **133** 5397

[9] Yucelen G I, Kang D Y, Guerrero-Ferreira R C, Wright E R, Beckham H W and Nair S 2012 *Nano. Lett.* **12** 827

[10] Cradwick P D, Wada K, Russell J D, Yoshinaga N, Masson C R and Farmer V C 1972 *Nature Phys. Sci.* **240** 187

[11] Bursill L A, Peng J L and Bourgeois L N 2000 *Phil. Mag. A* **80** 105

[12] Levard C, Rose J, Mason A, Doelsch E, Borschneck D, Olivi L, Dominici C, Grauby O, Woicik J C and Bottero J-Y 2008 *J. Am. Chem. Soc.* **130** 5862

[13] Konduri S, Mukherjee S and Nair S 2006 *Phys. Rev. B* **74** 033401

[14] Levard C, Rose J, Thill A, Masion A, Doelsch E, Maillet P, Spalla O, Olivi L, Cognigni A, Ziarelli F and Bottero J Y 2010 *Chem. Mater.* **22** 2466

[15] Maillet P, Levard C, Larquet E, Mariet C, Spalla O, Menguy N, Masion A, Doelsch E, Rose J and Thill A. 2010 *J. Am. Chem. Soc.* **132** 1208

[16] Maillet P, Levard C, Spalla O, Masion A, Rose J and Thill A 2011 *Phys. Chem. Chem. Phys.* **13** 2682

[17] Thill A, Maillet P, Guiose B, Spalla O, Belloni L, Chaurand P, Auffan M, Olivi L, and Rose J. 2012 *J. Am. Chem. Soc.* **134** 3780

[18] Amara M-S, Paineau E, Bacia-Verloop M, Krapf M-E M, Davidson P, Belloni L, Levard C, Rose J, Launois P and Thill A 2013 *Chem. Comm.* **49** 11284

[19] Kang D Y, Zang J, Jones C W, Nair S 2011 *J. Phys. Chem. C.*, **115** 7676

[20] Zanzottera C, Armandi M, Esposito S, Gorrone E and Bonelli B 2012 *J. Phys. Chem. C.* **116** 20417

[21] Zanzottera C, Vicente A, Celasco E, Fernandez C, Garrone E and Bonelli B 2012 *J. Phys. Chem. C.*, **116** 7499

[22] Bonelli B, Armandi M, and Garrone E 2013 *Phys. Chem. Chem. Phys.* **15** 13381

[23] Bottero I, Bonelli B, Ashbrook S E, Wright, P A, Zhou W, Tagliabue M, Armandi M and Garrone E 2011 *Phys. Chem. Chem. Phys.* **13** 744

[24] Kang D Y, Brunelli N A,. Yucelen G I, Venkatasubramanian A, Zang J, Leisen J, Hesketh P J, Jones C W and Nair S 2014 *Nature Comm.* **5** 3342

[25] Amara M S, Paineau E, Rouzière S, Guiose B, Krapf M-E M, Taché O, Launois P, and Thill A 2015 *Chem. Mater.* **27** 1488

[26] Katsumata K, Hou X, Sakai M, Nakajima A, Fujishima A, Matsushita N, MacKenzie K J D and Okada K 2013 *Appl. Catal B-Environ.* **138** 243

[27] Marzan L L and Philipse A P 1994 *Colloid Surface A* **90** 95

[28] Ma W, Yah W O, Otsuka H and Takahara A 2012 *J. Mater. Chem.* **22** 11887

[29] M. Ookawa, in Clay Minerals in Nature – Their Characterization, Modification and Application, ed. M. Valaskova, InTech, 2012, p. 2708.

[30] Arancibia-Miranda N, Escudey M, Pizarro C, Denardin J C, García-González M T, Fabris J D and Charlet L 2014 *Mater. Res. Bull.* **51** 145

[31] Avellan A, Levard C, Kumar N, Rose J, Olivi L, Thill A, Chaurand P, Borschneck D and Masion A 2014 *RSC Adv.* **4** 49827

[32] Yucelen G I, Choudhury R P, Leisen J, Nair S and Beckham H W 2012 *J. Phys. Chem. C.* **116** 17149

[33] Diebold U. Surf. Science. Rep. 2003 **48** 53.

[34] Bliem R., McDermott E., Ferstl P., Setvin M., Gamba O., Pavelec J., Schneider M. A., Schmid M., Diebold U., Blaha P., Hammer L., Parkinson G. S. *Science* 2014 **346** 1215.

[35] Goniakowski J., Finocchi F., Noguera C. *Report on Progress in Phys*. 2008 **71** 016501.

[36] Perdew J, Burke K, and Ernzerhof M 1996 *Phys. Rev. Lett.* **77** 3865.

[37] Gonze X, Stumpf R, Scheffler M 1991 *Phys. Rev. B* **44** 8503.

[38] Pfrommer B G, Côté M, Louie S G, and Cohen M. L 1997 *J. Comput. Phys.* **131** 233.

[39] Van de Walle C. G., Neugebauer J. *J Appl Phys 2004* **95** 3851.

[40] Hine N D M, Dziedzic J, Haynes P. D, Skylaris C-K. 2011 *J. Chem. Phys.* **135** 204103.

[41]. N. D. M. Hine, W. Avraam, Tangney and D. Haynes: *J. Phys.: Conf. Ser.*, 2012, **367**, 012002.

[42] Mukherjee S, Kim K and Nair S 2007 *J. Am. Chem. Soc.* **129** 6820

Chapter 8

Conclusions

8.1 Synopsis

In this Thesis we explored by computational modelling the potential of Imogolite Nanotubes (Imo-NTs) as photo-catalyst. The available experimental results on Imo-NTs composition, structure, synthesis, functionalisation and doping suggest that Imo-NTs integrate 1D structuring, permanent polarization, and the possibility of reactant nano-confinement (separation) in one material. This promising set of properties motivated the study reported in this thesis. In spite of unavoidable accuracy-viability compromises, which were ameliorated by the use of linear-scaling Density Functional Theory (LS-DFT), we believe the results reported here are an important and very original complement to ongoing experimental work on this class of materials.

In the first Chapter, an overview of the current state of the art in photo-catalysis was presented. Particular attention was paid to the structural factors and physical processes determining the efficiency of a photo-catalytic event. The theoretical framework to describe charge transfer processes at the atomic scale was also outlined. At the end of the Chapter, a short section was dedicated to existing work on one-dimensional nanostructured photo-catalysts, given our interest in the Imo-NTs.

The second Chapter presented an introduction to the LS-DFT method. Detailed consideration was given to the density-matrix formulation of Kohn-Sham DFT, the introduction of support functions, known as NGWFs, and their construction from a psinc basis set. Various techniques implemented in ONETEP such as the Coulomb cutoff, the conduction-state optimisation, and the simulation of absorption spectra, used through this Thesis were also exposed at the end of the Chapter.

Chapter 3 presented a small literature review about Imo-NTs. The available experimental results on Imo-NTs composition, structure, synthesis, functionalisation and doping were summarised to highlight how Imo-NTs integrate 1D structuring, permanent polarization and the possibility of reactant nano-confinement (separation) in one material, which is believed to hold great promise for photo-catalytic applications. The Chapter exposed also a short report

regarding the state of the art in electronic structure simulations of the Imo-NTs. The results presented were then related to the potential of the systems as photo-catalyst.

In Chapter 4, we analysed the applicability of the linear-scaling (LS-DFT), in situ optimised basis-set, ONETEP approach to the Imo-NTs. To find the best parameters to perform accurate and viable simulations on the NTs, several simulations set-ups were tested and computationally benchmarked. Analysis of the optimised structure for differently-sized models of the tube extremities reveals heavy biases in the simulation for systems shorter than 2 nm (~1,100 atoms), highlighting the necessity of efficient LS-DFT implementations for accurate simulation of the NT-terminations. Overall, we find the NT extremities to relax inwards leading to a narrower cavity at the tube extremities, with minimal effects on the NT-length.

In Chapter 5, we reported the simulations on different type of Imo-NTs: Single Wall (SW)-$AlSi_{24}$, SW-$AlSi_{28}$-Me, SW-$AlSi_{34}$-Me, SW-$AlGe_{36}$ and Double Wall (DW)-$AlGe_{36,54}$ either isolated or interacting with two H_2O molecules. It was found that the NT wall-polarisation can be changed by controlling the NTs composition and curvature. All the different NTs simulated were found to be insulator with band gaps ranging from 2.81 eV (DW-$AlGe_{36,54}$) to 4.75 eV ($AlSi_{28}$-Me). For all the different NTs composition, the VB (CB) edge was consistently modelled to be mostly localised at the NT inner (outer) surface. The absolutely vacuum-aligned NT VB edges were modelled to be noticeably high in energy (>-5.97 eV), suggesting possible hole-scavenging applications for this type of material. The NT CB edges were also found to be remarkably high in energy (>-1.49 eV), anticipating possible photo-reduction applications for Imo-NTs. The simulated optical activity of SW-$AlGe_{36}$ and DW-$AlGe_{36,54}$ NTs were noticeably larger than SW-$AlSi_{24}$ NTs, which in turn had substantially larger UV absorbance than methylated SW-$AlSi_{28,34}$-Me NTs. The NT wall-polarisation was found to markedly affect the electronic alignment of H_2O molecules interacting with either surface of the NTs. The computed alignment of the CB-edges hinted the possibility of energetically viable photo-reduction of H_2O at the outer surface of all the considered NT models apart from DW-$AlGe_{36,54}$. Photo-oxidation of H_2O inside the NT-cavity by the top VB edge was modelled to be energetically favoured for all the non-methylated NTs (SW $AlSi_{24}$, SW $AlGe_{36}$, DW-$AlGe_{36,54}$).

Chapter 6 focused on simulation on the five defect structures (D1-5) proposed by Nair et al. in their Nuclear Magnetic Resonance study of aluminosilicate Imo-NTs. The hydrogenated counterparts of D3-D5 defects were also considered. It was observed that the presence of defects induces local deformations to the NT involving almost exclusively the outer Al-O octahedrons and the external O-H bonding. All the defect-states were found to be localised in

energy at the top of the VB. The occupied defect states were computed to be highly localised around the defect site. The vacuum alignment of the VB and CB edges for the considered defects implies the possibility of defect-mediated separation of photo-generated e*-h pairs via preferential diffusion of e* and h to different defects (e*: D3; h: D2 or h-D4). The optical absorbance of the defective NTs was found to be notably larger with respect to the pristine NTs. The presence of defects causes a decrease of the NT-wall dipole density in all the cases simulated. Nonetheless, apart from one defect (h-D3), the residual dipole density was not inverted with respected to the pristine NTs, and found to markedly affect the absolute alignment of the electronic states for H_2O molecules interacting with either sides of the NT-cavity.

The last Chapter (7) reports the simulations of differently extended finite-models of SW-$AlSi_{24}$, SW-$AlSi_{28}$-Me and SW-$AlGe_{36}$ NTs with two alternative (H_2O and OH) terminations. It was discovered that the use of models longer than 30 Å is necessary to account for relaxation of the NT-ends in systems with a bulk-like core-region. The simulation performed shown that the physical truncation of the AlSi, AlSi-Me and AlGe NTs consistently narrows the calculated band gap with respect to the results for periodically repeated NT-models. Electronic-sate vacuum-alignment for the NT finite-models resulted in higher VB and lower CB edges than the periodic counterparts. In all cases analysed, the separation between VB and CB edges on opposite sides of the NT-cavity, typical of the periodic NTs, was maintained. In all cases apart from the H_2O termination of the AlSi NTs, the NTs VB-edge was computed to be localised at the NT ends. Conversely, the CB-edge resided mostly at the NT-core. NT-truncation led to small, yet non-negligible shifts (±0.3 eV) of the main optical absorbance peak at about 5 eV. Although optical excitation of the VB-edge at the NT-ends was computed to be active, the main absorbance peak was dominated by optical excitations from deep VB-states at the NT-core. The computed longitudinal band-bending suggested energetically advantageous relaxation of photo-generated e* (h) towards the NT-core (periphery). These could be beneficial for possible photo-catalytic reactivity. In spite of this, separate relaxation of e* and h at different defect-states in the NT-core should be energetically favoured.

8.2 Future work

To conclude this Thesis we briefly comment on future developments that could build on the work presented.

Moving forward from the results of Chapter 5 to continue our exploration of the Imo-NTs potential as photo-catalyst, we have already performed calculation of the absolute-vacuum alignment and electronic coupling between different types of Imo-NTs and various reactant of

interest such as CO_2 and N_2 adsorbed at their surface. Once finalised, these will expand the insight into the feasibility of photo-redox reactions at the Imo-NTs surfaces in terms of both energy of acceptor-donor states and transfer kinetics. In the long term, the idea is to gradually move (in the limits of computational viability) towards description of the solvent, in order to reproduce the real interface between the solvated NTs and the reactants. To this end, some test calculations with explicit solvation of the pristine SW-$AlSi_{24}$ NTs have been already started.

The results of Chapter 6 suggest a different course of action for extension of this work. Starting from the electronic alignment of the VB edges of the different defective structure, it would be very relevant to explore the possibility of hole localisation at the defect sites. Our future aim is to determine, using the implemented constrained DFT routine in ONETEP the most stable configuration for a NTs with a hole state. After this step, the ideal continuation would focus on the assessment of the reactivity of the defect centres.

The findings in Chapter 7 motivate further analysis on truncated systems with less idealised terminations. Of extreme interest is also the behaviour of physically truncated NTs in solution. While some test calculations have been performed with the use of the implicit solvent scheme, explicit solvation of the truncated NTs is, at the moment, unfeasible given the extension of the resulting system (~8,000 atoms). If possible, study of defects in finite- and solvated NT-models, is an unavoidable step towards further understanding of Imo-NTs and their potential as (co-)photo-catalysts.

Appendix A

Potential step in co-axial cylindrical condenser (Derivation of Eq 5.2)

Although not reported in the thesis (for the sake of compactness) all the tube simulated in spite of the NT-wall polarization, and owing to the NT cylindrical symmetry, presented a flat electrostatic potential [$V(\mathbf{r})$] inside and outside the cavity. An example of this behavior can be seen in Fig 7 in Ref [1]. Since the electrostatic field, minus the sign, is given by gradient the electrostatic potential ($E = -\nabla V(\mathbf{r})$ [2]), no electrostatic field is present inside and outside the NT. As a result, it is possible to model the NT electrostatics on the basis of an overall neutral co-axial (hollow) cylindrical condenser (Figure A1).

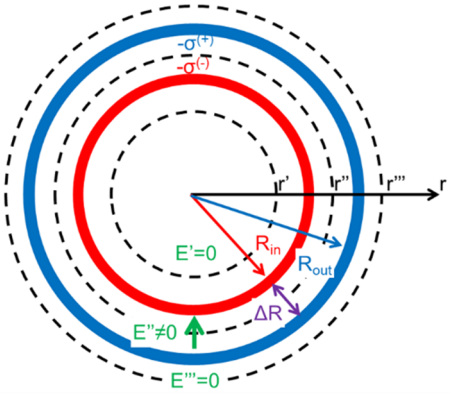

Figure A1. Front view of a cylindrical co-axial condenser with charge $-Q = -\sigma^{-}2\pi R_{in}L$ and $Q = -\sigma^{+}2\pi R_{in}L$ on the inner and outer hollow cylinder, respectively. L is the length of the inner and outer hollow cylinders. The three cylindrical Gaussian surfaces of radius r', r'' and r''' are also indicated.

Gauss' flux theorem relates the flux of the electrostatic field ($\vec{\mathbf{E}}$) across a closed surface (S) with the charge Q contained inside the closed surface [2]:

$$\frac{Q}{\varepsilon_0} = \oint_S \vec{\mathbf{E}} \cdot \mathbf{d}\hat{\mathbf{s}} \tag{A.1}$$

where ε_0 is the electric permittivity of vacuum, and $\mathbf{d}\hat{\mathbf{s}}$ a vector of unitary module locally normal to the infinitesimal surface element. Eq. A.1 allows definition of three electrostatic regions with different in the co-axial condenser in Figure A1:

Region 1. For $r < R_1$, the electric field is zero ($E = 0$) since the Gaussian surface of radius r' does not contain any net charge ($E = 0$).

Region 2. For $R_{in} \leq r < R_{out}$, the electric field is not zero ($E \neq 0$) since the Gaussian surface of radius r'' does contain a net charge ($-Q < 0$, see Figure A1). Since the hollow cylinders are taken to be in electrostatic equilibrium, with no net transfer of charge, $\mathbf{E} = E\hat{\mathbf{r}}$ i.e. the electrostatic field lies parallel to the tube radius ($\mathbf{E} = E\hat{\mathbf{r}}$), with zero components along the tube (lateral) surface.

Region 3. For $r > R_{out}$, the electric field is zero ($E = 0$) since the Gaussian surface of radius r''' does not contain any net charge ($Q = 0$), being the cylindrical condenser overall neutral.

We thus focus in Region 2 to calculate the electric field and potential difference between R_{in} and R_{out} by Gauss' flux theorem. We start by expanding both sides of Eq. A.1 as:

$$\frac{Q}{\varepsilon_0} = \frac{-2\pi R_{in} L \sigma^{(-)}}{\varepsilon_0} = \oint_S \vec{\mathbf{E}} \cdot \mathbf{d}\hat{\mathbf{s}} = 2\pi r'' LE \tag{A.2}$$

Where in the right-side term we have taken advantage of **E** being locally parallel to $\mathbf{d}\hat{\mathbf{s}}$ and that the **E** between the cylinders is directed parallel to the surface normal with zero components along the cylinder axis.

Eq. A.2 can be rearranged to read:

$$\frac{-R_{in}\sigma^{(-)}}{\varepsilon_0 r''} = E = -\frac{dV}{dr''} \tag{A.3}$$

which allows the integration of the electrostatic potential between R_{in} and R_{out} as:

$$\Delta V = V(R_{in}) - V(R_{out}) = \int_{R_{out}}^{R_{in}} dr'' E = \frac{R_{in}\sigma^{(-)}}{\varepsilon_0} \int_{R_{out}}^{R_{in}} dr' \frac{1}{r''} = \frac{R_{in}\sigma^{(-)}}{\varepsilon_0} \ln\left(\frac{R_{in}}{R_{out}}\right) \tag{A.4}$$

It is worth noting that in Eq. A.4, the overall negative sign of $\Delta V = V(R_{in}) - V(R_{out})$ [$\ln(R_{in}/R_{out}) < 0$], is consistent with **E** being directed from the outer (positively charged) to the inner (negatively charged) cylinder (Figure A1).

In analogy with the treatment for the surface dipole density (μ_0) due to two charged surfaces (of surface charge-density σ) locally parallel and separated by a distance *d* [2]:

$$\lim_{d \to 0} \sigma d = \mu_\sigma \tag{A5}$$

for infinitesimally small separation ΔR, leading to $R_{in} = R_{out}$ and $\sigma^{(-)} = \sigma^{(+)} = \sigma$, the separation in surface charge-density (σ) between the inner and outer cylinders (Figures A2) can be described via a surface dipole-density as:

$$\lim_{\Delta R \to 0} \sigma \Delta R = \mu_\sigma \tag{A6}$$

which in turn can be used to write:

$$\sigma = \frac{\mu_\sigma}{\Delta R} \tag{A7}$$

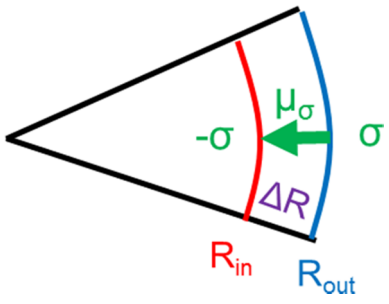

Figure A2. Separation of charge-density (σ) between the co-axial cylinders, leading to a surface dipole-density μ_0.

Based on Eq. A.7, Eq. A.4 can be rearranged into:

$$\Delta V = V(R_{in}) - V(R_{out}) = \frac{R_{in}\sigma}{\varepsilon_0}\ln\left(\frac{R_{in}}{R_{out}}\right) = \frac{R_{in}}{\varepsilon_0}\frac{\mu_\sigma}{\Delta R}\ln\left(\frac{R_{in}}{R_{out}}\right) = 4\pi R_{in}\frac{\mu_\sigma}{\Delta R}\ln\left(\frac{R_{in}}{R_{in}+\Delta R}\right) \tag{A.8}$$

where we have used the fact that in atomic units $1/\varepsilon_0 = 4\pi$.

For consistency with the convention in some DFT-codes of calculating the electrostatic potential using the (negatively charged) electron as test charge, leading to lower (higher) electrostatic potential for electron-rich (poor) regions, the sign of Eq. A.8 needs to be changed leading to:

$$\Delta V = V(R_{in}) - V(R_{out}) = -4\pi R_{in}\frac{\mu_\sigma}{\Delta R}\ln\left(\frac{R_{in}}{R_{out}}\right) = -4\pi R_{in}\frac{\mu_\sigma}{\Delta R}\ln\left(\frac{R_{in}}{R_{in}+\Delta R}\right) \tag{A.9}$$

which correctly describes regions of high (low) electrostatic potential for the electron-rich (poor) side of the NT-cavity (See Fig.7 Ref. [1]). Eq. A.8 allows computation of dipole-density from the step in the electrostatic potential of inside and outside the NT-wall. Given the solution of the DFT problem via discretized grids [3], and in analogy with the planar dipole densities it is convenient to angularly and longitudinally average the electrostatic potential (expressed in cylindrical coordinates):

$$\overline{V}(r) = \frac{1}{2\pi L}\int_0^{2\pi} d\phi \int_0^{L} dl\, V(r,\phi,l) \tag{A.10}$$

obtaining:

$$\Delta\overline{V} = \overline{V}(R_{in}) - \overline{V}(R_{out}) = -4\pi R_{in}\frac{\mu_\sigma}{\Delta R}\ln\left(\frac{R_{in}}{R_{out}}\right) = -4\pi R_{in}\frac{\mu_\sigma}{\Delta R}\ln\left(\frac{R_{in}}{R_{in}+\Delta R}\right) \tag{A.11}$$

Eq. A.11 is used to compute μ_0 on the basis of the potential step ($\Delta\bar{V}$) between the electrostatically derived between R_{in} and R_{out} (Figure 3e).

Furthermore, for increasingly large R_{in} ($R_{out} = R_{in} + \Delta R$), the cylindrical condenser asymptotically tends to a planar condenser, and Eq. A.11 recovers the established $\Delta\bar{V}/\mu_0 = 4\pi$ relationship (Figure A3).

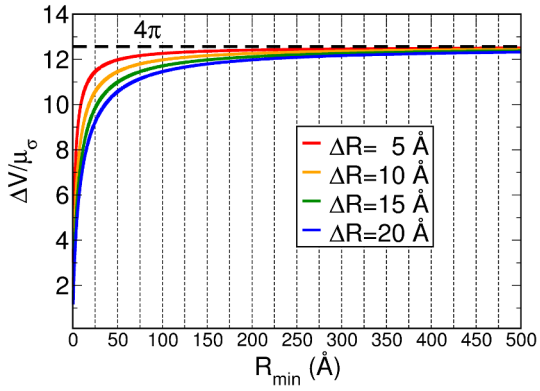

Figure A3. Asymptotic behavior of $\Delta\bar{V}/\mu_0 = 4\pi\,(R_{in}/\Delta R)\ln(R_{in}/R_{in} + \Delta R)$ (obtained from Eq. A.11) for increasing values of R_{in}. As the NT-radius increases, the cylindrical condenser tends to a planar one, for which $\Delta\bar{V}/\mu_0 = 4\pi$ [2].

Eq. A.11 allows exploration of the role of the geometric factors and interplay between R_{in} and ΔR in damping the relationship between surface dipole-density μ_0 and potential step across the NT-wall $\Delta\bar{V}$. As shown in Figures A4,

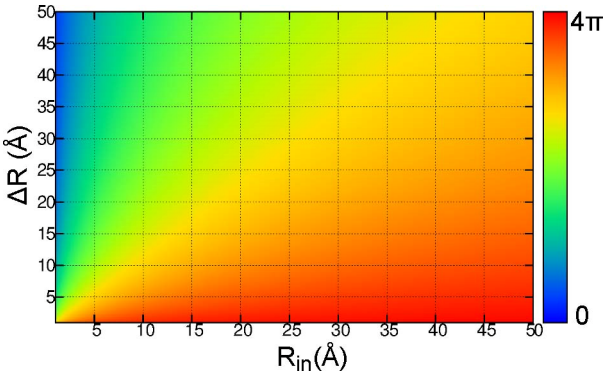

Figure A4. Two-dimensional plot of $\Delta\bar{V}/\mu_0 = 4\pi\,(R_{in}/\Delta R)\ln(R_{in}/R_{in} + \Delta R)$ (obtained from Eq. A.11) as a function of R_{in} and ΔR. Large R_{in} and small ΔR values allow maximization of the potential difference ($\Delta\bar{V}$) for a given surface dipole-density (μ_0). Conversely, smaller $\Delta\bar{V}$ values can be obtained for the same μ_0 provided R_{in} (ΔR) is decreased (increased).

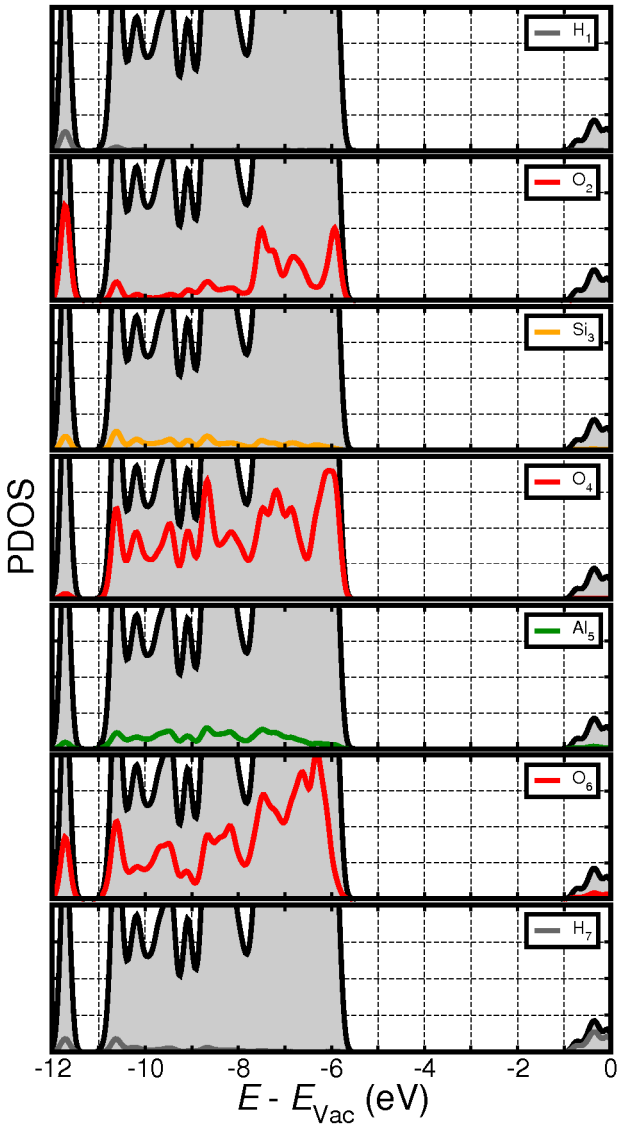

Figure A5. PBE vacuum-aligned, total (filled grey) and layer-resolved PDOS for **$AlSi_{24}$**. See figure 1 for the adopted layer labelling.

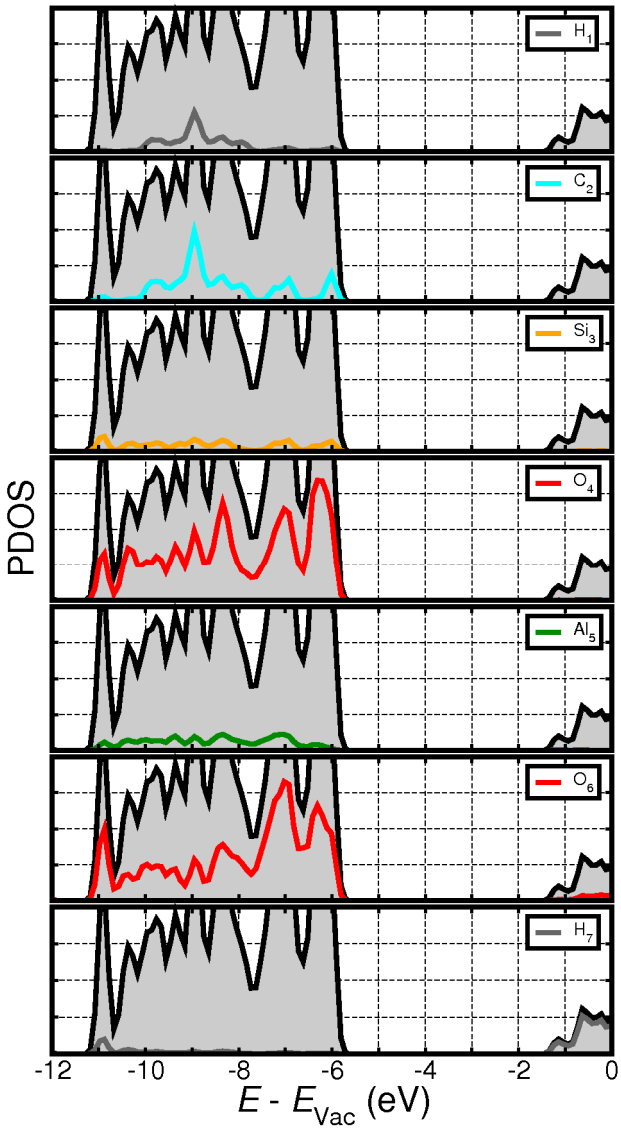

Figure A6. PBE vacuum-aligned, total (filled grey) and layer-resolved PDOS for **$AlSi_{28}$-Me**. See figure 1 for the adopted layer labelling.

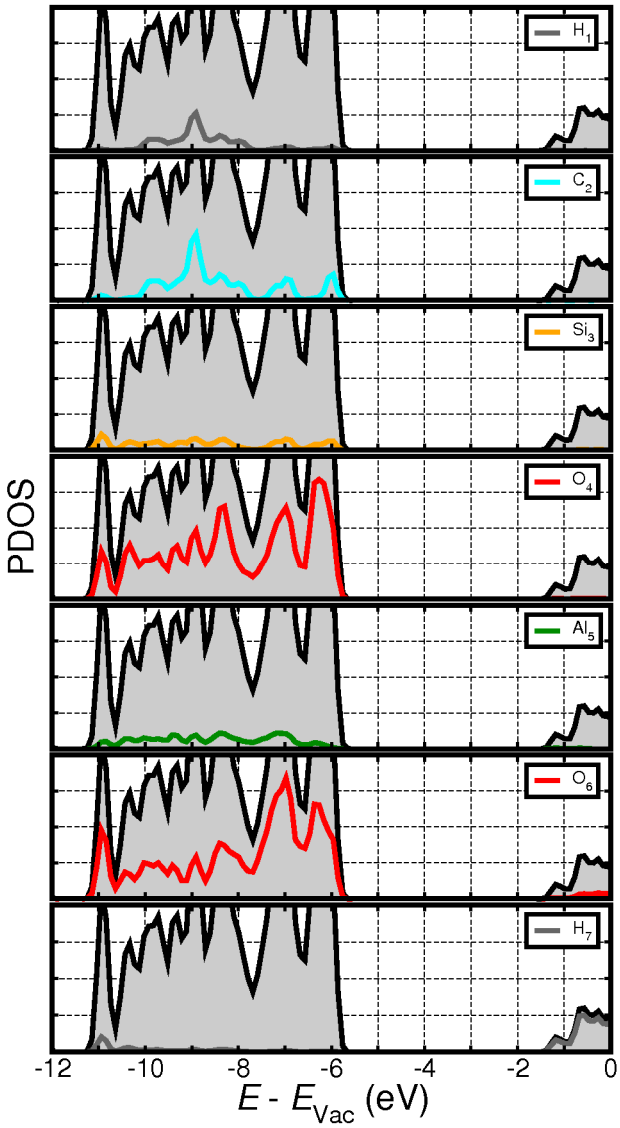

Figure A7. PBE-D2 vacuum-aligned, total (filled grey) and layer-resolved PDOS for **AlSi$_{28}$-Me**. See figure 1 for the adopted layer labelling.

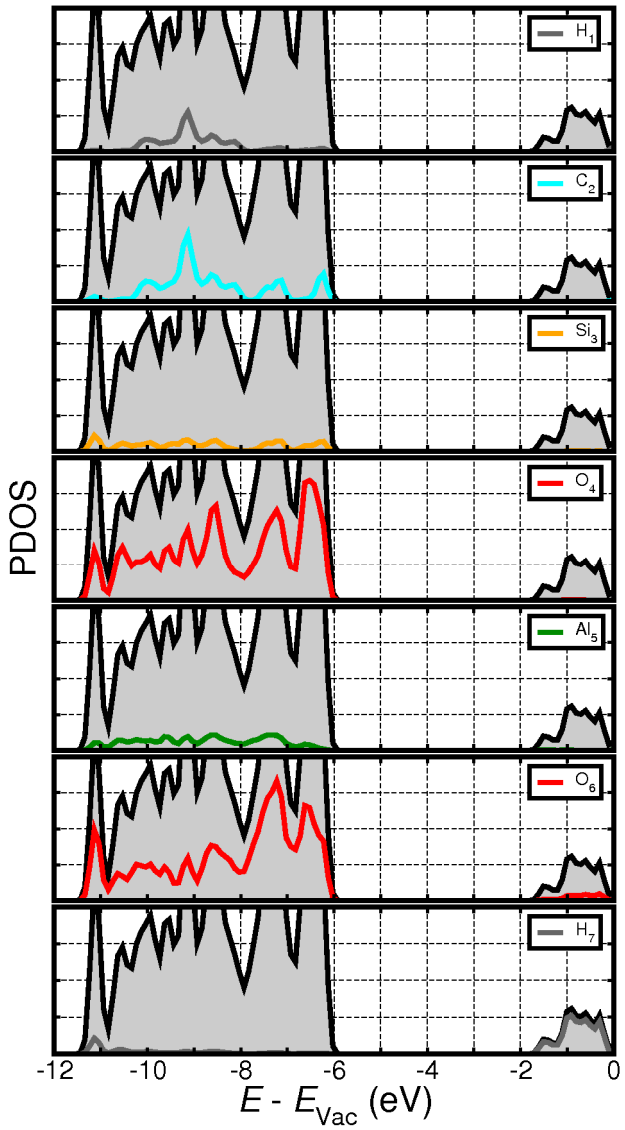

Figure A8. OPTB88 vacuum-aligned, total (filled grey) and layer-resolved PDOS for **$AlSi_{28}$-Me**. See figure 1 for the adopted layer labelling.

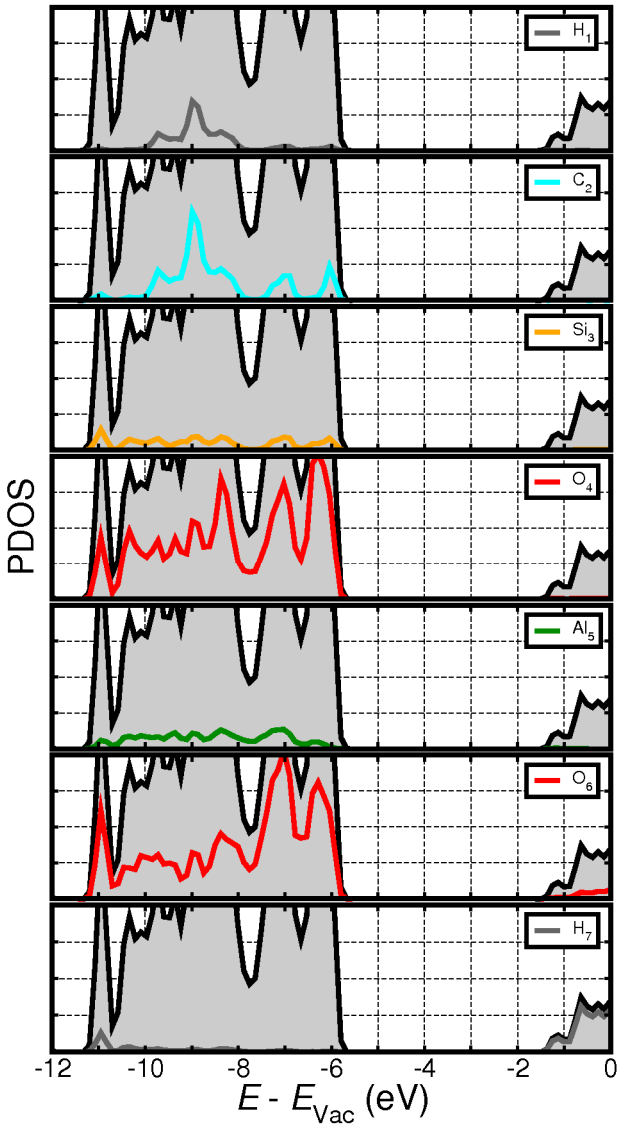

Figure A9. PBE vacuum-aligned, total (filled grey) and layer-resolved PDOS for **$AlSi_{34}$-Me**. See figure 1 for the adopted layer labelling.

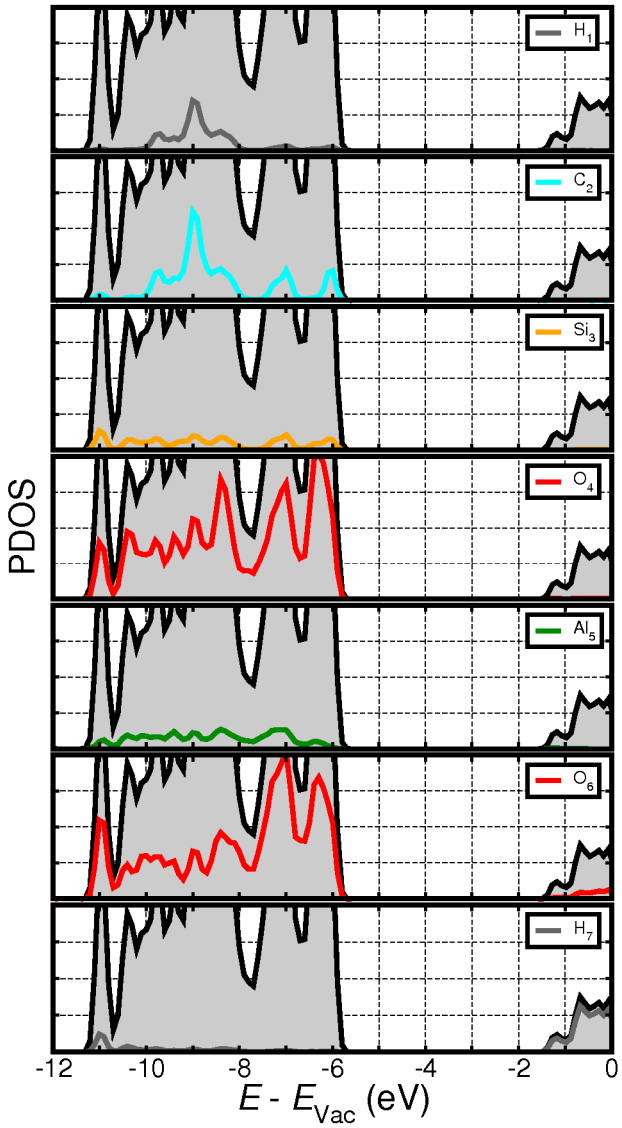

Figure A10. PBE-D2 vacuum-aligned, total (filled grey) and layer-resolved PDOS for **$AlSi_{34}$-Me**. See figure 1 for the adopted layer labelling.

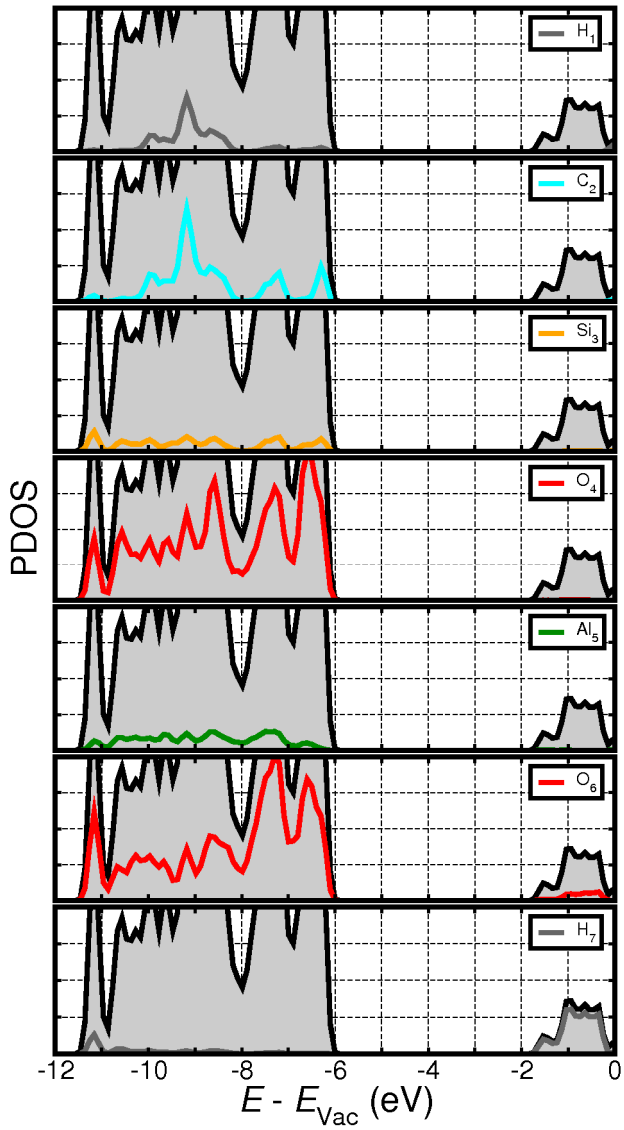

Figure A11. OPTB88 vacuum-aligned, total (filled grey) and layer-resolved PDOS for **$AlSi_{34}$-Me**. See figure 1 for the adopted layer labelling.

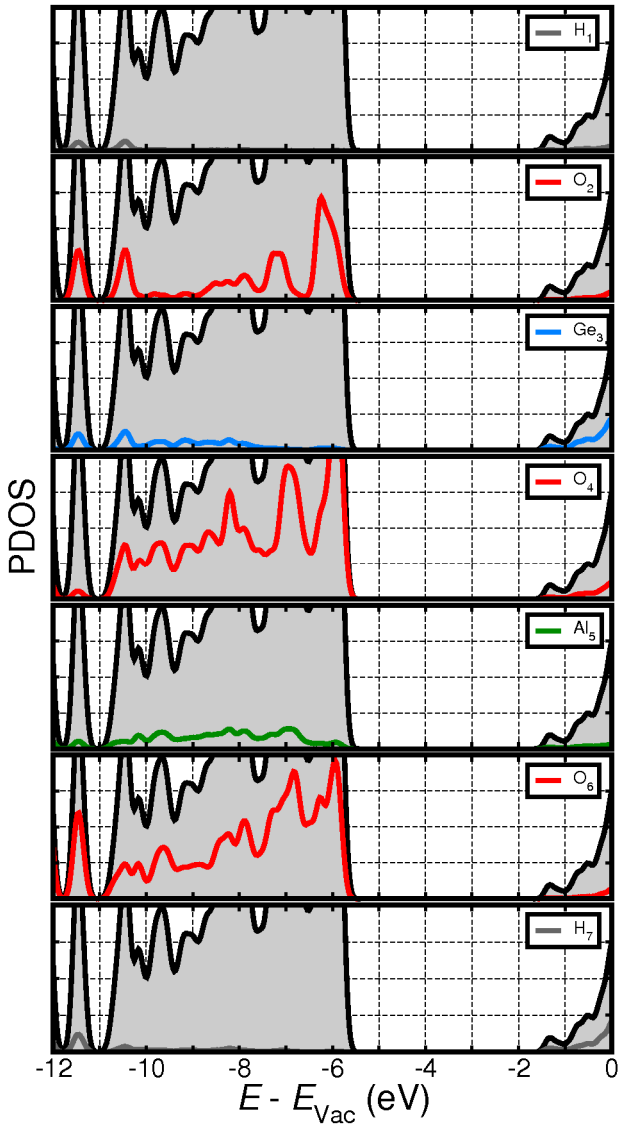

Figure A12. PBE vacuum-aligned, total (filled grey) and layer-resolved PDOS for **$AlGe_{36}$**. See figure 1 for the adopted layer labelling.

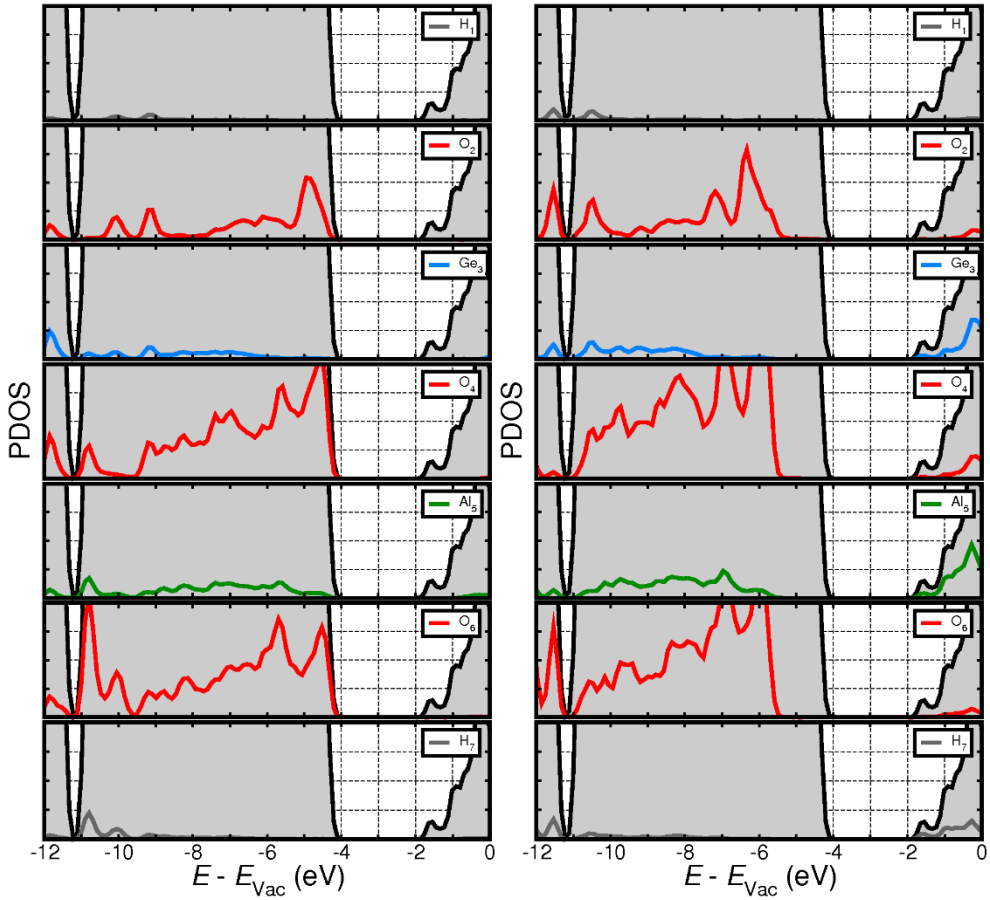

Figure A13. PBE vacuum-aligned, total (filled grey) and layer-resolved PDOS for **DW-AlGe$_{36,54}$**. The results for the inner (outer) tube are displayed on the left (right) panel. See figure 1 for the adopted layer labelling.

References

[1] Teobaldi G, Beglitis N S, Fisher A J, Zerbetto F and Hofer W A 2009 *J. Phys. Condens. Matter*. **21** 195301

[2] Jackson J. D. *Classical Elettrodynamics 3rd Edition* 1999 Wiley and Sons.

[3] C.K. Skylaris, P.D. Haynes, A.A. Mostofi, and M.C. Payne: *J. Chem. Phys.*, 2005, **122**, (8), 084119.

Appendix B

Bond type	D1	D2	D3	D4	D5
{Si-O} NN	1.65 ± 0.02 Å	1.65 ± 0.01 Å	1.65 ± 0.04 Å	1.65 ± 0.02 Å	1.65 ± 0.03 Å
{Al-O} NN	1.92 ± 0.04 Å	1.87 ± 0.08 Å	1.90 ± 0.05 Å	1.91 ± 0.05 Å	1.90 ± 0.04 Å
{O-H} NN	1.14 ± 0.28 Å	1.22 ± 0.37 Å	1.04 ± 0.16 Å	1.17 ±0.35 Å	1.15 ± 0.35 Å
{Si-O} SNN	1.65 ± 0.01 Å	1.65 ± 0.00 Å	1.65 ± 0.01 Å	1.65 ±0.01 Å	1.65 ± 0.01 Å
{Al-O} SNN	1.92 ± 0.03 Å	1.92 ± 0.03 Å	1.91 ± 0.03 Å	1.91 ± 0.04 Å	1.92 ± 0.03 Å
{O-H} SNN	0.96 ± 0.01 Å	0.96 ± 0.00 Å	0.96 ± 0.01 Å	1.11 ± 0.03 Å	0.96 ± 0.00 Å

Bond type	h-D3	h-D4	h-D5	Pristine
{Si-O} NN	1.64 ± 0.02 Å	1.65 ± 0.03 Å	1.65 ± 0.03 Å	1.65 ± 0.09 Å
{Al-O} NN	1.90 ± 0.02 Å	1.91 ± 0.04 Å	1.91 ± 0.03 Å	1.92 ± 0.16 Å
{O-H} NN	1.09 ± 0.02 Å	1.13 ± 0.32 Å	1.15 ± 0.29 Å	0.96 ± 0.08 Å
{Si-O} SNN	1.65 ± 0.01 Å	1.65 ± 0.01 Å	1.65 ± 0.01 Å	
{Al-O} SNN	1.92 ± 0.03 Å	1.91 ± 0.04 Å	1.92 ± 0.03 Å	
{O-H} SNN	0.96 ± 0.01 Å	1.10 ± 0.32 Å	0.96 ± 0.01 Å	

Table B.1: Average bond lengths for the NN and SNN atoms in the defective structures.

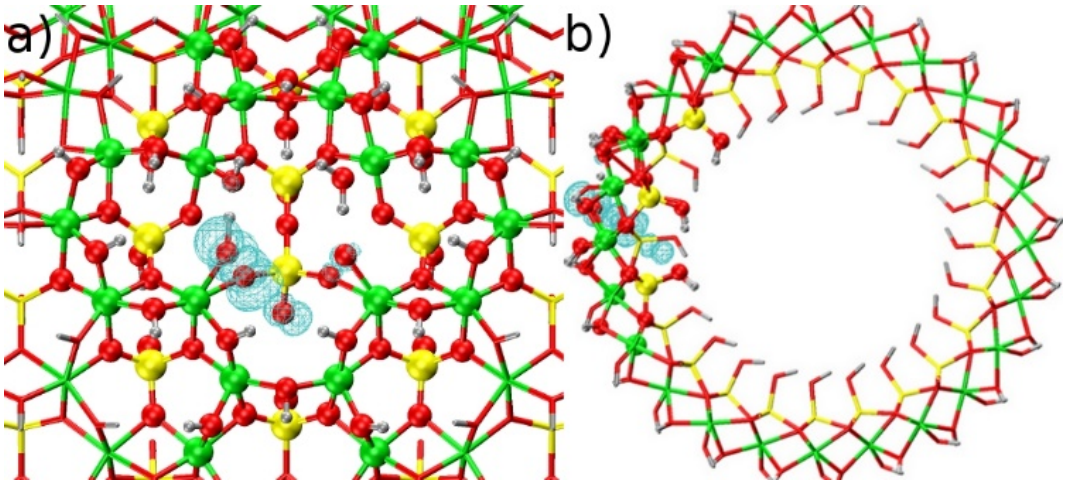

Figure B.1: Side (a) and front (b) view of the optimised D3 geometry (see also Fig. 6.5) together with the localised distribution of the lowest energy empty KS states (cyan contour).

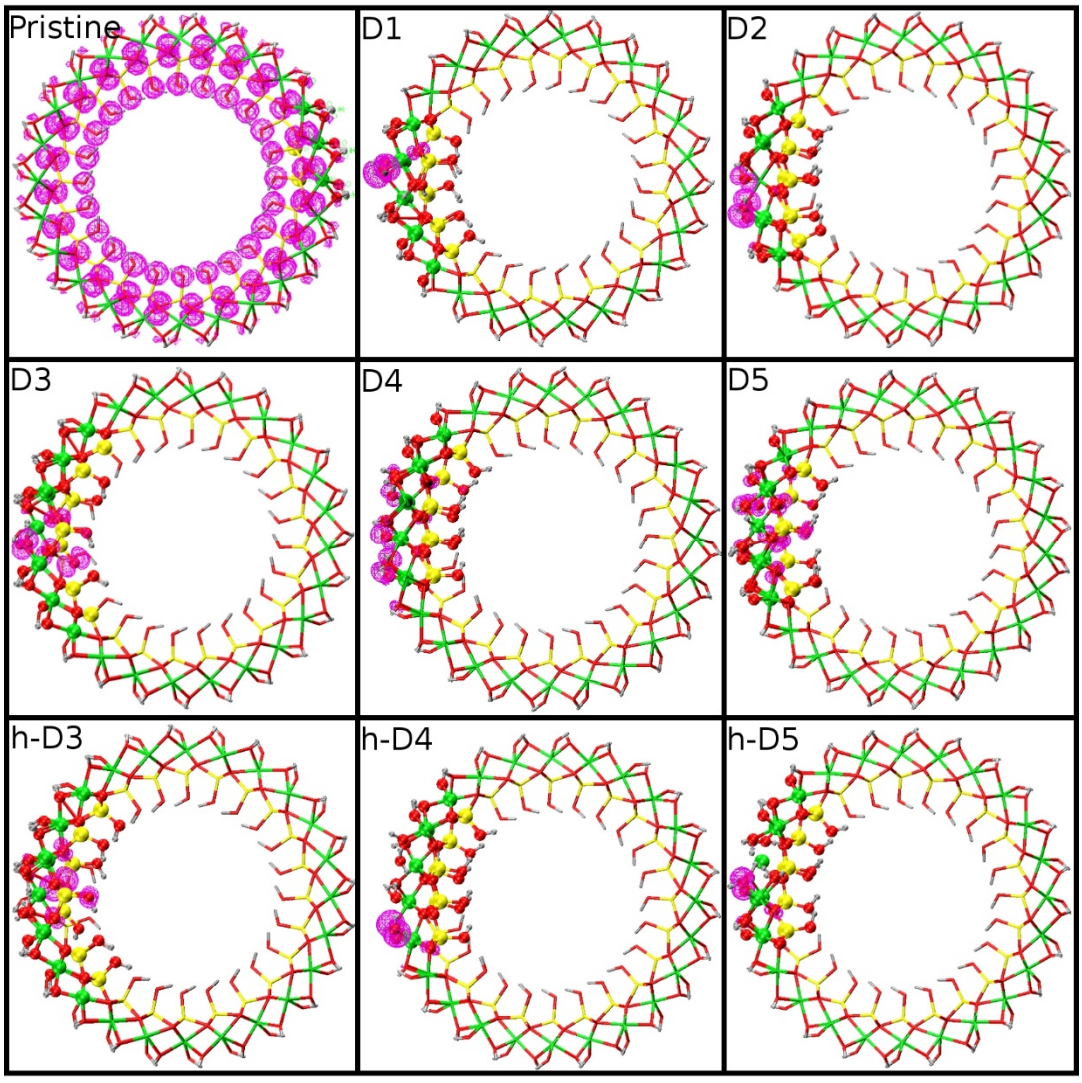

Figure B.2: Front view of the optimised defect geometries together with the contour-plot for the highest-energy occupied KS states (magenta). The side view is displayed in Fig. 6.8.

List of Figures

List of Tables